April 25, 2023

TP-LIC-LET-0070
Project Number 99902100

U.S. Nuclear Regulatory Commission
Washington, DC 20555-0001
ATTN: Document Control Desk

Subject: Transmittal of TerraPower, LLC Report, "An Analysis of Potential Volcanic Hazards at the Proposed Natrium™ Site near Kemmerer, Wyoming," Revision 0A

This letter transmits the TerraPower, LLC (TerraPower) topical report, "An Analysis of Potential Volcanic Hazards at the Proposed Natrium™ Site near Kemmerer, Wyoming," Revision 0A (enclosed). The volcanic hazards assessment documented in this report was conducted in accordance with U.S. Nuclear Regulatory Commission (NRC) Regulatory Guide (RG) 4.26, Revision 0. The report contains the characterization of quaternary volcanic systems, the regional tectono-magmatic model, the screening of volcanic hazards, and an evaluation of initial risk insights. The report also contains an analysis of mafic and silicic tephra-fall hazards, tephra-fall hazards and characteristics, and considerations for tephra falls at the proposed facility. TerraPower has plans in place to evaluate and address the impacts of volcanic hazards characterized in this report. For example, applicable volcanic hazard impacts may be addressed by operations and maintenance procedures.

TerraPower requests the NRC's review and approval of the volcanic hazard characterization presented in this report for design and operation of the Natrium Reactor Plant[1] at the Kemmerer Power Station Unit 1 site. TerraPower also requests the NRC's review and approval of the volcanic hazard characterization methodology presented in this report for potential use by future applicants, where applicable.

TerraPower requests that a nominal review duration of 12 months be considered.

[1] Natrium is a TerraPower and GE-Hitachi technology.

This letter and enclosure make no new or revised regulatory commitments.

If you have any questions regarding this submittal, please contact Ryan Sprengel at rsprengel@terrapower.com or (425) 324-2888.

Sincerely,

Ryan Sprengel
Director of Licensing, Natrium
TerraPower, LLC

Enclosure: TerraPower, LLC report, "An Analysis of Potential Volcanic Hazards at the Proposed Natrium™ Site near Kemmerer, Wyoming," Revision 0A

cc: Mallecia Sutton, NRC
William Jessup, NRC
Andrew Proffitt, NRC
Nathan Howard, DOE
Jeff Ciocco, DOE

TP-LIC-LET-0070
ENCLOSURE

TerraPower, LLC Topical Report
"An Analysis of Potential Volcanic Hazards at the Proposed Natrium™ Site near Kemmerer, Wyoming" Revision 0A

a TerraPower & GE-Hitachi technology

Document Title: An Analysis of Potential Volcanic Hazards at the Proposed Natrium™ Site near Kemmerer, Wyoming				
Natrium Document No.: NAT-3226	**Rev. No.:** 0A	**Page:** 1 of 168	**Effective Date:** See EDMS	**Target Quality Level:** QL-3
Alternate Document No.:	**Alt. Rev.:**	**Originating Organization:** Engineering		**Quality Level:** QL-3
Export Controlled: No	**Attachments:**			**Document Type:** Report
Open Items: No	**Status:** Released			**Natrium MSL #:**
Approval				
Approval signatures are captured and maintained electronically; see Electronic Approval Records in EDMS. ☐ Supplemental Signature Sheet Attached				

EXECUTIVE SUMMARY

During the last 2.6 million years, approximately 575 volcanoes have erupted within 320 km of the proposed Natrium™ site. The closest of these volcanoes, however, is located 117 km from the proposed site. A systematic assessment of potential hazards from these volcanoes was conducted using recently developed guidance from the U.S. Nuclear Regulatory Commission. This volcanic hazards assessment demonstrates that the proposed site is located at sufficient distances from sources of potential future volcanic eruptions to preclude most hazardous phenomena from reaching the site. Nevertheless, some future eruptions might be large enough to generate buoyant plumes of volcanic rock (i.e., tephra), which could reach altitudes of 5–40 km and be transported hundreds of kilometers down wind to the proposed site.

Detailed analyses in this report assess the characteristics of potential tephra-fall hazards at the proposed site, including an evaluation of the likelihoods for hazard occurrences. Tephra-fall hazards represent beyond-design-basis events, as the likelihood of the site experiencing any measurable tephra fall is $<1x10^{-5}$/yr. Tephra from most potential eruptions in the region has a limited potential to reach the site, due to the relatively low altitudes reached by eruption plumes and limits on the amount of time high-velocity winds are directed towards the proposed site. For most of these smaller potential eruptions, tephra-fall deposits would have an average thickness of ≈0.1 cm with a $6x10^{-6}$/yr probability of exceedance. The 95th percentile deposit thickness from these smaller eruptions is ≈17 cm, which has a $5x10^{-7}$/yr probability of exceedance.

Nevertheless, potential “supervolcano” eruptions from the Yellowstone caldera system also must be considered in the hazard analysis. At the proposed site, these large eruptions could produce an average tephra-fall deposit of 84 cm with an estimated $<5x10^{-7}$ annual probability of exceedance, and a 95th percentile thickness of 113 cm at an estimated $<7x10^{-8}$ annual probability of exceedance. Considering the potential for both small- and large-volume eruptions, the total tephra-fall hazard at the proposed site is bounded by a 130-cm-thick deposit (i.e., 95th percentile thickness), which has a $<5.7x10^{-7}$/yr probability of exceedance.

The tephra-fall deposit from a future Yellowstone supervolcano eruption would likely deposit enough material in ephemeral and intermittent stream channels surrounding the proposed site to affect the flow of water in these streams during infrequent flood events. Conservative, first-order models indicate that debris-flow conditions and associated overbank flooding might develop in some active stream channels in the North Fork of the Little Muddy Creek drainage basin, which encompasses the proposed site. However, these active channels are incised into wider, inactive channels, which have sufficient depth and width to contain overbank floods from potential debris flows. As a result, potential debris flows after a Yellowstone supervolcano eruption would not lead to flooding conditions at the proposed site. Tephra-fall deposits from smaller-volume eruptions also would not lead to flooding conditions at the proposed site.

Volcanic eruptions would be preceded by days-to-weeks of phenomena that indicate an eruption might occur. The occurrence of these precursory phenomena would provide sufficient warning time to alert facility staff of an enhanced potential for a tephra-fall event at the site, and implement any planned monitoring and mitigation activities. Once an eruption commences, there would likely be at least 1–4 hrs before tephra could be transported from the volcano to the site. Most potential tephra-fall eruptions would likely last 0.5–2 days, with tephra accumulation rates at the site of 1–5 mm/hr and airborne particle concentrations on the order of 10 g/m^3. Airborne particle concentrations on the order of 10 mg/m^3 would likely persist for days-to-weeks

after the eruption, then decrease exponentially with a half-life of approximately 40 days. However, a potential Yellowstone supervolcano eruption could increase these values by a factor of ten.

The advanced warning time for the onset of potential hazards at the site, and the relatively slow accumulation rates of tephra-fall deposits, allows for the practicable implementation of operator actions to mitigate many of the potentially adverse effects of tephra falls. Removal of deposits from building roofs and from external electrical systems appears practicable, even for the largest eruptions, as does the prevention of tephra ingress through air circulation systems. Tephra deposits can persist for months, to potentially years, after an eruption. Enhanced maintenance and inspection procedures for mechanical and electrical systems also appear capable of mitigating potentially adverse effects of prolonged exposure to volcanic tephra.

Table of Contents

EXECUTIVE SUMMARY i
List of Figures vi
List of Tables viii
1 INTRODUCTION 1
1.1 Applicable Regulatory Requirements 1
1.2 General Site Characteristics 2
2 CHARACTERIZATION OF QUATERNARY VOLCANIC SYSTEMS 4
2.1 Yellowstone Volcanic Field 4
2.2 Upper Wind River Basin Volcanic Field 10
2.3 Leucite Hills Volcanic Field 13
2.4 Northern Black Rock Desert Volcanic Field 15
2.5 Curlew Valley Volcanic Field 17
2.5.1 Black Mountain, Utah 20
2.6 Blackfoot Reservoir Volcanic Field 22
2.7 Eastern Snake River Plain Volcanic Field 26
2.8 Volcanoes >320 km from the Proposed Site 30
2.9 Summary of Quaternary Volcano Characteristics in the Site Region 31
3 REGIONAL TECTONO-MAGMATIC MODEL 33
4 SCREENING OF VOLCANIC HAZARDS 37
4.1 Opening of New Vents 37
4.2 Proximal Hazards 42
4.3 Lava Flows 43
4.4 Pyroclastic Density Currents 45
4.5 Tephra Falls 45
4.5.1 Debris Flows 47
4.6 Summary of Hazards Screening 49
5 EVALUATION OF INITIAL RISK INSIGHTS 50
6 ANALYSIS OF MAFIC TEPHRA-FALL HAZARDS 51
6.1 Numerical Models for Tephra-fall Hazards 51
6.2 Modifications to ASHPLUME Version 1.0 53
6.3 Parameterization of ASHPLUME2 56
6.3.1 Mafic Eruption Volumes 58
6.3.2 Power and Duration of Mafic Eruptions 62
6.3.3 Total Grain-Size Distributions for Mafic Tephra Deposits 62

6.3.4 Wind Speed Data for Mafic Tephra Hazards Analyses 63
6.3.5 Summary of Input Parameters for Mafic Tephra Hazards Analyses 67
6.4 Mafic Tephra-Fall Hazards at the Proposed Natrium™ Site 68
6.4.1 Tephra-fall Hazards from the Leucite Hills Volcanic Field 68
6.4.2 Tephra-fall Hazards from the Upper Wind River Basin Volcanic Field 72
6.4.3 Mafic Tephra-fall Hazards from the Blackfoot Reservoir Volcanic Field 75
6.4.4 Mafic Tephra-fall Hazards from the Eastern Snake River Plain Volcanic Field 78
6.4.5 Summary of Mafic Tephra-fall Hazards at the Proposed Natrium™ Site 82
6.4.6 Potential for Debris-flow Hazards from Mafic Tephra-fall Deposits 84
7 ANALYSIS OF SILICIC TEPHRA-FALL HAZARDS 88
7.1 Silicic Tephra-Fall Characteristics 88
7.1.1 Silicic Tephra-Fall Volumes 88
7.2 Power and Duration of Silicic Eruptions 95
7.3 Total Grain-Size Distributions for Silicic Tephra Deposits 95
7.4 Wind Speed Data for Silicic Tephra Hazards Analyses 97
7.5 Summary of Input Parameters for Silicic Tephra Hazards Analyses 100
7.6 Silicic Tephra-Fall Hazards at the Proposed Natrium™ Site 100
7.6.1 Silicic Tephra-fall Hazards for the Blackfoot Reservoir Volcanic Field 101
7.6.2 Silicic Tephra-fall Hazards for the Curlew Valley Volcanic Field 104
7.6.3 Silicic Tephra-fall Hazards for the Eastern Snake River Plain Volcanic Field 107
7.6.4 Silicic Tephra-fall Hazards for Yellowstone Volcanic Field VEI3–4 Eruptions 110
7.6.5 Silicic Tephra-fall Hazards for Yellowstone Volcanic Field VEI4–5 Eruptions 113
7.6.6 Silicic Tephra-fall Hazards for Yellowstone Caldera (VEI8+) Eruptions 116
7.6.7 Summary of Silicic Tephra-fall Hazards at the Proposed Natrium™ Site 117
7.7 Potential for Debris-flow Hazards from Silicic Tephra-fall Deposits 120
8 TEPHRA-FALL HAZARDS AT THE PROPOSED NATRIUM™ SITE 123
9 CHARACTERISTICS OF TEPHRA FALLS 125
9.1 Composition 125
9.2 Particle Sizes 126
9.3 Thermal Conductivity 127
9.4 Thermal Emissivity 127
9.5 Deposit Densities 129
9.6 Tephra Eruption Characteristics 130
9.7 Post-Eruption Characteristics 131
10 CONSIDERATIONS FOR POTENTIAL TEPHRA-FALL EVENTS AT THE PROPOSED FACILITY 134

10.1 Human Health and Safety 134
10.2 SSC Performance 134
10.2.1 Air Handling Systems 135
10.2.2 Electrical Systems 135
10.2.3 Mechanical Systems 135
10.2.4 Structural Loads 136
10.3 Operational Activities 136
11 REFERENCES 138

List of Figures

Figure 1. Location Map of the proposed Natrium™ site (green dot). 3
Figure 2. Distribution of Quaternary faults and historical earthquake epicenters >M2.5. 5
Figure 3. Extent of pyroclastic flows from Quaternary Yellowstone caldera-forming eruptions. 7
Figure 4. YVF volcanic vents and lavas. 9
Figure 5. Location map of the UWRB volcanic field. 11
Figure 6. Map of the Leucite Hills Volcanic Field. 14
Figure 7. Map of the northern part of the Black Rock Desert volcanic field, Utah. 16
Figure 8. Map of the CVVF, Utah. 19
Figure 9. Location map of Black Mountain, Utah. 21
Figure 10. Map of the BRVF. 23
Figure 11. BRVF Rhyolite lavas and domes. 25
Figure 12. ESRP regional tectono-magmatic setting. 27
Figure 13. Eastern ESRP and Spencer-High Point rift zone. 29
Figure 14. Regional patterns of faulting and seismicity, and distribution of Quaternary volcanic rocks. 34
Figure 15. Smoothing factors (i.e., bandwidths) for (A) Gaussian and (B) Epanechnikov kernels. 39
Figure 16. Evaluation of changes in smoothing bandwidth for a Gaussian kernel, using PVHA_YM Version 2.0. 40
Figure 17. Evaluation of changes in smoothing bandwidth for an Epanechnikov kernel, using PVHA_YM Version 2.0. 41
Figure 18. Topographic characteristics of the site region. 44
Figure 19. Distribution of pyroclastic density current deposits from Yellowstone Caldera. 46
Figure 20. Map of the NFLMC drainage basin that surrounds the proposed site. 48
Figure 21. Wind sectors that encompass potential source volcanoes and the proposed site. 65
Figure 22. Distributions of wind speeds for selected pressure levels above the proposed Natrium™ site. 66
Figure 23. Results of hazard calculations for LHVF eruption sources. 70
Figure 24. Annual exceedance probabilities for mafic tephra-fall hazards from the LHVF. 72
Figure 25. Results of hazard calculations for UWRB eruption sources. 73
Figure 26. Annual exceedance probabilities for mafic tephra-falls from the UWRB volcanic field. 75
Figure 27. Results of hazard calculations for BRVF eruption sources. 76
Figure 28. Tephra-fall hazard curve for the BRVF volcanic field. 78
Figure 29. Results of hazard calculations for ESRP eruption sources. 80
Figure 30. Tephra-fall hazard curve for the ESRP volcanic field. 82
Figure 31. Summary of mafic tephra-fall hazards at the proposed site. 84
Figure 32. Regional wind sectors used for silicic tephra-fall hazards analyses. 99
Figure 33. Results of silicic tephra-fall hazard calculations for BRVF eruption sources. 102
Figure 34. Annual exceedance probabilities for silicic tephra-fall hazards from the BRVF. 104
Figure 35. Results of silicic tephra-fall hazard calculations for CVVF eruption sources. 105
Figure 36. Tephra-fall hazard curve for CVVF volcanic field silicic eruptions. 107
Figure 37. Results of silicic tephra-fall hazard calculations for ESRP eruption sources. 108
Figure 38. Annual exceedance probabilities for silicic tephra-fall hazards from the ESRP volcanic field. 110
Figure 39. Results of silicic tephra-fall hazard calculations for YVF VEI3–4 eruption sources. 111
Figure 40. Annual exceedance probabilities for silicic tephra-fall hazards from YVF VEI3–4 eruptions. 113

Figure 41. Results of silicic tephra-fall hazard calculations for YVF VEI4–5 silicic pyroclastic eruptions. 114
Figure 42. Annual exceedance probabilities for silicic tephra-fall hazards from YVF VEI4–5 pyroclastic eruptions. 116
Figure 43. Compilation of annual exceedance probabilities for silicic tephra-fall hazards from potential VEI2–5 silicic eruptions in the site region. 119
Figure 44. Site location map showing nearby stream channels (aqua lines). 121
Figure 45. Summary of annual exceedance probabilities for tephra-fall hazards from potential VEI1–5 eruptions in the site region. 124
Figure 46. Representative thermal emissivities of volcanic tephra, from figure 2 in Williams and Ramsey (2019). 128
Figure 47. Detailed thermal emissivities of volcanic tephra, showing sensitivity to particle size. 129

List of Tables

Table 1. Volcanic Explosivity Index, after Newhall and Self (1982). 4
Table 2. YVF summary of distances represented by maximum-magnitude events. 10
Table 3. UWRB volcanic field summary of distances represented by maximum-magnitude events. 13
Table 4. LHVF summary of distances represented by maximum-magnitude events. 15
Table 5. NBRD volcanic field summary of distances represented by maximum-magnitude events. 17
Table 6. CVVF summary of distances represented by maximum-magnitude events. 20
Table 7. BRVF summary of distances represented by maximum-magnitude events. 26
Table 8. ESRP summary of distances represented by maximum-magnitude events. 30
Table 9. Summary of Quaternary volcanoes in the site region. 32
Table 10. Screening summary for potential volcanic hazards at the proposed Natrium™ site. 49
Table 11. Cone and lava volumes for the LHVF, from Lange et al. (2000). 60
Table 12. Summary of tephra volumes for mafic eruptions in the site region. 62
Table 13. Calculated column height, duration, power and eruption rate for the range of mafic eruptions interpreted for volcanic fields in the site region. 62
Table 14. Median diameter and sorting characteristics for mafic tephra-fall deposits, after Costa et al. (2016). 63
Table 15. Wind speed statistics for atmospheric pressure levels and volcanic fields that are used in the ASHPLUME2 analysis of mafic tephra-fall hazards. 67
Table 16. Input parameters for ASHPLUME2 analysis of mafic tephra-fall hazards. 67
Table 17. Summary of ASHPLUME2 calculations for LHVF mafic tephra hazards. 69
Table 18. Probability that winds from LHVF are directed towards proposed site. 71
Table 19. Summary of ASHPLUME2 calculations for UWRB mafic tephra hazards. 72
Table 20. Probability that winds from UWRB are directed towards proposed site. 74
Table 21. Summary of ASHPLUME2 calculations for BRVF mafic tephra hazards. 75
Table 22. Probability that winds from BRVF are directed towards proposed site. 77
Table 23. Summary of ASHPLUME2 calculations for ESRP mafic tephra hazards. 79
Table 24. Probability that winds from ESRP are directed towards proposed site. 81
Table 25. Summary of conditional tephra-fall hazards at the proposed site, from mafic volcanoes in the site region. 82
Table 26. Summary of exceedance probabilities for mafic tephra-fall hazards at the proposed site, from potential mafic volcanic eruptions in the site region. 83
Table 27. Calculated discharge rates for stream channels in the NFLMC basin, using equations 24–29 in Hedman and Osterkamp (1982). 86
Table 28. Calculated scour depths for stream channels in the NFLMC basin, using Equation 5 from Leopold et al. (1966). 86
Table 29. Thicknesses of scour zones that represent the source of <0.25 mm particles, which can be suspended during flooding events in the NFLMC basin. 87
Table 30. Compilation of Holocene silicic dome and lava eruption characteristics. 89
Table 31. Volumes of CPR rhyolite eruptions, from Christiansen et al. (2007, Table 2), and Robinson et al. (2016). 91
Table 32. Volumes of silicic volcanoes in the BRVF, from Ford (2005). 92
Table 33. Summary of silicic volcano volumes for the ESRP volcanic field. 93
Table 34. Estimates of tephra-fall volumes for silicic volcanoes in the site region, based on assumed relationship to dome and lava flow volumes. 94
Table 35. Calculated eruption *duration* and *power* for VEI eruptions that are representative of silicic tephra-fall eruptions in the site region. 95

Table 36. Median diameter and sorting characteristics for silicic tephra-fall deposits, after Costa et al. (2016). 96
Table 37. Densities of tephra particles reported for analogue volcanoes in Table 30. 96
Table 38. Wind speed statistics for atmospheric pressure levels and volcanic fields that are used in the ASHPLUME2 analysis for silicic tephra-fall hazards. 97
Table 39. Input parameters for ASHPLUME2 analysis of silicic tephra-fall hazards....100
Table 40. Summary of ASHPLUME2 calculations for BRVF silicic tephra hazards. 101
Table 41. Probability that winds from BRVF silicic eruptions are directed towards the proposed site. 103
Table 42. Summary of ASHPLUME2 calculations for CVVF silicic tephra hazards. 104
Table 43. Probability that winds from CVVF silicic eruptions are directed towards the proposed site. 106
Table 44. Summary of ASHPLUME2 calculations for ESRP silicic tephra hazards. 107
Table 45. Probability that winds from ESRP silicic eruptions are directed towards the proposed site. 109
Table 46. Summary of ASHPLUME2 calculations for YVF VEI3–4 silicic tephra hazards....110
Table 47. Probability that winds from YVF VEI3–4 silicic eruptions are directed towards the proposed site. 112
Table 48. Summary of ASHPLUME2 calculations for YVF VEI4–5 silicic tephra hazards....114
Table 49. Probability that winds for YVF VEI4–5 silicic pyroclastic eruptions are directed towards the proposed site. 115
Table 50. Summary of conditional tephra-fall hazards at the proposed site, from silicic volcanoes in the site region. 118
Table 51. Summary of exceedance probabilities for silicic tephra-fall hazards at the proposed site, from potential silicic eruptions in the site region. 118
Table 52. Thickness of additional tephra-fall deposits that would be required to transition from flood flow (10% suspended particles) to flood flow (60% suspended particles) conditions. 120
Table 53. Calculated depths needed for a 300-m-wide channel to contain potential debris flows in the NFLMC basin following deposition of a Yellowstone VEI8 tephra fall. 122
Table 54. Combined mafic (Table 26) and silicic (Table 51) tephra-fall hazards from all potential volcanic sources in the proposed site region. 123

1 INTRODUCTION

The proposed TerraPower Natrium™ site is located approximately 10 km south of the town of Kemmerer in southwestern Wyoming. Within the last 2.6 Myr (i.e., the Quaternary Period of geological time), volcanoes have erupted in a broad region around the site. Because volcanic eruptions in this region occurred in the geologically recent past, there is likely some undefined potential for future volcanic eruptions to occur. Consequently, a volcanic hazards assessment (VHA) appears warranted to evaluate the potential for future volcanic eruptions in this region. The VHA also would characterize the types of volcanic phenomena those potential eruptions might produce, and determine if those phenomena could present an external-event hazard at the proposed Natrium™ site. This document describes the technical basis for a VHA that was conducted for the proposed Natrium™ site, in support of a planned license application to the U.S. Nuclear Regulatory Commission (NRC) for this facility.

1.1 Applicable Regulatory Requirements

For nuclear power reactors licensed under 10 CFR Part 50 regulatory requirements, the need to evaluate potential volcanic hazards arises in part from 10 CFR Part 100, which establishes siting requirements for power and test reactors subject to licensing under 10 CFR Part 50. 10 CFR 100.23(c) states that "…each applicant shall investigate all geologic and seismic factors (for example, volcanic activity) that may affect the design and operation of the proposed nuclear power plant irrespective of whether such factors are explicitly included in this section."

In addition, 10 CFR Part 50, Appendix A, General Design Criterion 2, item (1), addresses the importance of "appropriate consideration of the most severe of the natural phenomena that have been historically reported for the site and surrounding area, with sufficient margin for the limited accuracy, quantity, and period of time in which the historical data have been accumulated." For potentially hazardous geologic phenomena that have low rates of recurrence (e.g., earthquakes), the NRC has considered the Quaternary Period as providing sufficient margin to the historical period to accurately evaluate the timing and character of past events (i.e., NUREG 0800, Section 2.5.1).

The NRC issued Regulatory Guide 4.26 (Nuclear Regulatory Commission, 2021) to provide potential license applicants with methods and approaches that the NRC staff considers acceptable for conducting a VHA, and to facilitate the staff's review of VHAs in anticipated license applications. The Regulatory Guide 4.26 methodology provides a systematic approach to assessing volcanic hazards, including a graded approach that allows for the development of increasingly detailed information as risk insights warrant. The VHA for the Natrium™ site was conducted following the approach outlined in Regulatory Guide 4.26, with the exception of using a Senior Seismic Hazards Analysis Committee (SSHAC) process to conduct this VHA. Based on initial site characterization activities, and recognition that the nearest Quaternary volcano was >117 km from the proposed site, uncertainties in the available information appeared sufficiently constrained to successfully conduct the VHA without using the SSHAC process. If, during the VHA, it was determined that uncertainties in the available information could not be sufficiently constrained, then a SSHAC process could be implemented to address those uncertainties.

The Regulatory Guide 4.26 methodology consists of an initial characterization stage, which identifies Quaternary volcanoes in the site region (i.e., <320 km of the proposed site) and any deposits within the site vicinity (i.e., <40 km of the proposed site) that originated from large

Quaternary volcanic eruptions >320 km from the proposed site. After relevant volcanoes are identified, the various types of potentially hazardous phenomena (e.g., lava flows) are characterized, and the maximum magnitudes of these phenomena are then used in a screening assessment. Only volcanic systems that have some potential to create phenomena that could reach the proposed site are included for further, detailed analysis. In addition, the VHA can consider whether future volcanic activity would be consistent with the tectonic and magmatic conditions that controlled past volcanic eruptions in the region, or if this activity would be controlled by different tectonic or magmatic conditions. Only those volcanic systems that are consistent with current tectono-magmatic conditions need to be assessed further in the VHA.

For those volcanic systems that have a potential for eruptive phenomena to reach the site, the VHA can first assess the conditional hazard represented by these phenomena by conducting more detailed investigations. Typically, these investigations use insights from volcanoes that are analogous to those in the region, and numerical models of different volcanic processes. The conditional hazards (i.e., conditional on the eruption occurring) can be used to develop risk insights and determine if a fully probabilistic hazard should be assessed. This probabilistic hazard considers both the likelihoods that an initiating eruption will occur in the future, in addition to the likelihoods of different hazard-levels occurring at the proposed site. The results of this stage of the VHA can then be used to support additional analyses that evaluate the performance or design of structures, systems and components (SSC) that are important to safety, or the development of operational actions to mitigate the adverse effects of the hazards on SSC.

Volcanic hazards represent potential external events, which might initiate the unacceptable performance of safety-significant SSCs. The facility response to the initiating event is represented by an ensuing sequence of successes and failures of dependent SSCs, which culminates in a defined end state (Nuclear Energy Institute, 2019). Guidance in Nuclear Regulatory Commission (2020) and Nuclear Energy Institute (2019) identifies event sequences that must be included in the facility's design basis (i.e., Design Basis Event sequences) as having average occurrences of $1x10^{-2}$ to $1x10^{-4}$/reactor year. Beyond Design Basis Event sequences (i.e., not included in the facility design but evaluated in the probabilistic risk assessment) have average occurrences of less than $1x10^{-4}$ but greater than $5x10^{-7}$/reactor year. Importantly, the 5th and 95th percentile confidence intervals about the average also must be considered in identifying these event sequences (Nuclear Energy Institute, 2019). If volcanic hazards need to be evaluated in detail for the proposed site, these analyses will need to develop estimates of average and 95th percentile hazard levels for use in subsequent analyses of potential event sequences.

1.2 General Site Characteristics

The location of the proposed Natrium™ site is shown in Figure 1, along with the major physiographic provinces of the western United States. The site footprint covers approximately 1 km^2, and 320 km and 40 km buffers (Nuclear Regulatory Commission, 2021) around the site footprint also are shown. The proposed site is located in the Middle Rocky Mountain physiographic province (Fenneman and Johnson, 1946). In most of the site vicinity, bedrock geology consists of Paleozoic and Mesozoic sedimentary rocks that were faulted and deformed by compressional tectonic forces primarily between 50–150 Ma during the Sevier Orogeny (e.g., Dixon, 1982; Malone et al., 2022). In the eastern part of the site vicinity in the Wyoming Basin (Figure 1), the Sevier thrust-belt bedrock is overlain by Cenozoic sedimentary rocks that post-date the Laramide Orogeny (e.g., Dickinson et al., 1988). There is no evidence to suggest that any volcanic eruptions have occurred within the site vicinity during the last 150 Myr.

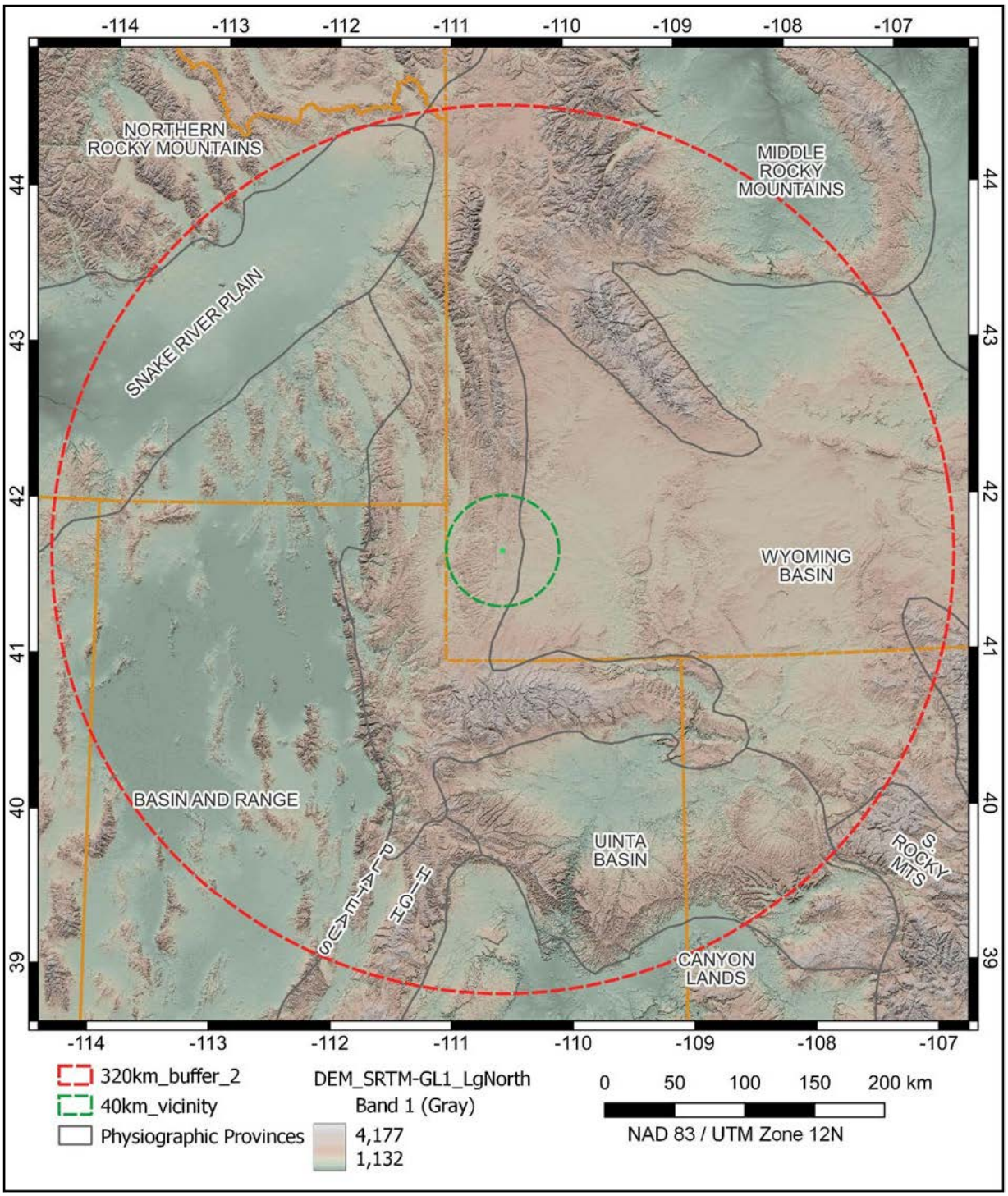

Figure 1. Location Map of the proposed Natrium™ site (green dot). 40 km (green dash) site vicinity and 320 km (red dash) site region, major rivers (U.S. Geological Survey, 2022b), and physiographic provinces and sections (Fenneman and Johnson, 1946). Digital Elevation model SRTM-1 (30 m resolution) from Open Topography (2013).

2 CHARACTERIZATION OF QUATERNARY VOLCANIC SYSTEMS

The objective of this chapter is to provide a summary of Quaternary volcanic systems that are located within 320 km of the proposed Natrium™ site. These volcanic systems were identified by information published by the U.S. Geological Survey, State Geological Surveys, independent research in peer-reviewed publications, digital data sets, and graduate student theses. In addition, information also is developed on the identification of volcanic deposits from sources more than 320 km from the proposed site. The volcanological summaries focus on the identification and characterization of key features that are most significant to the early stages of the VHA: the ages and locations of individual volcanic vents, and the types and magnitudes of potentially hazardous phenomena.

A Volcanic Explosivity Index (VEI) is commonly used to characterize explosive volcanic eruptions (Newhall and Self, 1982). The VEI is based primarily on the volumes of tephra produced during explosive volcanic eruptions, which is used to represent the magnitude of eruption explosivity on a logarithmic scale (Table 1). In addition, Newhall and Self (1982) provide a range of characteristic column heights, based on the analysis of historical and well-characterized explosive volcanic eruptions. In the discussion of volcanoes within the site region, the general VEI characteristic is a useful descriptor of the potential for different volcano types to generate explosive eruptions.

Table 1. Volcanic Explosivity Index, after Newhall and Self (1982). Values with "*" are calculated from the volumes and column heights in Newhall and Self (1982), assuming general characteristics of mafic to silicic (i.e., increasing silica content with increasing explosivity) volcanic eruptions. DRE = dense rock equivalent.

VEI	Tephra-fall volume (m^3)	*Magma Density (kg/m^3)	*Deposit Density (kg/m^3)	*Deposit Volume DRE (m^3)	*Deposit Mass (kg) DRE	Column Heights (km)
1	1.0E+06	2700	1250	4.6E+05	1.3E+09	0.1–1
2	1.0E+07	2600	1200	4.6E+06	1.2E+10	1–5
3	1.0E+08	2500	1200	4.8E+07	1.2E+11	3–15
4	1.0E+09	2450	1150	4.7E+08	1.2E+12	10–25
5	1.0E+10	2400	1100	4.6E+09	1.1E+13	25–40
6	1.0E+11	2300	1000	4.3E+10	1.0E+14	30–50
7	1.0E+12	2300	800	3.5E+11	8.0E+14	30–50

2.1 Yellowstone Volcanic Field

The Yellowstone Volcanic Field (YVF) represents the latest stage of extensive bimodal (i.e., both mafic and silicic magmas erupted) volcanism that has progressively migrated since 15 Ma from south-central Idaho to the northeast, in response to the North American tectonic plate travelling southwest over a mantle hotspot (Morgan, 1972; Pierce and Morgan, 1992; Camp and Wells, 2021). High fluxes of mantle-derived basalt were intruded into the crust and generated large volumes of silicic magma by partial crustal melting (e.g., Doe et al., 1982; Hildreth et al., 1991), which formed large-volume caldera eruptions. In eastern Idaho, the crust was deformed by earlier Basin and Range extensional faulting prior to the onset of deformation associated with

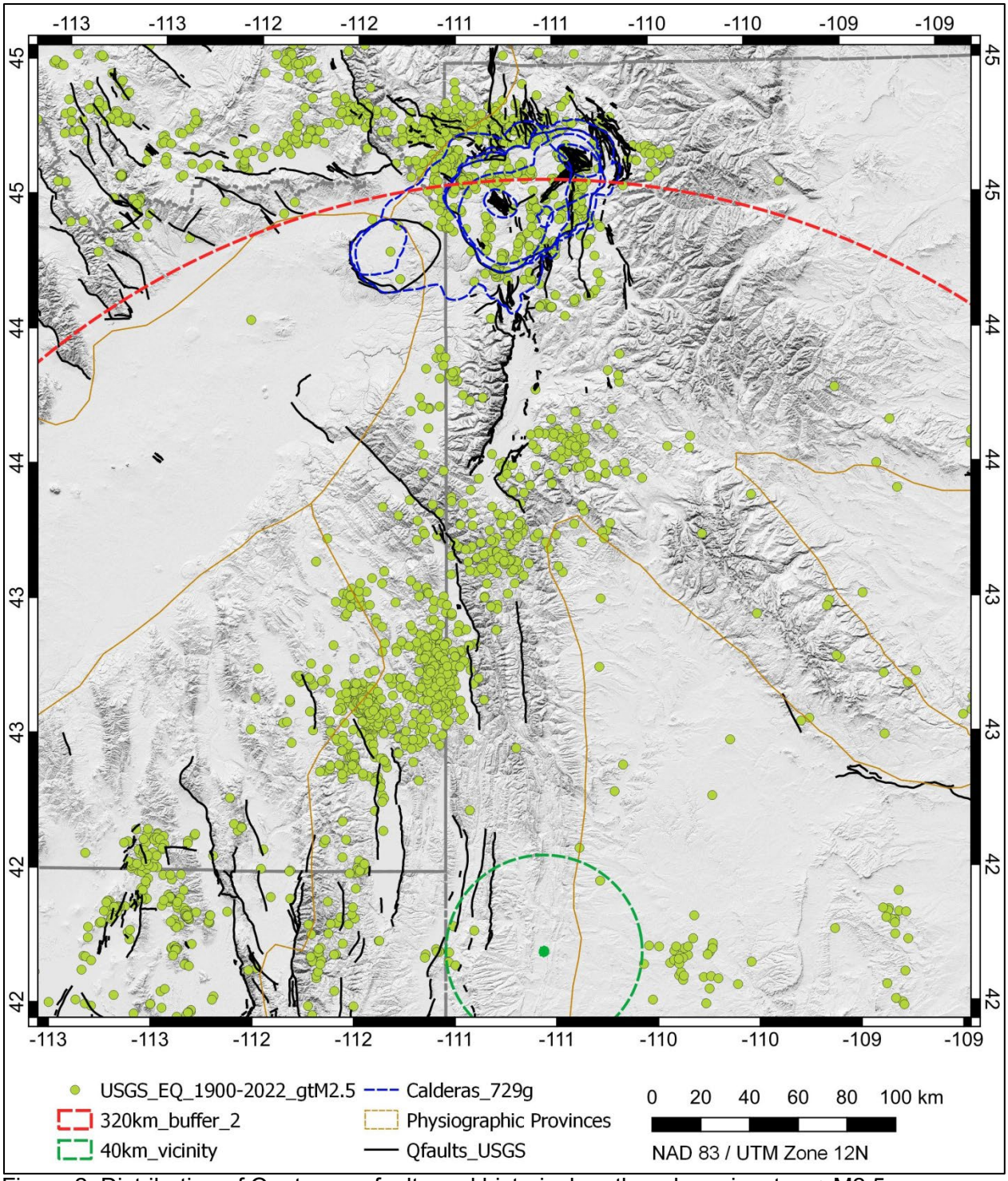

Figure 2. Distribution of Quaternary faults and historical earthquake epicenters >M2.5. Natrium™ site (green dot), with 40 km (green dash) site vicinity and 320 km (red dash) site region. Digital Elevation model SRTM-1 (30 m resolution) (OpenTopography, 2013). Quaternary faults in black lines (Schmitt, 2017), and historical earthquake epicenters in green circles (U.S. Geological Survey, 2022a).

passage of the Yellowstone hotspot (e.g., Janecke, 2007; Camp et al., 2015). Passage of the North American plate over the Yellowstone hotspot created a large area of enhanced crustal deformation, which is expressed as a pattern of faults and historical seismicity that is distributed parabolically (Figure 2) around the YVF (e.g., Anders et al., 1989; Janecke, 2007).

The YVF is the largest Quaternary volcanic system in the site region, having undergone three major caldera-forming eruptions (VEI7–8) since 2.1 Ma that produced more than 3,700 km^3 of magma as pyroclastic deposits (Christiansen, 2001). Large volumes of rhyolitic lava also erupted between the caldera-forming eruptions, much of which has been buried by younger deposits but is inferred from subsurface investigations (e.g., Christiansen, 2001). Since the end of the last caldera-forming eruption, numerous rhyolitic and basaltic lavas have erupted from vents located within and outside the caldera margins. Christiansen (2001) estimates that the volume of effusive magma is equivalent to the volume of magma that erupted explosively, indicating the total magmatic volume of this Quaternary volcanic system is >6,400 km^3.

The large-volume Quaternary pyroclastic units from the YVF (i.e., Christiansen, 2001) are:

- Huckleberry Ridge, erupted 2,450 km^3 at 2.1 Ma, with 3 distinct flow members (A–C).
- Mesa Falls, erupted >280 km^3 at 1.29 Ma, with a single flow underlain by tephra fall.
- Lava Creek, erupted >1,000 km^3 at 0.64 Ma, with 2 distinct flow members (A–B).

The distribution of these pyroclastic units is shown in Figure 3. Although caldera-forming eruptions have not been observed, there is general agreement (e.g., Wilson, 2008) that such large-volume pyroclastic flows originate from multiple vents located primarily along the caldera margins. Early stages of the caldera eruption might produce tephra plumes that rise to tens of kilometers altitude, but often such plumes are absent. Massive pyroclastic fountains issue from the vent(s), and form pyroclastic density currents that flow radially from the vent. As the eruption progresses, mass-flow rates increase as the vent area increases due to faulting and foundering of the caldera roof, leading to increasing run-out distances for the pyroclastic flows. Fine ash can be elutriated from the hot pyroclastic flows, which rises buoyantly and is dispersed downwind for hundreds to thousands of kilometers (e.g., Woods and Wohletz, 1991; Wilson, 2008). These co-ignimbrite ash plumes, and not Plinian eruption columns, are the likely source of some of the widespread Yellowstone ash deposits that have been observed in scattered locations throughout much of the western U.S.A. (Izett and Wilcox, 1982).

These Yellowstone pyroclastic flows are some of the largest-volume pyroclastic flows that have erupted from Quaternary calderas in North America. Nevertheless, these flows traveled a maximum of 120 km from the presumed source located along the rim of the caldera (Figure 3). This flow distance was limited, in part, by the steep topography that surrounds the Yellowstone caldera system, because pyroclastic flows have a limited ability to travel up large topographic gradients (e.g., Legros and Kelfoun, 2000). For example, approximately 120 km south of the Yellowstone caldera, the Huckleberry Ridge Tuff would have had to overcome a >1,000-m-high topographic barriers to continue southward flow. Based on the present day topography, the Yellowstone pyroclastic flows overtopped broad topographic obstacles on the order of 300–700 m high within 100 km of the caldera, but did not travel up channels with more than 800 m of relief within approximately 50 km of the caldera (Figure 3).

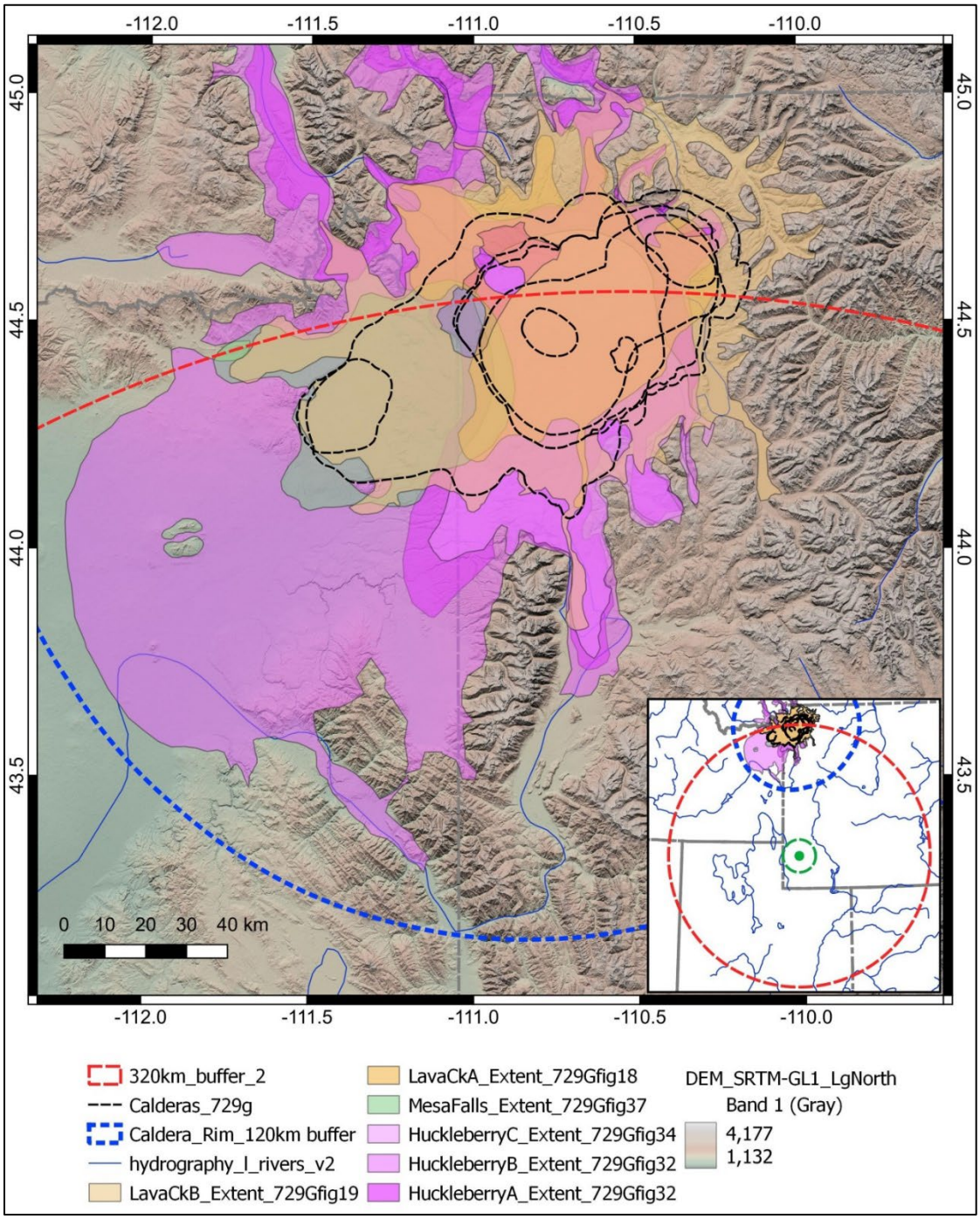

Figure 3. Extent of pyroclastic flows from Quaternary Yellowstone caldera-forming eruptions. From Christiansen (2001) and Christiansen et al. (2007). Blue dashed line represents a 120 km maximum distance for pyroclastic flow run-out from the caldera boundary. Inset map showing relationship to the proposed Natrium™ site (green dot), with 40 km (green dash) site vicinity and 320 km (red dash) site region, along with major rivers. Digital Elevation model SRTM-1 (30 m resolution) (OpenTopography, 2013).

Following the 0.64 Ma eruption of the Lava Creek Tuff, several episodes of rhyolitic lava and dome formation occurred within the Yellowstone caldera (Christiansen and Blank Jr., 1972). The youngest of these episodes occurred from 0.072–0.17 Ma, with the eruption of rhyolitic magma that is compositionally and petrogenetically distinct from the preceding post-caldera rhyolite (Christiansen et al., 2007). The youngest rhyolite is the Central Plateau Member of the Plateau Rhyolite of Christiansen (2001), which represents the eruption of >585 km^3 of rhyolitic magma (Christiansen et al., 2007) that has nearly filled the Yellowstone caldera (Figure 4). Christiansen et al. (2007) consider the Central Plateau Rhyolite (CPR) as representative of potential future hazards, because the petrogenesis of this rhyolite has remained consistent for the 26 eruptions that have occurred since 0.17 Ma. Within the site region there are 11 identified rhyolite vents associated with the CPR, and an additional 7 vents representing older rhyolite eruptions (Christiansen et al., 2007) (Figure 4). Although tephra-fall deposits have not been identified for most of the CPR eruptions (Christiansen, 2001), their large volumes (<0.1–70 km^3) suggest that an early, explosive phase and associated tephra deposits might be buried by later lava flows. If 10% of these eruption volumes formed tephra deposits, it would suggest that VEI2 (smallest volumes) to VEI5 (largest volumes) might be possible for a future CPR eruption (cf. Table 1).

Two smaller-volume pyroclastic flows erupted as part of the <170 ka CPR: the Tuff of Bluff Point (173±5 ka, ≈15 km^3 magma) and the Tuff of Cold Mountain Creek (143±5 ka, ≈3 km^3 magma) (Izett, 1981; Christiansen et al., 2007). The source for these pyroclastic eruptions is not known, although Christiansen et al. (2007) infer that the source for the Tuff of Bluff Point formed a small caldera at West Thumb basin on Yellowstone Lake. Distinct tephra-fall units are not recognized beneath these pyroclastic flows, but Christiansen et al. (2007) suggest such tephra falls might be buried beneath the voluminous rhyolite lava flows. Nevertheless, Izett (1982) correlated Quaternary ash deposits at “Hebgen Narrows” and “Natural Trap” to these two Tuffs, at locations 60–220 km from the Yellowstone Central Plateau. These ash deposits are compositionally and stratigraphically distinct from the underlying ash deposits that formed during the large-volume caldera eruptions (Izett, 1981). The volume and dispersivity of these two deposits suggests that they were produced by VEI4–5 eruptions (cf. Table 1).

Basaltic magmas have erupted throughout the history of the YVF. Most of these eruptions were small volumes (<0.1 km^3) of olivine tholeiite magma, similar to the Quaternary basalt erupted on the Eastern Snake River Plain (e.g., Christiansen et al., 2007). Several of the larger-volume lavas (<20 km^3) flowed up to 60 km from the source vent along principal drainages, or have covered the floor of the Island Park basin. A total of 20 basaltic vents occur in the site region, mostly as glaciated fissure vents or small shield volcanoes (i.e., Christiansen et al., 2007) (Figure 4). Christiansen (2001) observes that basalt generally is restricted to within approximately 40 km around the caldera system, but does not erupt within the calderas until approximately 1 Myr after the caldera formed. This process is thought to reflect the amount of time for the underlying rhyolitic magma system to cool sufficiently to allow basaltic magma to rise through the shallow crust and erupt (Christiansen, 2001; Christiansen et al., 2007). Typically, tholeiitic shield volcanoes do not produce convective tephra plumes (e.g., Walker, 1973), and would have a VEI≤1.

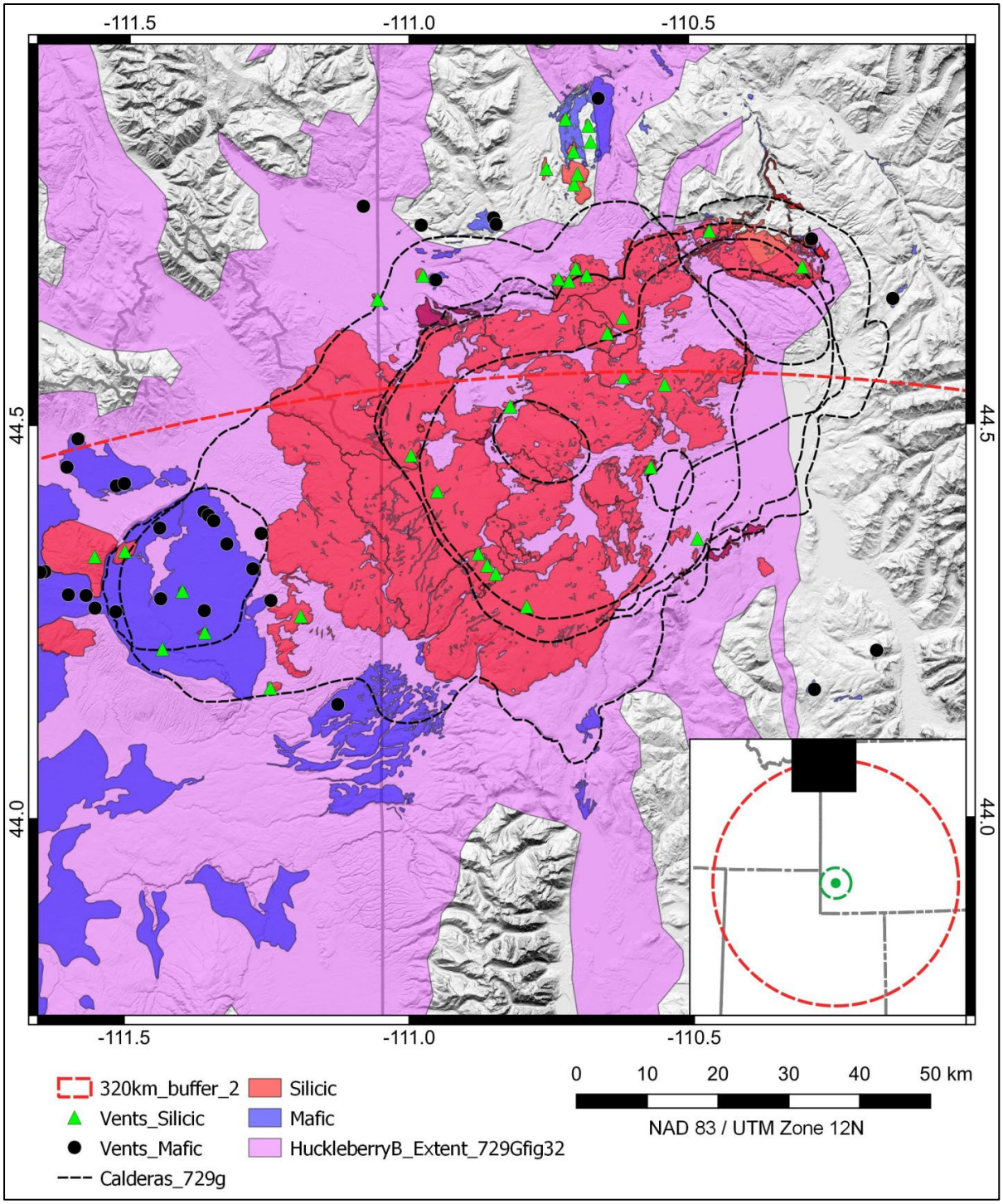

Figure 4. YVF volcanic vents and lavas. Inset map showing relationship to proposed Natrium™ site (green dot), with 40 km (green dash) site vicinity and 320 km (red dash) site region. Data sources: (Wyoming State Geological Survey, 2022), (National Park Service), (Horton, 2017), (Christiansen, 2001), (Christiansen et al., 2007). Digital Elevation model SRTM-1 (30 m resolution) from (OpenTopography, 2013).

Following the approach outlined in Regulatory Guide 4.26, the distances that maximum-magnitude hazards have traveled from the vent areas are summarized in Table 2 for mafic volcanoes, silicic volcanoes, and silicic calderas in the YVF. Note that the proximal hazard distance of 40 km is based on the criteria in Regulatory Guide 4.26, which restricts potential hazards to within 40 km of an erupting volcano.

Table 2. YVF summary of distances represented by maximum-magnitude events. VEI = Volcanic Explosivity Index; PDC = pyroclastic density currents. "?" indicates a maximum-magnitude distance cannot be developed based on current information, but the phenomena is characteristic of these volcanoes.

YVF	*Vents in Region*	*Ages (Ma)*	*General VEI*	*Tephra (km)*	*Opening of New Vent*	*Lava flows (km)*	*Proximal Hazards (km)*	*PDC (km)*
Mafic vents	20	<0.64	≤1	?	Yes	<60	<40	No
Silicic vents	11	<0.17	3–6	>220	Yes	<30	<40	<120
Calderas	3	<2.1	7–8	>1,000	Yes	No	<40	<120

2.2 Upper Wind River Basin Volcanic Field

Since approximately 5 Ma, five mafic-to-intermediate composition volcanoes developed in different parts of the Upper Wind River Basin (UWRB). One of these volcanoes formed during the Quaternary Period. The UWRB volcanoes are located approximately 60–100 km southeast of the Yellowstone caldera, in an area that has no mapped Quaternary faulting and relatively low historical seismicity (Figure 5). Petrological studies (Brueseke et al., 2018) indicate that the UWRB magmas are genetically distinct from similar-composition magma in the YVF, and likely originated from the partial melting of mantle that was metasomatized during a significantly older (i.e., pre-Sevier Orogeny) period of tectonic plate subduction. In contrast, mafic-to-intermediate composition magmas in the YVF lack geochemical enrichments related to mantle metasomatism (e.g., Hildreth et al., 1991). A combination of crystal fractionation, magma mixing, and crustal assimilation is thought to produce the compositional diversity in the UWRB magmas (Downey, 2015; Brueseke et al., 2018). Volcanoes in the UWRB also are spatially associated with local and regional (i.e., Laramide-age) normal faults, which localized magma ascent in the upper crust (Downey, 2015; Brueseke et al., 2018).

Magmatism in the <5 Ma UWRB volcanic field is thought to originate through interaction between the outer periphery of the thermal anomaly associated with passage of the Yellowstone hotspot (i.e., the "tectonic parabola" of Anders et al., 1989) and the extended lithosphere in the Upper Wind River area (Brueseke et al., 2018). Evidence supporting this hypothesis includes the general eastward progression of younger volcanism between the 6–9 Ma volcanoes near Jackson Hole, WY and the UWRB, and the location of the UWRB with respect to current seismicity on the outer periphery of the Yellowstone parabola (i.e., Figure 5).

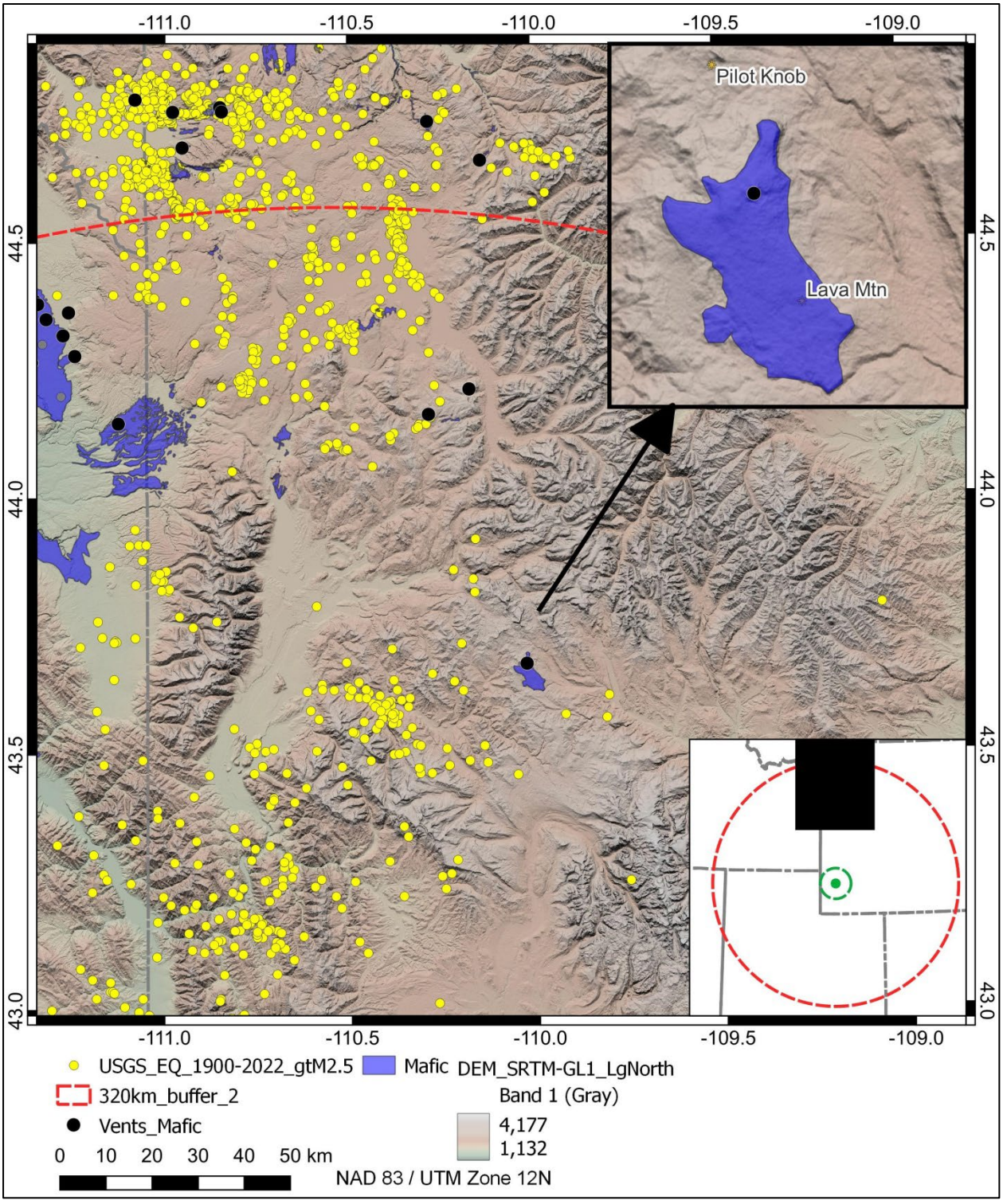

Figure 5. Location map of the UWRB volcanic field. Historical earthquake epicenters >M2.5 (Data sources in Figure 2). Lower inset map showing map relationship to the site region (red dashed line), site vicinity (green dashed line), and proposed site (green dot). Upper inset map showing detailed distribution of lava flows from Quaternary Lava Mountain, based on Horton (2017) and Downey (2015).

The four older (<2.6 Ma) volcanoes in the UWRB consist of:

- Pilot Knob, 3.40±0.06 Ma, eroded subvolcanic mafic intrusion (U.S. Geological Survey, 1978).
- Spring Mountain, 4.8±0.3 Ma, highly eroded basaltic lava flows and vent remnants (Keefer, 1957; Brueseke et al., 2018).
- Wildcat Hill, not dated, eroded subvolcanic andesitic intrusion, similar to Pilot Knob.
- Crescent Mountain, 3.6±1 Ma, eroded ~150-m-high cinder cone, partially covered by a 60-m-thick sequence of intermediate composition lavas (Blackstone, 1966; Brueseke et al., 2018).

Lava Mountain is a thick (>100 m) Quaternary volcanic center in the UWRB that is constructed of at least 26 lava flows that range in composition from basaltic andesite to dacite, representing the eruption of ≈5 km^3 of magma (Downey, 2015; Brueseke et al., 2018). Maximum flow lengths are <10 km, although significant uplift and erosion has occurred in this area since the lavas were emplaced. A basaltic andesite lava flow at the base of the flow section has a $^{40}Ar/^{39}Ar$ date of 0.43±0.09 Ma (Brueseke et al., 2018), and a lava flow near the top of the section has a K/Ar date of 0.48±0.06 Ma (U.S. Geological Survey, 1978), for an average age of 0.46±0.05 Ma.

A moderately eroded andesitic scoria cone is exposed in the upper part of the Lava Mountain section, but no cogenetic tephra-fall deposits have been described. Downey (2015) determined that the basaltic andesite and dacite flows occur low in the flow section, whereas intermediate-composition andesite flows are prevalent in the upper flow section. Downey (2015) integrated petrological models with the field relationships to interpret the evolution of a magma system that had increasing amounts of magma mixing between mafic and silicic components to produce intermediate composition magmas late in the eruption sequence. The amount of time for this process to occur appears relatively short, based on the overlap of radiometric dates and the absence of non-volcanic deposits in the flow section. Similar ranges of compositional diversity have been erupted in Quaternary volcanoes at the Craters of the Moon, Idaho (Kuntz et al., 1986), and Cedar Butte, Idaho (McCurry et al., 1999), both within the Eastern Snake River Plain volcanic field.

Based on current information, the eruptive history of Lava Mountain might be represented by a single event with 26 different lava flows, or as 26 distinct events that occurred over a short (i.e., <0.1 Ma limits of uncertainty in dates) period of time. Resolving this uncertainty is not a significant issue for the VHA, because a range of 1–26 discrete eruptions can be evaluated to capture the epistemic uncertainty in the number of past events at Lava Mountain. The volume, vent characteristics, and range of magma compositions suggest that past eruptions were VEI2–3 (cf. Table 1)

Following the approach outlined in Regulatory Guide 4.26, the distances that maximum-magnitude hazards have traveled from UWRB vent areas are summarized in Table 3. Note that the proximal hazard distance of 40 km is based on the criteria in Regulatory Guide 4.26, which restricts potential hazards to within 40 km of an erupting volcano.

Table 3. UWRB volcanic field summary of distances represented by maximum-magnitude events. VEI = Volcanic Explosivity Index; PDC = pyroclastic density currents. "?" indicates a screening distance cannot be developed based on current information, but the phenomena is characteristic of the volcano type.

UWRB	*Vents in Region*	*Ages (Ma)*	*General VEI*	*Tephra (km)*	*Opening of New Vents*	*Lava flows (km)*	*Proximal Hazards (km)*	*PDC (km)*
Mafic vents	1	0.46±0.05	2–3	?	Yes	<10	<40	No

2.3 Leucite Hills Volcanic Field

The Leucite Hills volcanic field (LHVF) represents an unusual episode of highly evolved mafic magmatism (i.e., Lamproite) in the Wyoming Basin physiographic province, which occurred between 0.8–3.0 Ma (e.g., Lange et al., 2000). The LHVF was emplaced along the northeastern arm of the Rock Springs anticline, which is a Laramide-age structure in the Wyoming Basin (Figure 6). Many of the volcanoes in the LHVF are aligned parallel to a major tectonic lineament that trends N40W, parallel to the axis of the Rock Springs anticline (Lange et al., 2000).

Lamproitic basalts generally contain 45–50 wt% SiO_2, but are highly enriched in K_2O and other incompatible elements relative to the types of olivine tholeiites that characterize most of the basalt in the site region. Petrological studies have concluded that the lamproitic mafic magmas in the LHVF result from partial melting of ancient (i.e., 1 Gyr) metasomatized mantle, which has undergone several episodes of partial melting and metasomatic enrichment (e.g., Lange et al., 2000; Mirnejad and Bell, 2006). Experimental studies indicate that the LHVF lamproitic magmas likely contained >3 wt% H_2O (Lange et al., 2000), which suggests an enhanced potential for forming tephra-fall eruptions relative to typical olivine tholeiites.

The LHVF is located approximately 200 km south-southeast of the UWRB (cf. Figure 2), and appears far beyond the limits of the Yellowstone hotspot "tectonic parabola" of Anders et al. (1989). Nevertheless, some researchers have attributed increasing mantle temperatures from the Yellowstone hotspot as triggering mechanism for partial melting of highly metasomatized mantle beneath the LHVF (Mitchell and Bergman, 1991; Mirnejad and Bell, 2006). Alternatively, the northward migration or upwelling of relatively hot, deep mantle beneath the Colorado Plateau (≈100 km south of LHVF) into the cooler Archean mantle beneath the Wyoming Basin might have supplied the heat needed to induce partial melting of the metasomatized mantle beneath the LHVF (Lange et al., 2000; Long et al., 2019).

Lange et al. (2000) evaluated time-volume relationships for the LHVF, and identified the locations of Quaternary volcanic vents and Plio-Quaternary subvolcanic intrusions (Figure 6). By individual feature count, there are 19 extrusive vents and 7 subvolcanic intrusions in the LHVF (Ogden, 1979; Gunter et al., 1990; Lange et al., 2000). Some lava flows were constructed through the eruption of 2–3 scoria cones. Consequently, for the LHVF a volcanic event is considered to be 1–3 scoria cones of similar age, orientation, and petrology. Thus, there are 14 Quaternary volcanic events and 7 Plio-Quaternary subvolcanic intrusive events.

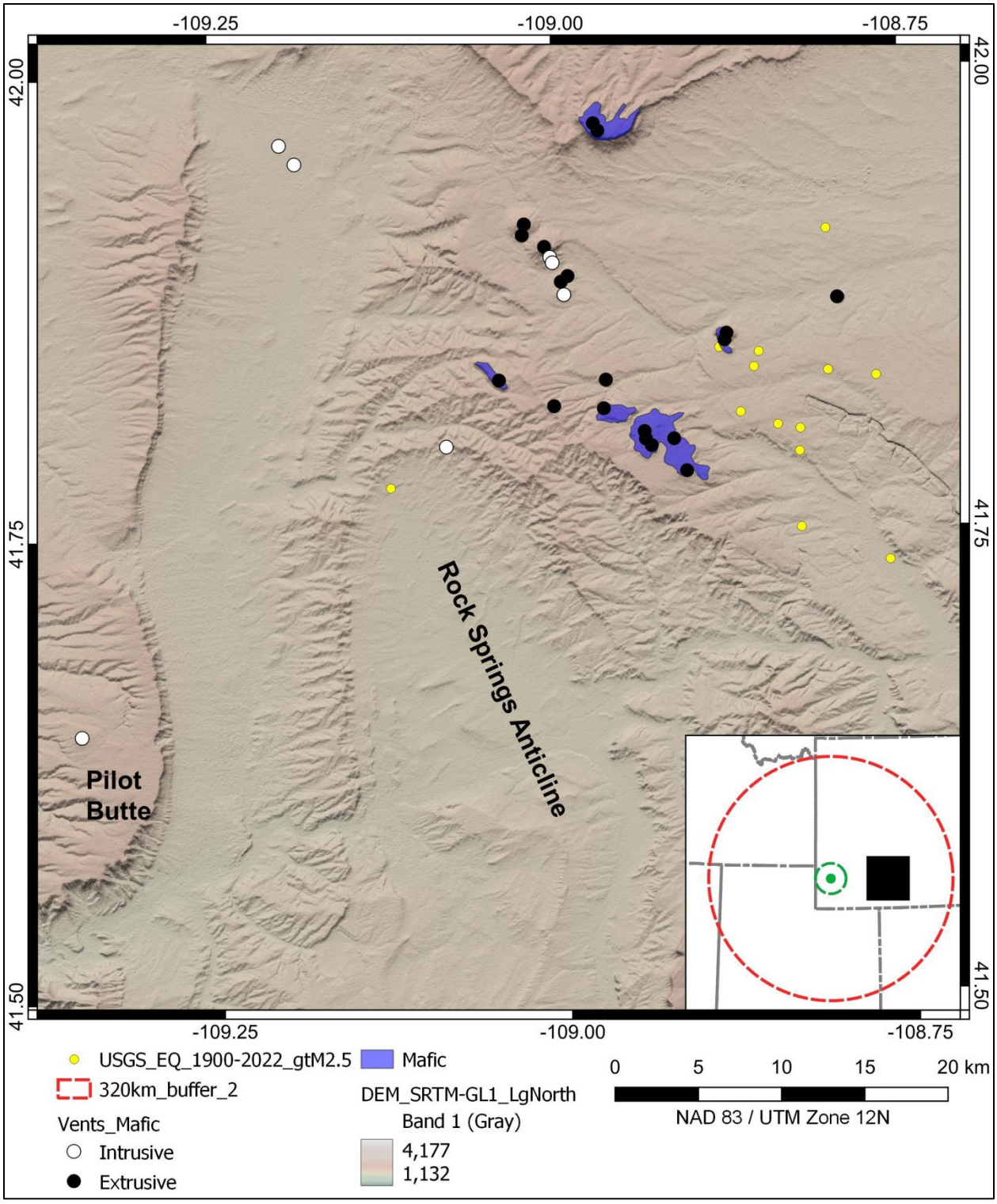

Figure 6. Map of the Leucite Hills Volcanic Field. Vent locations and lava flows modified from Lange et al. (2000) and Horton (2017). Other data sources given in Figure 2. Locations labeled for 3.0 Ma Pilot Butte, and the axis of the Rock Springs anticline.

After correcting for erosion, Lange et al. (2000) determined that eruptive events ranged in volume from $1x10^6$ m^3 to $3x10^8$ m^3, and that scoria cones represent approximately 5% of the total amount of magma erupted during each event. Although some of the scoria cones have been mined for aggregate (e.g., Root, 1972), tephra-fall deposits have not been reported for the LHVF (Root, 1972; Ogden, 1979; Lange et al., 2000). Visual examination of aerial imagery was used to verify the Lange et al. (2000) vent locations (i.e., Figure 6), and confirm the formation of scoria cones during the relevant LHVF eruptions. Based on the general characteristics of the scoria cones, and the likely volatile contents in the magma, past scoria-cone eruptions likely were VEI2–3. The maximum lava flow length in the LHVF is <5 km.

Following the approach outlined in Regulatory Guide 4.26, the distances that maximum-magnitude hazards have traveled from LHVF vent areas are summarized in Table 4. Note that the proximal hazard distance of 40 km is based on the criteria in Regulatory Guide 4.26, which restricts potential hazards to within 40 km of an erupting volcano.

Table 4. LHVF summary of distances represented by maximum-magnitude events. Number of vents identified in the region of interest expanded to include 3.0 Ma Pilot Butte and 2 nondated vents; VEI = Volcanic Explosivity Index; PDC = pyroclastic density currents. PDC = pyroclastic density currents. "?" indicates a screening distance cannot be developed based on current information, but the phenomena is characteristic of the volcano type.

LHVF	*Vents in Region*	*Ages (Ma)*	*General VEI*	*Tephra (km)*	*New Vent Hazard*	*Lava flows (km)*	*Proximal Hazards (km)*	*PDC (km)*
Mafic vents	26	0.8–3.0	2–3	?	Yes	<5	<40	No

2.4 Northern Black Rock Desert Volcanic Field

The northernmost part of the Quaternary Black Rock Desert volcanic field (NBRD) in Utah extends to within 320 km of the proposed Natrium™ site (Figure 7); the majority of the volcanic field continues approximately 100 km south into the Black Rock Desert. Two Quaternary volcanoes in the NBRD are located within 320–322 km of the site: Crater Springs and Smelter Knolls. Consistent with the guidance in Regulatory Guide 4.26, only these 2 volcanoes from the NBRD are considered in the VHA.

Fumarole Butte (Figure 7) is a large, basaltic andesite shield volcano (Galyardt and Rush, 1981) that erupted at 0.88±0.01 Ma (Peterson and Nash, 1980). The shield has been moderately eroded by Lake Bonneville inundation, and only a small remnant of the vent area is preserved (Peterson and Nash, 1980). The vent consists of low ramparts of moderately to highly welded scoria and spatter, which is characteristic of mafic shield volcano vents (e.g., Cas and Wright, 1987). The composition and degree of welding in the vent ejecta indicates the Fumarole Butte shield volcano eruption was likely VEI≤1. Lava flows are restricted to <10 km of the vent (Figure 7).

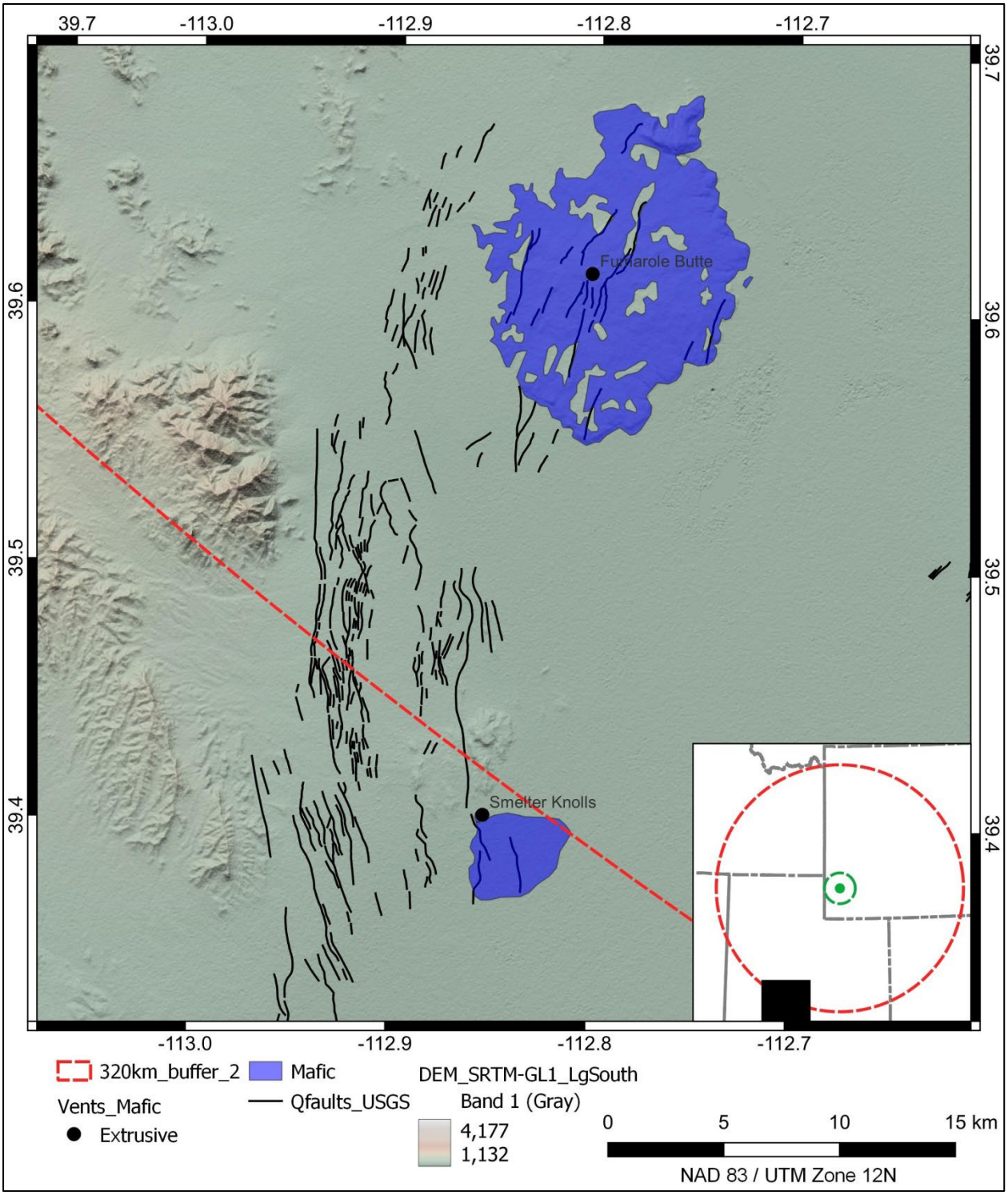

Figure 7. Map of the northern part of the Black Rock Desert volcanic field, Utah. Lava flows from Oviatt (1989) and Galyardt and Rush (1981); other data sources given in Figure 2.

Smelter Knolls (Figure 7) is a phreatomagmatic vent that produced a tholeiitic lava flow during the later stages of the eruption (Oviatt, 1989). Smelter Knolls formed at 0.31±0.08 Ma (Turley and Nash, 1980). The phreatomagmatic eruption created a small (≈400 m diameter) tuff ring, but pyroclastic deposits beyond the tuff ring have not been identified (Oviatt, 1989). For similar-sized phreatomagmatic eruptions, pyroclastic deposits are restricted to within 10 km of the vent (e.g., Self et al., 1980; Cas and Wright, 1987). Explosive magma-water interactions can generate tephra plumes that can rise to 5–6 km altitudes, but the plumes are dilute and most tephra fall occurs within about 10 km of the vent (e.g., Self et al., 1980). Based on comparison to the comparably sized 1977 Ukinrek Maar eruption in Alaska (Kienle et al., 1980; Self et al., 1980), the Smelter Knolls phreatomagmatic eruption might have involved 10^6 m^3 of basaltic magma, and would have represented a VEI1 eruption. Lava flows are restricted to <4 km of the vent (Figure 7).

Both Fumarole Butte and Smelter Knolls originated from typical Basin and Range mafic magmatic processes. In response to crustal extension, the mantle lithosphere decompresses and generates mafic partial melts at typical depths of 60 km. Magma ascends to the base of the crust and can further differentiate, or continue to ascend and erupt (e.g., Peterson and Nash, 1980; Johnsen et al., 2010). Neogene-age mafic and silicic rocks also have erupted in the vicinity of Fumarole Butte and Smelter Knolls, further demonstrating that this part of the Black Rock Desert, Utah, has been a locus of magmatism since at least 6 Ma (e.g., Johnsen et al., 2010).

Following the approach outlined in Regulatory Guide 4.26, the distances that maximum-magnitude hazards have traveled from NBRD volcanic field vent areas are summarized in Table 5. Note that the proximal hazard distance of 40 km is based on the criteria in Regulatory Guide 4.26, which restricts potential hazards to within 40 km of an erupting volcano.

Table 5. NBRD volcanic field summary of distances represented by maximum-magnitude events. VEI = Volcanic Explosivity Index; *PDC = pyroclastic density currents from phreato-magmatic eruptions.

NBRD	*Vents in Region*	*Ages (Ma)*	*General VEI*	*Tephra (km)*	*New Vent Hazard*	*Lava flows (km)*	*Proximal Hazards (km)*	**PDC (km)*
Mafic vents	2	0.3–0.9	≤1	<10	Yes	<10	<40	<10

2.5 Curlew Valley Volcanic Field

The Curlew Valley Volcanic Field (CVVF) is a small, distributed volcanic field that developed in a ≈600 km^2 area around a Plio-Quaternary rhyolite dome complex at the Wildcat Hills in north central Utah (Figure 8). In the Wildcat Hills, at least 3 episodes of rhyolitic lava-flow eruptions occurred between 4.9±0.4 Ma and 3.6±0.1 Ma, with an additional episode occurring at 2.1±0.06 Ma (Miller et al., 1995). A $^{39}Ar/^{40}Ar$ date of 2.33±0.01 Ma on the Wildcat Hills rhyolite confirms the Quaternary age of this unit (Felger et al., 2016). Based on mapped distributions (Felger et al., 2016), ≈1 km^3 of rhyolite was emplaced during the 2.3–4.9 Ma Wildcat Hills eruptions. There is no evidence of pyroclastic eruptions at Wildcat Hills, although deposits from such eruptions might be buried or eroded. If the 2.3 Ma eruption produced 25% of the total erupted volume Wildcat Hills, and 10% of the 2.3 Ma eruption was pyroclastic, general VEI-magnitude relationships (i.e., Newhall and Self, 1982) suggest a VEI2–3 eruption might have occurred.

In addition to the rhyolite flows, a series of highly eroded of 2.24±0.02 Ma basaltic fissures are exposed 10–15 km north-northeast of the Wildcat Hills rhyolite (Figure 8). This basalt is thought to be part of the same eruptive episode that produced the 2.33±0.01 Ma rhyolite (Felger et al., 2016). A small fissure and spatter rampart occurs at the vent area, which indicates these basalts erupted through fire fountains and did not produce convective tephra plumes (e.g., Walker, 1973) .

After an approximately 1 Myr hiatus in activity, a series of four basaltic volcanoes erupted 10–15 km east of the Wildcat Hills rhyolite (Figure 8), at 1.16±0.08 Ma (Cedar Hill), 0.72±0.15 Ma (Curlew), 0.52±0.02 Ma (N. Cedar), and 0.44±0.1 Ma (Locomotive Spring) (Miller et al., 1995; Felger et al., 2016). These younger volcanoes are generally aligned parallel to nearby Basin and Range normal faults, but are not associated with any mapped Quaternary fault (Figure 8). An isolated eruption of 1.1±0.1 Ma basalt also occurred at Sheep Mountain, approximately 45 km to the southwest (Miller et al., 1995), and is being included herein as part of the CVVF. Based on mapped distributions (Felger et al., 2016) and assuming an average flow thickness of 10 m, ≈2 km^3 of <1.2 Ma basalt was erupted.

Reconnaissance petrological studies indicate that the basalt in the CVVF is primarily olivine tholeiite, and is similar to basalt in the Eastern Snake River Plain and Blackfoot Reservoir volcanic fields (Kerr, 1987). Partial melting of a garnet lherzolite mantle source, with subsequent crystal fractionation and minor crustal assimilation, appears capable of producing the compositional variations observed in the CVVF basalt (Kerr, 1987). Decompression of the mantle was likely induced by Basin and Range extension, which led to the development of basaltic magmatism in the CVVF area during the Neogene (i.e., Miller et al., 1995). Rhyolitic magmas were likely produced by partial crustal melts that resulted when ascending basaltic magma stagnated in the crust (Kerr, 1987). Approximately 2 km^3 of basalt was erupted during the <1.2 Ma eruptions.

The <1.2 Ma basalt erupted from eroded shield volcanoes, which have shallow depressions in the summit areas and discernible spatter ramparts with agglutinated scoria. As was observed for the Fumarole Butte volcano in the NBRD volcanic field, such mafic shield volcanoes are characterized by VEI≤1 eruptions (e.g., Walker, 1973; Cas and Wright, 1987). Lava flows are restricted to within 5 km of the vent (Figure 8).

Miller et al. (1995) describe a thin (<1 cm) basaltic ash that occurs at the base of Lake Bonneville lacustrine marl deposits in Hansel Valley, approximately 20 km east southeast of the <1.2 Ma CVVF volcanoes. Miller et al. (1995) trace this ash approximately 80 km eastward to near Brigham City, where it thins to a several-mm-thick bed in Lake Bonneville lacustrine deposits. Based on the westward-thickening pattern, and a general geochemical correlation, Miller et al. (1995) attribute the Hansel Valley ash to an eruption from an unknown phreatomagmatic vent associated with the <1.2 Ma CVVF volcanoes.

The Hansel Valley ash deposits (i.e., Thiokol ash of Oviatt et al., 1992) are only observed in early Lake Bonneville sedimentary deposits, which have ages of <26,500 yrs (Felger et al., 2016). In addition, the composition of the Hansel Valley ash is a significantly more evolved olivine tholeiite (i.e., higher TiO_2 and FeO contents) than reported for the <1.2 Ma CVVF basalts (Miller et al., 1995), which indicates the ash is not reworked tephra from those eruptions. The shoreline of Lake Bonneville was likely around 1,340 m elevation when the Thiokol ash was deposited (Oviatt et al., 1992), and likely reached a peak elevation of ≈1,500 m in the CVVF area (Benson et al., 2011). For reference, the <1.2 Ma CVVF eruptions occurred at 1,300–1,400 m elevation.

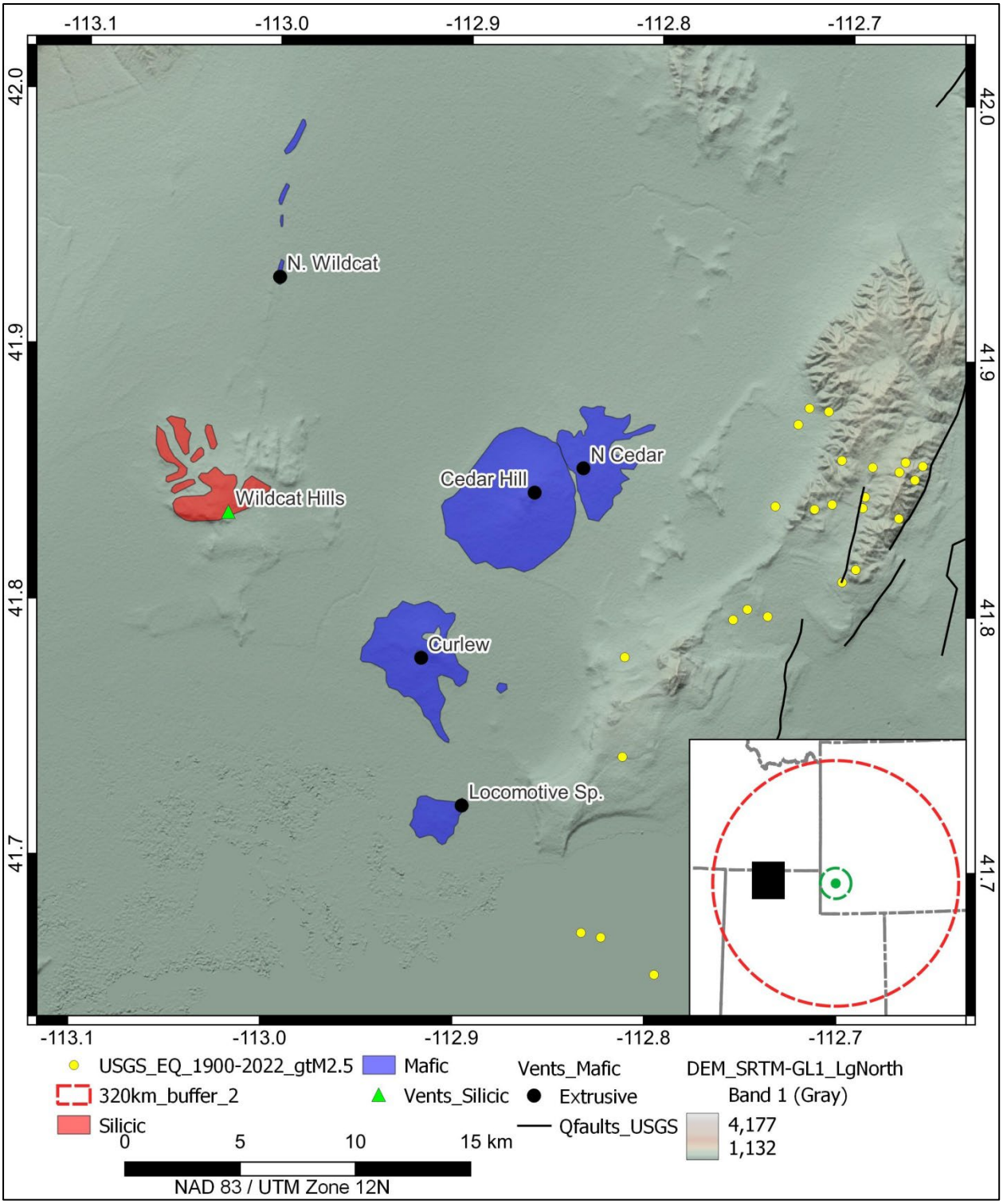

Figure 8. Map of the CVVF, Utah. Geology from Miller et al. (1995), Felger et al. (2016), and Horton (2017). Inset map showing relationship to proposed Natrium™ site (green dot), with 40 km (green dash) site vicinity and 320 km (red dash) site region. Quaternary faults (Schmitt, 2017), historical seismicity (U.S. Geological Survey, 2022a), and DEM SRTM-1 (30 m resolution) (OpenTopography, 2013).

Small, phreatomagmatic vents typically form low-angle maar volcanoes consisting of poorly to moderately consolidated tephra falls and surge deposits, which are readily eroded (e.g., Cas and Wright, 1987). If the source of the 26.5 ka Thiokol/Hansel Valley ash was a phreatomagmatic vent in proximity to the <1.2 Ma CVVF basalt, shoreline advance and retreat of Lake Bonneville might have obscured or buried the vent (Felger et al., 2016). Nevertheless, it appears that the most likely source of the 26.5 ka Thiokol/Hansel Valley ash was a phreatomagmatic eruption from a potentially buried volcano in the CVVF, which is the nearest volcanic field to recognized exposures of the Thiokol/Hansel Valley ash.

Following the approach outlined in Regulatory Guide 4.26, the distances that maximum-magnitude hazards have traveled from CVVF vent areas are summarized in Table 6. Note that the proximal hazard distance of 40 km is based on the criteria in Regulatory Guide 4.26, which restricts potential hazards to within 40 km of an erupting volcano.

Table 6. CVVF summary of distances represented by maximum-magnitude events. VEI = Volcanic Explosivity Index; PDC = pyroclastic density currents from phreatomagmatic vents. "?" indicates a screening distance cannot be developed based on current information, but the phenomena is characteristic of the volcano type.

CVVF	*Vents in Region*	*Ages (Ma)*	*General VEI*	*Tephra (km)*	*New Vent Hazard*	*Lava flows (km)*	*Proximal Hazards (km)*	**PDC (km)*
Mafic vents	6	0.4–2.2	≤1	<10	Yes	<5	<40	No
Phreato-magmatic	1?	0.027	1	<80	Yes	No	<10	<10
Silicic vents	1	2.3	2–3	?	Yes	<5	<40	No

2.5.1 Black Mountain, Utah

An isolated, highly eroded and dissected exposure of basaltic lava flow and scoria is exposed at the summit of Black Mountain, Utah, immediately east of Bear Lake and 62 km northwest of the proposed Natrium™ site (Figure 9). The lavas overlie the Eocene Wasatch Formation (Richardson, 1941; McClurg, 1970), but no other age constraints are available (Puchy, 1981). Although Richardson (1941) considered the Bear Lake basalt to be Tertiary age, McClurg (1970) speculates that the basalt age might be Pliocene to early Quaternary based on the degree of erosion he observed. However, McClurg (1970) does not provide any morphological comparisons to comparable-aged basaltic features in the region. Based on visual inspection of satellite imagery (Figure 9), the degree of dissection and erosion appears significantly more extensive at Black Mountain than at other Quaternary scoria cones and lavas in the site region. In contrast, Black Mountain morphology appears more comparable to the morphology of Pliocene lavas and vents in the UWRB. Consequently, Black Mountain appears to represent an isolated eruption of pre-Quaternary basalt, which occurred in close proximity to the basin-bounding Bear Lake fault (Figure 9). It has been included in this report for completeness based on its mention in the available literature, but is not thought to represent a Quaternary volcano in the site region based on its highly eroded morphology.

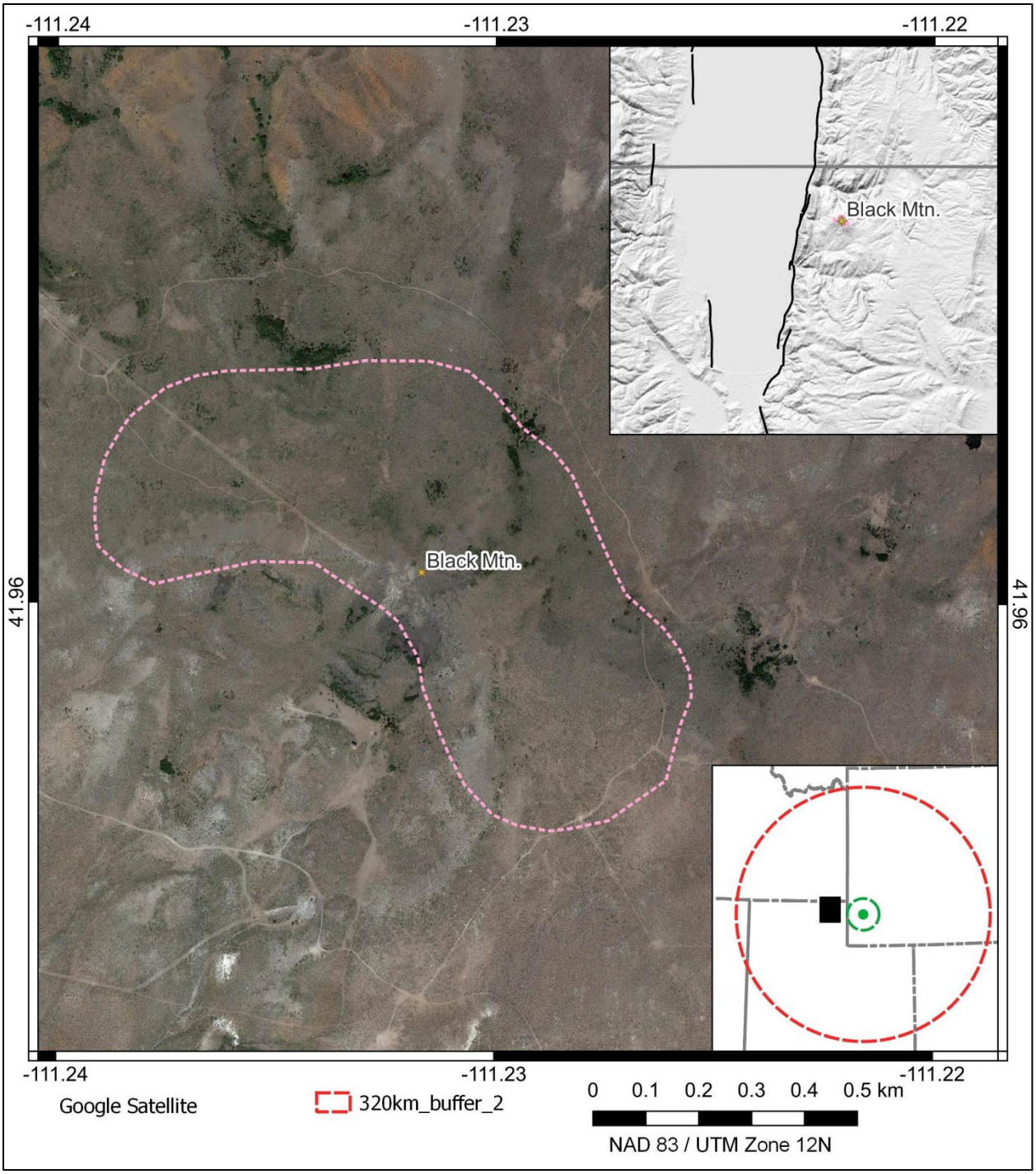

Figure 9. Location map of Black Mountain, Utah. General location and satellite imagery of basalt exposures outlined in pink. Inset map in upper right showing larger area around Black Mountain (Dover, 1995), digital elevation model (OpenTopography, 2013) and Quaternary Faults (Schmitt, 2017). Satellite imagery ©Google, ©CNES/Airbus, Maxar Technologies, State of Utah, USDA/FPAC/GEO.

2.6 Blackfoot Reservoir Volcanic Field

The Blackfoot Reservoir volcanic field (BRVF) is a large, distributed volcanic field in southeastern Idaho that has produced both mafic and silicic eruptions during the Quaternary Period. The BRVF is located in the northeastern Basin and Range tectonic province, in a transition between the active Intermontane Seismic Belt (Anders et al., 1989) and Idaho Thrust Belt (e.g., Dixon, 1982) to the east, and the tectonically stable Eastern Snake River Plain to the northwest (Figure 10). Volcanoes in the BRVF generally occur in northwest-trending basins, with intra-basin faults providing some degree of structural control on mafic and silicic vent locations (e.g., Polun, 2011; Welhan, 2016; Hastings et al., 2021).

Although the BRVF has been the focus of numerous petrological (McCurry et al., 1999; Pickett, 2004; Ford, 2005; Lochridge, 2016), structural (Polun, 2011; Hastings et al., 2021) and geothermal resource investigations (Autenrieth et al., 2011; McCurry et al., 2011, 2015; McCurry and Welhan, 2012; Welhan et al., 2014; Welhan, 2016), only limited information is available on the age and character of the Quaternary mafic eruptions. The BRVF has erupted 85 mafic vents since approximately 1 Ma (Figure 10), with volcanic events represented by individual vents. Basalt with reversed paleomagnetic orientation (i.e., >0.78 Ma normal Brunhes subchron; Spell and McDougall, 1992) are generally located in the eastern and northern parts of the BRVF (Mabey and Oriel, 1970), including a 0.9±0.1 Ma lava flow (Armstrong et al., 1975) in the northwestern periphery of the field and a 1.04±0.08 Ma lava in Wooley Valley (Pickett, 2004), in the eastern periphery of the field.

The central and western parts of the BRFV appear to contain lavas with normal paleomagnetic orientation (i.e., <0.78 Ma normal Brunhes subchron), which have filled basins to 100–300 m depths in the central part of the field (Mabey and Oriel, 1970). Several exposed lavas have been dated radiometrically: the 0.43±0.07 Ma Portneuf Valley basalt (Rodgers et al., 2006), 0.1±0.03 Ma unnamed basalts in Gem Valley (Armstrong et al., 1975), and 0.09±0.03 Ma for the Alexander Cone basalt in Gem Valley (Pickett, 2004). Emplacement of lava flows in the southernmost part of Gem Valley dammed the Bear River and formed a large paleo-lake (i.e., Lake Thacher), which has sediments with ^{14}C dates of 27,500±1,000 yr BPE (Rubin and Alexander, 1960) and 34,000±1,600 yr BPE (Luedke and Smith, 1983). These dates indicate that basaltic volcanism in the BRVF occurred as recently as ≈0.03 Ma.

Fourteen of the 85 mafic vents produced moderately to well-preserved scoria cones, which were likely formed during moderately explosive eruptions of VEI2–3. A majority of the BRVF mafic lavas erupted from fissures or spatter cones, which likely represented VEI≤1 eruptions. Several mafic phreatomagmatic eruptions also occurred in the southern part of the BRVF, which formed small (i.e., <500 m) diameter maars and tuff rings (Pickett, 2004). Lava flows that were confined to drainages were able to travel <50 km from the source vents (Figure 10).

Two episodes of Quaternary rhyolitic volcanism also occurred in the BRVF at approximately 0.05 Ma and 1.4–1.6 Ma. The older, northern episode (Figure 11) consists of 3 rhyolite domes and lava flows that form a roughly northwest-trending alignment, parallel to the regional structural trend (Polun, 2011), which are dated at 1.59±0.06 Ma and 1.41±0.15 Ma (Luedke and Smith, 1983). An estimated 0.5 km^3 of rhyolitic magma was erupted effusively during this episode, and no pyroclastic deposits are present (Ford, 2005). A sequence of rhyolitic lavas also is exposed at Sheep Island (Figure 11) in the Blackfoot Reservoir lake, which has been dated at 1.4±0.2 Ma (Luedke and Smith, 1983). Based on comparisons to the sizes well-exposed northern domes, Sheep Island likely represents the effusive eruption of >0.1 km^3 of rhyolitic magma.

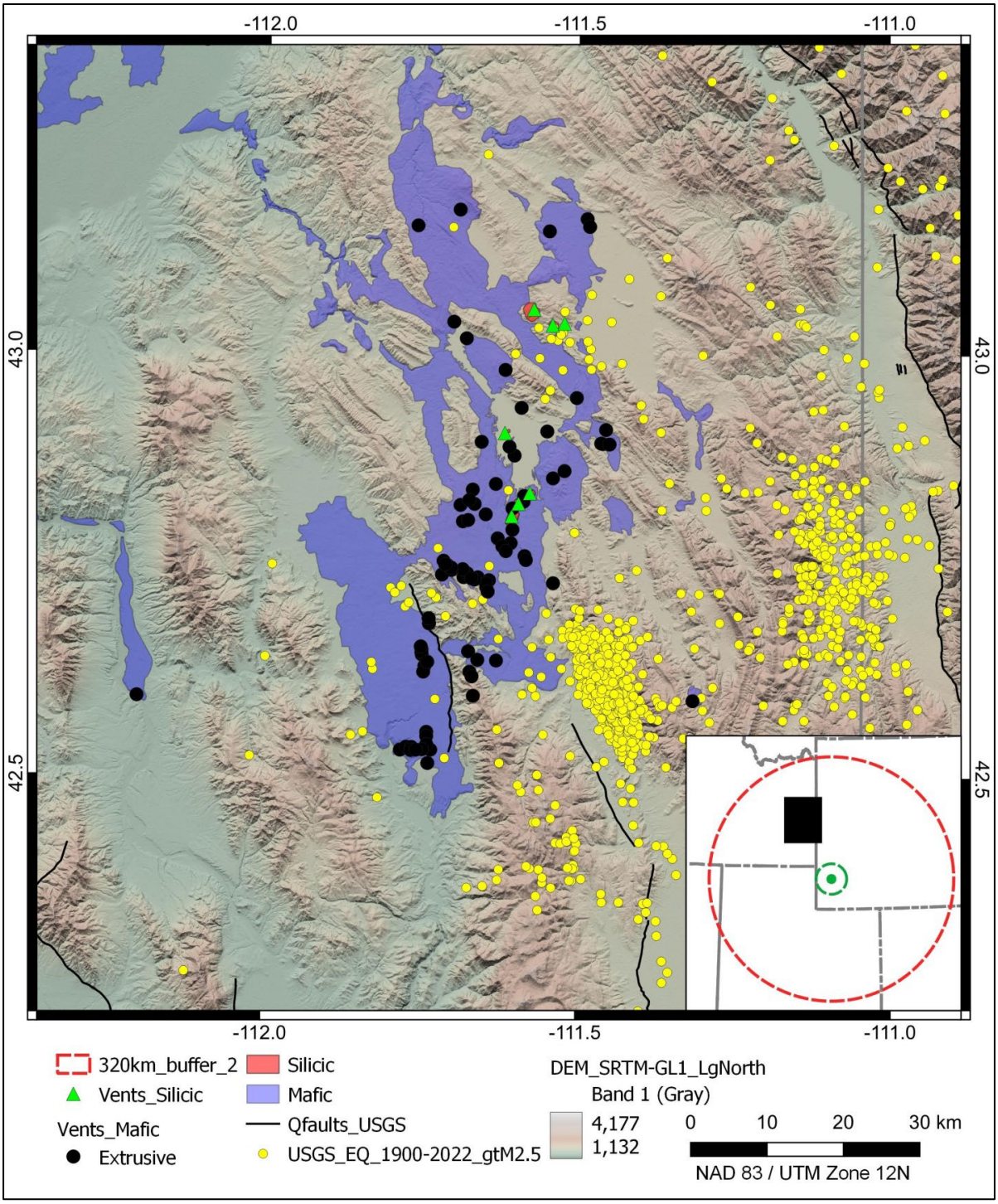

Figure 10. Map of the BRVF. Geology from (Mitchell and Bennet, 1979; Oriel and Platt, 1980; Pickett, 2004; Ford, 2005; Horton, 2017; Hastings et al., 2021). Inset map showing relationship to proposed Natrium™ site (green dot), with 40 km (green dash) site vicinity and 320 km (red dash) site region. Quaternary faults (Schmitt, 2017), historical seismicity (U.S. Geological Survey, 2022a), Digital Elevation model SRTM-1 (30 m resolution) (OpenTopography, 2013).

A northeast-trending alignment of rhyolitic domes and two associated maars represent the southern, younger episode of rhyolitic volcanism in the BRVF (Figure 11). The northeast trend to this alignment is thought to reflect structural control by trans-tensional faulting associated with a bend in the Blackfoot Rift Zone to the south (McCurry et al., 2015). These rhyolite domes are the youngest silicic volcanoes in the site region, with a $^{39}Ar/^{40}Ar$ date of 0.057±0.008 Ma (Heumann, 2004) best representing the eruptive age of this event (McCurry et al., 2015). An estimated 0.7 km^3 of rhyolitic magma was erupted in this youngest episode (Ford, 2005). Early phases of these eruptions produced phreatomagmatic surge and tephra-fall deposits that are exposed at the base of several domes. A thin tephra-fall deposit from a phreatomagmatic eruption has been identified in lake sediments 20 km northeast of these domes (McCurry et al., 2015).

Although the younger rhyolitic magmas initially contained water contents >3 wt% (Ford, 2005), the magmas appear to have been extensively degassed before eruption, as shown by a lack of vesiculation in the magmatic eruptive products (e.g., McCurry et al., 2015). Geophysical surveys indicate that shallow (i.e., <1 km) sill-like intrusions likely underlie these domes (Hastings et al., 2021), which likely represent magma bodies where ascending rhyolitic magma stagnated, and degassed, prior to eruption. Shallow intrusion and stagnation of ascending magma also appears to be a characteristic of rhyolitic magmatism in the Eastern Snake River Plain (e.g., McCurry et al., 2008).

An estimated 50 km^3 (Welhan et al., 2014) to 100 km^3 (McCurry et al., 2015) of basaltic magma was erupted in the BRVF, which filled structural basins to 100–300 m depths (Mabey and Oriel, 1970). The basalts are predominately olivine tholeiites, with the same compositional affinities as basaltic lavas in the Eastern Snake River Plain (e.g., Pickett, 2004). Melting in the lithospheric mantle occurred beneath the BRVF in response to the thermal anomaly, and possible mantle flow, associated with passage of the Yellowstone hotspot (Pickett, 2004; McCurry et al., 2015). Basaltic magma reservoirs developed at crustal density or structural discontinuities at 10–20 km depths, which formed magma reservoirs that fractionated to produce observed geochemical variations (Pickett, 2004). Extreme fractionation of the basaltic magmas at equilibration depths of 13±0.4 km likely formed the rhyolitic magmas (Ford, 2005), coupled with 15–30% assimilation of Archean crust (Lochridge, 2016). The rhyolitic magmas then ascended to shallow (<1 km) depths, stagnated, and degassed, before erupting. The observed basalt-to-rhyolite ratio of 50:1 to 100:1 appears consistent with this generalized petrologic model.

Although the oldest basalt lava in the BRVR is dated at 1.04±0.08 Ma, the close genetic relationship between BRVF rhyolite and basalt indicates that the 1.4–1.6 Ma rhyolite was necessarily associated with basaltic magmatism. In addition, many of the potentially older lavas and vents on the northern and eastern parts of the BRVF have not been investigated or dated. To account for this uncertainty in the age of the BRVF, calculated recurrence rates should use a 1.6 Myr period of activity (i.e., McCurry et al., 2015).

Following the approach outlined in Regulatory Guide 4.26, the distances that maximum-magnitude hazards have traveled from BRVF vent areas are summarized in Table 7. Note that the proximal hazard distance of 40 km is based on the criteria in Regulatory Guide 4.26, which restricts potential hazards to within 40 km of an erupting volcano.

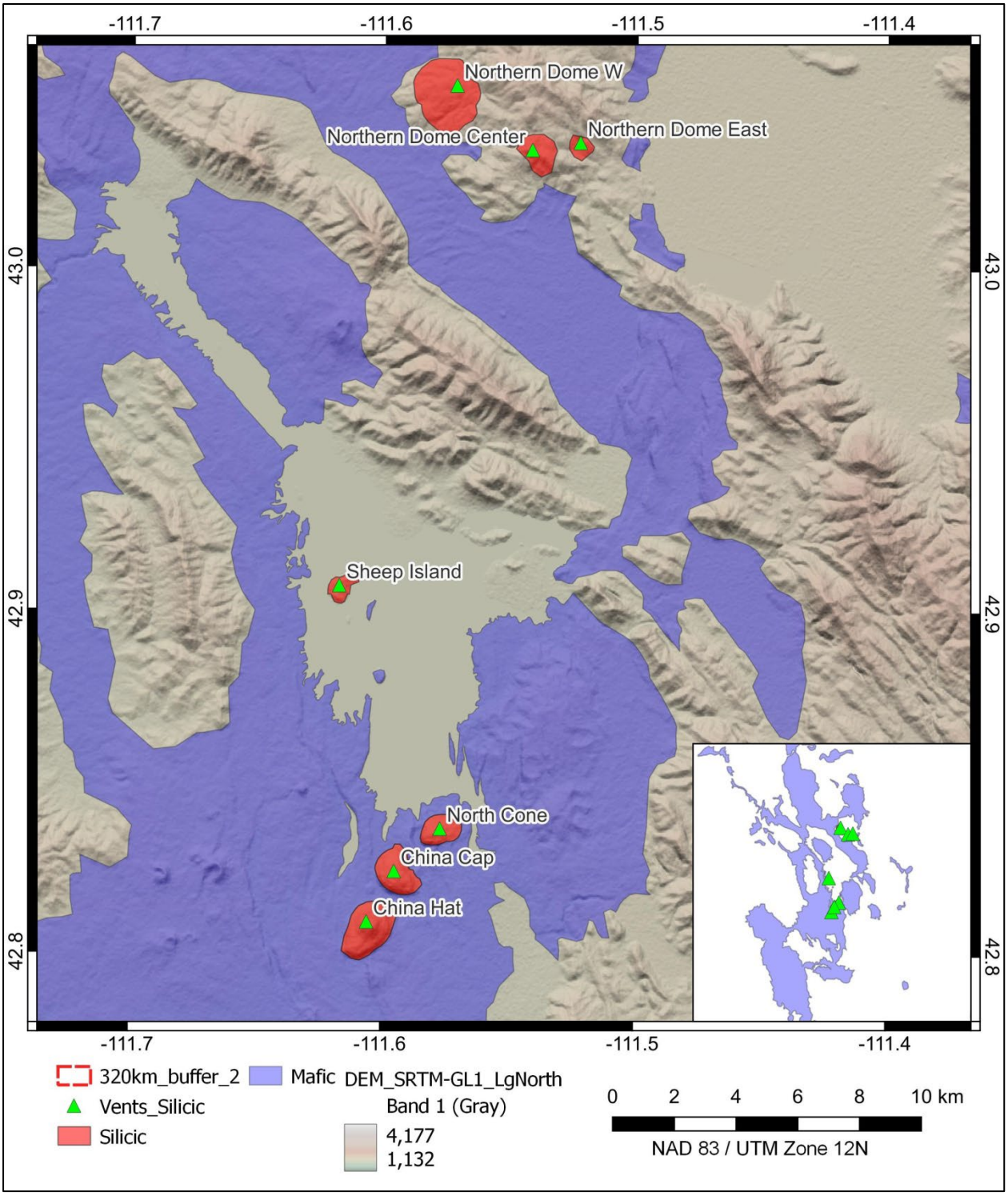

Figure 11. BRVF Rhyolite lavas and domes. Expanded map from large area shown in Figure 10, data sources the same as Figure 10.

Table 7. BRVF summary of distances represented by maximum-magnitude events. VEI = Volcanic Explosivity Index; *PDC = pyroclastic density currents from phreatomagmatic eruptions. "?" indicates a screening distance cannot be developed based on current information, but the phenomena is characteristic of the volcano type.

BRVF	*Vents in Region*	*Ages (Ma)*	*General VEI*	*Tephra (km)*	*New Vent Hazard*	*Lava flows (km)*	*Proximal Hazards (km)*	*PDC (km)*
Mafic vents	85	0.03–1.5	2–3	?	Yes	<50	<40	No
Silicic vents	7	0.05–1.6	2–3	?	Yes	<5	<40	<10

2.7 Eastern Snake River Plain Volcanic Field

The Eastern Snake River Plain (ESRP) volcanic field is one of the largest distributed basaltic volcanic fields in the United States. Magmas ranging in composition from basaltic to rhyolitic have erupted from the ESRP in the Quaternary Period, including a variety of intermediate compositions. The ESRP represents a distinct tectono-magmatic province, which was formed by the passage of the North American tectonic plate over the Yellowstone hotspot during the last 15 Myr (e.g., Kuntz et al., 1992). The YVF to the northeast represents the youngest expression of Yellowstone hotspot magmatism, whereas magmatism in the ESRP results from the lingering thermal and physical effects of hotspot passage since approximately 10 Ma (e.g., Pierce and Morgan, 1992). Quaternary faulting and historical seismicity are remarkably low in the ESRP, relative to the adjoining tectonic provinces (Figure 12). Low rates of strain in the ESRP may reflect densification and strengthening of the lower to middle crust by mafic intrusions (Payne et al., 2012), or the accommodation of horizontal tectonic stress by repeated intrusion of basaltic dikes rather than by faulting and seismicity (i.e., Parsons and Thompson, 1991).

Within the site region (Figure 12), most of the basalt exposed in the ESRP is younger than 0.78 Ma (i.e., normal paleomagnetic Brunhes subchron) (Kuntz et al., 1992), as are most of the rhyolitic and intermediate composition lavas and vents exposed at the surface. However, the mostly buried "Unnamed Butte" has a radiometric date of 1.42±0.02 Ma (Kuntz and Dalrymple, 1979), and older (i.e., >0.78 Brunhes subchron) lavas are abundant in the subsurface in the ESRP (e.g., Anderson et al., 1997), attesting to the persistence of igneous activity during the Quaternary Period. Numerous 2.1–15 ka eruptions have occurred in and around the Craters of the Moon area (e.g., Kuntz et al., 1986; Figure 12). An estimated 10,000 km^3 of primarily basaltic magma has erupted from the ESRP since the onset of mafic volcanism in the late Pliocene (McCurry et al., 2008).

Quaternary volcanism in the ESRP has been driven by an established subsurface magma system that originates from decompression-induced partial melts of metasomatically enriched lithospheric mantle (e.g., Leeman, 1982). The basaltic magma ascends into the lower to middle (i.e., 10–30 km), until it reaches a level of neutral buoyancy and arrests ascent. The basaltic magma differentiates, primarily through crystal fractionation, and some portion of the mid-crustal magma erupts at the surface. Through time, the magma system formed a ≈10-km-thick, anastomosing intrusive complex at mid-crustal (12–22 km) depths (e.g., Shervais et al., 2006), which is the primary source of erupted magma in the ESRP during the Quaternary Period. Intermediate and rhyolitic magmas formed primarily by a combination of crystal fractionation and magma mixing, with <10% assimilation of crustal rocks (e.g., McCurry et al., 2008).

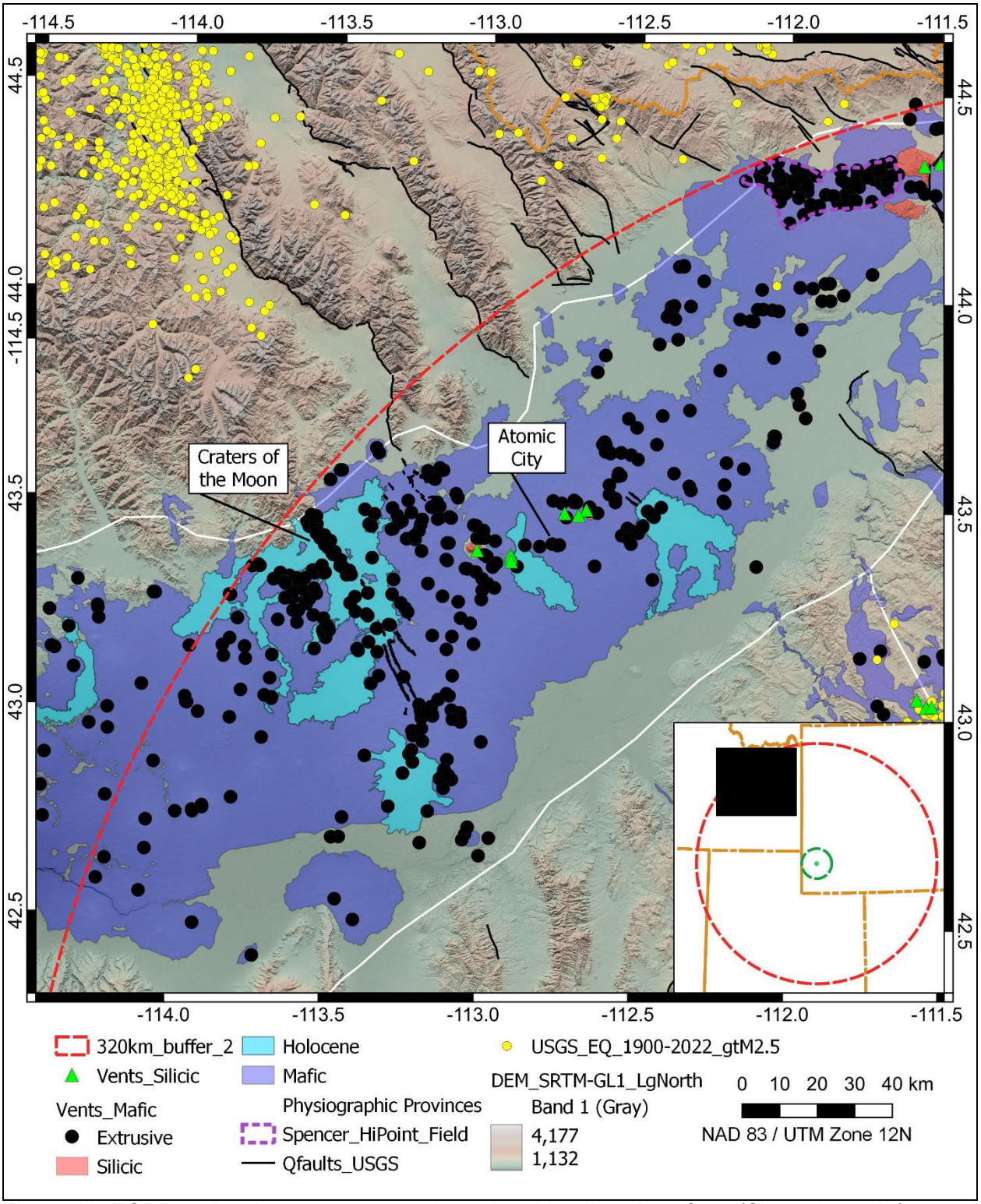

Figure 12. ESRP regional tectono-magmatic setting. Vent locations from (Shervais, 2015), boundary of the Spencer-High Point region after Iwahashi (2010), "Holocene" is mafic lavas <12 ka (i.e., Kuntz et al., 1992); other data sources listed in Figure 2.

The northeastern margins of the ESRP is defined by a relatively broad cluster of basaltic vents that form the Spencer-High Point rift zone (Kuntz et al., 1992). Vents within this rift zone generally trend easterly, in contrast to the northwesterly trend of vents within the central part of the ESRP (Figure 13), which reflects the influence of east-trending crustal structures (i.e., the Centennial Fault Zone) on magma ascent (Kuntz et al., 1992; Hughes et al., 2002; Iwahashi, 2010). Although some of the highest spatial densities of vents in the ESRP occur in the Spencer-High Point rift zone (Kuntz et al., 1992), spatial analysis shows that this zone likely represents a cluster of vents within the ESRP rather than a wholly separate volcanic field (i.e., Gallant et al., 2018). Geochemical similarities between the Spencer-High Point rift zone and the rest of the ESRP also support this association (Kuntz et al., 1992; Hughes et al., 2002; Iwahashi, 2010).

Most of the Quaternary basalt in the ESRP erupted from low-angle shield volcanoes or fissure vents, which produced localized deposits of agglutinated scoria and extensive lava flows (e.g., Kuntz et al., 1992; Hughes et al., 2002). These types of basaltic eruptions are characterized by low explosivity (i.e., VEI≤1) fire fountains, and limited distribution of elutriated ash within <10 km of the vent (e.g., Walker, 1973; Kuntz et al., 1988; Mueller et al., 2018). Several clusters of basaltic volcanoes in the Craters of the Moon, Spencer-Highpoint, and Atomic City areas also produced more energetic eruptions that formed small (<1 km^3), low-to-moderate angle cones of non-agglutinated to moderately agglutinated scoria (e.g., Kuntz et al., 1992; Hughes et al., 2002). These types of scoria cones typically represent Strombolian to potentially Violent Strombolian eruptions, which can produce VEI2–3 eruptions and associated tephra-fall deposits (e.g., Walker, 1973; Pioli et al., 2008). Although some tephra-fall deposits are partially preserved in the Craters of the Moon area, their distributions and volumes have not been investigated.

Lava flows from the ESRP shield volcanoes typically flowed over low topographic relief to distances of 25 km from the vent (Hackett et al., 2002). In contrast, more channelized flows erupted from vents in the northwestern periphery of the ESRP (i.e., higher elevation) were channelized and flowed 50–60 km from the source vent (Figure 12). Phreatomagmatic eruptions occurred at several locations in the ESRP, in association with near-surface water in the southern parts of the ESRP (e.g., Menan Buttes; Hackett et al., 2002). Potential hazards associated with phreatomagmatic vents are pyroclastic density currents that might extend to 10 km of the vent (e.g., Self et al., 1980; Cas and Wright, 1987), and tephra falls that might extend for 10's of kilometers from the vent (e.g., Self et al., 1980).

Silicic eruptions have not produced mapped tephra deposits, although trace amounts of pumice are preserved at the summit of 0.3 Ma Big Southern Butte. Small-volume block and ash deposits also are present at Big Southern Butte and in the subsurface 5 km from the vent, indicating some potential for block-and-ash flows (i.e., pyroclastic density currents) associated with the formation of a new rhyolite dome (e.g., Calder et al., 2015), with outflow distances extending to only 10's of kilometers from the vent (e.g., Brown and Andrews, 2015). Some analogous rhyolite dome eruptions are explosive (i.e., VEI2–3) and produce tephra falls from convective plumes (e.g., Calder et al., 2015).

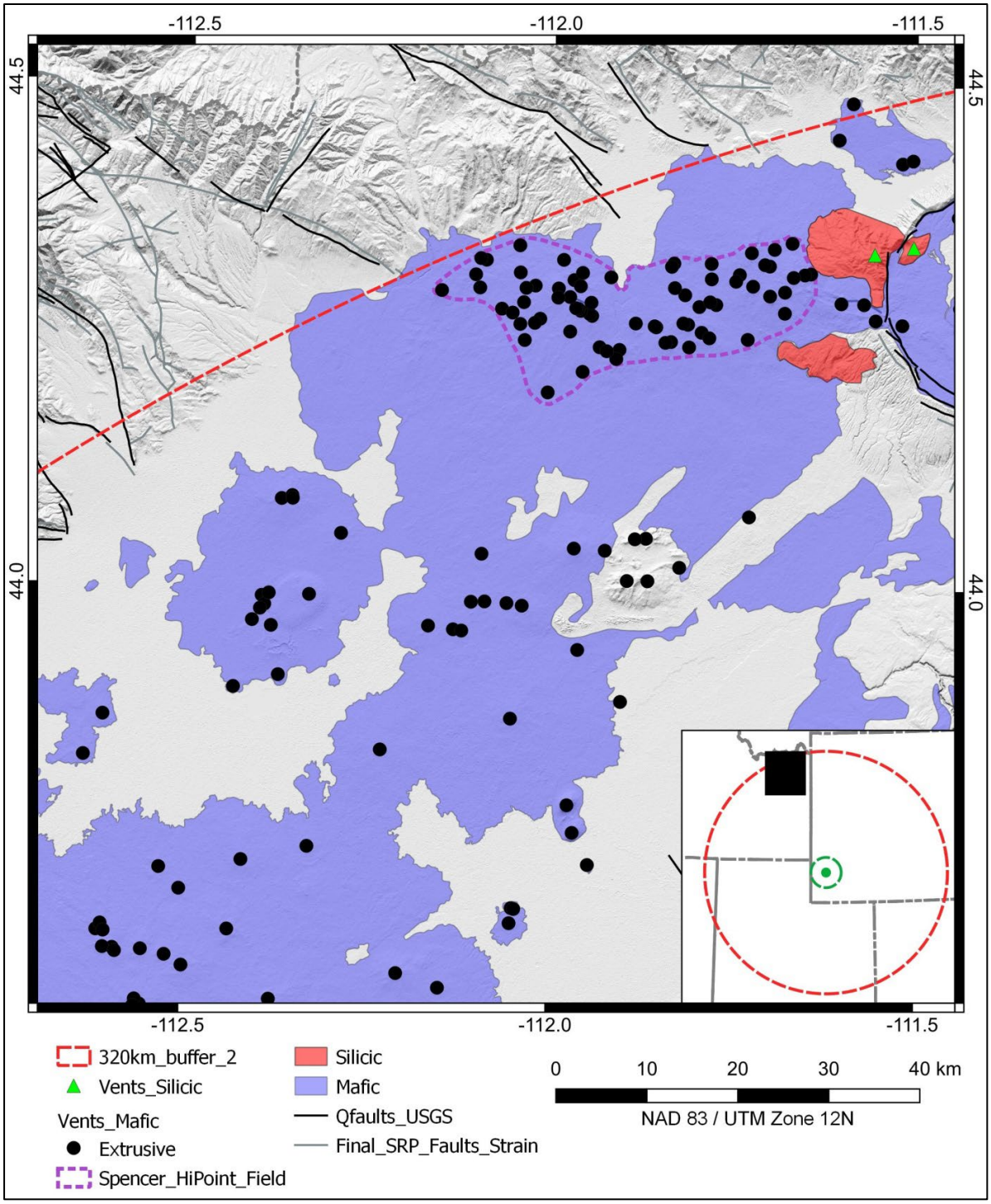

Figure 13. Eastern ESRP and Spencer-High Point rift zone. Basalt and rhyolite of the Yellowstone Volcanic field are located east of the boundary of the Spencer-High Point rift zone, and lavas from the Blackfoot Volcanic Field are located north of the inset map. Neogene faults (Shervais, 2015), boundaries of the Spencer-High Point rift zone (Iwahashi, 2010); Digital Elevation model SRTM-1 (30 m resolution) (OpenTopography, 2013), Quaternary faults (Schmitt, 2017), and geology after (Horton, 2017).

Following the approach outlined in Regulatory Guide 4.26, the distances that maximum-magnitude hazards have traveled from ESRP vent areas are summarized in Table 8. Note that the proximal hazard distance of 40 km is based on the criteria in Regulatory Guide 4.26, which restricts potential hazards to within 40 km of an erupting volcano.

Table 8. ESRP summary of distances represented by maximum-magnitude events. VEI = Volcanic Explosivity Index; *PDC = pyroclastic density currents from phreatomagmatic eruptions. "?" indicates a screening distance cannot be developed based on current information, but the phenomena is characteristic of the volcano type.

ESRP	*Vents in Region*	*Ages (Ma)*	*General VEI*	*Tephra (km)*	*New Vent Hazard*	*Lava flows (km)*	*Proximal Hazards (km)*	*PDC (km)*
Mafic vents	431	0.002–0.78	2–3	?	Yes	<60	<40	<10*
Silicic vents	7	0.3–1.4	2–3	?	Yes	<5	<40	<10's

2.8 Volcanoes >320 km from the Proposed Site

Regulatory Guide 4.26 identifies the need to characterize potential hazards from volcanoes >320 km from a proposed site, if deposits from past eruptions of those volcanoes are located within 40 km (i.e., site vicinity) of the site. Three large-volume tephra-fall eruptions have occurred from Quaternary calderas in the western United States, which might have had some potential to reach the proposed Natrium™ site based on interpreted distributions of their deposits:

- Bishop Tuff eruption at 0.76 Ma from the Long Valley Caldera in eastern California (≈840 km from site), erupted ≈100 km^3 of magma as tephra falls (Hildreth and Wilson, 2007).

- Upper Bandelier Tuff (Tshirege Member, Tsankawi Pumice) eruption at 1.23 Ma from the Valles Caldera, New Mexico (≈840 km from site), erupted ≈20 km^3 of magma as tephra falls (Self et al., 1996).

- Mt. Mazama (Crater Lake) eruption at 0.08 Ma from the Cascade Range, Oregon (≈950 km from site), erupted ≈45 km^3 of magma as tephra falls (Buckland et al., 2020).

Reworked tephra fall deposits from the 0.76 Ma Bishop Tuff eruption can be found in scattered exposures throughout much of the western United States, although undisturbed deposits are scarce >100 km from the Long Valley caldera (Izett et al., 1988). Mapped distributions of either intact or reworked Bishop Tuff tephra show that the nearest tephra-fall deposits are located >140 km from the proposed Natrium™ site (Izett et al., 1988; Sarna-Wojcicki et al., 1991). Nevertheless, interpreted distribution maps (Izett et al., 1988; Sarna-Wojcicki et al., 1991) suggest that the original Bishop Tuff ash might have been deposited in the site vicinity.

The tephra-fall from the 1.6 Ma Lower Bandelier Tuff eruption has been sufficiently investigated to determine that the eruption plume was directed east and southeast from the caldera (Self et al., 1986) and would not be expected in the site vicinity. In contrast, detailed distribution maps of the 1.23 Ma Tshirege tephra fall have not been developed (i.e., Izett, 1981; Izett et al., 1988). Proximal deposit distributions indicates the Tshirege tephra plume was directed to the north from the Valles Caldera (Self et al., 1996), and a generalized distribution map shows Tshirege

ash as far north as the Wyoming-Colorado border (Goff, 2010). Based on geochemical characteristics, a pluvially reworked 3-m-thick ash bed in southwestern Saskatchewan, Canada, has been correlated to the 1.23 Ma Tshirege tephra-fall eruption (Westgate et al., 2018). A geochemically similar ash deposit also occurs in central Utah, which led Westgate et al. (2019) to hypothesize that the Tshirege eruption plume was entrained by the jet stream, which had made an anomalous bend and flowed northward from New Mexico into Canada. As a result, it remains possible that ash from the 1.23 Ma Tshirege tephra-fall eruption might occur in the site vicinity.

Because of its relatively young (≈8 ka) age, tephra-fall deposits from Mt. Mazama have been mapped as distinctive marker horizons in Holocene alluvial deposits throughout the western United States (e.g., Mullineaux, 1974; Sarna-Wojcicki et al., 1991; Buckland et al., 2020). Tephra falls from the 8 ka Mazama climactic eruption formed multiple lobes directed to the northeast and southeast (Williams, 1942; Young, 1990), which are not shown in more generalized interpretations of distal ash extent (i.e., Mullineaux, 1974; Sarna-Wojcicki et al., 1991; Buckland et al., 2020). Identified localities with Mazama tephra-fall deposits only occur >200 km from the proposed Natrium™ site. Nevertheless, interpreted distribution maps (e.g., Mullineaux, 1974; Sarna-Wojcicki et al., 1991; Buckland et al., 2020) suggest that the 8 ka Mt. Mazama ash might have been deposited in the site vicinity.

In summary, tephra-fall distribution patterns have been interpreted by some investigators to indicate that ash deposits from three distant Quaternary caldera eruptions might have travelled as far as the proposed site. However, careful examination of actual distribution locations shows that no deposits from the Bishop and Mazama eruptions have been reported within 140–200 km of the proposed site. To address the uncertainty in the distribution of the Tshirege ash, and confirm the absence of other Quaternary ash deposits in the site vicinity, detailed geologic maps in the site vicinity were examined for indications of Quaternary volcanic ash in any Quaternary unit (e.g., alluvium, colluvium). There is no mention of any Quaternary volcanic ash in detailed 1:100,000 (Dover and McGonigle, 1993; Dover, 1995; M'Gonigle and Dover, 2004; Wittke and Heffern) and 1:24,000 (M'Gonigle, 1979, 1992; Schroeder and Lunceford, 1979b, 1979a; Schroeder, 1981, 1982) maps that cover the site vicinity.

2.9 Summary of Quaternary Volcano Characteristics in the Site Region

The first step in conducting a VHA is to identify Quaternary volcanoes in the site region, and characterize their potentially hazardous phenomena sufficiently to support a screening evaluation in Step 2 of Regulatory Guide 4.26. In addition, the site vicinity must be evaluated for potential deposits from Quaternary volcanoes located beyond the site region.

Based on discussions in Sections 2.1–2.7, sufficient information is available to determine the age and location of Quaternary volcanic events in the site region, and to characterize their potentially hazardous phenomena in sufficient detail to determine the maximum magnitude of past events. These characteristics are summarized in Table 9:

Table 9. Summary of Quaternary volcanoes in the site region. An "*" in the column indicates distance based on phreatomagmatic eruptions. Tephra falls with "?" indicate that the extent cannot be determined with available information, and additional analyses appear warranted.

Volcanic Field	*Vents in Region*	*Ages (Ma)*	*≈VEI*	*Tephra Falls (km)*	*Opening of New Vent*	*Lava flows (km)*	*Proximal Hazards (km)*	*PDC (km)*
YVF Mafic	20	<0.64	≤1	?	Yes	<60	<40	No
YVF Silicic	11	<0.17	3–6	>220	Yes	<30	<40	<120
YVF Calderas	3	<2.1	7–8	>1,000	Yes	No	<40	<120
UWRB Mafic	1	0.46±0.05	2–3	?	Yes	<10	<40	No
LHVF Mafic	26	0.8–3.0	2–3	?	Yes	<5	<40	No
NBRD Mafic	2	0.3–0.9	≤1–2	<10	Yes	<10	<40	<10*
CVVF Mafic	7	0.4–0.03	≤1	<80*	Yes	<5	<40	<10*
CVVF Silicic	1	2.3	2–3	?	Yes	<5	<40	No
BRVF Mafic	85	0.03–1.5	2–3	?	Yes	<50	<40	No
Silicic vents	7	0.05–1.6	2–3	?	Yes	<5	<40	<10
ESRP Mafic	431	0.002–0.78	2–3	?	Yes	<60	<40	<10*
ESRP Silicic	7	0.3–1.4	2–3	?	Yes	<5	<40	<10's

A total of 572 Quaternary mafic eruptive fissures, shield volcanoes, scoria cones, and maars occur in the site region, along with 3 silicic caldera systems and 26 intermediate-to-silicic domes and lava flows. The nearest Quaternary volcano is located >117 km from the proposed Natrium™ site. Mafic and silicic volcanoes have produced lava flows that have travelled up to 60 km from the vent, and calderas have produced pyroclastic density current that have travelled up to 120 km for the source area.

Based on the general characteristics of preserved volcanoes, shield and maar volcanoes would be expected to have relatively low explosivity eruptions (i.e., VEI≤1), with tephra-fall deposits restricted to tens of kilometers from the vent. Some mafic scoria cones and silicic domes may have had low explosivity eruptions (i.e., VEI2–3), but past tephra-fall deposits are not preserved for these eruptions. Larger silicic dome eruptions might have been moderately to highly explosive eruptions (i.e., VEI4–5), with tephra falls extending for hundreds of kilometers, and pyroclastic flows potentially within 120 km, from the vent. The large caldera-forming eruptions at Yellowstone were highly explosive (VEI7–8) and formed tephra falls that extended for >1,000 km from the source area. Pyroclastic flows, however, were restricted to <120 km from the source area. There are no deposits in the site vicinity (i.e., <40 km from the site) from Quaternary volcanoes that are located beyond the boundaries of the site region (i.e., >320 km from the site).

3 REGIONAL TECTONO-MAGMATIC MODEL

Regulatory Guide 4.26 emphasizes the need to evaluate the potential for future eruptions that could occur within 40 km of a proposed site (i.e., the site vicinity), because proximal hazards from such eruptions (e.g., the opening of new vents) might need to be included in the VHA. This evaluation typically occurs as Step 2a in the VHA, before the initial screening of potential hazards.

There is no evidence of igneous rock of any age within the site vicinity; the bedrock geology is composed of folded, faulted, and deformed sedimentary rocks of Eocene age or older (i.e., >34 Ma) (Dover and McGonigle, 1993; Dover, 1995; M'Gonigle and Dover, 2004; Wittke and Heffern). In addition, with the exception of an isolated exposure 62 km from the site of Tertiary basalt at Black Mountain, Utah (Section 2.5.1), igneous rocks <16 Ma only occur >100 km from the proposed site (Luedke and Smith, 1983). Consequently, the past patterns of activity show that the geological conditions within and beneath the site vicinity have not resulted in magmatic eruptions.

Nevertheless, the absence of past igneous activity within or in close proximity to the site vicinity does not, by itself, appear to provide an authoritative basis to conclude that future igneous activity could not occur in this area. Following guidance in Regulatory Guide 4.26, a tectono-magmatic model can be useful in evaluating the large-scale processes that led to the occurrence of Quaternary volcanism at specific locations in the site region. Those regional conditions can then be compared to the specific conditions that occur in the site vicinity, to provide additional rationale on the potential for new or, in the case of the proposed site, unprecedented eruptions to occur in the site vicinity. The tectono-magmatic model developed for this VHA is a conceptual framework that develops geologic rationale for the processes that control volcanic eruptions in the site region, to help determine if such processes might occur in the site vicinity.

Volcanism in the ESRP, YVF, and UWRB volcanic fields originates from the thermal and mechanical effects in the upper mantle from the passage of the North American tectonic plate over the Yellowstone hotspot (e.g., Pierce and Morgan, 1992). In the crust, the extent of these effects is expressed by patterns of faulting and historical seismicity (Figure 14) that form a broad parabola that extends to >90 km north and west of the site (i.e., Anders et al., 1989). In the uppermost mantle (i.e., 60–70 km depth), thermal effects also are expressed as a zone of low shear-wave velocity that extends from the Yellowstone caldera to >50 km northwest of the proposed site (Schmandt et al., 2015; Shen and Ritzwoller, 2016), and also encompasses the ERSP, YVF, and UWRB volcanic fields. Low shear-wave velocities typically are associated with areas of partial melting, or relatively high temperatures, in the upper mantle (e.g., Takei, 2017).

Volcanism in the site vicinity did not occur in response to the passage of the Yellowstone hotspot at approximately 10 Ma (e.g., Pierce and Morgan, 1992), and the site is located south of the present-day area where thermal and mechanical perturbations have initiated Quaternary volcanism. A reasonable conclusion is that there is a negligible potential for the effects of the Yellowstone hotspot to trigger the formation of a new volcanic system in the site vicinity, during the operational period of the proposed facility (i.e., on the order of 100 years).

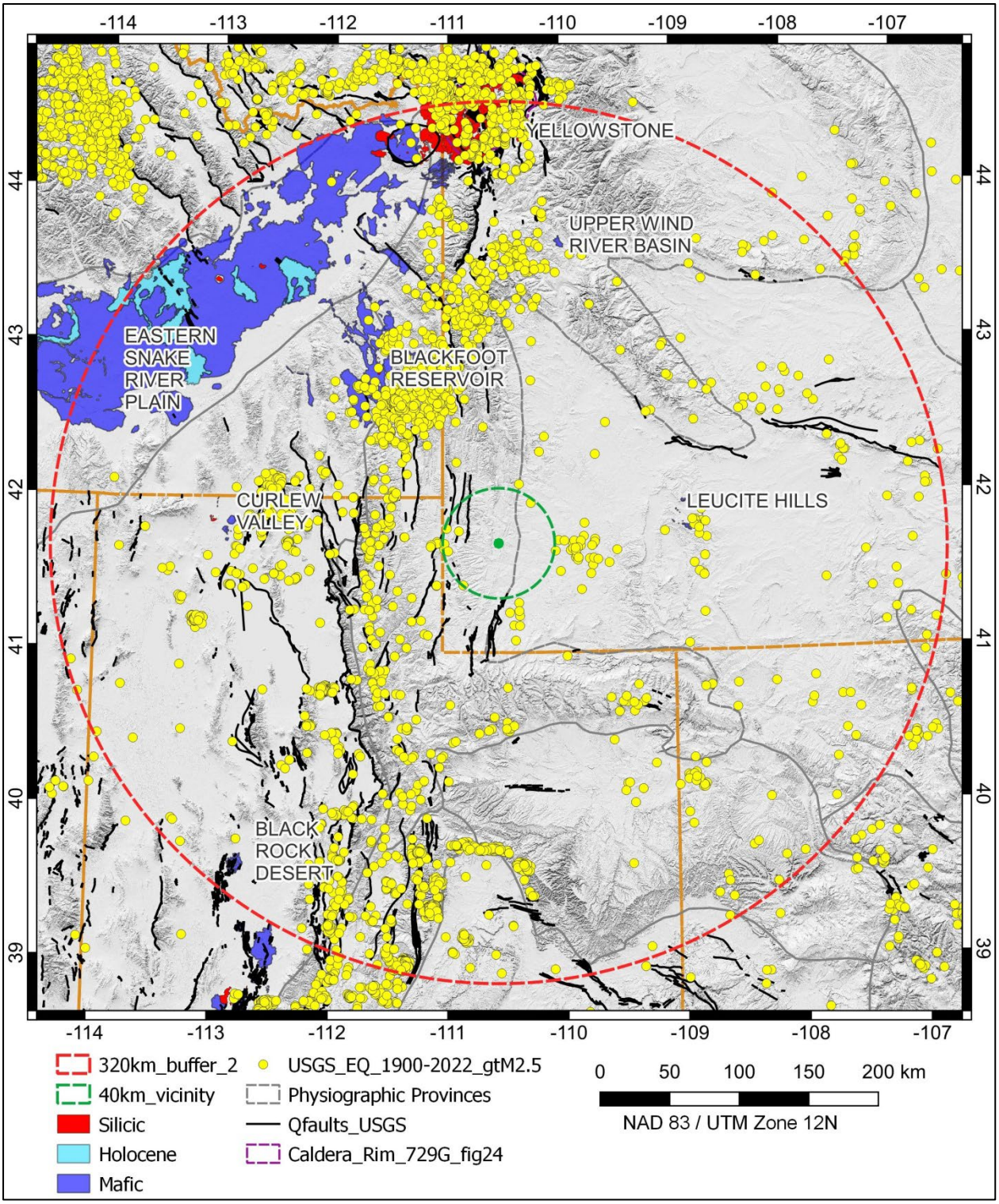

Figure 14. Regional patterns of faulting and seismicity, and distribution of Quaternary volcanic rocks. Data sources cited in Figure 2–Figure 12.

Volcanism in the CVVF and NBRD volcanic field represents the characteristic types of distributed volcanism that occurs throughout much of the Basin and Range tectonic province. A generalized model for the origins of Quaternary Basin and Range volcanism is that crustal extension facilitates the decompression of the mantle, which induces partial melting and mafic magmatism (e.g., Leeman and Harry, 1993; Harry and Leeman, 1995; Putirka and Platt, 2012). After >50% crustal extension, partial melts can be derived from both metasomatically enriched lithospheric mantle as well as non-metasomatized asthenospheric mantle (Harry and Leeman, 1995). The small volumes of Quaternary mafic and silicic eruptions in the CVVF and NBRD are consistent with this general model (Peterson and Nash, 1980; Turley and Nash, 1980; Kerr, 1987; Miller et al., 1995; Felger et al., 2016).

In contrast, the proposed site is located in the Sevier overthrust belt, which is characterized by compressional tectonic structures and has not experienced significant crustal extension in the last 60 Myr (e.g., Dixon, 1982). Consequently, the mantle beneath the proposed site has not experienced decompression due to crustal extension, and partial melts have not been generated, as has occurred in the CVVF and NBRD. A reasonable conclusion is that there is a negligible potential for the effects of Basin and Range-type crustal extension to trigger the formation of a new volcanic system in the site vicinity, during the operational period of the proposed facility (i.e., on the order of 100 years).

The BRVF is located at the northeastern part of the Basin and Range province (Figure 14). Similar to the NBRD and CVVF, magmatism in the BRVF is related to interactions between Basin and Range crustal extension and additional thermo-mechanical effects from passage of the Yellowstone hotspot (Hughes et al., 2002; Pickett, 2004). The upper mantle beneath the BRVF also is within the zone of anomalously low shear-wave velocities that includes the ESRP, indicating that the upper mantle likely contains some fraction of magma (e.g., Schmandt et al., 2015; Shen and Ritzwoller, 2016). Abundant historical seismicity (Figure 14) and Quaternary faulting (Polun, 2011; Hastings et al., 2021) also are characteristics of the BRVF.

In contrast, the site vicinity is located southeast of the low velocity mantle zone, and has sparse historical seismicity and Quaternary faulting (Figure 14). Consequently, the absence of igneous activity since 16 Ma in the site vicinity is consistent with the absence of geophysical features intimately linked to igneous activity in the site region. A reasonable conclusion is that there is a negligible potential for the effects of Yellowstone hotspot or Basin and Range-type crustal extension to trigger the formation of a new volcanic system in the site vicinity, during the operational period of the proposed facility (i.e., on the order of 100 years).

Compared to the other volcanic fields in the site region, the Leucite Hills volcanic field is not associated with an obvious tectonic feature that would help explain the occurrence of mafic magmatism during 0.8–3.0 Ma. Although the influence of thermo-mechanical effects from the Yellowstone hotspot have been proposed as an initiator for LHVF magmatism (Mitchell and Bergman, 1991; Mirnejad and Bell, 2006), the upper mantle beneath the LHVF has shear-wave seismic velocities that are significantly higher than associated with the Yellowstone hotspot parabola and associated volcanic fields (Schmandt et al., 2015; Shen and Ritzwoller, 2016).

Alternatively, LHVF magmatism might have been initiated by northward migration or upwelling of relatively hot, deep mantle beneath the Colorado Plateau into the cooler Archean mantle beneath the Wyoming Basin (Lange et al., 2000; Long et al., 2019). The upper mantle between 70–120 km depths has relatively high shear-wave velocities beneath the LHVF (Shen and Ritzwoller, 2016), which do not indicate anomalous upwelling of hot (i.e., slower velocity) mantle. However, a sharp upward gradient in the depth to the upper-lower mantle transition

zone (i.e., 410 km) and upper-lower mantle boundary (i.e., 660 km) occurs in the area beneath the LHVF. A shallowing of these boundaries would be expected if upwelling of deep mantle from beneath the Colorado Plateau had occurred beneath the LHVF (i.e., Lange et al., 2000; Long et al., 2019). In contrast, the 410 and 660 mantle boundaries beneath the site vicinity show much broader and lower amplitude gradients than beneath the LHVF, in addition to high shear-wave velocities relative to the Yellowstone parabola.

The mantle beneath the site vicinity lacks the geophysical characteristics associated with deep mantle upwelling that is most likely associated with Quaternary mafic magmatism in the LHVF. A reasonable conclusion is that there is a negligible potential for the effects of deep mantle upwelling from the beneath the Colorado Plateau to trigger the formation of a new volcanic system in the site vicinity, during the operational period of the proposed facility (i.e., on the order of 100 years).

In summary, the large-scale tectonic processes that control Quaternary volcanism in the region have been sufficiently investigated to support development of a tectono-magmatic model for the site region. The structural, crustal, and mantle characteristics that have resulted in Quaternary volcanism at various locations in the site region do not occur in or beneath the site vicinity. Although <16 Ma volcanism occurred throughout the site region, no volcanic activity occurred during that time within the site vicinity. The absence of volcanic activity in the site vicinity is consistent with the absence of tectonic characteristics in the site vicinity that resulted in Quaternary volcanism elsewhere in the site region.

4 SCREENING OF VOLCANIC HAZARDS

Following the recommended approach in Regulatory Guide 4.26 (Nuclear Regulatory Commission, 2021), the next step in the VHA is to screen potential hazards based on the maximum magnitude of past events. The screening should give appropriate consideration to the current topographic characteristics between potential volcanic vents and the proposed site. Only those phenomena that are characteristic of Quaternary volcanoes in the site region need to be considered, and Quaternary volcanic systems that are inconsistent with the tectono-magmatic model do not warrant additional investigation.

The screening evaluation should consider uncertainties in the potential locations for new vents when evaluating maximum-magnitude screening distances for potentially hazardous phenomena. In addition, the potential effects of burial or erosion should be considered when determining the characteristics of past maximum-magnitude events (Nuclear Regulatory Commission, 2021).

The results of the screening analysis are used to determine if a potential hazard should be considered further in the VHA, or if sufficient information exists to determine that the volcanic phenomenon would not affect the proposed site (i.e., screens out).

4.1 Opening of New Vents

In distributed basaltic volcanic fields, new volcanoes can form at locations that lack previous eruptions. Most distributed basaltic volcanic fields show some form of spatial clustering in vent locations, often due to tectonic controls on magma ascent and eruption (e.g., Valentine and Connor, 2015). The past locations of vents, however, rarely bound the area where future vents might occur. Unless there is compelling geological evidence to preclude new vent formation for specific areas, vent distributions typically are analyzed using spatial statistics to determine the likelihoods of new vent formation in a distributed volcanic field (e.g., Connor and Hill, 1995; Gallant et al., 2018). A common statistical method is to use kernel density functions, which calculate vent densities for each point on a grid using a smoothing function. The gridded densities are then used to develop spatially dependent likelihoods of new vent formation, assuming that an eruption occurs in the volcanic field (e.g., Connor et al., 2019).

As part of the Yucca Mountain program, the U.S. NRC sponsored development of the computer code PVHA_YM Version 2.0 (Connor et al., 2002), to conduct confirmatory analyses for the likelihood of new vent formation at the proposed repository site. The PVHA_YM Version 2.0 code implemented the kernel density functions in Connor and Hill (1995). Most importantly, this code was developed and accepted under the quality assurance requirements applicable to 10 CFR Part 63, which are identical to quality assurance requirements under 10 CFR Part 50, which included formal review and validation testing programs (Nuclear Regulatory Commission, 2002).

PVHA_YM Version 2.0 implements two different kernel density functions: Gaussian and Epanechnikov (Connor and Hill, 1995). The Gaussian kernel is spatially homogeneous (i.e., no directionality), and essentially assumes that vent distributions are a random process with no bounds (i.e., probability is very small but not zero at large distances from past events). In contrast, the Epanechnikov kernel uses a bivariate distribution, and has some bounds on the extent that the spatial probability would be non-zero (Connor et al., 2019). For either kernel, the most important assumption is the selection of a smoothing bandwidth, which controls the shape of the probability distribution for the volcanic field. Numerical inversion techniques are available

to optimize the smoothing bandwidth, which can be useful when complex patterns of vents and small variations in spatial recurrence rate are significant (i.e., Connor et al., 2019). For more generalized applications, visual examination of a range of smoothing bandwidths can be used to evaluate geological rationale to select or reject specific bandwidth values.

To confirm the results of the tectono-magmatic model (Section 3), the probability of new vent formation was evaluated using the PVHA_YM Version 2 code for the LHVF. The LHVF is the closest Quaternary volcanic field to the proposed site, (117 km; 3.0 Ma subvolcanic intrusion at 101 km), and is located in the same geologic province (i.e., Wyoming Basin) as the eastern parts of the site vicinity. Although the geologic conditions that resulted in Quaternary volcanism at the LHVF do not occur beneath the site vicinity, the proximity of this volcanic field to the proposed site supports the utility of a confirmatory analysis for the opening of new vents.

The first stage of the probability analysis is the determination of an appropriate smoothing bandwidth for the distribution of LHVF vents. Using the vent locations in Figure 6 and assuming a recurrence rate of $7x10^{-6}$/yr (i.e., 21 events in 3.0 Myr; Section 6.4.1), a Gaussian smoothing bandwidth of >25 km is needed before a probability of new vent formation can even be calculated (i.e., $\geq 10^{-15}$/yr) for the proposed site (Figure 15A). A maximum probability of $4x10^{-10}$/yr would result from a smoothing bandwidth of ≈85 km. For an Epanechnikov kernel, a smoothing bandwidth of >100 km is needed before a probability of new vent formation can even be calculated (i.e., $\geq 10^{-15}$/yr) for the proposed site (Figure 15B). A maximum probability of $5x10^{-10}$/yr would result from a smoothing bandwidth of ≈180 km.

The reasonableness of different smoothing bandwidths must be evaluated by examination of maps that show patterns spatial recurrence for the probability of new vent formation at the proposed site. Using the same LHVF vent location data and recurrence rates as in Figure 15, spatial distributions of the probability of new vent formation are shown for a Gaussian kernel in Figure 16 and an Epanechnikov kernel in Figure 17. For either kernel function, the selection of a 5 km smoothing bandwidth partitions the volcanic field into unrealistic groupings of isolated vents, or small clusters of events (Figure 16A, Figure 17A). Increasing the smoothing bandwidth to 10 km (Gaussian, Figure 16B) or 20 km (Epanechnikov, Figure 17B) is needed to include all the past events within the lowest probability contour. However, note that at these smoothing bandwidths most of the northwesterly trends in vent alignments are missing, and existing vent locations only have a small influence on spatial probability distributions. These broader patterns suggest that important geologic information is being lost on the underlying processes that control vent location, and that the smoothing bandwidths are becoming unrealistically large.

An additional doubling of these smoothing bandwidths results in essentially uniform distributions of spatial probability, as the kernel functions begin to evaluate the volcanic field as a point source that localizes a symmetrical distribution of smoothly-decreasing probability (Gaussian, Figure 16C, Epanechnikov, Figure 17C). The only geologic information reflected in these distribution patterns is the locus of the volcanic field. Note that due to the unbounded nature of the Gaussian distribution, a probability of $3x10^{-15}$/yr can be calculated for a smoothing bandwidth of 20 km (Figure 16C). Increasing the smoothing bandwidth to distances that produce the highest probability values (Figure 15) results in highly unrealistic spatial patterns, which treat the vent distributions simply as a point to use for calculating a nearly isotropic distribution of spatial recurrence (Gaussian, Figure 16D, Epanechnikov, Figure 17D).

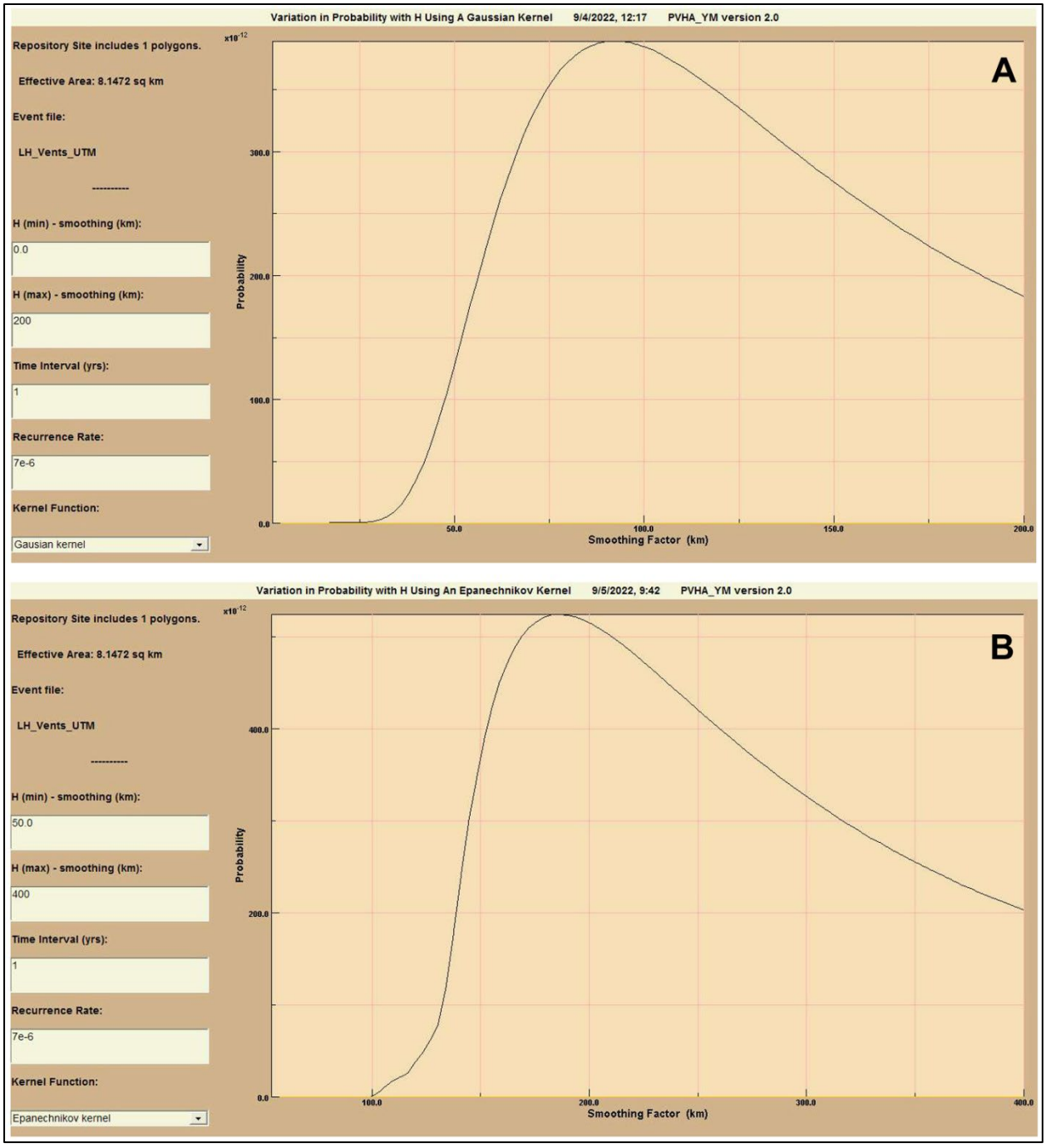

Figure 15. Smoothing factors (i.e., bandwidths) for (A) Gaussian and (B) Epanechnikov kernels. "Repository Site" is the location of the proposed Natrium™ site. Note the change in scale for "Smoothing Factor" from (A) to (B). Distributions calculated from PVHA_YM Version 2.0 for the LHVF vent locations (Figure 6).

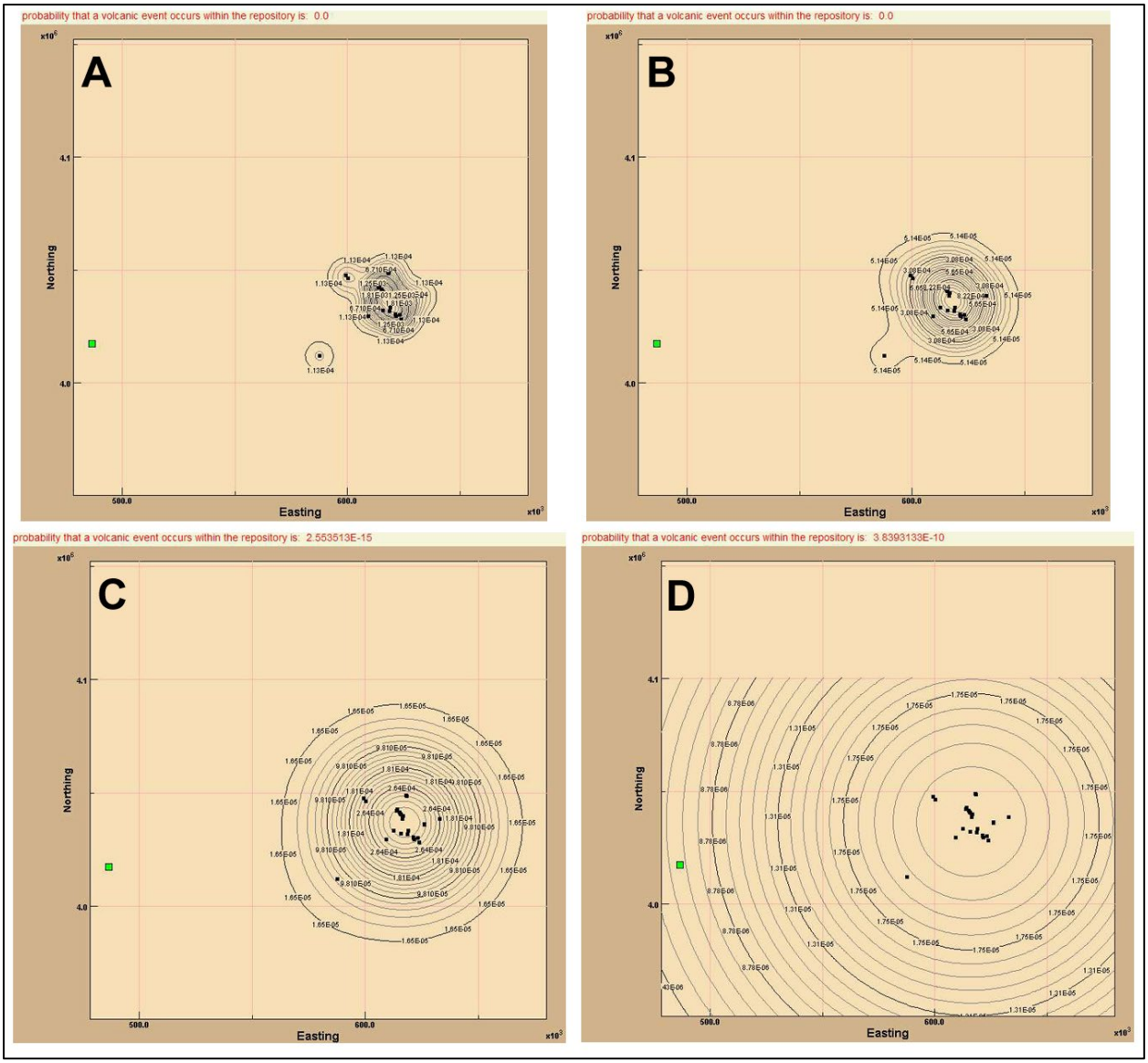

Figure 16. Evaluation of changes in smoothing bandwidth for a Gaussian kernel, using PVHA_YM Version 2.0. Smoothing bandwidths of 5 km (Figure 16A), 10 km (Figure 16B), 20 km (Figure 16C), and 85 km (Figure 16D). Data sources in Figure 15; “repository” (green square) is the 1-km-wide buffer zone around the proposed Natrium™ site. Note that the UTM coordinates for the vent locations have been adjusted (Easting −50 km, Northing −600 km) to allow for analysis within the static map boundaries used in PVHA_YM Version 2.0; all spatial inter-relationships are preserved accurately.

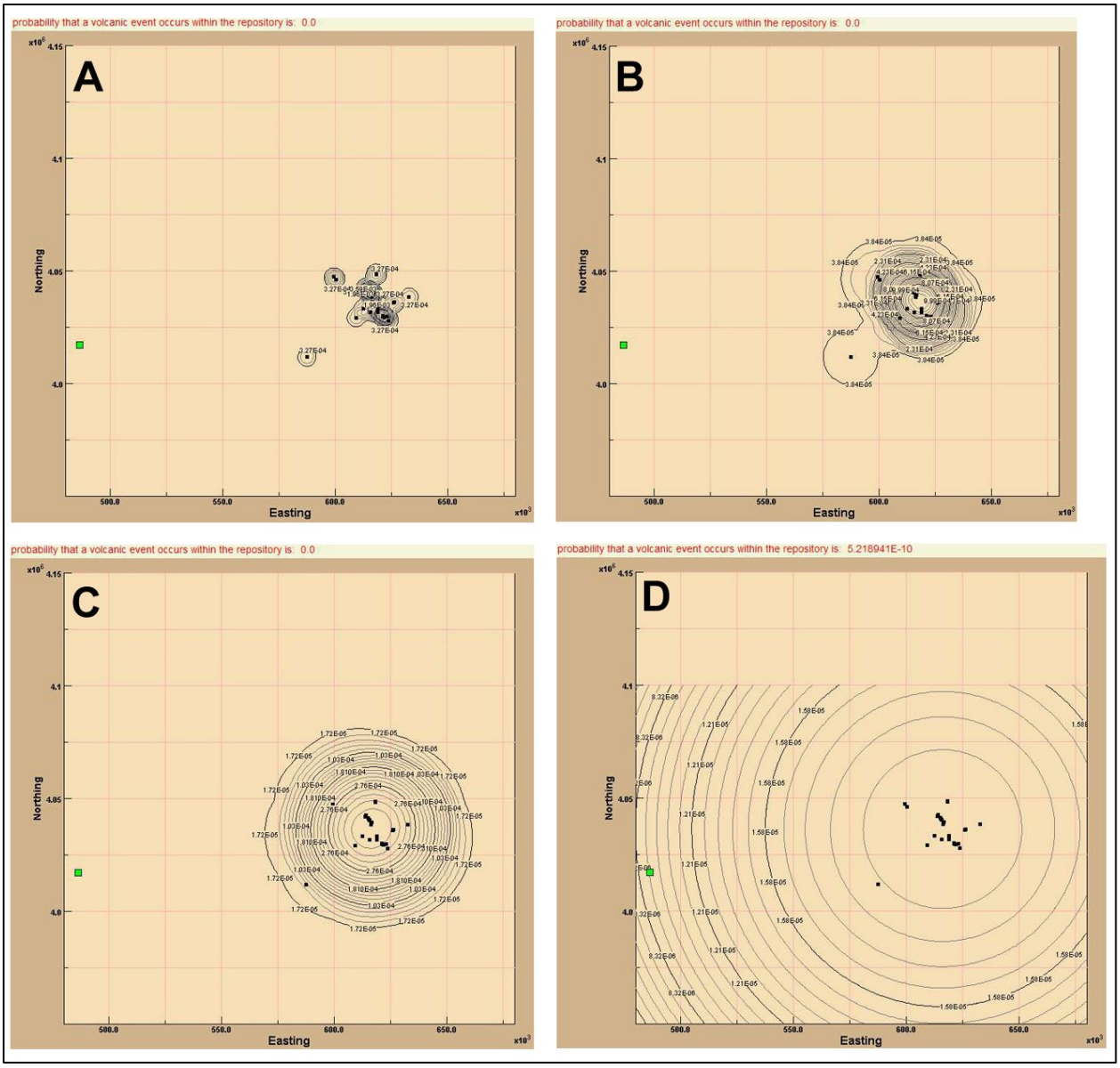

Figure 17. Evaluation of changes in smoothing bandwidth for an Epanechnikov kernel, using PVHA_YM Version 2.0. Smoothing bandwidths of 5 km (Figure 17A), 20 km (Figure 17B), 40 km (Figure 17C), and 180 km (Figure 17D). Data sources in Figure 15; "repository" (green square) is the 1-km-wide buffer zone around the proposed Natrium™ site. Note that the UTM coordinates for the vent locations have been adjusted (Easting −50 km, Northing −600 km) to allow for analysis within the static map boundaries used in PVHA_YM Version 2.0; all spatial inter-relationships are preserved accurately.

In summary, kernel density methods commonly are used evaluate the spatial distribution of vents in distributed volcanic fields, and to calculate the probability of new vent formation based on past patterns of activity. The NRC-accepted computer code PVHA_YM Version 2.0 is used to evaluate the probability of new vent formation at the proposed Natrium™ site, from future activity at the closest volcanic field to the site in Leucite Hills, Wyoming. Smoothing bandwidths for the Gaussian and Epanechnikov kernel density functions that produce geologically realistic patterns (i.e., reflect existing patterns of past activity) show that there is a $\leq 10^{-15}$/yr probability of a new vent forming at the proposed site. Increasing the smoothing bandwidth to the point where a $>3 \times 10^{-15}$/yr probability of new vent formation can be calculated results in geologically unrealistic patterns of spatial probability, in which the vent distributions in the LHVF simply serve as a locus for the calculation of nearly isotropic probability gradients. Further increases in smoothing bandwidths result in spatial patterns that are clearly unrealistic, and form spatial distributions that indicate a new vent would need to form at distances 2–3 times farther than the width or length of the volcanic field.

In conclusion, the opening of new vents at or within 1 km of the proposed Natrium™ site is not a potentially hazardous phenomenon, and can be screened-out from further consideration in the VHA, because:

- There is no record of past volcanic activity occurring in the site vicinity during the last 150 Myr.

- The nearest Quaternary volcano is 117 km from the proposed site, in the LHVF; a 3.0 Ma subvolcanic intrusion is located 101 km from the proposed site. The dimensions of the LHVF are on the order of 40x30 km.

- The tectonic and geologic conditions that have led to Quaternary volcanism in parts of the site region can be understood sufficiently to demonstrate that similar conditions do not occur in or beneath the site vicinity. There is no evidence to suggest that existing Quaternary volcanic systems >100 km from the site could somehow extend into the site vicinity, which has geologic conditions that have not resulted in the generation and ascent of magma since at least 150 Ma.

- Past patterns of activity in the Leucite Hills volcanic field also are analyzed using kernel density functions, which show that the probability of a new Leucite Hills vent opening at the proposed site is $\leq 10^{-15}$/yr for any geologically reasonable assumption in the numerical models.

4.2 Proximal Hazards

As discussed in Regulatory Guide 4.26, these proximal hazards can occur within 40 km of a new or existing volcanic vent:

- Debris avalanches, landslides, and slope failures.
- Volcanic missiles.
- Volcanic gases and aerosols.
- Atmospheric phenomena such as lightning.
- Ground deformation.
- Hydrothermal systems and groundwater effects.

The proposed Natrium™ site is located >40 km from any existing Quaternary volcano, and there is a negligible potential (i.e., $\leq 10^{-15}$/yr) for a new vent from the Leucite Hills volcanic field, the nearest volcanic field to the proposed site, to form within the site vicinity (Section 4.1). Based on these relationships, there is sufficient information to conclude that proximal hazards from volcanic eruptions do not need to be evaluated further in the VHA.

4.3 Lava Flows

All of the Quaternary volcanic fields in the site region have produced lava flows, with maximum flow lengths extending to 60 km in channeled terrain (Table 9). In addition to lava effusion rates (Walker et al., 1973), lava-flow paths are strongly controlled by the topographic gradient and degree of channeling, and typically flow the longest distances in steeply channeled terrain with moderate down-slope gradients (e.g., Kilburn, 1996). An analysis of potential effusion rates might be necessary if detailed analyses of lava-flow hazards are needed for the VHA (e.g., Connor et al., 2012), but are not necessary for screening analyses based on the maximum magnitude of past events. Consequently, the terrain between the proposed site and potential sources of lava flows needs to be evaluated, to determine if a maximum-magnitude lava flow might result in potential hazards at the site.

Except for the LHVF, all other Quaternary volcanic fields in the site region are located in drainage basins that are isolated from the drainage basin that includes the proposed site (Figure 18). In order to flow towards the proposed site, lava flows from vents in these volcanic fields would have to flow up-slope for tens to potentially hundreds of kilometers, and overtop topographic barriers hundreds of meters high. Such a scenario is physically unrealistic for the short (<60 km), relatively small volume (<10 km^3) lava flows that represent maximum-magnitude events for most Quaternary volcanoes in the site region.

Although the LHVF is located within the same drainage basin that contains the proposed site, the topography within this basin would prevent lava flows from reaching the site. The Green River is located between potential lava-flow sources in the LHVF and the proposed site (Figure 18). If a future vent formed in the southwest part of the volcanic field (i.e., Figure 17B), the lava would flow for several kilometers before reaching the Green River. It is physically unrealistic to conclude the lava would continue westward travel >75 km and overcome >330 m of elevation rise, rather than continue southward flow along the Green River drainage.

In conclusion, the proposed Natrium™ site is located in a drainage basin that is separated from the drainage basins that contain most of the Quaternary volcanic fields in the site region. Based on the topographic characteristics of these basins, potential basaltic lava flows <60 km long (i.e., maximum magnitude event) would not reach the proposed site. Although the LHVF is located in the same drainage basin that contains the proposed site, the Green River would capture and divert any potential lava flow that erupted from the farthest western extent of this field. In addition, the >75 km distance between the Green River and the proposed site exceeds the 60 km length of the maximum-magnitude lava-flow hazard. Based on these characteristics, there is sufficient information to conclude that lava flows from potential volcanic eruptions in the site region do not need to be evaluated further in the VHA.

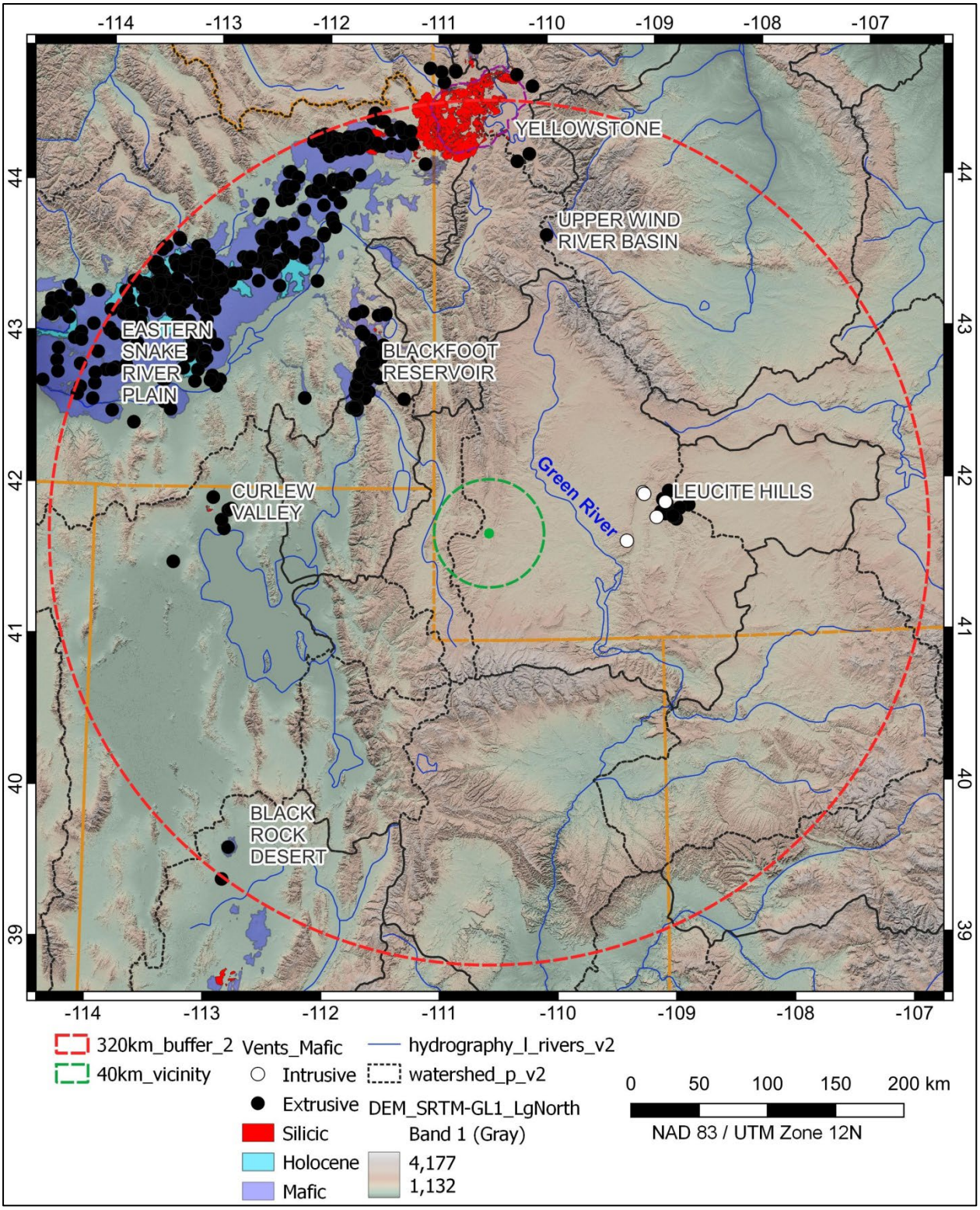

Figure 18. Topographic characteristics of the site region. Major rivers and lakes (Commission for Environmental Cooperation, 2022a), and boundaries of drainage basins (Commission for Environmental Cooperation, 2022b). Digital Elevation model SRTM-1 (30 m resolution) (OpenTopography, 2013).

4.4 Pyroclastic Density Currents

The three large-volume (>200 km^3) silicic eruptions from the Yellowstone caldera produced pyroclastic density currents (PDCs), most of which were restricted to within 50 km of the caldera rim. Near calderas, large-volume PDCs readily overtop topographic obstacles on the order of a thousand meters, due to the immense mass and mobility of the hot, high-velocity flows (e.g., Legros and Kelfoun, 2000; Dufek et al., 2015). As large-volume PDCs continue to travel from the caldera, mass and thermal energy are lost from the flow, which results in a more channelized flow that can be controlled by topographic obstacles of hundreds of meters or less (e.g., Sulpizio et al., 2014). These flow characteristics are well represented by the distribution of Yellowstone PDC deposits (Figure 19). Within about 50 km of the caldera rim, the largest-volume Huckleberry Ridge PDCs overtopped topographic obstacles 500–700 m high. In contrast, the smaller-volume Mesa Falls and Lava Creek PDCs were channeled by these topographic features, and were able to overtop only 100–200-m-high topographic obstacles (Figure 19). Between 50–120 km (i.e., maximum run-out distance) from the caldera, the Yellowstone PDCs were strongly channeled by topography (Figure 19).

The 0.64–2.1 Ma Yellowstone PDC eruptions clearly represent maximum-magnitude hazards. If smaller-volume PDCs occurred as part of silicic lava flow and dome eruptions, the distance these PDCs could travel would be significantly less than the large-volume Yellowstone PDCs. Nevertheless, the Yellowstone PDCs were restricted to <120 km from the eruptive caldera, and would have had to travel an additional >160 km to reach the area of the proposed Natrium™ site. In addition, that travel would have required overtopping 900–1100-m-high topographic obstacles in order to reach the drainage basin that includes the proposed site. There is no evidence that the Yellowstone PDCs were able to overtop such large topographic obstacles, or flow significantly farther than 120 km from the source caldera. Based on these straightforward observations, there is sufficient information to conclude that PDCs from potential silicic volcanic eruptions in the site region do not need to be evaluated further in the VHA.

4.5 Tephra Falls

Tephra falls from the 2.1 Ma Huckleberry Ridge eruption covered much of the western United States (Izett and Wilcox, 1982), most likely including the proposed Natrium™ site (Mastin et al., 2014). Scattered tephra-fall deposits from the 173±5 ka Bluff Point and 143±5 ka Cold Mountain Creek eruptions also occur 60–220 km from sources in the Yellowstone CPR (Section 2.1), which suggests that future larger-volume rhyolite pyroclastic eruptions from the Yellowstone CPR might have the potential for tephra falls to reach the proposed site. Although tephra falls from other mafic and silicic Quaternary volcanoes in the site region have not been preserved, comparison to similar, historically active volcanoes suggests that tephra falls might extend for tens to hundreds of kilometers from the source.

Based on the information presented in Section 2.8, tephra-fall deposits from Quaternary eruptions >320 km from the proposed site do not occur in the site vicinity. Using the criteria in Regulatory Guide 4.26 (Nuclear Regulatory Commission, 2021), the absence of these deposits in the site vicinity appears sufficient to conclude that future eruptions from Quaternary volcanoes >320 km from the proposed site do not need to be considered further in the VHA. There is some uncertainty associated with this conclusion, because any potential deposits from such past eruptions that might have occurred in the site vicinity likely would have been thin (centimeters or less) and easily eroded. In comparison, relatively thick (50–100 cm) tephra-fall deposits from the Yellowstone caldera-forming eruptions probably occurred in the site vicinity (Mastin et al., 2014). However, even these significantly thicker tephra-fall deposits have not

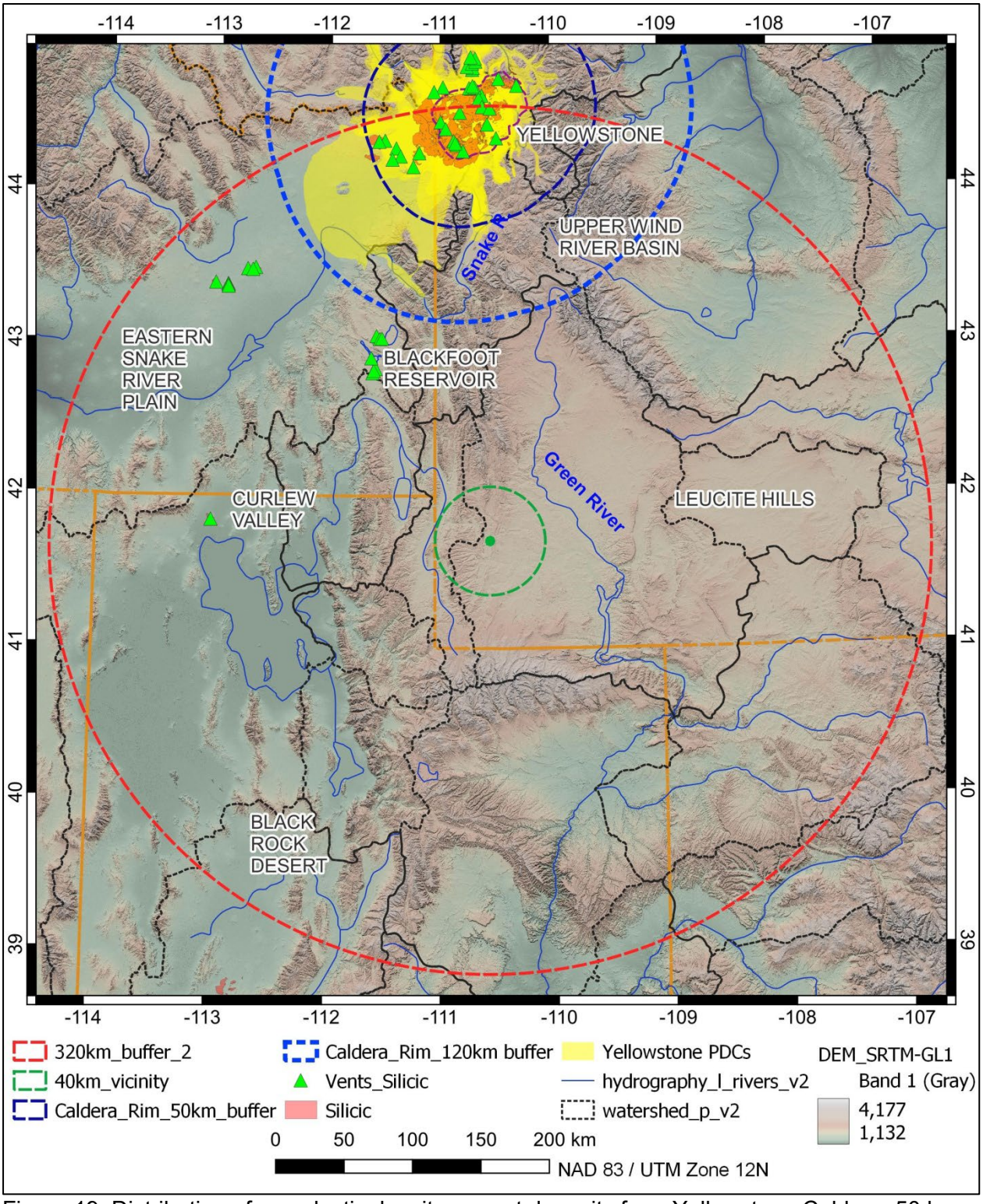

Figure 19. Distribution of pyroclastic density current deposits from Yellowstone Caldera. 50 km (dark blue dashed line) and 120 km (light blue dashed line) buffers from the outer rim of the Yellowstone caldera system, based on (Christiansen, 2001). Other data sources listed in Figure 18.

been preserved in the site vicinity. Nevertheless, additional analyses are warranted for tephra-falls from potential Yellowstone caldera-forming eruptions, because these Quaternary eruptions occurred in the site region. Any potential uncertainties regarding tephra-fall hazards from Quaternary calderas >320 km from the proposed site will be bounded by evaluations of significantly larger hazards from Yellowstone caldera eruptions in the site region.

Consequently, there is sufficient information to indicate that tephra-fall hazards should be evaluated in the more detailed VHA, for the range of volcano types that are characteristic of Quaternary volcanoes in the site region.

4.5.1 Debris Flows

Pyroclastic flow and fall deposits that are remobilized during heavy rainfall events can produce debris flows in drainages that are covered by these deposits. Debris flows significantly increase the sediment load transported during flood conditions, and consequently can overtop active channels and embankments to create a range of hazards that can occur for tens to potentially hundreds of years after an eruption (e.g., Gudmundsson, 2015; Thouret et al., 2020). Consequently, debris flows can create potential hazards in areas that were not adversely affected by pyroclastic flows and falls. The potential for debris-flow hazards to exist at a site is dependent on the topographic and drainage characteristics of a site, because debris flow transport is controlled by the hydrologic framework of the area surrounding a site.

The proposed Natrium™ site is located in the upper reaches of a small drainage basin that supports the North Fork of the Little Muddy Creek (NFLMC), which is an ephemeral to intermittent stream system (Figure 20). This basin isolates the site from the larger Green River drainage basin that encompasses the site and much of the site vicinity (i.e., Figure 19), which lies down gradient from the NFLMC basin. Consequently, any fluvially remobilized tephra-fall or PDC deposits located outside of the NFLMC basin would be unable to flow up topographic gradient and affect the proposed site.

However, tephra-fall deposits that might occur in the NFLMC basin would likely have some potential to be remobilized during heavy rainfall events, which occur infrequently in this part of Wyoming. In addition to tephra that is deposited directly in the drainages, tephra-fall deposits on hillslopes surrounding the drainages also can remobilize if overland flow occurs and erodes these deposits (e.g., Jones et al., 2017).

Based on the topographic characteristics of the proposed site, there is sufficient information to conclude that fluvial remobilization of pyroclastic deposits outside of the NFLMC basin would not create debris-flow hazards that could affect the proposed Natrium™ site. In contrast, the topographic characteristics of the NFLMC basin suggest that tephra-fall deposits within this basin might have some potential to be remobilized during heavy rain-fall events, which might create a potential hazard at the proposed site. Consequently, additional analyses appear warranted in the VHA to evaluate the potential for debris-flow hazards to occur at the proposed site from the fluvial remobilization of tephra-fall deposits that might occur within the NFLMC basin.

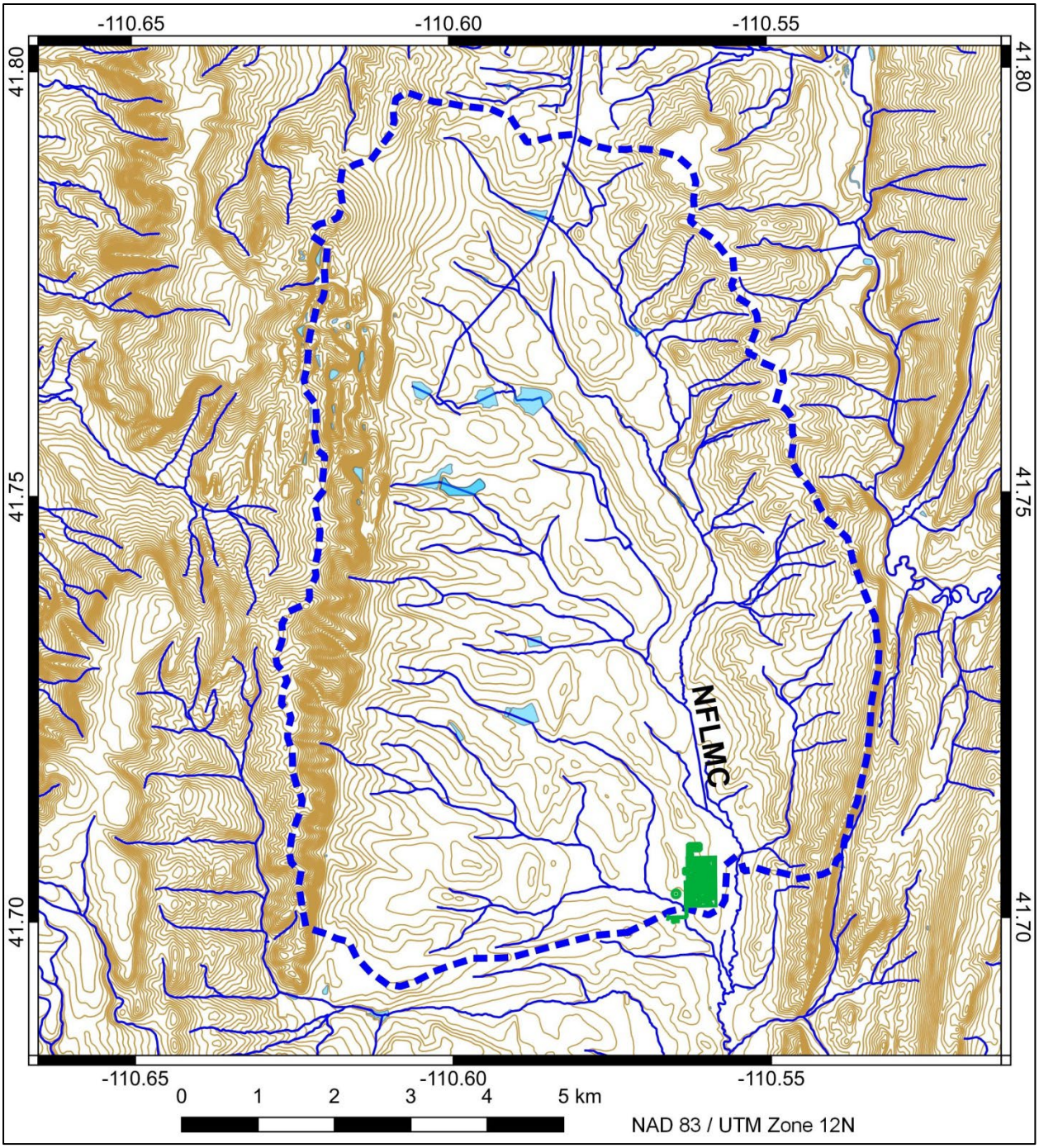

Figure 20. Map of the NFLMC drainage basin that surrounds the proposed site. Proposed site location outlined in green; boundaries of the NFLMC basin in dashed blue line; topography (20' contours, brown lines) and hydrology (thin blue lines) from U.S. Geological Survey (2022c).

4.6 Summary of Hazards Screening

Potential hazards from Quaternary volcanoes in the site region have been evaluated to determine if eruptive and non-eruptive phenomena might affect the proposed Natrium™ site. Based on the technical rationales discussed in Sections 4.1–4.5, screening decisions for potential volcanic hazards at the proposed Natrium™ site are summarized in Table 10.

Table 10. Screening summary for potential volcanic hazards at the proposed Natrium™ site.

Hazard	*Screen*	*Rationale*
Opening of New Vents	Out	- Geologic setting of site not consistent with tectono-magmatic conditions that form Quaternary volcanism in the region. - Nearest volcanic field is sufficiently distant to preclude new vent formation at the site.
Proximal Hazards	Out	- Site is >40 km from a Quaternary volcano or potential new vent.
Lava Flows	Out	- Site is topographically isolated and >60 km (maximum flow length) from any potential source.
Pyroclastic Density Currents	Out	- Site is topographically isolated and >120 km (maximum flow length) from any potential source.
Tephra Falls	Out	- For Quaternary volcanic systems beyond the site region.
Tephra Falls	In	- For Quaternary volcanic systems in the site region.
Debris Flows	In	- For potential tephra falls that deposit within the NFLMC basin surrounding the site; other sources screen-out due to topographic isolation of the site.

5 EVALUATION OF INITIAL RISK INSIGHTS

Tephra falls from mafic and silicic volcanoes, and localized remobilization of those deposits into debris flows, are the only potentially significant volcanic hazards at the proposed Natrium™ site. After conducting the screening analysis (i.e., Section 4), Regulatory Guide 4.26 allows for the development of initial risk insights (Step 3) as part of the VHA (Nuclear Regulatory Commission, 2021). These risk insights can be used to determine if additional hazard analyses are warranted, based on the potential significance of the screened-in hazards to the design and operation of the proposed facility.

The proposed Natrium™ facility relies on air circulation systems to provide cooling and ventilation to various safety- and non-safety-related structures, systems, and components. Fine-grained particles of volcanic tephra might affect the performance of air filtration systems. In addition, volcanic ash has relatively low thermal conductivity and thermal emissivity characteristics, which might affect the ability of some air-handling systems to remove heat. Some buildings will be designed to support static roof loads. Dry volcanic tephra deposits are heavy compared to snow (800–1,200 kg/m^3, versus 100–300 kg/m^3), and deposit densities can double when wet. Volcanic tephra-fall deposits can persist for weeks to months, and sometimes longer, after an eruption, and fine-grained particles can be resuspended from wind and surface disturbing activities. These resuspended particles could affect filtration and air circulation systems, and facility operations, for an extended period after an eruption. Remobilized tephra-fall deposits might be able to form debris flows, which could have the ability to produce flooding conditions at a site that was located above the level of a probable maximum flood.

Based on these first-order risk insights, there is sufficient information to conclude that tephra-fall hazards have the potential to adversely affect the performance of structures, systems, and components that are important to safety at the proposed Natrium™ site. A detailed hazard analysis appears warranted for tephra falls, and associated local debris flows from fluvially remobilized tephra-fall deposits.

6 ANALYSIS OF MAFIC TEPHRA-FALL HAZARDS

Tephra falls can occur from mafic volcanoes that have explosive eruptions, if eruption conditions create enhanced fragmentation of the magma and sufficient mass-flow rates to generate buoyant tephra plumes (e.g., Walker, 1973). Buoyant tephra plumes from mafic eruptions typically rise to altitudes of 1–10 km above ground level, and form deposits that can extend from tens to potentially hundreds of kilometers from the source volcano (e.g., Pioli et al., 2008; Alfano et al., 2019). Tephra-fall deposits from Quaternary mafic volcanoes, however, are not preserved in the site region. Nevertheless, tephra-fall hazards from future volcanic events in the site region can be evaluated using a four-step process, which will be presented in this section:

- Identify an appropriate model for calculating tephra-fall hazards 100–320 km from source.
- Develop a technical basis for model parameters, using information from existing and analogue volcanoes.
- Calculate probabilistic thickness distributions for tephra-fall at the proposed site location.
- Evaluate the potential for fluvial remobilization of the tephra-fall deposits to create debris-flow hazards.

6.1 Numerical Models for Tephra-fall Hazards

There are a variety of published numerical models that calculate tephra-fall distributions from erupting volcanoes. Some models rely on detailed, time-dependent representations of atmospheric conditions to calculate dispersal of tephra through a three-dimensional grid (e.g., FALL3D, Costa et al., 2006; ash3D, Mastin et al., 2014). These models are useful for calculating real-time plume trajectories and potential deposit locations. Nevertheless, they are computationally intensive and typically are not used for stochastic hazards analyses, which require intensive sampling of model parameters to account for large aleatory and epistemic uncertainties.

Another class of models implements a more simplified mass-conservation approach, which use generalized advective-diffusion-sedimentation relationships to calculate the dispersal of tephra through the atmosphere and subsequent deposition (e.g., Suzuki, 1983; Bonadonna et al., 2005). Because these models typically use semi-empirical representations of the atmosphere, eruption column formation, and particle sedimentation, they are computationally efficient and allow for many stochastic realizations to be performed in a short amount of time. Consequently, these models can represent appropriate ranges of both epistemic and aleatory uncertainty in the hazard calculations. Because there are potentially significant uncertainties on the characteristics of past tephra-fall eruptions in the site region, an advection-diffusion-sedimentation model appears best suited to evaluate these uncertainties in the hazard analysis.

There are several different implementations of the Suzuki (1983) advection-diffusion-sedimentation relationships, which have various modifications for particle sedimentation, representation of the eruption column, and wind-field characteristics (e.g., Scollo et al., 2008a; Bonasia and Scaini, 2015). Typical applications of these models are to calculate tephra-fall hazards across large areas (e.g., Bonadonna et al., 2005), simulate recent eruptions (Scollo et al., 2008b), or invert well-preserved deposits to determine eruption parameters (Connor and Connor, 2006). In contrast, the goal of this VHA is to assess tephra-fall hazards at a single,

specific site located 100–320 from potential vents, by capturing appropriate ranges of epistemic and aleatory uncertainty in the interpreted characteristics of past tephra-fall eruptions in the site region.

Advection-diffusion-sedimentation models have been published in the peer-reviewed literature and used in various tephra-fall hazard assessments for a variety of volcanic systems. Although there have been some comparisons made between the performance of different models (Scollo et al., 2008a; Folch, 2012), these models have not undergone structured verification or validation testing that would meet the quality assurance requirements in Appendix B to 10 CFR Part 50 (cf. Whitney, 2015).

The NRC sponsored development of the ASHPLUME code to allow staff to perform independent evaluations of potential tephra-fall hazards associated with the proposed radioactive waste repository at Yucca Mountain, Nevada. This code implemented the advection-diffusion-sedimentation model of Suzuki (1983), which uses tephra deposit and eruption characteristics to calculate the dispersal of tephra in a simplified wind field (Jarzemba et al., 1997). ASHPLUME was developed under NRC quality assurance requirements, and was accepted for use in confirmatory testing for regulatory reviews (Nuclear Regulatory Commission, 1997). During testing, an error was discovered in the formula used to simulate particle diffusion out of the eruptive column, which resulted in underestimation of eruption volumes. This error was corrected in ASHPLUME Version 1.0, Revision 1 (Nuclear Regulatory Commission, 1997), but is present in the code shown in Jarzemba et al. (1997).

The strengths of the ASHPLUME code are that most of the code parameters are derived from measurable eruption characteristics, such as deposit volume, column heights, and grain-size distributions. Uncertainties in these and other parameters are evaluated through stochastic sampling of distribution functions, which results in a probabilistic distribution of tephra-fall deposit thicknesses for a given location. The ASHPLUME model had been shown to reasonably represent the distribution of tephra-fall deposits (e.g., Jarzemba et al., 1997; Hill et al., 1998). The code is written in FORTRAN 77, which can compile and run on a desktop computer. Simulations involving 1,000 realizations for a single grid point can be run in several minutes, in contrast to more complex codes that require advanced processing capabilities.

There are, however, several limitations to the ASHPLUME code:

- The code represents the wind-field between the source and deposition site with a single vector, which is sampled from an exponential distribution of wind speeds that is correlated to wind direction (Jarzemba et al., 1997). However, wind speed and direction usually vary with increasing altitude. The directionality issue can be addressed by setting the wind direction towards the site for all realizations, but a height-dependent speed would better represent the natural variations in wind speed that occur with increasing altitude.

- The generalized advection-diffusion-sedimentation relationships do not capture the transport of very fine-grained (i.e., <15–30 μm) particles, which do not settle gravitationally from the tephra plume (Jarzemba et al., 1997). Although mafic eruptions typically have low abundances of such very fine-grained particles, some large silicic eruptions can have higher abundances of these particles. Consequently, ASHPLUME might underestimate deposit thicknesses for distal deposits from large silicic eruptions.

- The eruption column is abstracted by Suzuki (1983) as a simple diffusion process, with a parameter that varies the amount of mass removed from the vertical plume. Variations in this parameter can range from a uniform release of mass from the eruption column with height, or strongly weighting the mass release to occur near the top of the plume. Although the latter parameterization approximates the formation of umbrella clouds in larger eruptions (e.g., Constantinescu et al., 2021), the approximation is not exact and is only reasonable in the downwind direction of the plume (i.e., in 2D). Consequently, proximal deposit thicknesses might be overestimated by the ASHPLUME model (e.g., Hill et al., 1998).

- The code calculates deposit volume and eruption column height using empirical relationships for eruption power and duration (i.e., Wilson et al., 1978; Walker et al., 1984). The power and duration parameters are evaluated independently in the ASHPLUME code, which can lead to inaccurately large eruption volumes or column heights unless care is taken in selecting appropriate distributions for power and duration.

In summary, there are a variety of tephra dispersal models available that implement the generalized advection-diffusion-sedimentation relationships from Suzuki (1983). Many of these codes implement different approaches for representing eruption columns, wind advection, and particle settling, and have demonstrated utility in representing well-characterized tephra deposits in 3D and in plume forecasting. Nevertheless, these codes have not been evaluated through structured validation testing, and have not been developed with the need for compliance with the requirements in Appendix B to 10 CFR Part 50. The ASHPLUME code was developed under these NRC requirements, and was accepted by NRC for use in licensing reviews.

The ASHPLUME code represents a basic implementation of the generalized advection-diffusion-sedimentation relationships from Suzuki (1983). Some of the code limitations can be overcome by conducting calculations on a 2D, rather than 3D, grid, and directing the tephra plume towards the proposed site for all realizations. In addition, limitations in the eruption column abstraction affect calculations of proximal deposit thicknesses. The proposed site, however, is located 100–320 km from potential eruption sources, which is sufficiently distant to not be affected by eruption column dynamics. Alternative particle-settling models (e.g., Bonadonna and Phillips, 2003) most strongly affect the sedimentation of coarser-grained particles (i.e., >2 mm diameter) (i.e., Suzuki, 1983). Most of these coarser-grained particles, however, will sediment from the eruption plume by 100–320 km distances (e.g., Cashman and Rust, 2016), Thus, the ASHPLUME code is considered a reasonable approach for calculating potential tephra-fall deposit thicknesses from eruptions in the site region, for volcanic sources 100–320 km from the proposed site.

6.2 Modifications to ASHPLUME Version 1.0

ASHPLUME Version 1.0 (Jarzemba et al., 1997) contained an error in the column diffusion function, which was corrected in Revision 1 of the code (Nuclear Regulatory Commission, 1997). Revision 1 of the code was used to successfully model the tephra-fall deposit from the 1995 eruption of Cerro Negro, Nicaragua, which had a 2.5 km high eruption column (Hill et al., 1998).

Revision 2 of the code (referred to as ASHPLUME2 for clarity) is developed for this VHA, which modifies the approach used to represent wind speed and direction. The tephra-fall analyses in this VHA only need to consider deposits at the proposed Natrium™ site, and not deposits

across a large area. This allows the computational domain to be represented in 2D, rather than 3D. Directing the plume towards the proposed site for all realizations removes the need to account for variations in the wind direction, and ensured that all realizations calculated the maximum deposit thickness at the proposed site. The likelihood of wind being directed from the source volcano to the proposed site can be incorporated in post-processing of the simulation results.

The ASHPLUME2 code modification was achieved by first commenting the subroutine call for *WINDDIRECT*, and set the parameter *udir*=0.0d0 at line 1098. This set the wind direction to blow the plume along the +x-axis of dispersion, towards the site, for all realizations. However, ASHPLUME still implements a single wind-speed distribution for all altitudes.

An altitude-specific wind speed is needed to achieve a more realistic approach for eruption plume dispersal in the ASHPLUME2 code. The mafic and silicic volcanoes in the site region (excluding the Yellowstone caldera) appear capable of producing eruptions that might range from VEI1 to potentially VEI5, which suggests that eruption columns might reach altitudes >25 km above ground level (i.e., Newhall and Self, 1982). Wind speed information for the site region is available from the National Oceanic and Atmospheric Agency as part of the Reanalysis II program (NOAA, 2022). These data are available for 17 different atmospheric pressure levels, which correspond to ground level up to ≈26 km altitudes. To capture the appropriate variability in wind speeds, the atmosphere above the proposed site was divided into 5-km-high levels, for <5.6 km (850 mbar); 5.6–10.4 km (500 mbar); 10.4–15.8 km (250 mbar); 15.8–19.3 km (100 mbar); 19.3–25.9 km (50 mbar); and >25.9 km (10 mbar, the highest altitude in the reanalysis data).

To implement these wind-speed levels in the ASHPLUME2 code, the original subroutine WINDSPEED is commented out in line 1076, and new relationships inserted beginning at line 1078:

```
BEH 7/18/22 Windspeed sub commented, use lambda relationship
c         with rnd from power and hmax (line 1082) NOTE lambda /100 for
c         more accurate sampling, then *100 once sampled.
c         Use hmax to select appropriate wind speeds for ROI, 5km levels
c         Field-specific speeds must be used                  c
c
         if (hmax.le.1.5d0) then
               ulambda=0.3012d0
               u=-dlog(1-rnd3)/ulambda
          u=u*100.d0
c        Cap speed <1370 cm/s as >95%ile.                     c
           if (u.gt.1370d0) then
            u=1370d0
           end if
              end if
              if (hmax.gt.1.5d0.and.hmax.le.5.6d0) then
               ulambda=0.0719d0
               u=-dlog(1-rnd3)/ulambda
          u=u*100.d0
c        Cap speed <4590 cm/s as >95%ile.                   c
           if (u.gt.4590d0) then
            u=4590d0
           end if
              end if
              if (hmax.gt.5.6d0.and.hmax.le.10.4d0) then
               ulambda=0.0412d0
               u=-dlog(1-rnd3)/ulambda
```

```
           u=u*100.d0
c         Cap speed < cm/7940s at 95%ile.                    c
            if (u.gt.7940d0) then
             u=7940d0
            end if
               end if
               if (hmax.gt.10.4d0.and.hmax.le.15.8d0) then
                ulambda=0.0791d0
                u=-dlog(1-rnd3)/ulambda
           u=u*100.d0
c         Cap speed <4160 cm/s as >95%ile.                  c
            if (u.gt.4160d0) then
             u=4160d0
            end if
               end if
c                 REGIONAL VALUES                                 c
               if (hmax.gt.15.8d0.and.hmax.le.19.3d0) then
                ulambda=0.3928d0
                u=-dlog(1-rnd3)/ulambda
           u=u*100.d0
c         Cap speed <1250 cm/s at 95%ile.                 c
            if (u.gt.5100d0) then
             u=1250d0
            end if
               end if
               if (hmax.gt.19.3d0) then
                ulambda=0.0819d0
                u=-dlog(1-rnd3)/ulambda
           u=u*100.d0
c         Cap speed <8,100 cm/s at 95%ile.                  c
            if (u.gt.8100d0) then
            u=8100d0
            end if
          end if
```

The ASHPLUME2 code uses previously calculated column-height *hmax* to determine the representative altitude bin for each realization, then calculates an altitude-specific speed using *ulambda* (inverse of the average wind speed), sampled from an exponential distribution (i.e., Jarzemba et al., 1997). This wind speed is then used for the tephra transport and deposition calculations. Note that the unbounded exponential distribution can produce wind speeds that exceed the maximum wind speed recorded in the jet stream of 443 km/hr (US Department of Commerce, 2022). Consequently, maximum wind speeds for each atmospheric level are capped at the faster of either the maximum speed in the re-analysis data (NOAA, 2022), or the 95th percentile speeds in the distributions of those data. These straightforward code modifications were verified to produce the correct distribution of wind speeds for appropriate column heights.

In each ASHPLUME2 realization, wind speed and direction are sampled based on the altitude of the eruption plume, using 5-km-high atmospheric levels. As shown in Table 38, for example, average wind speeds decrease above 10.4 km in the site region, due to the waning influence of the atmospheric jet stream above approximately 13 km altitudes. When a single wind speed is used, tephra particles from some larger (i.e., VEI≥4) eruptions would only be transported laterally by a lower wind speed, and would not be exposed to lateral transport by falling through potentially higher-speed winds at some lower altitudes (i.e., the jet stream) after sedimentation from the eruption plume.

The potential significance of this effect can be evaluated using the wind speeds in Table 36 for the YVF, and a general particle fall speed of 1 m/s. Using an average wind speed of 21.8 m/s, a tephra particle settling from a plume 10.4 km high would travel 227 km laterally. In contrast, settling through a layered wind field from 10.4 km would result in 156 km of lateral transport. If the plume height increased to 15.8 km, however, a single wind speed of 7.7 m/s would result in 122 km of lateral transport, whereas a layered wind field would result in 198 km of lateral transport. These average relationships suggest that lateral tephra transport (i.e. deposit thickness) might be underestimated for larger explosive eruptions (i.e., VEI4–5, which reach >10.4 km altitudes) by using a single wind speed in the realizations. In contrast, deposit thicknesses might be overestimated for VEI1–3 eruptions that use a single wind speed in each realization, compared to deposition through a layered atmosphere that contained lower wind speeds at lower altitudes. Nevertheless, scaling relationships discussed in Section 8 show that deposit thicknesses calculated for VEI4–5 eruptions are reasonable, and that the potential effects of lower wind speeds >10.4 km do not significantly underestimate the resulting deposit thicknesses.

6.3 Parameterization of ASHPLUME2

The ASHPLUME2 code samples parameter distributions to evaluate epistemic and aleatory uncertainties in the source-terms for tephra-fall hazards. In addition to specifying the *x,y* coordinates for potential volcano locations in relationship to the site, additional parameters for the ASPLUME2 code are:

Tlogmin, Tlogmax	Log of the minimum and maximum eruption duration (s)
Powerlogmin, Powerlogmax	Log of the minimum and maximum eruption power (W)
Betalogmin, Betalogmax	Log of the minimum and maximum column-diffusion parameter β
Dmeanmin	Log of the minimum value for particle mean diameter (cm)
Dmeanmed	Log of the median value for particle mean diameter (cm)
Dmeanmax	Log of the maximum value for particle mean diameter (cm)
Dsigmamin	Log of the minimum value for particle sorting (cm)
Dsigmamax	Log of the maximum value for particle sorting (cm)
AshDensitymin	Minimum particle density (g/cm^3)
AshDensitymax	Maximum particle density (g/cm^3)
Ashrholow	Log of the minimum particle diameter for density calculation (cm)
Ashrhohigh	Log of the maximum particle diameter for density calculation (cm)
Fshape	Particle shape factor (0.1–1)
Airden	air density, 0.001293 g/cm^3 (Suzuki, 1983)
Airvis	Air viscosity, 1.8×10^{-4} g/cm s (Suzuki, 1983)
C	Eddy diffusivity constant, 400 $cm^2/s^{5/2}$ (Suzuki, 1983)
Dmax	Maximum particle diameter transported (cm), typically 10 cm
Hmin	Minimum height of the eruption column (km), typically 0.1 km
Acutoff	Lower limit on ash accumulation calculation (g/cm^2), 1×10^{-10} g/cm^2
Fd parameters	Unused parameter for diameters of dense particulate contaminant
Rhocut	Unused parameter for incorporation ratio for contaminants
Uran	Unused parameter for mass of contaminants incorporated (g)

Tdur (duration) and *Power* are calculated through an iterative process, that begins by first determining the appropriate range of tephra mass (kg) for the eruptions (e.g., Table 12). Once tephra mass is determined, a range of eruption durations are estimated based on the general characteristics of analogous volcanoes. Equation 1 from Walker et al. (1984) is then used to

calculate column height *H*, using the assumed eruption durations and masses to calculate mass flow *M*:

Equation 1 $$H = 0.24M^{\frac{1}{4}}$$

The calculated column heights (*H*) are then compared to the representative column heights for the VEI of the interpreted eruptions, and eruption duration is adjusted until appropriate column heights are obtained. Once the range of column heights is acceptable, eruption power *Q* is calculated using equation 2 from Wilson et al. (1978):

Equation 2 $$H = 8.2Q^{\frac{1}{4}}$$

Where *H* is column height (meters) and *Q* is *Power* (Watts).

An independent check on the deposit volume resulting from specific *Power* and *Duration* values can be conducted using equation 3 from Wilson et al. (1978):

Equation 3 $$Q = \rho u \pi r^2 s(\theta_i - \theta_f)F$$

Where:

Q is eruption *Power* (Watts)
ρ is the bulk density of the erupting tephra column (g/cm^3), which is approximately 50% of the magma density for a fragmented basaltic eruption, and 30% for a highly fragmented silicic eruption (Wilson, 1976; Woods, 1988)
πr^2 is the area of the assumed circular conduit (m^2)
s is the specific heat of the erupting magma (J/kg ºK), 1484 J/kg ºK for basalt and 1604 J/kg ºK for rhyolite with 2 wt% H_2O (Lesher and Spera, 2015)
θ_i is the initial temperature of the magma (ºK)
θ_f is the final temperature of the magma (ºK), typically 270 ºK (Wilson et al., 1978)
F is the efficiency factor of heat usage, typically given as 0.7 (Wilson et al., 1978)

If eruption *Power* (Q) is known (or sampled), the mass eruption rate (m^3/s) can be calculated from Equation 3. The bulk volume of the simulated eruption then can be calculated by multiplying the mass eruption rate derived from Equation 3 with the sampled *Duration* of the eruption. This calculated volume can be compared with the representative deposit volumes that initially were used to derive the *Power* and *Duration*, and confirm that the range of eruption volumes calculated by ASHPLUME2 is appropriate for the eruptions being evaluated. The approach for calculating these parameters from volcano characteristics in the site region is discussed in Section 6.3.2.

Beta is the dimensionless number that reflects the mass release fraction in the ascending eruption column. Low values favor release more linearly through the column, whereas high values favor mass release at the top of the plume. A *Beta* range of 0.1 to 10 reasonably represents a range of VEI 1–3 eruptions (i.e., Suzuki, 1983), and larger values can be used to simulate the 2D development of umbrella clouds for VEI4–5 eruptions.

Particle diameters are calculated based on variations in mean diameter (*Dmean*) and degree sorting (i.e., variance; *Dsigma*) in the total grain-size distribution for the tephra-fall deposit.

Derivation of these parameters for mafic volcanoes in the site region is discussed in Section 6.3.3

Particle densities are calculated based on the range of particle densities (*AshDensity*) within a given particle-size range (*Ashrho*). Densities of mafic tephra particles can range from nearly magmatic densities for poorly vesiculated ash (i.e., 2.5 g/cm^3), to densities of 1 g/cm^3 for highly vesiculated ash and lapilli (i.e., 60% vesicularity).

Fshape is a particle shape factor to depict the eccentricity of the particle shape, which typically ranges from 1 (symmetrical) to 0.1 (platy) for volcanic ash (Wilson and Huang, 1979). A value of 0.5 is commonly used for tephra particles.

The parameters for *Fd*, *Rhocut*, and *Uran* were implemented by Jarzemba et al. (1997) to calculate the dispersion of tephra that was contaminated with dense radioactive waste. These parameters not used in the ASPLUME2 calculations in this VHA.

6.3.1 Mafic Eruption Volumes

Tephra volumes are the most significant parameter in any tephra-fall hazard model. However, mafic tephra-fall deposits are not preserved in the site region, except for isolated remnants in the immediate vicinity of several young scoria cones. Nevertheless, the morphologies of the preserved eruptive vents can be used to infer the characteristics of past eruptions, and estimate likely tephra volumes for past explosive mafic eruptions in the site region.

Many of the basaltic volcanoes in the site region formed through fissure-type eruptions, which created near-vent accumulations of pyroclastic spatter and scoria. In addition, the small shield volcanoes in the region typically are capped by low-lying (i.e., tens of meters) mounds of spatter and scoria. These near-vent deposits have been observed at many historical eruptions of basaltic magma, and are formed predominantly by the ballistic ejection of coarsely fragmented magma in fire fountains and jets (Walker, 1973; Cas and Wright, 1987, Ch. 13). The fire fountains can sometimes reach altitudes of hundreds of meters above the vent, where fine-grained tephra can be blown from the fountain by prevailing winds. Tephra-fall deposits from such fire-fountain eruptions are restricted to within approximately 10 km of the vent (e.g., Klawonn et al., 2014; Mueller et al., 2018), because the dense tephra particles settle gravitationally and there is no buoyant tephra plume to support lateral advection (i.e., Parfitt and Wilson, 1995). These types of eruptions are considered to be low explosivity, and would have a VEI≤1 (Newhall and Self, 1982). The proposed site is located >100 km from the nearest potential fissure or shield volcano. Consequently, tephra falls from a future shield or fissure volcano VEI≤1 eruption would not be deposited at the proposed site, and such eruptions can be screened-out from the mafic tephra-fall hazards assessment.

A relatively small number of mafic eruptions in the site region formed from phreatomagmatic interactions between shallow surface water and ascending magma. Although phreatomagmatic eruptions can produce deposits of highly fragmented magma and wall rock, tephra-falls from such eruptions are restricted to within tens of kilometers from the vent (e.g., Self et al., 1980; Cas and Wright, 1987). The nearest location of a Quaternary phreatomagmatic eruption is ≈150 km from the proposed site, in the Blackfoot Reservoir volcanic field. Consequently, tephra falls from a future phreatomagmatic eruption would not be deposited at the proposed site, and such eruptions can be screened-out from the mafic tephra-fall hazards assessment.

Most of the basaltic eruptions in the site region formed relatively low-lying cones of oxidized and agglutinated pyroclasts. Many of these cones formed during the simultaneous effusion of lava flows, and are incompletely formed (i.e., “horseshoe shaped”) due to continuous removal of near-vent pyroclasts accumulations by the lava. During these types of Strombolian mafic eruptions, large gas bubbles expanded and incompletely fragmented the erupting magma (Vergniolle and Jaupart, 1986). Mass-flow rates were sufficiently high to support predominantly ballistic ejection of pyroclasts, which accumulated around the vent to form low, often steep-sided, cones (Wood, 1980). Only small amounts of finely fragmented magma were formed during these processes, which were insufficient to form significant eruption columns or buoyant tephra plumes (Parfitt and Wilson, 1995). Tephra falls from these types of VEI≈1 Strombolian eruptions are deposited within tens of kilometers of the vent (e.g., Walker, 1973). The proposed site is located >100 km from the nearest Strombolian scoria-cone volcano. Consequently, tephra falls from future VEI≈1 Strombolian eruptions would not be deposited at the proposed site, and such eruptions can be screened-out from the mafic tephra-fall hazards assessment.

In contrast, some Quaternary scoria cones in the site region are constructed of relatively non-agglutinated pyroclasts, which form relatively steep-sided cones on the order of 50–100 m high. The smaller size of the pyroclasts and lack of agglutination indicates that the erupting magma was relatively fragmented, and that pyroclasts were relatively cool when deposited. These features suggest that these cone-forming eruptions were sufficiently energetic to form kilometers-high eruption columns and buoyant tephra plumes (McGetchin et al., 1974; Wood, 1980). Although there are no definitive criteria to apply, some of these scoria-cone eruptions might have been sufficiently explosive and dispersive to be considered “Violent Strombolian” (Pioli et al., 2008), with the potential to disperse tephra hundreds of kilometers from the vent. Consequently, these scoria cones might have been formed from VEI2–3 eruptions, with the potential to have eruption columns to ≈15 km high and tephra dispersal hundreds of kilometers from the vent (i.e., Newhall and Self, 1982). These types of mafic eruptions warrant evaluation in the mafic tephra-fall hazards analysis, because a new vent forming within 100 km to possibly 320 km from the site might have the potential to deposit tephra at the site.

Relationships between scoria-cone, lava-flow, and tephra-fall volumes have been developed for basaltic volcanoes that produced distributed tephra-falls primarily from large, Violent Strombolian eruptions (Alfano et al., 2019). For the characterized volcanoes, scoria-cone volumes represent 10%–300% of the lava-flow volumes, when corrected for dense rock equivalent (DRE). Scoria cone volumes also represent 10%–400% of the tephra-fall volumes, but scoria cones <0.05 km^3 often represent >100% of the tephra-fall volume (i.e., Alfano et al., 2019). These volumetric relationships can be used to develop estimates of tephra-fall volumes for the Quaternary basaltic volcanoes in the site region.

6.3.1.1 Tephra Volumes for the Leucite Hills Volcanic Field

Lange et al. (2000) calculated the volumes of scoria cones and lava flows for the preserved volcanoes in the LHVF, which are given in Table 11. Note that the cone volumes are corrected for 40% vesicularity, and lavas for 15% vesicularity in the DRE conversion (Lange et al., 2000). In addition, Lange et al. (2000) accounted for 20% erosion of lava flows <1 Ma, and 50% erosion for lava flows >1 Ma.

Table 11. Cone and lava volumes for the LHVF, from Lange et al. (2000).

Vent	DRE Cones (km^3)	# of Cones Represented	DRE Lava (km^3)	Cone/Lava	Estimated Tephra Fall (DRE m^3)
Spring Butte	2.0E-03	2	5.1E-02	4%	9.9E+05
Deer Butte	1.7E-03	1	2.6E-02	7%	8.4E+05
Zirkel Mesa	2.2E-02	5	3.4E-01	6%	1.1E+07
Steamboat Mtn.	2.6E-03	2	8.7E-02	3%	1.3E+06
Middle Table			1.4E-03		
Boar's Tusk			4.0E-03		
North Table			6.9E-03		
South Table			1.9E-03		
Hatcher Mesa			2.3E-03		
Pilot Butte			2.7E-03		
Emmons Mesa	1.7E-03	1	3.0E-02	6%	8.4E+05
Black Rock			1.6E-03		
Cabin Butte			2.6E-03		
Badgers Teeth			1.3E-04		
Matthews Hill			1.3E-04		
Pilot Buttes			3.8E-04		

The calculated scoria cone volumes represent <10% of the lava flow volumes, which is at the lowest end of the range determined by Alfano et al. (2019) for energetic Strombolian eruptions. Assuming that the Zirkel Mesa eruption represents the potential for the largest-volume future eruption, the relationships in Alfano et al. (2019) indicate that scoria cones likely represented 200% of the cogenetic tephra-fall volume, or $8.4x10^5$ m^3 to $1.1x10^7$ m^3 (DRE) of tephra.

6.3.1.2 Upper Wind River Basin

There is only 1 scoria cone exposed in the UWRB volcanic field, at Lava Mountain. Examination of topographic maps and satellite imagery within a Geographic Information System (GIS) shows that this eroded cone has a basal diameter of ≈500 m, crater diameter of ≈200 m, and a height of ≈100 m. Representing the cone as a frustum morphology, the cone volume is $5.1x10^8$ m^3. After accounting for 30% erosion and 40% vesicularity (i.e., Lange et al., 2000), the cone DRE volume is $4.0x10^8$ m^3. Downey (2015) reports a total volume for Lava Mountain of $5.46x10^9$ m^3. Thus, the Lava Mountain cone likely represents 8% of the lava volume. As observed for the LHVF, the relationships in Alfano et al. (2019) indicate that the Lava Mountain cone likely represented 200% of the cogenetic tephra-fall volume.

Lava Mountain, however, is constructed from at least 26 lava-flow eruptions. Consequently, the number of events that constructed the scoria cone may range from 1–26, with each event potentially producing a tephra-fall eruption. This uncertainty can be evaluated in the tephra-fall VHA by considering tephra-fall volumes that range from $7.7x10^6$ m^3 (i.e., 26 individual events) to $2.0x10^8$ m^3 (i.e., 1 large event).

6.3.1.3 Mafic Tephra Volumes for the Blackfoot Reservoir Volcanic Field

Of the 85 identified basaltic volcanoes in the BRVF, 14 of these volcanoes are scoria cones with sufficient diameters (i.e., >300 m) and heights (50–100 m) to suggest the occurrence of an explosive eruption that produced buoyant plumes and associated tephra falls. The volumes of these cones were calculated using dimensions determined by examination of topographic maps and satellite imagery within a GIS, and a frustum morphology to the cones. After correcting for 40% vesicularity (i.e., Lange et al., 2000), the DRE cone volumes ranged from $8x10^5$ m^3 to $1.2x10^8$ m^3 (i.e., Red Mountain), with most of the cone volumes 10^6–10^7 m^3. Lava flows are not sufficiently mapped to permit correlation with respective scoria cones. Using the general relationships from Alfano et al. (2019), scoria cones volumes in the BRVF likely represented 200% of the tephra-fall volumes. Thus, the BRVF scoria-cone eruptions likely produced $4x10^5$ m^3 to $6x10^7$ m^3 (DRE) of cogenetic tephra falls.

6.3.1.4 Mafic Tephra Volumes for the Eastern Snake River Plain Volcanic Field

Most of the 431 Quaternary mafic volcanoes in the ESRP volcanic field are fissure vents, spatter cones, or shield volcanoes. Scoria cones that indicate an eruption might have formed buoyant tephra plumes occur in several specific locations: Craters of the Moon, Atomic City, and Spence High-Point (Kuntz et al., 1992; Hughes et al., 2002). Visual examination of topographic maps and satellite imagery in a GIS confirmed that similar morphology scoria cones do not occur in other areas of the ESRP within the site region. Scoria cone volumes were calculated using the same frustum morphology and correcting for 40% vesiculation (i.e., Lange et al., 2000) as for other scoria cones in the site region. Volumes of these 14 scoria cones ranged from $6x10^7$ m^3 to $2x10^8$ m^3 (DRE). Due to burial by younger deposits, area and volume estimates were not available for the lava flows associated with the 14 scoria cones in the Craters of the Moon, Atomic City, and Spence High-Point areas. Using the same general relationships from Alfano et al. (2019), these 14 scoria cones likely represented 200% of the tephra-fall volume from their respective eruptions. Thus, the ESRP scoria-cone eruptions likely produced $3x10^7$ m^3 to $1x10^8$ m^3 (DRE) of cogenetic tephra falls.

6.3.1.5 Mafic Tephra Volumes for Other Volcanic Fields

As previously discussed, mafic scoria cones are not present in the Yellowstone (Section 2.1), Black Rock Desert (Section 2.4), and Curlew Valley (Section 2.5) volcanic fields. Mafic eruptions in these volcanic fields formed fissure vents and small shield volcanoes, which resulted from low explosivity eruptions (i.e., VEI≤1) that did not produce buoyant and dispersed tephra plumes (cf. Section 6.3.1). Consequently, tephra-fall hazards from these volcanic fields are not considered in the detailed VHA.

6.3.1.6 Summary of Mafic Tephra Volumes

Only 6% of the 516 Quaternary mafic volcanoes in the site region have scoria-cone characteristics that suggest potential formation from explosive and dispersive eruptions. The remainder of the mafic volcanoes produced low explosivity eruptions that have tephra-fall deposits restricted to <100 km from the vent, and generally less than 10's of kilometers from the vent. Because these distances are less than the 117 km distance between potential eruption sources and the proposed site, tephra-fall hazards from non-explosive mafic eruptions are not considered in the VHA.

The calculated ranges of scoria cone and interpreted tephra-fall volumes for potentially explosive Quaternary eruptions in the site region are summarized in Table 12. The bulk volumes (i.e., in-situ deposit) and fall-deposit mass are calculated assuming a mafic magma density of 2,500 kg/m^3 (i.e., McBirney and Murase, 1984) and a deposit density of 1,200 kg/m^3 (e.g., Osman et al., 2022). Tephra-fall bulk volumes for VEI ranges in Newhall and Self (1983) are VEI1 (1x10^6 m^3), VEI2 (1x10^7 m^3), VEI3 (1x10^8 m^3), and VEI4 (1x10^9 m^3). Note that VEI is provided as a reference only, and is not used directly in the ASHPLUME2 model.

Table 12. Summary of tephra volumes for mafic eruptions in the site region.

Volcanic Field	*Cone Vol. DRE (m^3)*	*Fall Vol. DRE (m^3)*	*Fall Vol. Bulk (m^3)*	*Fall Mass (kg)*	*Estimated VEI*
UWRB - Upper	4.0E+08	2.0E+08	4.2E+08	5.0E+11	3.4
UWRB - Lower	1.5E+07	7.7E+06	1.6E+07	1.9E+10	2.1
LH - Upper	2.2E+07	1.1E+07	2.3E+07	2.8E+10	2.2
LH - Lower	1.7E+06	8.5E+05	1.8E+06	2.1E+09	1.1
BRVF - Upper	1.2E+08	6.0E+07	1.3E+08	1.5E+11	3.1
BRVF - Lower	8.0E+05	4.0E+05	8.3E+05	1.0E+09	<1
ESRP - Upper	2.0E+08	1.0E+08	2.1E+08	2.5E+11	3.2
ESRP - Lower	6.0E+07	3.0E+07	6.3E+07	7.5E+10	2.6

6.3.2 Power and Duration of Mafic Eruptions

Using the range of potential eruption volumes for each volcanic field (Table 12), representative column heights from Newhall and Self (1983) were derived for the estimated VEIs for these volumes. Using guidance from analogue basaltic eruptions, various eruption *Durations* were evaluated using Equation 1 until the calculated column height reasonably encompassed the range of column heights that were characteristic of the eruption VEI.

Table 13. Calculated column height, duration, power and eruption rate for the range of mafic eruptions interpreted for volcanic fields in the site region. The range of *VEI Col. Height* is interpreted from Newhall and Self (1983), for the characteristic tephra-fall deposit volumes for these eruptions.

Volcanic Field	*Fall Vol. Bulk (m^3)*	*VEI*	*Duration (s)*	*Calc. Col. Height (km)*	*VEI Col. Height (km)*	*Power (W)*	*Eruption Rate (kg/s)*
UWRB - Upper	4.2E+08	3.4	1.0E+05	13.0	3–15	6.0E+12	5.0E+06
UWRB - Lower	1.6E+07	2.1	5.0E+04	6.7	1–5	4.5E+11	3.8E+05
LH - Upper	2.3E+07	2.2	1.0E+05	6.2	1–5	3.4E+11	2.8E+05
LH - Lower	1.8E+06	1.1	5.0E+04	3.8	≤1	5.1E+10	4.3E+04
BRVF - Upper	1.3E+08	3.1	1.0E+05	9.5	3–15	1.5E+12	1.5E+06
BRVF - Lower	8.3E+05	<1	5.0E+04	3.1	≤1	2.4E+10	2.0E+04
ESRP - Upper	2.1E+08	3.2	1.0E+05	10.9	3–15	3.0E+12	2.5E+06
ESRP - Lower	6.3E+07	2.6	9.0E+04	8.2	1–10	1.0E+12	8.3E+05

6.3.3 Total Grain-Size Distributions for Mafic Tephra Deposits

The ASHPLUME2 code requires estimates for the total grain-size distribution of the tephra fall deposits. There are only a few studies that have measured these distributions in well-preserved mafic tephra-fall deposits. A compilation by Costa et al. (2016) included 5 mafic tephra-fall

deposits that had measured median diameter and sorting characteristics (Table 14). In addition, Costa et al. (2016) developed semi-empirical relationships to calculate the total grain-size distribution of a tephra-fall deposit using the estimated eruption column height and magma viscosity. This approach was applied to an average composition of ESRP olivine tholeiite from Leeman (1982) and for basalt from Inferno Cone at Craters of the Moon from Kuntz et al. (1985) (Table 14).

Table 14. Median diameter and sorting characteristics for mafic tephra-fall deposits, after Costa et al. (2016). Total deposit parameters also shown for Sunset Crater, AZ (Alfano et al., 2019) and Cerro Negro (Hill et al., 1998). "*Calculated*" uses column height-magma viscosity relationships (Costa et al., 2016) to calculate grain-size characteristics for ESRP olivine tholeiite (Leeman, 1982) and Inferno Cone at Craters of the Moon (Kuntz et al., 1985) compositions.

Mafic	*Median diameter Log cm*	*Sorting Log cm*	Col Height (km)	Viscosity (log Pa s)
Etna 2007	-0.8	1.2		
Etna 2011	-0.4	1.4		
Fuego 1974	-1.1	1.3		
Vesuvio 1906	-0.3	1.4		
St Vincent 1979	-1.8	1.3		
Sunset Crater	-0.9	1.3		
Cerro Negro 1995	-1.2	0.3		
Calculated				
ESRP	0.3	1.0	5	1.4
Inferno Cone	0.2	1.4	10	2
ASHPLUME2 Parameters				
Dmeanmin	-1.8			
Dmeanmed	-1			
Dmeanmax	0.3			
DSigmamin		0.5		
DSigmamax		1.5		

These data are used to estimate the range of median diameters and sorting for the mafic eruption calculations in ASHPLUME2. As shown in Costa et al. (2016), small variations in magma viscosity (i.e., basalt to andesite) and eruption column height (i.e., 5–10 km) would have only a minor (<10%) effect on the calculated median diameter and sorting for a deposit. In contrast, the range encompassed for the median diameter (*Dmean*) and sorting (*DSigma*) parameters significantly exceeds the variations resulting from relatively small changes in magma viscosity and column height among the characteristic mafic eruptions in the site region.

6.3.4 Wind Speed Data for Mafic Tephra Hazards Analyses

The ASHPLUME2 model is configured to direct the eruption plume towards the proposed site for all realizations. However, the potential eruption sources can vary spatially within each volcanic field, so that winds originating only from specific sectors have the potential to direct an actual tephra plume towards the proposed site. Consequently, the VHA for tephra falls needs to quantify the orientation of the sector that includes the proposed site and potential sources of

tephra plumes from each volcanic field. Average wind speeds are then calculated within these sectors for each of the 5-km-high altitude bins implemented in the ASHPLUME2 model.

The distribution of Quaternary volcanoes guided the selection of wind sectors, which included consideration for uncertainty in the potential locations of new vents around the periphery of each volcanic field. These sectors are shown in Figure 21 and encompass azimuths of 68º–113º for LHVF, 0º–45º for the UWRB, 315º–340º for the BRVF, and 292º–340º for the ESRP. Note that the sector for the UWRB is anomalously broad (i.e., extends east of potential vent locations). Winds are rarely directed from the NE sector in this region. Consequently, a broad sector was required in order to develop a statistically meaningful sample of wind speeds and directions for modeling potential events from the UWRB. A wide sector is conservative, as it will not underestimate the amount of time that a potential tephra plume could be directed towards the proposed site from the UWRB.

Average daily observations for the proposed Natrium™ site location (41.7048 N, -110.5616 W) of u-wind (i.e., E–W component) and v-wind (i.e., N–S component) speeds for the date range 1/1/1979 to 1/1/2022 (15,709 days of data) were downloaded from NOAA (2022), for the 10 mbar (25.9 km), 50 mbar (19.3 km), 100 mbar (15.8 km), 250 mbar (10.4 km), 500 mbar (5.6 km), and 850 mbar (1.5 km) pressure levels. These pressure levels correspond to the ≈5-km-high altitude intervals used in the ASHPLUME2 code (Section 6.2). The u-wind and v-wind data were then converted into azimuth and speed, to obtain 15,709 daily averages for each pressure level. The distribution of wind speeds for each pressure level is shown in Figure 22. Note that the speeds form strongly log-normal distributions at low pressure levels, which decrease to moderately log-normal distributions for pressure levels >100 mbar.

To determine the average wind speed for each of the four volcanic fields being evaluated for tephra-fall hazards, the 15,709 daily averages were sub-sampled to include only those wind directions that had azimuths within the appropriate sector for each volcanic field. The average wind speed and standard deviation were calculated for each log-normal distribution, to derive the appropriate average wind speeds for each sector and pressure level. A summary of these data are compiled in Table 15. The greater of either the maximum measured wind speed or the 95th percentile wind speed (i.e., +2σ) also is used to bound the exponential wind-speed distribution used in ASHPLUME2 (Section 6.2).

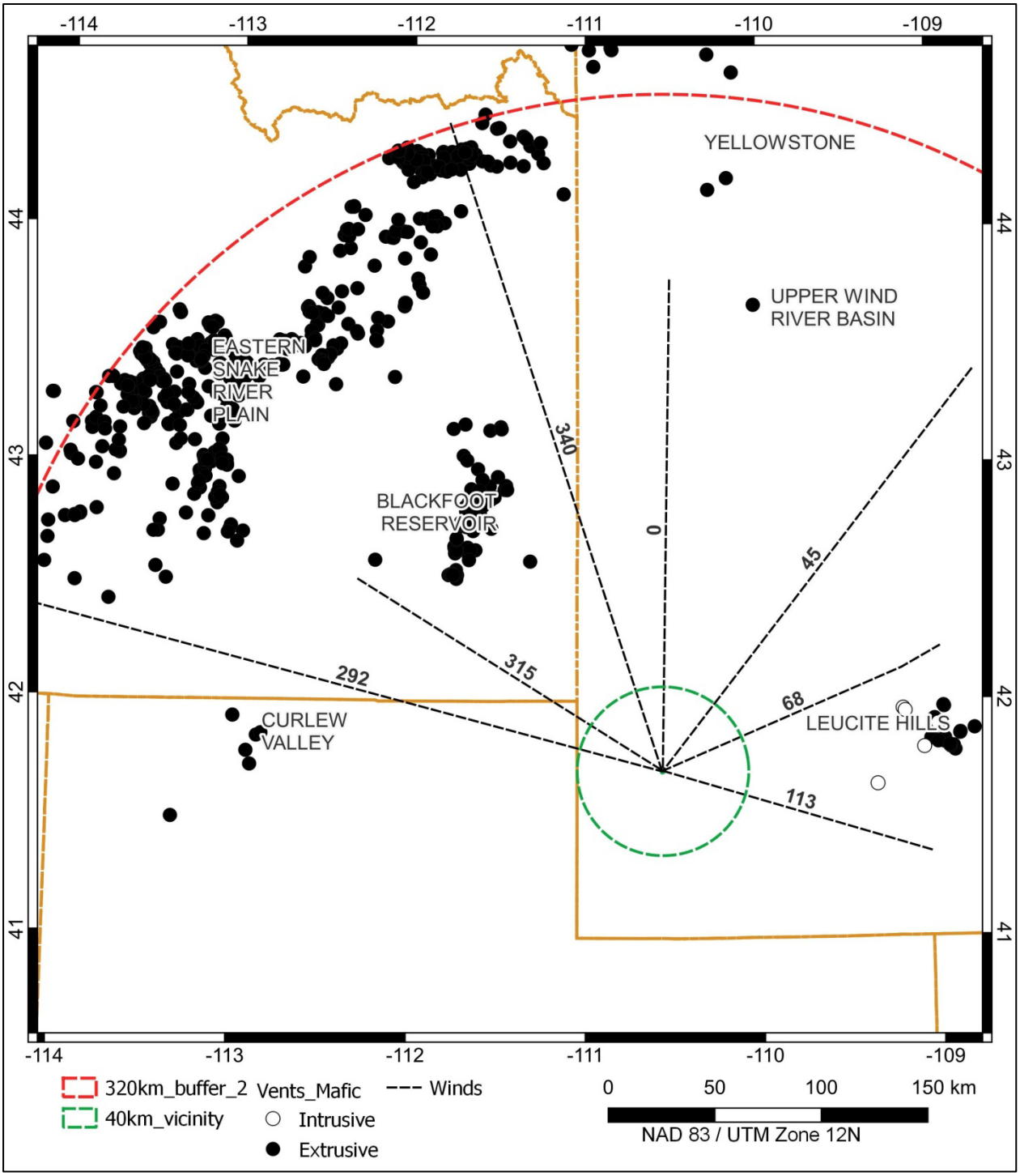

Figure 21. Wind sectors that encompass potential source volcanoes and the proposed site. NOAA Reanalysis II data provide daily average wind speeds and directions for locations in the continental United States, for altitudes to ≈26 km above ground level.

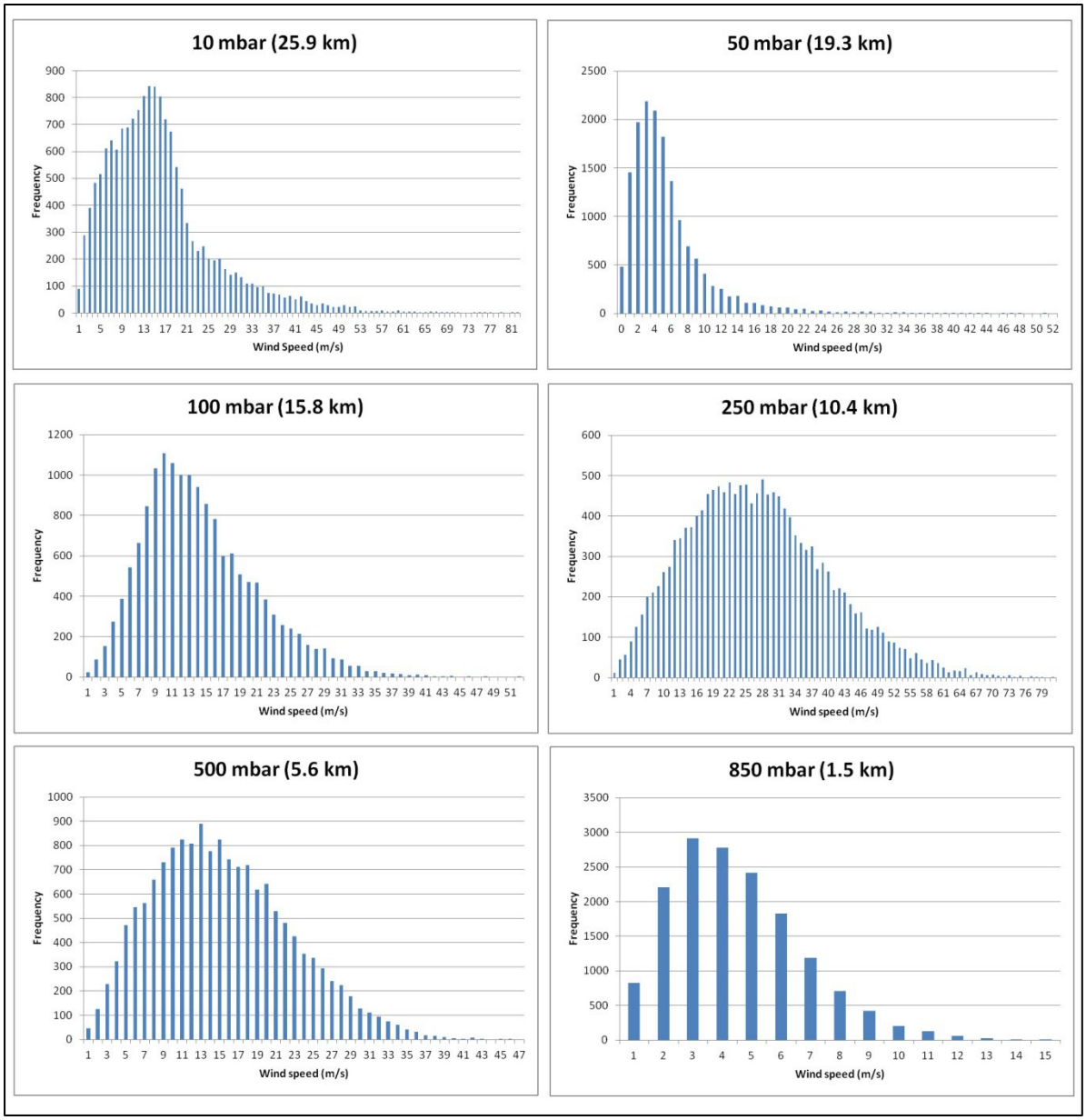

Figure 22. Distributions of wind speeds for selected pressure levels above the proposed Natrium™ site.

Table 15. Wind speed statistics for atmospheric pressure levels and volcanic fields that are used in the ASHPLUME2 analysis of mafic tephra-fall hazards. *H* is altitude for corresponding pressure level, *Avg Speed* is the average of the log-normal distribution, *Std Dev* is the standard deviation of the log-normal distribution, $+2\sigma$ is the calculated 95th percentile wind speed based on the standard deviation, *Max Spd* is the maximum speed observed in the data, *Sector%* is the percentage of time the wind is directed from this sector to the proposed Natrium™ site, and *Lambda* is the inverse of the average wind speed.

Level (mbar)	*H (km)*	*Avg Speed (m/s)*	*Std Dev (m/s)*	*+2σ (m/s)*	*Max Spd (m/s)*	*Sector %*	*Lambda (cm/s)*
LHVF: 68º–113º sector							
850	1.5	2.0	2.0	7.8	8.9	4.4	0.005087
500	5.6	5.4	2.1	23.2	18.3	0.9	0.001859
250	10.4	8.7	2.1	37.8	27.3	1.0	0.001153
100	15.8	2.5	2.2	12.5	9.7	0.2	0.003928
UWRB: 0º–45º sector							
850	1.5	2.0	2.1	8.6	11.0	3.7	0.004925
500	5.6	9.1	2.0	38.1	32.6	3.1	0.001102
250	10.4	17.5	2.1	73.6	66.3	3.8	0.000572
100	15.8	5.6	2.2	26.3	28.3	0.7	0.001776
BRVF: 315º–340º sector							
850	1.5	2.8	2.0	11.4	12.3	7.6	0.003560
500	5.6	13.4	1.9	47.5	45.9	13.7	0.000744
250	10.4	23.7	1.9	84.3	76.7	14.6	0.000422
100	15.8	10.7	1.8	35.0	40.4	7.0	0.000937
ESRP: 292º–340º sector							
850	1.5	3.3	2.3	13.0	13.7	12.9	0.003012
500	5.6	13.9	1.8	45.7	45.9	23.9	0.000719
250	10.4	24.3	1.8	79.7	76.7	22.7	0.000412
100	15.8	12.6	1.7	37.3	41.6	20.5	0.000791

6.3.5 Summary of Input Parameters for Mafic Tephra Hazards Analyses

Parameters are input into the ASHPLUME2 code through the ASHPLUM.IN file. The *xmin* and *xmax* distances (Table 16) represent the closest and farthest potential vent locations, relative to the proposed Natrium™ site, for each volcanic field. The ASHPLUME2 code is limited to 1,000 realizations for each spatial grid-point in a simulation (Jarzemba et al., 1997). Consequently, the x-axis length of each volcanic field was divided into 1–5-km-long segments (*nptsx*, Table 16), and 1,000 realizations were performed on the nodes of each segment. For example, the 34-km-long LHVF is divided into 2-km-long segments, and 1,000 realizations were calculated for presumed vent locations occurring every 2 km. As a result, 18,000 realizations can be performed to calculate potential tephra-fall hazards from the LHVF, which includes spatial variability in vent location.

Table 16. Input parameters for ASHPLUME2 analysis of mafic tephra-fall hazards.

Parameter	**UWRB**	**LHVF**	**BRVF**	**ESRP**
x min (km) distance	220	116	117	250
x max (km) distance	230	150	193	320
y min (km) distance	0	0	0	0

Parameter	UWRB	LHVF	BRVF	ESRP
y max (km) distance	0	0	0	0
nptsx = # of points x	11	18	16	18
nptsy = # of points y	1	1	1	1
t log min (s)	4.70	4.70	4.70	4.95
t log max (s)	5.00	5.00	5.00	5.00
Pow log min (W)	11.65	10.71	10.38	12.00
Pow log max (W)	12.78	11.53	12.18	12.48
Beta log min	-1			
Beta log max	1			
D meanmin (log cm)	-1.8			
D meanmed (log cm)	-1			
D meanmax (log cm)	-0.3			
D sigma min	0.5			
D sigma max	1.5			
AshDensity min (g/cm3)	1			
AshDensity max (g/cm3)	2.5			
Ash rho low	-2			
Ash rho high	-1			
fshape	0.5			
Airdens, visc	0.001293d0 1.8d-04			
C cm2/s5/2	400			
D max (cm)	10			
Hmin (km)	0.01			
a cutoff (g/cm2)	1d-10d0			
rho cut	1			
Uran (g) mass fuel	0			

6.4 Mafic Tephra-Fall Hazards at the Proposed Natrium™ Site

Mafic tephra-fall hazards are calculated using the ASHPLUME2 code and input parameters described in Section 6.3, for each of the four volcanic fields that have the potential to produce tephra fall from VEI1–3 mafic eruptions. The ensuing sections present the conditional tephra-fall hazards for each of these fields, then develop a probabilistic framework to determine the likelihoods i) of a future mafic eruption; ii) that the eruption will form tephra-fall deposits; and iii) that regional winds are directed from the eruption source to the propose site. These analyses develop fully probabilistic tephra-fall hazard curves for each of the four volcanic fields, which are then integrated into a total mafic tephra-fall hazard assessment for the proposed site.

6.4.1 Tephra-fall Hazards from the Leucite Hills Volcanic Field

Potential vents for the LHVF are located 116–150 km from the proposed Natrium™ site. To account for spatial variability in vent locations, 1,000 ASHPLUME2 realizations were conducted every 2 km along a 34-km-long axis, for a total of 18,000 realizations.

Results of the ASHPLUME hazard calculations are presented in Table 17 and Figure 23. The calculated range of deposit volumes ($1.8x10^6$–$2.3x10^7$ m^3) corresponds to the interpreted range of deposit volumes for the LHVF (Table 12; $1.8x10^6$–$2.3x10^7$ m^3), and the calculated range of eruption column heights (3.9–6.3 km) compares reasonably with the interpreted range of column heights (Table 13; 3.8–6.2 km) for the LHVF. The calculated tephra-fall deposit thicknesses form a log-normal distribution, which is reflected in the summary statistics (Table 17). As discussed in Section 1.1, average and 95th percentile deposit thicknesses are calculated for use in the evaluation of potential event sequences (e.g., Nuclear Regulatory Commission, 2020).

Table 17. Summary of ASHPLUME2 calculations for LHVF mafic tephra hazards.

	Power (W)	*Duration (s)*	*Deposit Volume (m^3)*	*Col H (km)*	*Wind (km/hr)*	*Deposit Thick (cm)*
Avg	1.5E+11	7.4E+04	7.6E+06	5.0	25.5	1.2E-03
Min	5.1E+10	5.0E+04	1.8E+06	3.9	0.01	1.2E-09
Max	3.4E+11	1.0E+05	2.3E+07	6.3	136	0.61
95th percentile thickness: 0.06 cm						

As would be expected, the thickest calculated deposits at the proposed site result from the largest eruption volumes (Figure 23A), the highest eruption columns (Figure 23B), and the fastest wind speeds (Figure 23C). The conditional tephra-fall hazard curve is shown in Figure 23D, which yields a 95th percentile deposit thickness of 0.06 cm. Note that this amount of tephra-fall assumes that i) a mafic eruption occurs in the LHVF, ii) the eruption produces a buoyant tephra plume, and iii) the prevailing wind is directed from the LHVF vent towards the proposed Natrium™ site.

To calculate a fully probabilistic tephra-fall hazard curve for potential LHVF eruption sources, the following three probabilities must be determined:

1) *Probability of a future mafic eruption in the LHVF:*

Since 3.0 Ma, there have been (14+7) 21 mafic events in the LHVF(Section 2.3), assuming that each identified subvolcanic intrusion represents a single eruptive event (i.e., Lange et al., 2000). A simple recurrence rate is thus 21 events ÷ $3x10^6$ yr = $7.0x10^{-6}$/yr. If only Quaternary volcanic vents are considered, the recurrence rate increases slightly to 14 events ÷ $2.53x10^6$ yr = $5.5x10^{-6}$/yr.

The probability of a future eruption in the LHVF can be calculated using a homogeneous Poisson probability model. The Poisson process assumes that events occur randomly and independently in time, and involve the fewest number of assumptions about the processes controlling eruption recurrence (e.g., Bebbington, 2013; Connor et al., 2015). In simplest form, the probability of a future eruption is expressed as:

Equation 4

$$\Pr[N(t) = 1] = e^{-\lambda_T u}$$

where
$N(t)$ = Number of events in the time interval u
λ_T = Event recurrence rate, constant through time u
u = Time interval

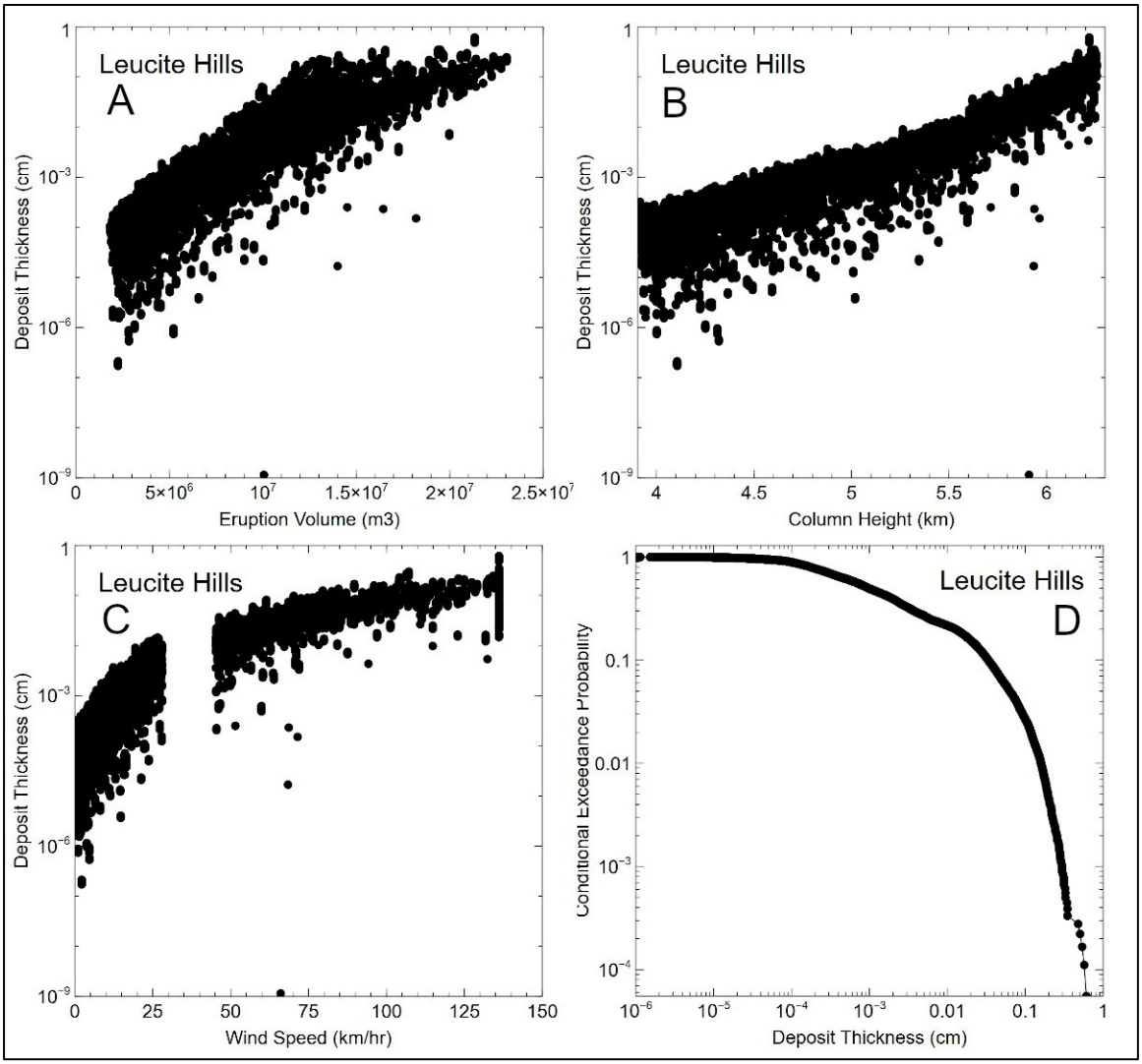

Figure 23. Results of hazard calculations for LHVF eruption sources.

Using the LHVF recurrence rate of 5.5×10^{-6}/yr in Equation 4 results in a 5.5×10^{-6}/yr probability for the next volcanic eruption. As an additional perspective, there is a 1.3% likelihood that no events would have occurred in the LHVF since the last activity at 0.79 Ma, if these eruptions were randomly distributed in time (i.e., Equation 4). This indicates that activity from 0.79–3 Ma, and no eruptions since 0.79 Ma, reflects control by a non-random process and that the homogeneous Poisson assumption likely overestimates the eruption probability (i.e., Bebbington, 2013).

2) Probability the LHVF mafic eruption will VEI2–3

Five of the fourteen Quaternary mafic eruption events in the LHVF produced scoria cones, which indicates a (5 ÷ 14) = 36% likelihood the next mafic eruption will be sufficiently explosive to produce buoyant tephra plumes.

3) Probability that winds will be directed from LHVF to proposed site

The calculated column heights for the 18,000 realizations were binned into the corresponding altitude ranges used in the ASHPLUME2 model, and used to calculate a weighted value for each altitude range (Table 18). This weight is applied to the percentage of time the winds in each altitude range are directed towards the site (i.e., from the corresponding sector in Table 15**)**, and used to calculate a weighted percentage for the amount of time the wind in each altitude range is directed toward the site. The sum of the weighted percents shows that for the 18,000 ASHPLUME2 realizations, only 0.9% of the eruptions would have had winds directed towards the proposed site.

Table 18. Probability that winds from LHVF are directed towards proposed site.

Bin (km)	*Frequency*	Weight	Sector %	Weight Percent
1.5	0	0%	4.4%	0.00%
5.6	13782	77%	0.9%	0.69%
10.4	4218	23%	1.0%	0.23%
15.8	0	0%	0.2%	0.00%
			Winds to Site 0.9%	

Thus, the probability of a tephra-fall eruption from a future eruption from the LHVF is

$$5.5\text{x}10^{-6}\text{/yr x } 0.36 \text{ x } 0.009 = 1.8\text{x}10^{-8}\text{/yr},$$

which is then multiplied by the conditional probability of exceedance for tephra-deposit thickness, to generate the exceedance probabilities for mafic tephra-falls from the LHVF (Figure 24). There is $9.1\text{x}10^{-10}$/yr probability of exceeding the 95th percentile thickness of 0.06 cm, and an $8.3\text{x}10^{-9}$/yr probability of exceeding the average thickness of 0.0013 cm. Note that there is no tephra-fall hazard at probabilities of exceedance >$5\text{x}10^{-7}$/yr, which represents the smallest likelihood for a potential initiating event associated with beyond-design-basis event sequences (Nuclear Energy Institute, 2019).

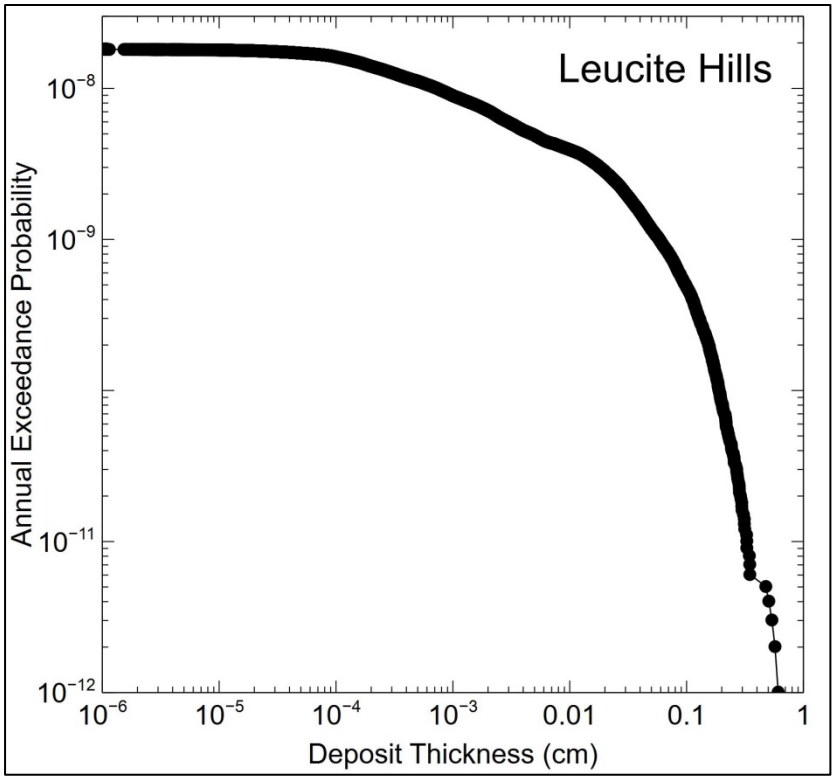

Figure 24. Annual exceedance probabilities for mafic tephra-fall hazards from the LHVF.

6.4.2 Tephra-fall Hazards from the Upper Wind River Basin Volcanic Field

Potential vents for the UWRB are located 220–230 km from the proposed Natrium™ site. To account for spatial variability in vent locations, 1,000 ASHPLUME realizations were conducted every 1 km along a 10-km-long axis, for a total of 11,000 realizations.

Results of the ASHPLUME hazard calculations are presented in Table 19 and Figure 25. The calculated range of deposit volumes ($1.6x10^7$–$3.8x10^8$ m^3) corresponds reasonably to the interpreted range of deposit volumes for the UWRB (Table 12; $1.6x10^7$–$4.2x10^8$ m^3), and the calculated range of eruption column heights (6.7–12.9 km) compares reasonably with the interpreted range of column heights for the UWRB (Table 13; 6.7–13.0 km). The calculated tephra-fall deposit thicknesses form a log-normal distribution, which is reflected in the summary statistics (Table 19).

Table 19. Summary of ASHPLUME2 calculations for UWRB mafic tephra hazards.

	Power (W)	*Duration (s)*	*Deposit Volume (m^3)*	*Col H (km)*	*Wind (km/hr)*	*Deposit Thick (cm)*
Avg	2.1E+12	7.2E+04	1.1E+08	9.4	32.8	0.01
Min	4.5E+11	5.0E+04	1.6E+07	6.7	0.03	4.0E-07
Max	6.0E+12	1.0E+05	3.8E+08	12.9	101.9	0.9
95^{th} percentile thickness: 0.17 cm						

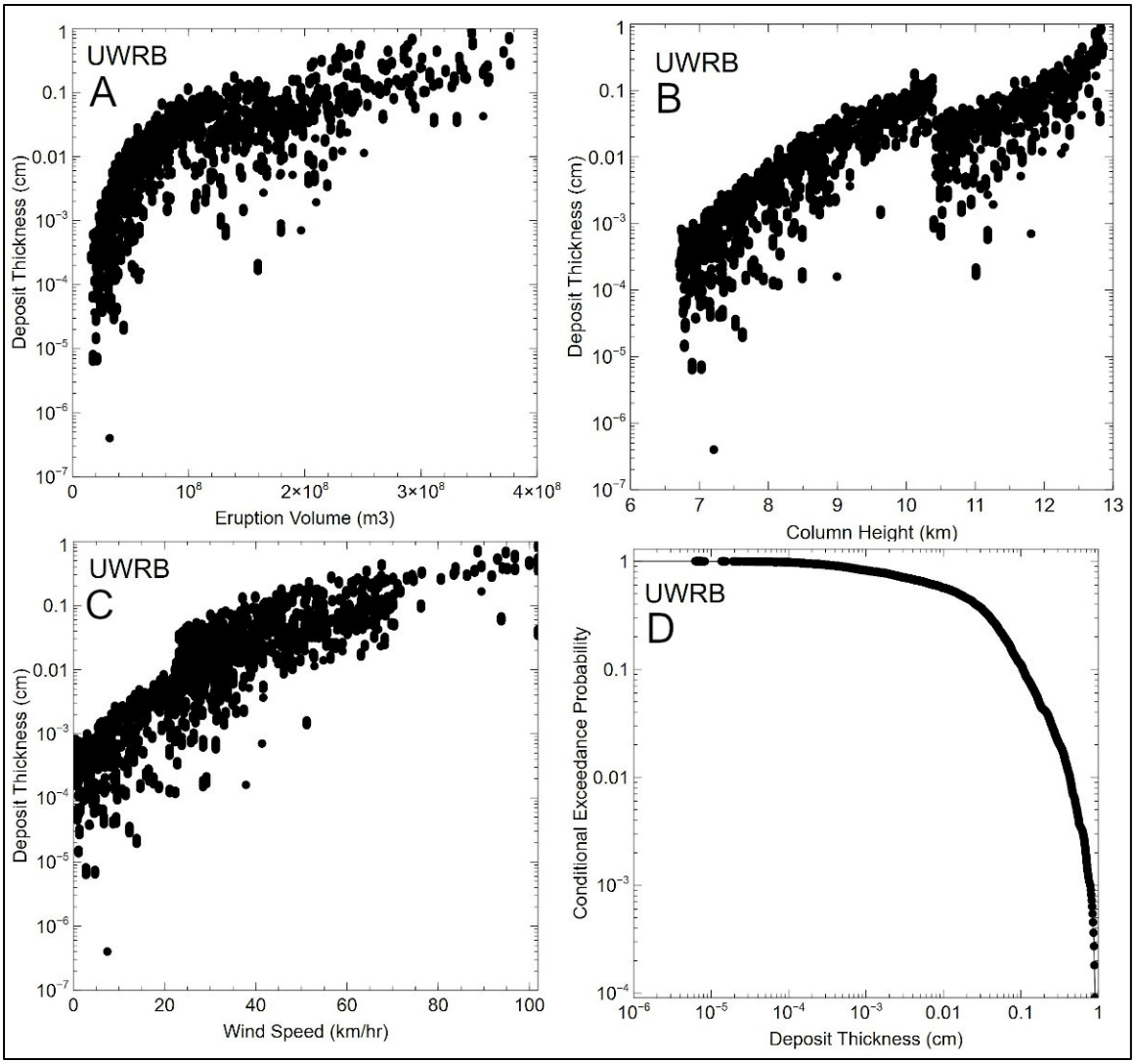

Figure 25. Results of hazard calculations for UWRB eruption sources.

As would be expected, the thickest calculated deposits at the proposed site result from the largest eruption volumes (Figure 25A), the highest eruption columns (Figure 25B), and the fastest wind speeds (Figure 25C). The conditional tephra-fall hazard curve is shown in Figure 25D, which yields a 95th percentile deposit thickness of 0.17 cm. Note that this amount of tephra-fall assumes that i) a mafic eruption occurs in the UWRB volcanic field, ii) the eruption produces a buoyant tephra plume, and iii) the prevailing wind is directed from the UWRB vent towards the proposed Natrium™ site.

To calculate a fully probabilistic tephra-fall hazard curve for potential UWRB eruption sources, the following three probabilities must be determined:

1) *Probability of a future mafic eruption in the UWRB:*

There are only a few past events in the UWRB to use for estimates of eruption probabilities (Section 2.2). If the 0.46 Ma Lava Mountain is interpreted as a single event, there have been 5 mafic eruption events in the UWRB since 4.8 Ma, for a Plio-Quaternary recurrence

rate of $1x10^{-6}$/yr. Considering only the Quaternary Lava Mountain eruption as a single event, or 26 separate events, gives a recurrence rate of $2.2x10^{-6}$/yr to $5.7x10^{-5}$/yr. In order to capture the epistemic uncertainty in the UWRB recurrence rate, the upper bound of $5.7x10^{-5}$/yr is a conservative value.

Using a $5.7x10^{-5}$/yr recurrence rate in Equation 4 results in an annual probability of $5.7x10^{-5}$/yr for a future mafic eruption in the UWRB. As an additional perspective on this probability value, there is a $5.x10^{-12}$ likelihood that no events would have occurred in the UWRB since the last activity at 0.46 Ma, if these eruptions were randomly distributed in time with a $5.7x10^{-5}$/yr recurrence rate (i.e., Equation 4). In contrast, there is a 62% likelihood that that no events would have occurred in the UWRB since the last activity at 0.46 Ma, if these eruptions were randomly distributed in time with a long-term recurrence rate of $1x10^{-6}$/yr. Consequently, the use of a $5.7x10^{-5}$/yr recurrence rate for the UWRB likely overestimates eruption probability, and would not readily explain the absence of activity in the UWRB since 0.46 Ma.

2) Probability the UWRB mafic eruption will be VEI2–3

Based on the characteristics of Lava Mountain, it is assumed that 100% of future eruptions in the UWRB will have the potential to develop buoyant tephra plumes from VEI2–3 events. This assumption is conservative, as it is likely that some, if not many, of the 26 eruptions at Lava Mountain were not sufficiently energetic to support buoyant tephra plumes.

3) Probability that winds will be directed from UWRB to proposed site

The calculated column heights for the 11,000 realizations were binned into the corresponding altitude ranges used in the ASHPLUME2 model, and used to calculate a weighted value for each altitude range (Table 20). This weight is applied to the percentage of time the winds in each altitude range are directed towards the site (i.e., from the corresponding sector in Table 15**)**, and used to calculate a weighted percentage for the amount of time the wind in each altitude range is directed toward the site. The sum of the weighted percents shows that for the 11,000 ASHPLUME2 realizations, only 2.8% of the eruptions would have had winds directed towards the proposed site.

Table 20. Probability that winds from UWRB are directed towards proposed site.

Bin (km)	*Frequency*	Weight	Sector %	Weight Percent
1.5	0	0%	3.7%	0.00%
5.6	0	0%	3.1%	0.00%
10.4	7381	67%	3.8%	2.55%
15.8	3619	33%	0.7%	0.23%
			Winds to Site 2.8%	

Thus, the probability of a tephra-fall eruption from a future eruption from the UWRB volcanic field is

$$5.7x10^{-5}\text{/yr} \times 1 \times 0.028 = 1.6x10^{-6}\text{/yr},$$

which is then multiplied by the conditional probability of exceedance for tephra-deposit thickness, to generate the exceedance probabilities for mafic tephra-falls from the UWRB (Figure 26). There is $7.9x10^{-8}$/yr probability of exceeding the 95th percentile thickness of 0.17 cm, and an $9x10^{-7}$/yr probability of exceeding the average thickness of 0.01 cm. Note that a

0.04 cm tephra-fall hazard occurs at an exceedance probability of $5x10^{-7}$/yr, which represents the smallest likelihood for a potential initiating event associated with beyond-design-basis event sequences (Nuclear Energy Institute, 2019).

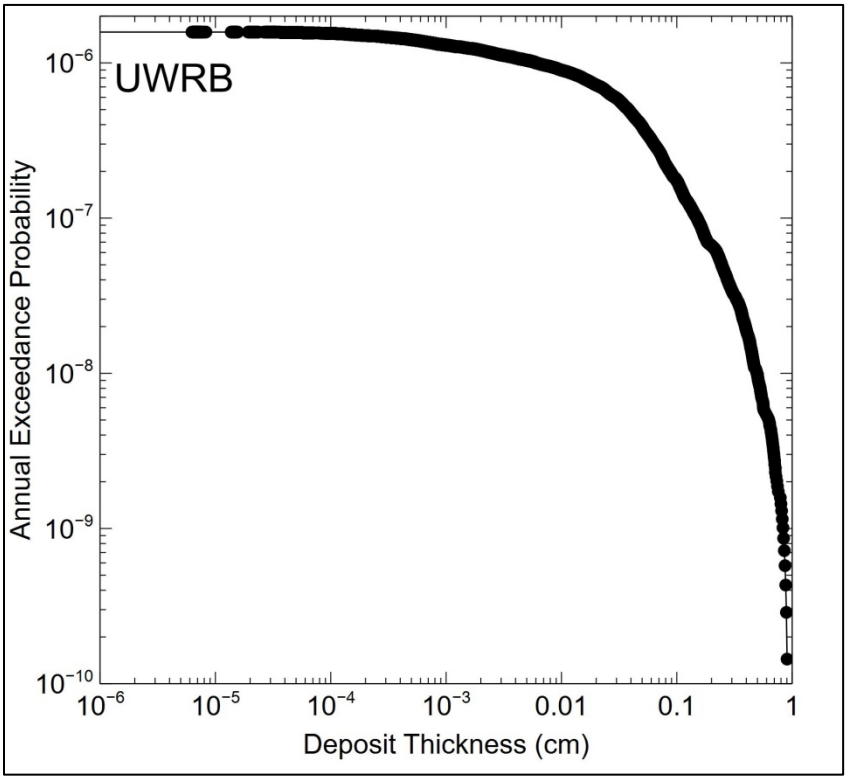

Figure 26. Annual exceedance probabilities for mafic tephra-falls from the UWRB volcanic field.

6.4.3 Mafic Tephra-fall Hazards from the Blackfoot Reservoir Volcanic Field

Potential vents for the BRVF are located 119–193 km from the proposed Natrium™ site. To account for spatial variability in vent locations, 1,000 ASHPLUME realizations were conducted every 5 km along a 74-km-long axis, for a total of 16,000 realizations.

Results of the ASHPLUME hazard calculations are presented in Table 21 and Figure 27. The calculated range of deposit volumes ($8.7x10^5$–$9.3x10^7$ m^3) corresponds reasonably to the interpreted range of deposit volumes for the BRVF (Table 12; $8.3x10^5$–$1.3x10^8$ m^3), and the calculated range of eruption column heights (3.1–9.1 km) compares reasonably with the interpreted range of column heights for the BRVF (Table 13; 3–9.5 km). The calculated tephra-fall deposit thicknesses form a log-normal distribution, which is reflected in the summary statistics (Table 21).

Table 21. Summary of ASHPLUME2 calculations for BRVF mafic tephra hazards.

	Power (W)	*Duration (s)*	*Deposit Volume (m^3)*	*Col H (km)*	*Wind (km/hr)*	*Deposit Thick (cm)*
Avg	3.6E+11	7.2E+04	2E+07	5.6	76	0.006
Min	2.4E+10	5.0E+04	8.7E+05	3.2	0.03	8.3E-11
Max	1.5E+12	1.0E+05	9.3E+07	9.1	303	9.3
95^{th} percentile thickness: 2.11 cm						

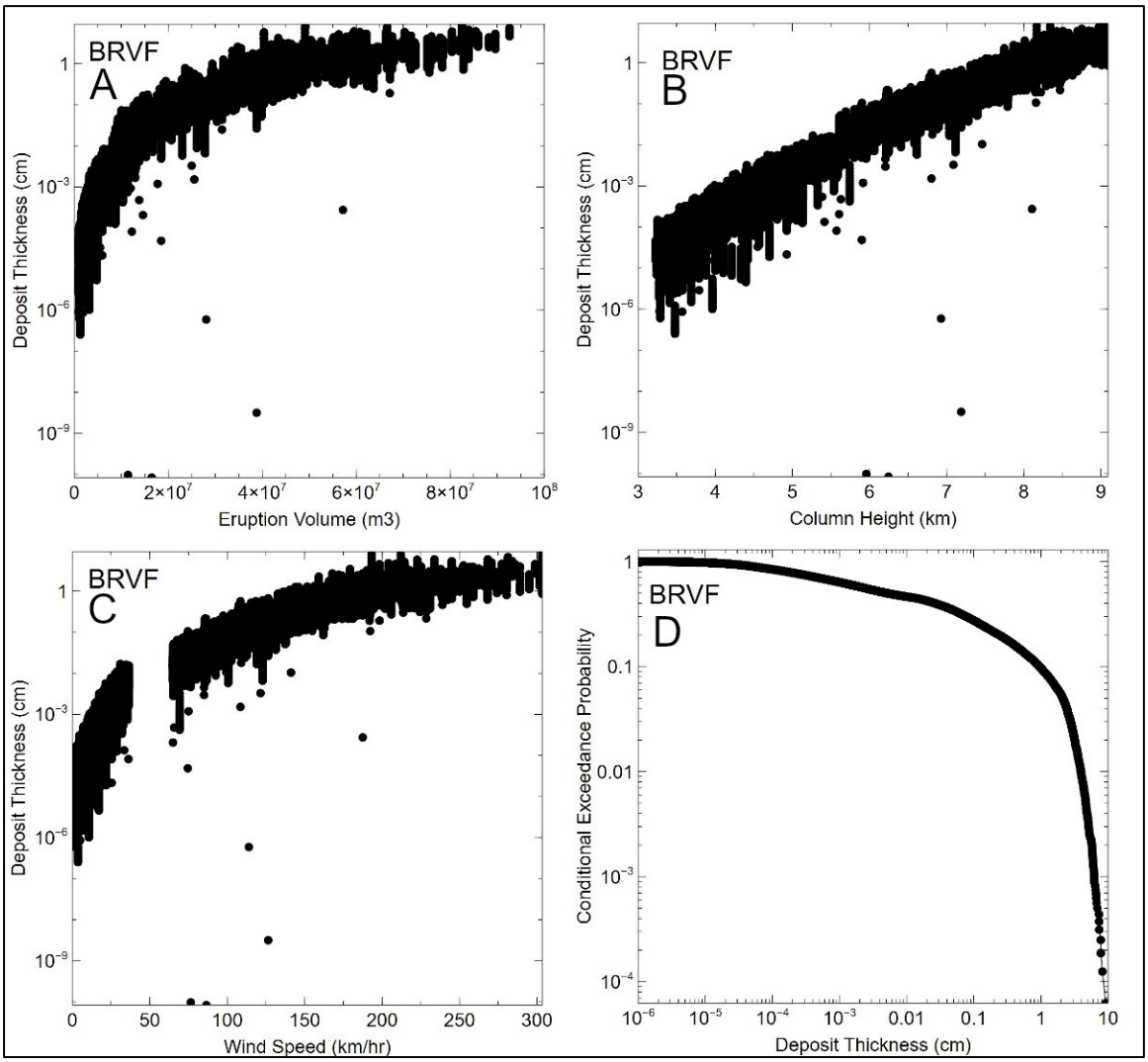

Figure 27. Results of hazard calculations for BRVF eruption sources.

As would be expected, the thickest calculated deposits at the proposed site result from the largest eruption volumes (Figure 27A), the highest eruption columns (Figure 27B), and the fastest wind speeds (Figure 27C). The conditional tephra-fall hazard curve is shown in Figure 27Figure 27D, which yields a 95th percentile deposit thickness of 2.11 cm. Note that this amount of tephra-fall assumes that i) a mafic eruption occurs in the BRVF volcanic field, ii) the eruption produces a buoyant tephra plume, and iii) the prevailing wind is directed from the BRVF vent towards the proposed Natrium™ site.

To calculate a fully probabilistic tephra-fall hazard curve for potential BRVF eruption sources, the following three probabilities must be determined:

1) *Probability of a future mafic eruption in the BRVF:*

Only a few of the past mafic eruptions in the BRVF have been dated radiometrically, with the oldest reported date of 1.04±0.08 Ma (Section 2.6). Nevertheless, petrogenetic studies conclude that generation 1.4–1.6 Ma rhyolite required coeval basaltic magmatism. A

recurrence rate of $5.3x10^{-5}$/yr results from the eruption of 85 mafic events since 1.6 Ma in the BRVF. Shorter intervals of time (i.e., 1.04 Myr) do not account for the epistemic uncertainties associated with the lack of radiometric dates in the BRVF, and are not consistent with the generation of rhyolitic magmas at 1.4–1.6 Ma. Based on comparison with the well-dated ESRP, it is likely that basaltic magmatism preceded rhyolitic magmatism by potentially hundreds of thousands of years. In the absence of additional age constraints for the BRVF, it appears conservative to use the age of the oldest rhyolitic eruption (i.e., 1.6 Ma) for estimating the recurrence rate of mafic volcanism, because an older range of activity would result in lower recurrence rate estimates.

Using a $5.3x10^{-5}$/yr recurrence rate in Equation 4 results in an annual probability of $5.3x10^{-5}$/yr for a future mafic eruption in the BRVF. As an additional perspective on reasonableness of this probability value, there is a 20% likelihood that no events would have occurred in the BRVF since the last activity at 0.03 Ma (i.e., age of youngest mafic lava flow), if these eruptions were randomly distributed in time with a $5.3x10^{-5}$/yr recurrence rate (i.e., Equation 4).

2) Probability the BRVF mafic eruption will be VEI1–3

There are 14 of the 85 scoria cones in the BRVF that have morphologies indicative of potentially explosive eruptions that might have produced buoyant tephra plumes from VEI1–3 events (Section 6.3.1.3). Thus, 16.1% of mafic eruptions in the BRVF have the potential for VEI1–3 events.

3) Probability that winds will be directed from BRVF to proposed site

The calculated column heights for the 16,000 realizations were binned into the corresponding altitude ranges used in the ASHPLUME2 model, and used to calculate a weighted value for each altitude range (Table 22). This weight is applied to the percentage of time the winds in each altitude range are directed towards the site (i.e., from the corresponding sector in Table 15**)**, and used to calculate a weighted percentage for the amount of time the wind in each altitude range is directed toward the site. The sum of the weighted percents shows that for the 16,000 ASHPLUME2 realizations, 14.1% of the eruptions would have had winds directed towards the proposed site.

Table 22. Probability that winds from BRVF are directed towards proposed site.

Bin (km)	*Frequency*	Weight	Sector %	Weight Percent
1.5	0	0%	7.6%	0.00%
5.6	8464	53%	13.7%	7.25%
10.4	7533	47%	14.6%	6.88%
15.8	0	0%	7.0%	0.00%
			Winds to Site 14.1%	

Thus, the annual probability of a tephra-fall eruption from a future eruption from the BRVF volcanic field is

$$5.3x10^{-5}\text{/yr} \times 0.161 \times 0.141 = 1.2x10^{-6}\text{/yr},$$

which is then multiplied by the conditional probability of exceedance for tephra-deposit thickness, to generate the tephra-fall hazard curve for BRVF (Figure 28). There is $6.0x10^{-8}$/yr probability of exceeding the 95th percentile thickness of 2.11 cm, and an $5.9x10^{-7}$/yr probability

of exceeding the average thickness of 0.006 cm. Note that a 0.022 cm tephra-fall hazard occurs at an exceedance probability of $5x10^{-7}$/yr, which represents the smallest likelihood for a potential initiating event associated with beyond-design-basis event sequences (Nuclear Energy Institute, 2019).

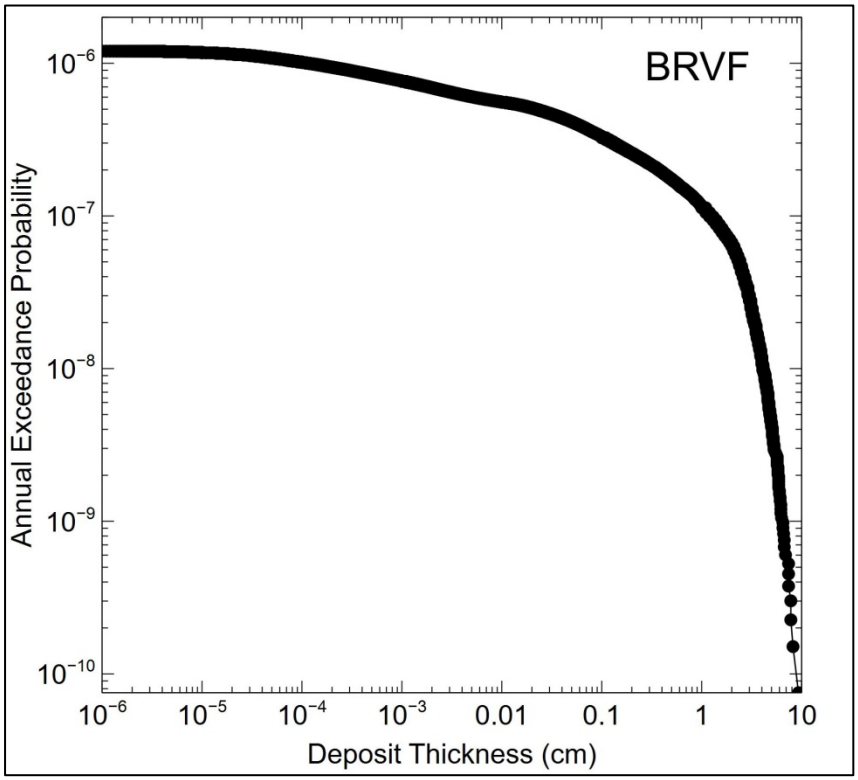

Figure 28. Tephra-fall hazard curve for the BRVF volcanic field.

6.4.4 Mafic Tephra-fall Hazards from the Eastern Snake River Plain Volcanic Field

Potential vents for the ESRP are located 250–320 km from the proposed Natrium™ site. To account for spatial variability in vent locations, 1,000 ASHPLUME realizations were conducted every 4 km along a 70-km-long axis, for a total of 18,000 realizations.

Results of the ASHPLUME hazard calculations are presented in Table 23 and Figure 29. The calculated range of deposit volumes ($6.3x10^7$–$2.1x10^8$ m^3) corresponds reasonably to the interpreted range of deposit volumes for the ESRP (Table 12; $6.3x10^7$–$2.1x10^8$ m^3), and the calculated range of eruption column heights (8.2–10.8 km) compares reasonably with the interpreted range of column heights for the ESRP (Table 13; 8.2–10.9 km). The calculated tephra-fall deposit thicknesses form a log-normal distribution, which is reflected in the summary statistics (Table 23).

Table 23. Summary of ASHPLUME2 calculations for ESRP mafic tephra hazards.

	Power (W)	*Duration (s)*	*Deposit Volume (m^3)*	*Col H (km)*	*Wind (km/hr)*	*Deposit Thick (cm)*
Avg	1.8E+12	9.4E+04	1.2E+08	9.4	67	0.019
Min	1.0E+12	8.9E+04	6.3E+07	8.2	0.05	8.3E-11
Max	3.0E+12	1.0E+05	2.1E+08	10.8	170	0.96
95^{th} percentile thickness: 0.32 cm						

As would be expected, the thickest calculated deposits at the proposed site result from the largest eruption volumes (Figure 29A), the highest eruption columns (Figure 29B), and the fastest wind speeds (Figure 29C). The conditional tephra-fall hazard curve is shown in Figure 29D, which yields a 95^{th} percentile deposit thickness of 0.32 cm. Note that this amount of tephra-fall assumes that i) a mafic eruption occurs in the ESRP volcanic field, ii) the eruption produces a buoyant tephra plume, and iii) the prevailing wind is directed from the ESRP vent towards the proposed Natrium™ site.

To calculate a fully probabilistic tephra-fall hazard curve for potential ESRP eruption sources, the following three probabilities must be determined:

1) *Probability of a future mafic eruption in the ESRP:*

Although the ESRP is one of the best-investigated volcanic fields in the United States, the relatively large size and number of Quaternary eruptions create challenges for estimating recurrence rates of mafic eruptions. Subsurface drilling studies have been used to infer the locations of potentially buried Quaternary volcanoes, which might affect calculations of spatial recurrence rates or long-term temporal recurrence rates (Gallant et al., 2018). Nevertheless, the probability need for this VHA is an estimate of temporal recurrence rates of Quaternary basaltic eruptions, in order to assess tephra-fall hazards at a remote (>250 km) site location. This VHA relies on the characteristics of ESRP vents that are exposed at the surface, to determine potential for forming dispersed tephra-fall deposits. Thus, buried ESRP volcanoes do not provide needed information on the characteristics of past events, and should be excluded from the recurrence rate calculations.

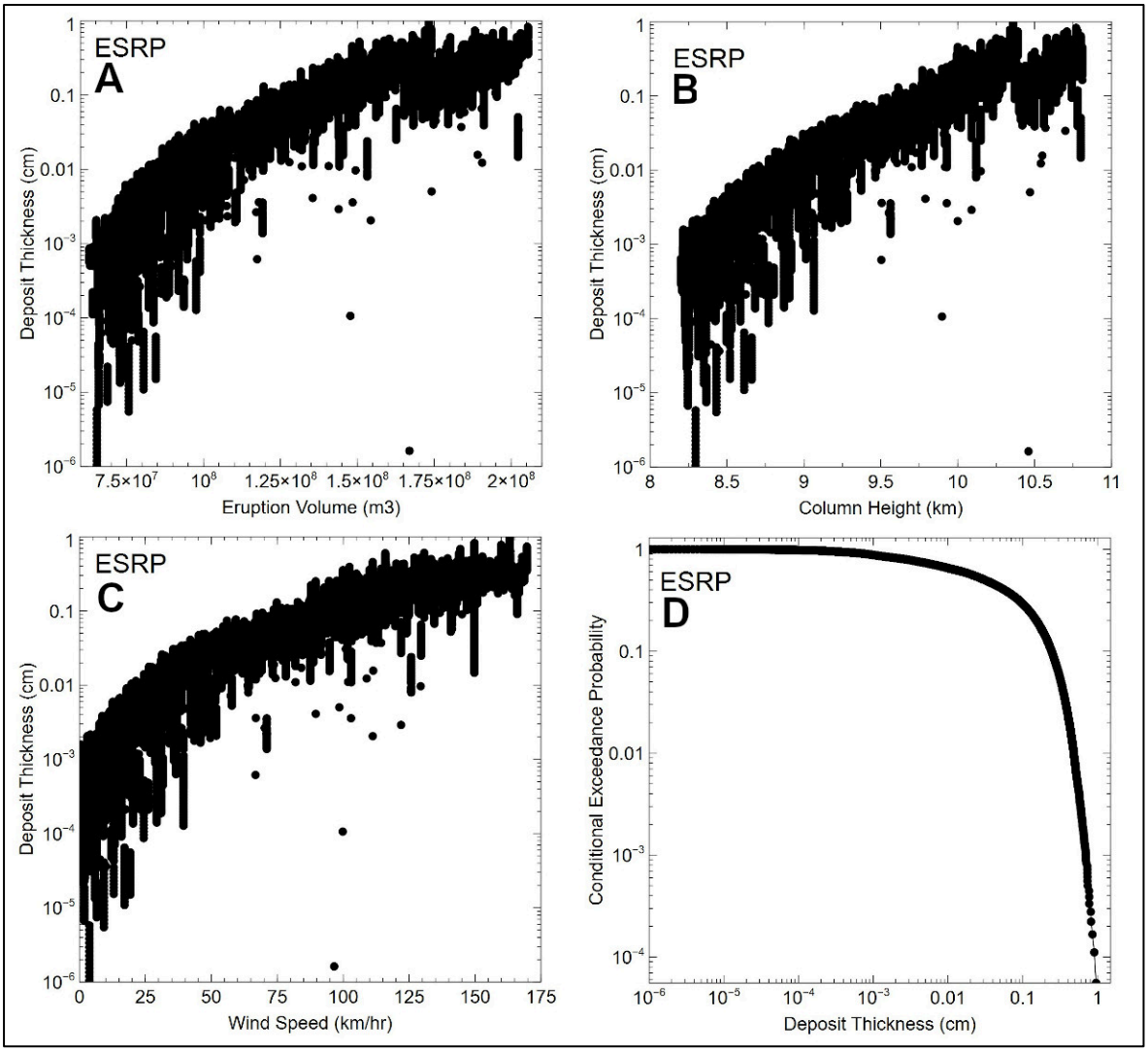

Figure 29. Results of hazard calculations for ESRP eruption sources.

Gallant et al. (2018) determined that eruption recurrence rates in the ESRP are relatively steady since 0.5 Ma, and that >0.5 Ma recurrence rates are likely biased due to burial of some older units. Although burial of older Quaternary volcanoes has unquestionably occurred in the central part of the ESRP, some vents >0.5 Ma are preserved on the outer parts of the volcanic field (e.g., Kuntz et al., 1992). Some of these peripheral vents are of more significance to this VHA, because they are located closer to the proposed site than volcanoes in the center of the field. Kuntz et al. (1992) concluded that 99% of the exposed volcanoes in the ESRP formed during the Brunhes normal polarity chron (i.e., Spell and McDougall, 1992) and would thus be <0.78 Ma. Using this conclusion, a recurrence rate of (0.99*431 events)/0.78 Myr = 5.5×10^{-4}/yr appears reasonable for the ESRP. Using a 5.5×10^{-4}/yr recurrence rate in Equation 4 results in an annual probability of 5.5×10^{-4}/yr for a future mafic eruption in the ESRP.

As an additional perspective on reasonableness of this probability value, there is only a 33% likelihood that no events would have occurred in the ESRP since the last activity at

2 ka (i.e., estimated age of youngest eruption), if these eruptions were randomly distributed in time with a $5.5x10^{-4}$/yr recurrence rate (i.e., Equation 4).

2) Probability the ESRP mafic eruption will be VEI1–3

There are 13 scoria cones out of 431 mafic volcanoes in the ESRP that have morphologies indicative of potentially explosive eruptions that might have produced buoyant tephra plumes from VEI2–3 events (Section 6.3.1.4). Thus, only 3.0% of mafic eruptions in the ESRP have the potential for VEI2–3 events.

3) Probability that winds will be directed from the ESRP to proposed site

The calculated column heights for the 18,000 realizations were binned into the corresponding altitude ranges used in the ASHPLUME2 model, and used to calculate a weighted value for each altitude range (Table 24). This weight is applied to the percentage of time the winds in each altitude range are directed towards the site (i.e., from the corresponding sector in Table 15**)**, and used to calculate a weighted percentage for the amount of time the wind in each altitude range is directed toward the site. The sum of the weighted percents shows that for the 18,000 ASHPLUME2 realizations, 22.4% of the eruptions would have had winds directed towards the proposed site.

Table 24. Probability that winds from ESRP are directed towards proposed site.

Bin (km)	*Frequency*	Weight	Sector %	Weight Percent
1.5	0	0%	12.9%	0.00%
5.6	0	0%	23.9%	0.00%
10.4	15308	85%	22.7%	19.33%
15.8	2666	15%	20.5%	3.04%
			Winds to Site 22.4%	

Thus, the annual probability of a tephra-fall eruption from a future eruption from the ESRP volcanic field is

$$5.5x10^{-4}/yr \times 0.03 \times 0.224 = 3.7x10^{-6}/yr,$$

which is then multiplied by the conditional probability of exceedance for tephra-deposit thickness, to generate the tephra-fall hazard curve for ESRP (Figure 30). There is $1.9x10^{-7}$/yr probability of exceeding the 95th percentile thickness of 0.32 cm, and an $2.1x10^{-6}$/yr probability of exceeding the average thickness of 0.02 cm. Note that a 0.21 cm tephra-fall hazard occurs at an exceedance probability of $5x10^{-7}$/yr, which represents the smallest likelihood for a potential initiating event associated with beyond-design-basis event sequences (Nuclear Energy Institute, 2019).

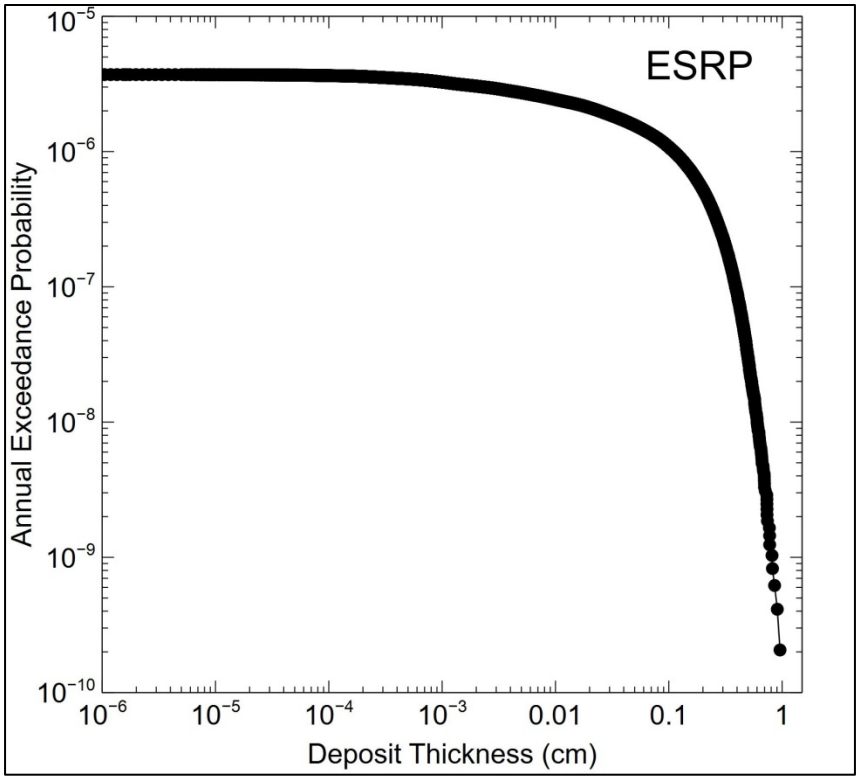

Figure 30. Tephra-fall hazard curve for the ESRP volcanic field.

6.4.5 Summary of Mafic Tephra-fall Hazards at the Proposed Natrium™ Site

In summary, tephra-fall hazards for the LHVF, UWRB, BRVF, and ESRP have been analyzed using the ASHPLUME2 code. These analyses evaluated a range of potential conditions that appear representative of the types of VEI1–3 eruptions that can be interpreted from preserved scoria cones in these fields. Potential sources of future tephra falls are located 116–320 km from the proposed site, and regional winds are directed to the site from these sources approximately 1–23% of the year (Table 25).

Table 25. Summary of conditional tephra-fall hazards at the proposed site, from mafic volcanoes in the site region.

Volcanic Field	VEI	Average Deposit (cm)	95th% deposit (cm)	Column Heights (km)	Max. Wind Speed (km/hr)	Wind to site (%yr)	Distance from site (km)
LHVF	2–3	0.001	0.063	3.9–6.3	136	0.9	116–150
UWRB	2–3	0.010	0.172	6.7–12.9	102	2.8	220–230
BRVF	1–3	0.006	2.106	3.2–9.1	303	14.1	117–192
ESRP	2–3	0.019	0.324	8.2 –10.8	170	22.4	250–320

Table 26. Summary of exceedance probabilities for mafic tephra-fall hazards at the proposed site, from potential mafic volcanic eruptions in the site region.

Mafic Fields	Avg. Deposit (cm)	Avg. Prob. (/yr)	95%ile deposit (cm)	95%ile Prob (/yr)	$5x10^{-7}$/yr deposit (cm)
LHVF	0.001	8.3E-09	0.063	9.10E-10	0.000
UWRB	0.010	9.0E-07	0.172	7.90E-08	0.038
BRVF	0.006	5.9E-07	2.106	6.00E-08	0.022
ESRP	0.019	2.1E-06	0.324	1.90E-07	0.210
Total	**0.036**	**3.6E-06**	**2.665**	**3.3E-07**	**0.27**

Mafic tephra-fall eruptions represent independent events in the site region, as the likelihood of an eruption in one volcanic field does not affect the likelihood of an eruption in a separate volcanic field. Consequently, the probability of exceeding specific thicknesses of a tephra-fall deposit can be represented by the sum of the probabilities for that thickness (i.e., eruptions represent mutually exclusive, independent events). Considering the four mafic volcanic fields in the site region, this approach shows that an average mafic tephra-fall deposit of 0.04 cm has a $3.6x10^{-6}$/yr probability of exceedance (Table 26). The 95th percentile tephra-fall hazard is 2.7 cm with a $3.3x10^{-7}$/yr probability of exceedance. As discussed in Section 1.1, average and 95th percentile deposit thicknesses are calculated for use in the evaluation of potential event sequences (e.g., Nuclear Regulatory Commission, 2020).

The cumulative mafic tephra-fall hazard at the proposed site also can be represented by the combined probabilities of exceedance for specific deposit thicknesses from each volcanic field (Figure 31). This approach shows that the probability of exceeding 0.1 cm of mafic tephra at the proposed site is approximately $1.6x10^{-6}$/yr, whereas the probability of exceeding 1 cm is approximately $1.2x10^{-7}$/yr. Mafic tephra-fall hazards >1 cm only occur from potential eruptions of the BRVF (Figure 31).

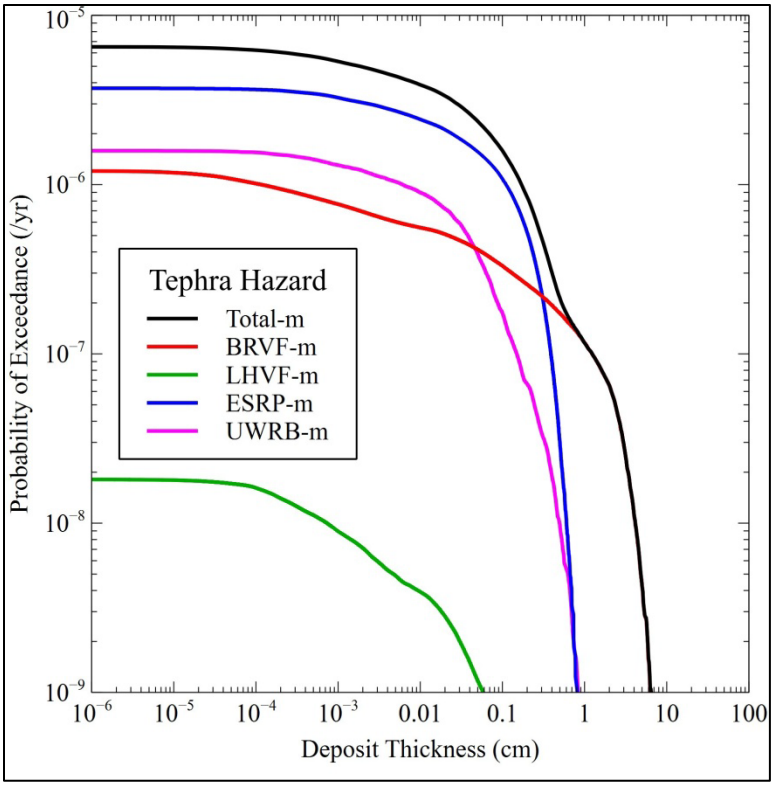

Figure 31. Summary of mafic tephra-fall hazards at the proposed site.

6.4.6 Potential for Debris-flow Hazards from Mafic Tephra-fall Deposits

As discussed in Section 4.5.1, the proposed Natrium™ site is located in a small (67.7 km^2) drainage basin that supports the North Fork of the Little Muddy Creek (NFLMC), which is an ephemeral to intermittent stream system (Figure 20). Tephra deposited in this drainage basin might have the potential to be remobilized by water during infrequent, extreme rainfall events. Tephra particles generally will be lower density than normal stream sediments, due to the vesicularity of the fine-grained tephra (i.e., <2 g/cm^3 versus >2 g/cm^3 for ambient sediments). As a result, tephra can be more readily entrained in flowing water, and could enhance the amount of suspended material in the flow during extreme events. As the amount of suspended material increases in a flow, the flow can transition from a turbulent flood-flow regime to a hyperconcentrated flow regime (10–60 volume percent suspended particles), and ultimately to a debris-flow regime at >60 volume% (e.g., Pierson, 2005). Debris flows can overtop stream channels and lead to flooding conditions from overbank flow.

Tephra-fall deposits in stream channels and surrounding hill slopes could provide a source of new particles that could potentially increase the amount of suspended material in a flood flow. Deposits on surrounding hill slopes eventually can be washed into these drainages during extreme rainfall events, through a complex process of overland water flow and interactions with surface obstacles. However, these processes operate on years-to-decades time scales after eruptions (e.g., Pelletier et al., 2008), long after the channels have been scoured of initial tephra-fall deposits. Consequently, the greatest potential for initiating debris flows appears to result from remobilized tephra-fall deposits during the first flooding event after an eruption, when channels have the maximum amount of tephra available for suspended-load fluvial transport. Although debris-flow initiation is not an instantaneous process (e.g., Pierson and Major, 2014),

the conservative approach developed in this section assumes that all the tephra in a channel is instantaneously mobilized by a flooding event. Tephra from surrounding hill slopes would not be instantaneously mobilized, but could likely contribute to smaller-volume debris flows in the future depending on rainfall, topographic, and deposit weathering conditions. As a result, the longer-term contribution of potentially remobilized hill slope tephra deposits is not incorporated into the debris-flow analysis, which assumes instantaneous incorporation of available tephra in existing stream channels.

To determine the potential for mafic tephra-fall deposits to create debris-flow conditions in drainages near the proposed site, the VHA needs to consider the:

i) Frequency of extreme rainfall events that could trigger flood flow in the NFLMC drainage basin:

> Extreme rainfall events occur infrequently in the site vicinity. On average, the area around the proposed site receives measurable rainfall 80–100 days out of the year, but rainfall rates ≥1 in/hr only occur <3% of the time (Wyoming State Climate Office, 2022). In comparison, 24-hr average rainfall rates of ≈1 in/hr are characteristic of the 100-yr recurrence rainfall event that is used to calculate probable maximum precipitation events for this part of southwestern Wyoming (Kappel et al., 2014).

ii) Potential flow characteristics of these flood events:

Drainages within the NFLMC basin are not monitored for discharge characteristics during extreme rainfall events. Nevertheless, flood frequencies for this basin can be estimated from the relationships in Carter and Green (1963). The NFLMC basin covers an area of 26.2 mi^2 (Figure 20), and is located at an altitude of approximately 7,000’ in hydrologic basin “6,” region “F,” of Carter and Green (1963). These characteristics indicate a mean annual flood discharge of 175 ft^3/s would characterize this basin (i.e., Carter and Green, 1963, fig. 8). This flood would have a 2 yr recurrence interval, with a flood discharge of ≈260 ft^3/s recurring every 10 yr and a 50 yr recurrence of ≈420 ft^3/s.

iii) Amount and source of particles suspended in typical floods:

Suspended sediments are entrained in flowing water as part of the erosion and scouring processes associated with flooding during extreme rainfall events in arid terranes, where sufficient overland runoff of water occurs to permit ephemeral and intermittent streams to flow (e.g., Leopold et al., 1966). Although most of the scoured sediments are transported as bed load, finer-grained sediments remain suspended through turbulence in the flow. In semi-arid to arid terrains, sediments in ephemeral stream channels typically contain <10% particles that are <0.25 mm in diameter, which represents the bulk of suspended-load particles (i.e., Yuill and Nichols, 2011).

The depth that ephemeral streams can scour and mobilize sediment through bed-load or suspended-load transport is proportional to the square root of the discharge per unit width of the channel (Leopold et al., 1966; Pelletier et al., 2008). The NFLMC has an active channel width of 15–20 m immediately east of the proposed site, which decreases to 10–15 m immediately northeast of the site. Widths of secondary and tertiary drainages are <10 m, and decrease to <5 m up slope into the primary catchments.

Hedman and Osterkamp (1982) developed equations to calculate the discharge rate of ephemeral streams, based on the width of the stream channel. The proposed Natrium™ site is located in their "Northern plains and intermontane areas east of the Rocky Mountains" zone. Using equations 24–29 in Hedman and Osterkamp (1982), calculated discharge rates for ephemeral streams in the NFLMC basin are given in Table 27.

Table 27. Calculated discharge rates for stream channels in the NFLMC basin, using equations 24–29 in Hedman and Osterkamp (1982). "Yr" refers to the recurrence interval for the discharge events.

Channel Width (m)	*Channel Width (ft)*	*2yr (ft^3/s)*	*5yr (ft^3/s)*	*10yr (ft^3/s)*	*25yr (ft^3/s)*	*50yr (ft^3/s)*	*100yr (ft^3/s)*
1	3.28	32	127	229	286	609	706
5	16.40	422	1205	2009	2316	4936	5282
10	32.81	1279	3181	5121	5703	12154	12563
15	49.21	2447	5612	8852	9661	20589	20855
20	65.62	3877	8395	13054	14043	29927	29881

Using these discharge rates, scour depths can be calculated for these streams using the relationship from Leopold et al. (1966):

Equation 5

$$Scour\ Depth = \frac{\sqrt{Discharge}}{Width}$$

Using the discharge rates from Table 27 and Equation 5, scour depths for the streams in the NFLMC basin are calculated in Table 28.

Table 28. Calculated scour depths for stream channels in the NFLMC basin, using Equation 5 from Leopold et al. (1966). "Yr" refers to the recurrence interval for the discharge events.

Channel Width (m)	*2yr (cm)*	*5yr (cm)*	*10yr (cm)*	*25yr (cm)*	*50yr (cm)*	*100yr (cm)*
1	53	105	141	157	229	247
5	38	65	83	89	131	135
10	33	52	66	70	102	104
15	31	46	58	61	89	89
20	29	43	53	55	80	80

iv) Potential for tephra to initiate debris-flow conditions

Approximately 10% of the sediments in the scour-depth are <0.25 mm in diameter. As discussed in *(iii),* these particles form the suspended sediment load during flood events. In essence, 10% of the scour depths in Table 28 represent the source of suspendable particles in the channel sediments, which is calculated in Table 29.

Table 29. Thicknesses of scour zones that represent the source of <0.25 mm particles, which can be suspended during flooding events in the NFLMC basin.

Channel Width (m)	*2yr (cm)*	*5yr (cm)*	*10yr (cm)*	*25yr (cm)*	*50yr (cm)*	*100yr (cm)*
1	*5.3*	*10.5*	*14.1*	*15.7*	*22.9*	*24.7*
5	*3.8*	*6.5*	*8.3*	*8.9*	*13.1*	*13.5*
10	*3.3*	*5.2*	*6.6*	*7.0*	*10.2*	*10.4*
15	*3.1*	*4.6*	*5.8*	*6.1*	*8.9*	*8.9*
20	*2.9*	*4.3*	*5.3*	*5.5*	*8.0*	*8.0*

The potential for forming debris-flow conditions can then be evaluated by first assuming that all of the tephra-fall deposit is <0.25 mm diameter and available for fluvial transport. Normal flood-flow conditions have <10% suspended sediment, and a conservative assumption is that all suspended sediment is derived from the scour zone (i.e., ignore wash-zone sources). Thus, the scour-zone thicknesses in Table 29 represent the ambient source of suspended-load sediments. The largest 95th percentile mafic tephra-fall thickness at the proposed site is 2.1 cm (Table 26) from the BRVF, which has 6x10^{-8}/yr probability of exceedance. In comparison, the scour-depth thicknesses for suspended load sediments is >2.9 cm (Table 29). Using these assumptions, a potential mafic tephra-fall deposit would no more than double the amount of suspended load transported during rare flood events in the NFLMC basin. Consequently, an increase in suspended-load particles from ≤10% (i.e., ambient flood) to ≤20% (i.e., tephra-enhanced flood) would be insufficient to generate debris-flow conditions in these channels.

Based on these empirical relationships and conservative bounding assumptions, potential mafic tephra-falls deposited in the NFLMC basin do not have the potential to generate debris-flow hazards either within this basin or at the proposed site. The amount of tephra deposited in the channel is insufficient to cause sufficient flow-bulking that could overtop ephemeral and intermittent stream channels during rare flood events. Although additional tephra deposits will gradually erode from surrounding hillsides, the rate of tephra released from this gradual process will be significantly lower than the instantaneous remobilization of tephra in the channels as assumed in these calculations.

7 ANALYSIS OF SILICIC TEPHRA-FALL HAZARDS

Tephra falls also can occur from silicic volcanoes that have explosive eruptions, due to enhanced fragmentation of the high viscosity magma and sufficient mass-flow rates to generate buoyant tephra plumes (e.g., Walker, 1973). Buoyant tephra plumes from silicic eruptions can rise to altitudes of tens of kilometers above ground level, depending on the volume and mass-flow rate of the eruption. Tephra-fall deposits from smaller silicic eruptions can extend for tens to hundreds of kilometers from the volcano. Although silicic caldera-forming eruptions have not been observed, deposits from these eruptions can extend for thousands of kilometers from the source area (e.g., Izett, 1981). Nevertheless, tephra-fall deposits from <1 km^3 eruptions of silicic magma are not preserved in the site region, and are only sparsely preserved for 1–100 km^3 eruptions. Even deposits from the largest-volume tephra fall (i.e., 2.1 Ma Huckleberry Ridge) are not preserved in the site vicinity, and at locations more than 100 km from the source caldera are found mostly as scattered, isolated deposits.

The approach used in this VHA to assess tephra-fall hazards from silicic volcanoes follows the approach used in Section 6 to assess hazards for mafic volcanoes, with the exception of the hazard assessment for Yellowstone caldera eruptions. The analysis first develops a technical basis to estimate the characteristics of past silicic tephra eruptions (i.e., volume, power, duration, grain size) in the site region. After the wind field characteristics are determined for each volcanic field, the ASHPLUME2 model is used to calculate tephra-fall hazards at the proposed site. The potential hazards from a future Yellowstone caldera are assessed as a separate analysis, which is then integrated into the overall hazards assessment from other silicic eruptions. The last step of the silicic tephra-fall hazards analysis is an assessment of the potential for debris-flow hazards to occur from fluvially remobilized tephra-fall deposits in the site vicinity.

7.1 Silicic Tephra-Fall Characteristics

The silicic tephra-fall hazards assessment uses the same ASHPLUME2 code as discussed in Sections 6.1–6.3. Consequently, the ASHPLUME2 models require characterization of i) eruption volumes; ii) eruption power and duration; iii) total grain-size distributions; and iv) wind speeds for each volcanic field with the potential for future silicic tephra-fall eruptions.

7.1.1 Silicic Tephra-Fall Volumes

In addition to three caldera-forming silicic eruptions, 33 smaller-volume Quaternary silicic eruptions have occurred within the site region in the YVF, BRVF, CVVF, and ESRP (Sections 2.1–2.7). Tephra-fall deposits from these smaller eruptions are not preserved, with the exception of several outcrops of distal ash from two <170 ka eruptions from the Yellowstone CPR (Section 2.1). As a result, tephra-fall deposit volumes will need to be estimated in order to assess potential hazards. The general approach used to evaluate mafic tephra-deposit volumes (Section 6.3.1) appears adaptable to constraining silicic tephra-fall volumes, and provides a traceable basis for the VHA. To apply that approach, the physical characteristics of silicic volcanoes in the site region will need to be compared to the physical characteristics of well-preserved silicic eruptions at analogous volcanoes.

Silicic volcanoes in the site region erupted as domes or lava flows, which formed through either single or multiple episodes of activity. A general characteristic of these eruptions is a lack of abundant pyroclastic deposits near the vent areas, with the exceptions of phreatomagmatic deposits near the 57 ka domes in the BRVF (Section 2.6) and the largest silicic dome eruptions

from the YVF. The absence of pyroclastic deposits, lack of vesiculation in erupted lavas and domes, and petrological studies, all indicate that most silicic lavas and domes in the site region had experienced shallow-level degassing prior to eruption (e.g., McCurry et al., 2015). Nevertheless, these studies are not definitive, and it is possible that pyroclastic deposits from these past eruptions have been buried or eroded. To account for the potential uncertainty in the character of past silicic eruptions, the VHA assumes that these past eruptions had some potential to develop buoyant tephra plumes and form tephra-fall deposits at some distances from the volcano.

The relationship between tephra-fall volume and the volume of associated domes or lava flows can be evaluated at well-studied volcanoes, to determine the potential volume of tephra-fall deposits for Quaternary volcanoes in the site region (cf. Section 6.3.1). A number of VEI2–4 silicic eruptions have occurred in the late Holocene (i.e., last several thousand years) and have been studied in sufficient detail to help guide their use as analogues for silicic eruptions in the site region. A common characteristic of these analogue eruptions is that tephra falls typically form during the early phases of activity, and are buried by the eruption of later lavas (e.g., Fink, 1990; Nawotniak and Bursik, 2010).

There are, however, limitations in the utility of these analogue volcanoes, which are all located in volcanic arc settings. Silicic magmas in arcs tend to have relatively higher water contents (e.g., >3-5 wt%; Grove and Donnelly-Nolan, 1986) than are thought to occur in the site region. Additionally, most of these analogue eruptions have both early pyroclastic phases of activity as well as extrusion of glassy and highly vesiculated lavas. In contrast, the silicic volcanoes in the site region form either crystalline or nearly aphyric lavas, which lack vesiculated or glassy intervals. These contrasts also support the interpretation that silicic magmas in the site region were significantly degassed before eruption, and did not form highly vesiculated magmas or explosive eruptions. Nevertheless, these comparisons are not definitive and it remains possible that pyroclastic deposits from past eruptions in the site region have been buried or eroded.

The volumes of well-studied Holocene silicic dome and lava eruptions are compiled in Table 30. These data show that although large explosive eruptions can accompany silicic lava flows (e.g., Cordon Caulle), similar-sized eruptions might produce only minor to negligible amounts of tephra (e.g., Medicine Lake). This is in marked contrast to basaltic scoria cone eruptions discussed in Section 6.3.1, which show a general relationship between the size of the eruptive cone and associated tephra deposit.

Table 30. Compilation of Holocene silicic dome and lava eruption characteristics. Reported tephra deposit volumes converted to DRE using deposit density = 30% magma density from Scott (1987). Data sources: (1) Scott (1987); (2) Miller (1985); (3) Nawotniak and Bursik (2010); (4) Gardner et al. (1998); (5) Donnelly-Nolan et al. (2016); (6) Heiken (1978); (7) Tuffen et al. (2013): (8) Farquharson et al. (2015); (9) Collini et al. (2013).

Volcano	*Age (yr BP)*	*Tephra Vol DRE (m^3)*	*Dome Vol DRE (m^3)*	*Tephra/ Dome*	*Source*
S. Sister, OR - Rock Mesa	2300	3.0E+07	5.0E+08	6.0%	1
S Sister, OR - Devils Hill	2200	2.0E+07	3.0E+08	6.7%	1
Inyo, CA - N. Deadman	6000	0	4.0E+07	0%	2
Inyo, CA - Wilson Butte	1350	0	5.0E+07	0%	2
Inyo, CA - South Deadman	700	5.0E+07	1.3E+08	38.5%	2

Volcano	*Age (yr BP)*	*Tephra Vol DRE (m^3)*	*Dome Vol DRE (m^3)*	*Tephra/ Dome*	*Source*
Inyo, CA - Obsidian Flow	650	3.0E+07	1.7E+08	17.6%	2,3
Inyo, CA - Glass Creek	600	1.0E+08	1.0E+08	100%	2
Newberry, OR - Big Obsidian	1300	1.0E+08	1.0E+08	100%	4
Medicine Lake, CA - Glass Mtn.	950	2.7E+07	1.0E+09	2.7%	5
Medicine Lake, CA - Little Glass Mtn	900	1.4E+07	3.5E+08	3.9%	5, 6
Medicine Lake, CA - Glass Flow	5200	0	8.0E+07	0%	5
Cordon Caulle, Chile (High est)	10	2.0E+08	5.0E+08	40%	7,8,9
Cordon Caulle, Chile (Low estimate)	10	4.0E+08	5.0E+08	80%	7,8,9

Consequently, the volume of silicic domes and lavas in the site region does not provide a straightforward basis to determine the potential volumes of past tephra-fall eruptions, because well-studied analogue volcanoes do not show consistent tephra volume to lava or dome volume relationships. Nevertheless, the volumes of silicic domes and lavas in the site region still need to be determined, in order to develop a technical basis for estimating possible volumes of past tephra-fall eruptions.

7.1.1.1 Silicic Volcano Volumes in the Yellowstone Volcanic Field

Christiansen et al. (2007) highlights the petrogenetic distinction between the <170 ka CPR and older post-caldera rhyolite, and concludes that hazards from future eruptions are best characterized by the CPR. This conclusion appears reasonable, because the petrology of the well-characterized CPR indicates that since ≈170 ka the Yellowstone silicic magma system began a distinct phase of activity, which reasonably should represent the characteristics of potential future activity.

Most of the eruptions from the CPR formed domes and larger-volume lava flows. Pyroclastic deposits from these eruptions are not exposed, potentially due to burial by younger deposits. Nevertheless, information from analogue volcanoes suggests that early phases of these eruptions might have produced buoyant tephra plumes (e.g., Fink, 1990). However, two of the CPR eruptions produced pyroclastic flows and associated tephra falls: the 143±5 ka Cold Mountain Tuff and the 173±5 ka Bluff Point Tuff. Tephra-fall deposits from these two eruptions occur 60–230 km from the likely vent areas (Section 2.1). Volumes of the CPR deposits are shown in Table 31. Note that numerous rhyolite effusive eruptions have volumes 2–5x larger than the volume of the Cold Mountain and Bluff Point Tuffs, yet pyroclastic deposits from these larger eruptions have not been observed in the Yellowstone area (Christiansen, 2001). The CPR cumulative volume of 329 km^3 does not include the estimated 256 km^3 from “unobserved units” (Christiansen et al., 2007). These volumes indicate a rhyolite effusion rate of 1.9 km^3/kyr, which increases to 3.4 km^3/kyr if the “unobserved” units are included.

Table 31. Volumes of CPR rhyolite eruptions, from Christiansen et al. (2007, Table 2), and Robinson et al. (2016).

	Unit Name	***Age±1σ (ka)***	***Mean group age (ka)***	***DRE Volume (km^3)***	***Cumul. Volume (km^3)***
1	Pitchstone Plateau	79±11		70	329
2	Grants Pass	72±3	76±5	0.5	259
3	Crystal Spring	80±2		0.2	259
4	Gibbon River	90±2		4	258
5	Solfatara Plateau	103±8		7	254
6	Paintpot Hill Dome	110±20		0.04	247
7	Hayden Valley	102±4	103±1	2	247
8	West Yellowstone	114±1		41	245
9	Trischman Knob			0.014	204
10	Moose Falls	115		1	204
11	Gibbon Hill	116		0.3	203
12	Douglas Knob			0.01	203
13	Bechler River	116±2		8	203
14	Summit Lake	124±10	118±5	37	195
15	**Cold Mtn. Ck. Tuff**	143±5		3	158
16	Spring Creek	135		7	155
17	Nez Perce Creek	148±5		6	148
18	Spruce Creek			3	142
19	Elephant Back	153±2		25	139
20	Aster Creek	155±3	150±5	10	114
21	Buffalo Lake	160±3		54	104
22	Mary Lake	165±4		2	50
23	West Thumb	173±11		11	48
24	**Bluff Point Tuff**	173±5		15	37
25	Dry Creek	166±9		9	22
26	Mallard Lake	164±14	225	13	13
	Unobserved units	167±5		256	256

7.1.1.2 Silicic Volcano Volumes in the Blackfoot Reservoir Volcanic Field

Seven Quaternary silicic domes and lava-flow complexes occur in the BRVF, which reflect two distinct episodes of silicic magmatism at 1.4–1.6 Ma and ≈60 ka (Section 2.6). Early stages of the youngest eruptions are characterized by periods of hydromagmatic activity, including formation of 2 small, cogenetic maars. Tephra deposits exposed in a quarry on the northern flank of China Hat dome are interpreted by McCurry et al. (2015) to represent the medial facies of a phreatomagmatic tuff cone, which contains interbedded sequences of flows and falls. Nevertheless, only 1% of magmatic pyroclasts in these deposits have significant vesiculation,

which McCurry et al. (2015) interpret as evidence of significant magma degassing prior to the eruption. Unlike most other Quaternary silicic rocks in the site region, the BRVF rhyolite has hydrous phenocrysts of hornblende and biotite that appear to have erupted in equilibrium with the magma (Ford, 2005). The absence of disequilibrium textures in these hydrous phenocrysts indicates that shallow degassing of the ascending magma must have occurred rapidly (McCurry et al., 2015). Except for the localized deposits of phreatomagmatic tephra, silicic tephra-fall deposits have not been observed in the BRVF. Volumes of BRVF silicic volcanoes are given in Table 32. Note that the 1.41 Ma Sheep Island rhyolite is not included in this compilation, because the lava flows represent multiple eruptive episodes and outcrops distributions are obscured by the Blackfoot Reservoir (Ford, 2005).

Table 32. Volumes of silicic volcanoes in the BRVF, from Ford (2005). Dome volumes corrected to DRE assuming bulk density is 85% of the magma density (i.e., Fink, 1990).

Volcano	*Age*	*DRE Vol. (m^3)*
N Dome West	1.59±0.06 Ma	3.8E+08
N Dome Middle	1.59±0.06 Ma	4.5E+07
N Dome South	1.59±0.06 Ma	2.3E+07
China Hat	57±8 ka	5.0E+08
China Cap	57±8 ka	1.5E+08
North Cone	57±8 ka	8.0E+07

7.1.1.3 Silicic Volcano Volumes in the Curlew Valley Volcanic Field

A sequence of rhyolitic lava flows is exposed in the Wildcat Hills, 4–10 km west of the Curlew Valley Quaternary basalts (Figure 8). At least four different silicic eruptions occurred in the Wildcat Hills at 4.9±0.4 Ma, 4.4±1.1 Ma, 3.6±0.1 Ma, and 2.1±0.06 Ma (Kerr, 1987; Miller et al., 1995). A $^{39}Ar/^{40}Ar$ date of 2.33±0.01 Ma confirms the Quaternary age of the youngest eruption (Felger et al., 2016). Nevertheless, the extent of Quaternary volcanic deposits has not been determined by previous investigations. Kerr (1987) describes pyroclastic rocks interbedded and adjacent to some rhyolite lava outcrops, which suggests that explosive eruptions occurred with at least some of the silicic eruptions. The Wildcat Hills rhyolite is a high-silica rhyolite (>75% SiO_2), with >5% K_2O, which Kerr (1987) interprets to represent partial crustal melts resulting from contemporaneous basaltic magmatism and intrusion in the area.

Based on Kerr (1987, Plate 1), the Wildcat Hills rhyolite has an approximate volume of 1 km^3 with thicknesses ranging from ≈60 m in northern exposures to ≈120 m in southern exposures. This volume suggests an average effusion rate of 1 km^3 in 2.8 Myr or ≈$4x10^{-4}$ km^3/kyr. Assuming the Quaternary rhyolite is 20% of the total volume of the Wildcat Hills indicates an eruption volume on the order of $2x10^8$ m^3.

7.1.1.4 Silicic Volcano Volumes in the Eastern Snake River Plain Volcanic Field

Several different types of silicic magmatism have occurred during the Quaternary Period in the ESRP volcanic field. The most prevalent type is the formation of rhyolite domes, which began with the 1.42±0.02 Ma eruption of Unnamed Butte (Kuntz and Dalrymple, 1979). Most of Unnamed Butte is buried by younger basaltic lava flows, and surface exposures indicate a volume >0.1 km^3. The 0.58±0.09 Ma (Armstrong et al., 1975) East Butte dome has a summit depression that has been interpreted as an eruptive crater (Spear, 1979) or a collapse feature related to late-stage magma withdrawal (Ganseke, 2006). Pyroclastic deposits have not been observed on or associated with East Butte. Nevertheless, East Butte is moderately eroded and

the base of the dome is buried by younger lava flows. The exposed volume of East Butte is on the order of >0.18 km^3. Big Southern Butte erupted at 0.304±0.022 Ma (Kuntz and Dalrymple, 1979), and has an estimated volume >8 km^3 (Kuntz et al., 1992). Big Southern Butte represents the progressive emplacement of a shallow rhyolitic laccolith, which continued to inflate, uplift roof rock, and eventually extrude rhyolite lava (Kuntz and Kork, 1978; Spear and King, 1982; McCurry et al., 1999). Remnants of pyroclastic deposits have been observed in the summit area, and a small block and ash flow occurs in shallow drill core north of Big Southern Butte (McCurry et al., 2008).

A second type of silicic magmatism in the ESRP formed cryptodomes, which resulted from the shallow (<1 km) intrusion of silicic magma. The shallow intrusion formed broad, dome-shaped laccoliths and associated uplift and surface deformation. A prominent cryptodome occurs in the ESRP at Middle Butte, which was formed by faulting and uplift of >1 Ma basaltic lavas due to emplacement of a shallow silicic intrusion (Kuntz and Kork, 1978; Spear and King, 1982; McCurry et al., 1999). Other prominent cryptodomes occur on the southeast margin of the ESRP at Buckskin Mesa and Ferry Butte (Kellogg and Marvin, 1988). Although these cryptodomes are related to silicic magmatism, the absence of eruptions precluded the formation of tephra-fall deposits. Consequently, cryptodomes do not represent sources of potential tephra-fall hazards at the proposed site.

Rhyolite lavas also erupted at 0.40±0.02 Ma as the earliest stage of activity at Cedar Butte (McCurry et al., 2008). During the ensuing stages of activity, Cedar Butte erupted increasing mafic lavas to form a broad, shield volcano that partially covers the early rhyolite, which has an estimated volume of ≈0.2 km^3 (Hayden, 1992; McCurry et al., 2008). No pyroclastic deposits have been observed with these rhyolitic lavas.

Table 33. Summary of silicic volcano volumes for the ESRP volcanic field. Data sources cited in text.

Volcano	*Age*	*DRE Vol. (m^3)*
Unnamed Butte	1.42±0.02 Ma	>1.0E+08
East Butte	0.58±0.09 Ma	>0.18E+08
Big Southern Butte	0.304±0.022 Ma	>8E+09
Cedar Butte	0.40±0.02 Ma	≈2E+08

7.1.1.5 Interpretation of Silicic Tephra Volumes

There is no clear correlation between the volume of a silicic dome or lava flow and the volume of an associated tephra-fall deposit (Section 7.1.1). Nevertheless, information from analogous volcanoes suggests that explosive eruptions might have occurred at silicic volcanoes in the site region. This interpretation is conservative, because the absence of preserved tephra deposits, preserved vent morphologies, observed rock characteristics, and magma compositions all indicate that explosive eruptions probably did not occur for most of these volcanoes.

In consideration of the multiple factors indicating effusive rather than explosive silicic eruption characteristics (e.g., lack of vesiculation or proximal pyroclastic deposits), the volume of potential silicic tephra falls in the site region appears reasonably represented by the lower end of the range of lava-to-fall volumetric relationships at analogue volcanoes (Table 30). Consequently, estimated tephra-fall volumes for Quaternary volcanoes in the site region are made by assuming that these deposits represented 5–25% of the Quaternary dome or lava flow volumes (Table 34). An upper volume of 25% allows for some uncertainty in the interpretation of

the older deposits in the site region (i.e., erosion or burial of possible early pyroclastic facies), while still being informed by the overall low-explosivity characteristics of the smaller-volume silicic volcanoes in the site region.

Table 34. Estimates of tephra-fall volumes for silicic volcanoes in the site region, based on assumed relationship to dome and lava flow volumes. Magma density of 2,400 kg/m^3, and deposit density of 800 kg/m^3 (i.e., Scott, 1987) used to calculate bulk volumes.

Volcano	*Effusive Vol DRE (m^3)*	*Bulk Tephra =5% DRE Effusive (m^3)*	*Bulk Tephra =25% DRE Effusive (m^3)*
BVF: N Dome West	3.8E+08	5.7E+07	2.9E+08
BVF: N Dome Mid	4.5E+07	6.8E+06	3.4E+07
BVF: N Dome South	2.3E+07	3.4E+06	1.7E+07
BVF: China Hat	5.0E+08	7.5E+07	3.8E+08
BVF: China Cap	1.5E+08	2.3E+07	1.1E+08
BVF: North Cone	8.0E+07	1.2E+07	6.0E+07
ESRP: Cedar Butte rhyo	2.0E+08	3.0E+07	1.5E+08
ESRP: Big Southern Bu	8.0E+09	1.2E+09	6.0E+09
ESRP: Unnamed	1.0E+08	1.5E+07	7.5E+07
ESRP: East Butte	1.8E+08	2.6E+07	1.3E+08
CV: Wildcat Hills	2.0E+08	3.0E+07	1.5E+08
YS: CPR low	1.0E+08	1.5E+07	7.5E+07
YS: CPR High	7.0E+10	1.1E+10	5.3E+10
YS: Tuff low	3.0E+09	4.5E+08	2.3E+09
YS: Tuff High	1.5E+10	2.3E+09	1.1E+10

A general pattern can be observed for the volume estimates in Table 34. The domes and lavas in the BRVF, CVVF, and ESRP might have produced tephra-fall deposits on the order of 10^7–10^8 m^3, which would represent VEI2–3 eruptions (Newhall and Self, 1982). Note that although the Big Southern Butte eruption exceeds this range, the lack of significant pyroclastic deposits strongly indicates that a VEI4 estimate for tephra-fall volume would be unrealistically large. In comparison, the two comparable-volume CPR pyroclastic eruptions in the YVF produced recognized tephra falls and flows. Consequently, Big Southern Butte appears reasonably represented by VEI2–3 eruptions.

The CPR in the YVF has a relatively large range of eruption volumes (Table 31). Many of CPR magmas contain 10–30% phenocrysts, and erupted at significantly lower temperatures (750–800ºC) and higher volatile contents (1–2.5 wt% H_2O) than interpreted for BRVF, CVVF, and ESRP magmas (i.e., Befus and Gardner, 2016). Nevertheless, distributed pyroclastic deposits are not associated with CPR dome and lava-flow eruptions. Considering the potentially higher volatile contents in CPR magmas, and higher viscosities due to lower eruption temperatures and higher crystallinities, these eruptions might have produced tephra-fall deposits on the order of 10^8–10^9 m^3. These volumes correspond to VEI3–4 eruptions (i.e., Newhall and Self, 1982). Note that although the largest CPR eruptions exceed this range, the lack of significant pyroclastic deposits from those eruptions strongly indicates that a VEI5 estimate for tephra-fall volume would be unrealistically large. In comparison, the two smaller-volume CPR pyroclastic eruptions produced recognized tephra falls and flows. Consequently, the upper bound on the CPR appears reasonably represented by VEI4 eruptions.

The two CPR pyroclastic eruptions deposited ash up to 250 km from the likely vent location. However, descriptions of the near-vent deposits do not identify tephra-fall deposits underlying the pyroclastic flows (Christiansen and Blank Jr., 1972; Christiansen, 2001; Christiansen et al., 2007), which suggests the distal ashes might originate from co-ignimbrite plumes rather than Plinian tephra-fall processes. Nevertheless, a reasonable assumption is that future VEI4–5 pyroclastic eruptions (i.e., volumes 10^9 to 10^{10} m^3) might occur in the CPR, because two relatively large volume (3–10 km^3 DRE) silicic pyroclastic eruptions occurred in the CPR since ~150 ka.

7.2 Power and Duration of Silicic Eruptions

The *Power* and *Duration* of silicic tephra-fall eruptions is determined using the same methodology discussed for mafic tephra-fall eruptions in Section 6.3.2. The range of VEI-specific tephra volumes for silicic eruptions was converted to bulk-fall volumes using a deposit density of 800 kg/m^3 and magma density of 2,400 kg/m^3 (i.e., Scott, 1987). The eruption *Duration* was adjusted until the range of column heights, eruption *Power*, and calculated fall-deposit volumes was reasonably consistent with the characteristic VEI range (Table 35).

Table 35. Calculated eruption *duration* and *power* for VEI eruptions that are representative of silicic tephra-fall eruptions in the site region.

VEI	DRE Fall vol. (m^3)	Bulk Fall vol. (m^3)	Calc. vol. (m^3)	Duration (sec)	Power (W)	Calc. Column H (km)
2–3 Lower	1.0E+07	3.0E+07	9.3E+06	1.0E+04	7.0E+11	10.9
2–3 Upper	1.0E+08	3.0E+08	1.3E+08	5.0E+04	2.0E+12	13.0
3–4 Lower	1.0E+08	3.0E+08	1.3E+08	5.0E+04	2.0E+12	13.0
3–4 Upper	1.0E+09	3.0E+09	2.6E+09	1.0E+05	2.0E+13	19.8
4–5 Lower	1.0E+09	3.0E+09	2.0E+09	5.0E+04	3.0E+13	23.7
4–5 Upper	1.0E+10	3.0E+10	1.6E+10	1.0E+05	1.2E+14	35.9

7.3 Total Grain-Size Distributions for Silicic Tephra Deposits

A compilation of total grain-size characteristics for tephra-fall deposits by Costa et al. (2016) included 3 silicic tephra-fall deposits that had measured median diameters and sorting from field data (Table 36). Using the same approach from Costa et al. (2016) as used in Section 6.3.3, total grain-size distributions for analogue silicic volcanoes also are calculated, using reported eruption column heights. Viscosities for these magmas are calculated using the methodology from McBirney and Murase (1984) for reported compositions.

Table 36. Median diameter and sorting characteristics for silicic tephra-fall deposits, after Costa et al. (2016). "Calculated" uses column height-magma viscosity relationships (Costa et al., 2016) to calculate grain-size characteristics for analogue volcanoes with reported eruption column heights. Values in "( )" are characteristics for VEI3–5 eruptions from the YVF. Data sources listed in Table 30.

Silicic	*Median diameter Log cm*	*Sorting Log cm*	Col Height (km)	Viscosity (log Pa s)
Cordon Calle	-0.5	2.0		
Askja 1875 C	-1.6	1.8		
Askja 1875 D	-0.1	3.9		
Calculated				
Cordon Caulle 2011	-1.1	1.5	12	4.4
Medicine Lake	-1.1	0.1	7	5.2
S Sister	-1.2	1.3	6	5.3
S Sister	-1.1	1.4	10	5.3
Newberry	-1.1	1.9	18	5.1
Mono - Hi	-1.2	1.3	7	5.2
Mono - Low	-1.1	1.4	10	5.3
ASHPLUME2 Parameters				
Dmeanmin	-1.8 (-2.0)			
Dmeanmed	-1.2 (-1.4)			
Dmeanmax	-0.6 (-0.8)			
DSigmamin		1.0		
DSigmamax		2.0 (3.0)		

These data are used to estimate the range of median diameters and sorting for the mafic eruption calculations in ASHPLUME2. For higher explosivity eruptions in the YVF (i.e., VEI3–5), the median diameters are decreased to capture expected (i.e., Costa et al., 2016) increases in fragmentation for high-silica rhyolite eruptions with column heights >20 km. As shown in Costa et al. (2016), small variations in magma viscosity and eruption column height (i.e., 5–10 km) would have only a minor (<10%) effect on the calculated median diameter and sorting for a deposit. In contrast, the range encompassed for the median diameters (*Dmean*) and sorting (*DSigma*) significantly exceeds the variations resulting from relatively small changes in magma viscosity and column height among the characteristic silicic eruptions in the site region.

Silicic tephra densities will be lower than observed for mafic tephra, due to the lower density of rhyolitic magma (typically 2.4 g/cm^3 vs 2.7 g/cm^3 for basalt) and larger degree of vesiculation in coarser particles. Particle densities are reported for several analogue volcanoes in Table 37.

Table 37. Densities of tephra particles reported for analogue volcanoes in Table 30.

Volcano	Density (low) g/cm^3	Density (high) g/cm^3	Source
Inyo Craters	0.2	1.0	Nawotniak and Bursik (2010)
Newberry	0.9	2.4	Gardner et al. (1998)
Cordon Caulle	1.0	2.2	Colloni et al. (2013)

The low reported density at Inyo Craters reflects the abundance of large pumice fragments near the vent, which are much coarser grained than the particles that represent median diameters (i.e., 0.06 cm). Using a magma density of 2.4 g/cm^3 (McBirney and Murase, 1984), an aphyric particle with 80% vesicularity would have a density of ~0.5 g/cm^3. Fine-grained particles (i.e., <0.06 cm) will have lower vesicularities and higher densities, until near-magmatic density is reached for nonvesiculated shards. Consequently, average particle densities ranging from 1.0 g/cm^3 to 2.0 g/cm^3 appear reasonable for silicic tephra particles used in the VHA.

7.4 Wind Speed Data for Silicic Tephra Hazards Analyses

Using the same approach discussed in Section 6.3.4, the distribution of Quaternary silicic volcanoes is used to determine wind sectors, which included consideration in the potential locations of new vents around the periphery of the volcanic field. These sectors encompass azimuths of 339º–22º for the YVF, and 246º–293º for the CVVF (Figure 32). The same wind information that was used in the mafic tephra-fall hazard analyses for the ESRP and BRVF is used for the silicic analyses. This approach is conservative, as the sector that encompasses potential silicic vents is smaller than the sector encompassing the entire mafic volcanic field. Summary statistics are presented in Table 38 for the wind-speed data used in the silicic tephra-fall analyses.

Table 38. Wind speed statistics for atmospheric pressure levels and volcanic fields that are used in the ASHPLUME2 analysis for silicic tephra-fall hazards. *H* is altitude for corresponding pressure level, *Avg Speed* is the average of the log-normal distribution, *Std Dev* is the standard deviation of the log-normal distribution, $+2\sigma$ is the calculated 95th percentile wind speed based on the standard deviation, *Max Spd* is the maximum speed observed in the data, *Sector%* is the percentage of time the wind is directed from this sector to the proposed Natrium™ site, and *Lambda* is the inverse of the average wind speed.

Level (mbar)	*H (km)*	*Avg Speed (m/s)*	*Std Dev (m/s)*	*+2σ (m/s)*	*Max Spd (m/s)*	*Sector %*	*Lambda (cm/s)*
YVF: 339º–22º sector							
850	1.5	2.4	2.1	10.1	12.2	4.7	0.004214
500	5.6	11.7	2.0	44.8	42.2	6.5	0.000855
250	10.4	21.8	1.9	82.0	74.5	7.4	0.000449
100	15.8	7.7	2.0	29.4	28.2	2.0	0.001304
50	19.3	4.0	2.0	15.3	32.3	8.7	0.002521
10	25.9	12.0	2.4	68.2	80.1	8.7	0.000835
CVVF: 246º–293º sector							
850	1.5	4.2	1.8	14.0	14.5	29.4	0.002409
500	5.6	13.7	1.7	40.6	44.9	38.1	0.000732
250	10.4	24.6	1.7	69.3	80.5	37.1	0.000406
100	15.8	13.4	1.6	35.7	51.9	51.7	0.000747
BRVF: 315º–340º sector							
850	1.5	2.8	2.0	11.4	12.3	7.6	0.003560
500	5.6	13.4	1.9	47.5	45.9	13.7	0.000744
250	10.4	23.7	1.9	84.3	76.7	14.6	0.000422
100	15.8	10.7	1.8	35.0	40.4	7.0	0.000937
ESRP: 292º–340º sector							
850	1.5	3.3	2.3	13.0	13.7	12.9	0.003012

Level (mbar)	*H (km)*	*Avg Speed (m/s)*	*Std Dev (m/s)*	*+2σ (m/s)*	*Max Spd (m/s)*	*Sector %*	*Lambda (cm/s)*
500	5.6	13.9	1.8	45.7	45.9	23.9	0.000719
250	10.4	24.3	1.8	79.7	76.7	22.7	0.000412
100	15.8	12.6	1.7	37.3	41.6	20.5	0.000791

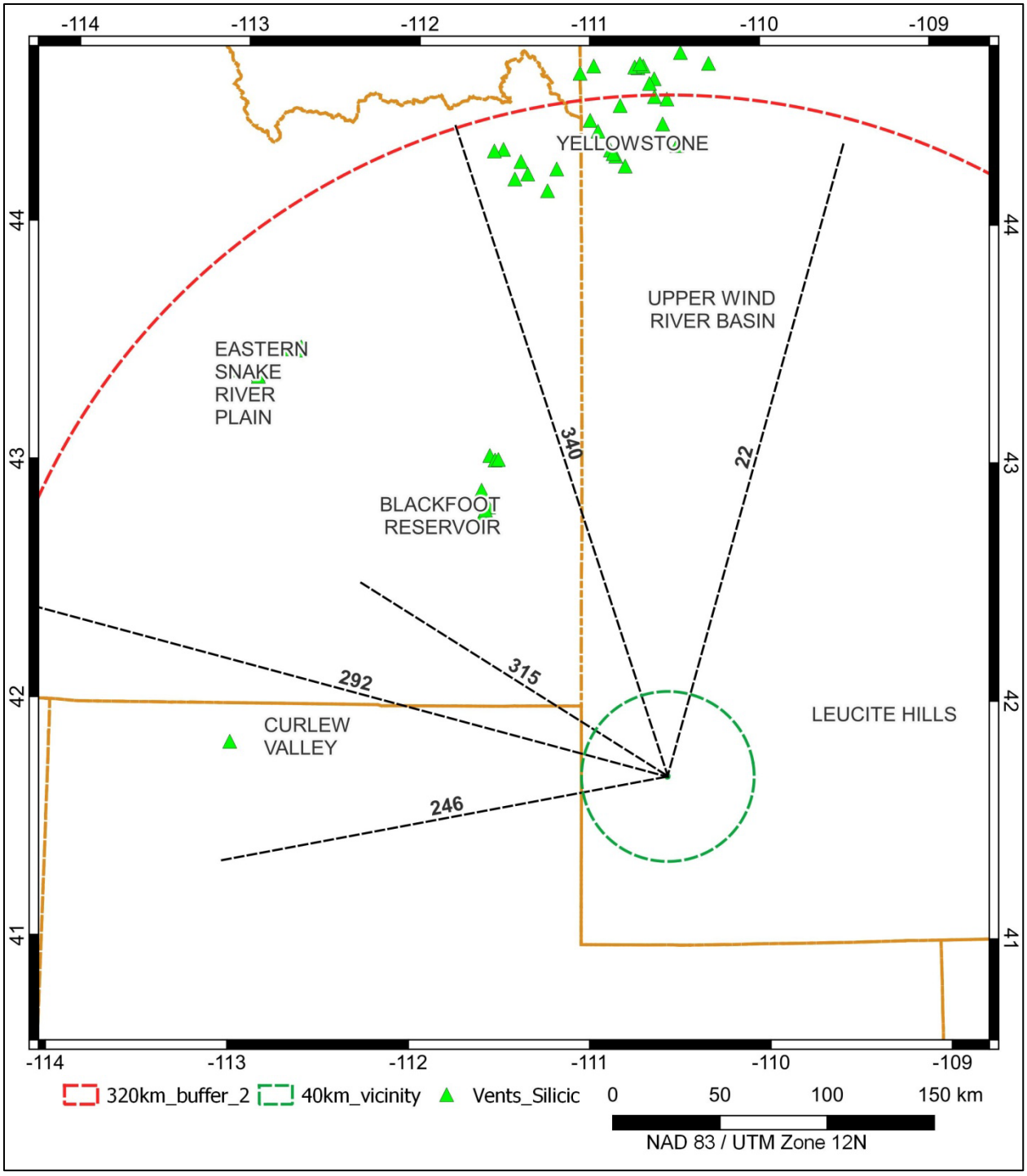

Figure 32. Regional wind sectors used for silicic tephra-fall hazards analyses.

7.5 Summary of Input Parameters for Silicic Tephra Hazards Analyses

Based on the information discussed in Sections 7.1–7.3, input parameters for the ASHPLUME2 code are summarized in Table 39. The distances for the BRVF and ESRP reflect the localization of silicic eruptions within these broadly distributed mafic volcanic fields.

Table 39. Input parameters for ASHPLUME2 analysis of silicic tephra-fall hazards.

Parameter	**BRVF VEI2–3**	**CVVF VEI2–3**	**ESRP VEI2–3**	**YSVF VEI3–4**	**YSVF VEI4–5**
x min (km) distance	150	200	260	280	280
x max (km) distance	170	210	280	320	320
y min (km) distance	0	0	0	0	0
y max (km) distance	0	0	0	0	0
nptsx = # of points x	11	11	11	11	11
nptsy = # of points y	1	1	1	1	1
t log min (s)	4.0	4.0	4.0	4.7	4.7
t log max (s)	4.7	4.7	4.7	5.0	5.0
Power log min (W)	11.8	11.8	11.8	12.3	13.5
Power log max (W)	12.3	12.3	12.3	13.3	14.1
Beta log min	0.4			1	
Beta log max	1			1.3	
D meanmin (log cm)	-1.8			-2.0	
D meanmed (log cm)	-1.2			-1.4	
D meanmax (log cm)	-0.6			-0.8	
D sigma min	1.0			1.0	
D sigma max	2.0			3.0	
AshDensity min (g/cm3)	1				
AshDensity max (g/cm3)	2.2				
Ash rho low	-2				
Ash rho high	-1				
fshape	0.5				
Airdens, visc	0.001293d0 1.8d-04				
C cm2/s5/2	400				
D max (cm)	10				
Hmin (km)	0.01				
a cutoff (g/cm2)	1d-10d0				
rho cut	1				
Uran (g) mass fuel	0				

7.6 Silicic Tephra-Fall Hazards at the Proposed Natrium™ Site

Following the approach presented in Section 6.4, silicic tephra-fall hazards are calculated using the ASHPLUME2 code and input parameters described in Section 7.5 for each of the four volcanic fields that have the potential to produce tephra falls from VEI2–5 silicic eruptions. The

ensuing sections will present the conditional tephra-fall hazards for each of these fields, then develop a probabilistic framework to determine the likelihood i) of a future silicic eruption; ii) that the eruption will form tephra-fall deposits; and iii) that regional winds are directed from the eruption source to the proposed site. These analyses develop fully probabilistic tephra-fall hazard curves for each of the four volcanic fields, which are integrated into a total tephra-fall hazard assessment for the proposed site.

7.6.1 Silicic Tephra-fall Hazards for the Blackfoot Reservoir Volcanic Field

Potential silicic volcanoes for the BRVF are located 150–170 km from the proposed Natrium™ site, in the trans-tensional structural zone that localized the 57 ka eruptions. To account for spatial variability in vent locations, 1,000 ASHPLUME realizations were conducted every 2 km along a 20-km-long axis, for a total of 11,000 realizations.

Results of the ASHPLUME hazard calculations are presented in Table 40 and Figure 33. The calculated range of deposit volumes ($8.5x10^6$–$1.2x10^8$ m^3) corresponds reasonably to the interpreted range of deposit volumes for the BRVF (Table 34; $3x10^6$–$4x10^8$ m^3), and the calculated range of eruption column heights (7.3–9.7 km) compares reasonably with the interpreted range of column heights for VEI2–3 eruptions (Table 35; 10.9–13.0 km). The calculated tephra-fall deposit thicknesses form a log-normal distribution, which is reflected in the summary statistics (Table 40). As discussed in Section 1.1, average and 95th percentile deposit thicknesses are calculated for use in the evaluation of potential event sequences (e.g., Nuclear Regulatory Commission, 2020).

Table 40. Summary of ASHPLUME2 calculations for BRVF silicic tephra hazards.

	Power (W)	*Duration (s)*	*Deposit Volume (m^3)*	*Col H (km)*	*Wind (km/hr)*	*Deposit Thick (cm)*
Avg	1.2E+12	2.5E+04	3.9E+07	8.5	82	0.034
Min	6.3E+11	1.0E+04	8.5E+06	7.3	0.05	1.25E-10
Max	2.0E+12	5.0E+04	1.2E+08	9.7	303	2.69
95th percentile thickness: 0.94 cm						

As would be expected, the thickest calculated deposits at the proposed site result from the largest eruption volumes (Figure 33A), the highest eruption columns (Figure 33B), and the fastest wind speeds (Figure 33C). The conditional tephra-fall hazard curve is shown in Figure 33D, which yields a 95th percentile deposit thickness of 0.94 cm. Note that this amount of tephra-fall assumes that i) a silicic eruption occurs in the BRVF volcanic field, ii) the eruption produces a buoyant tephra plume, and iii) the prevailing wind is directed from the BRVF vent towards the proposed Natrium™ site.

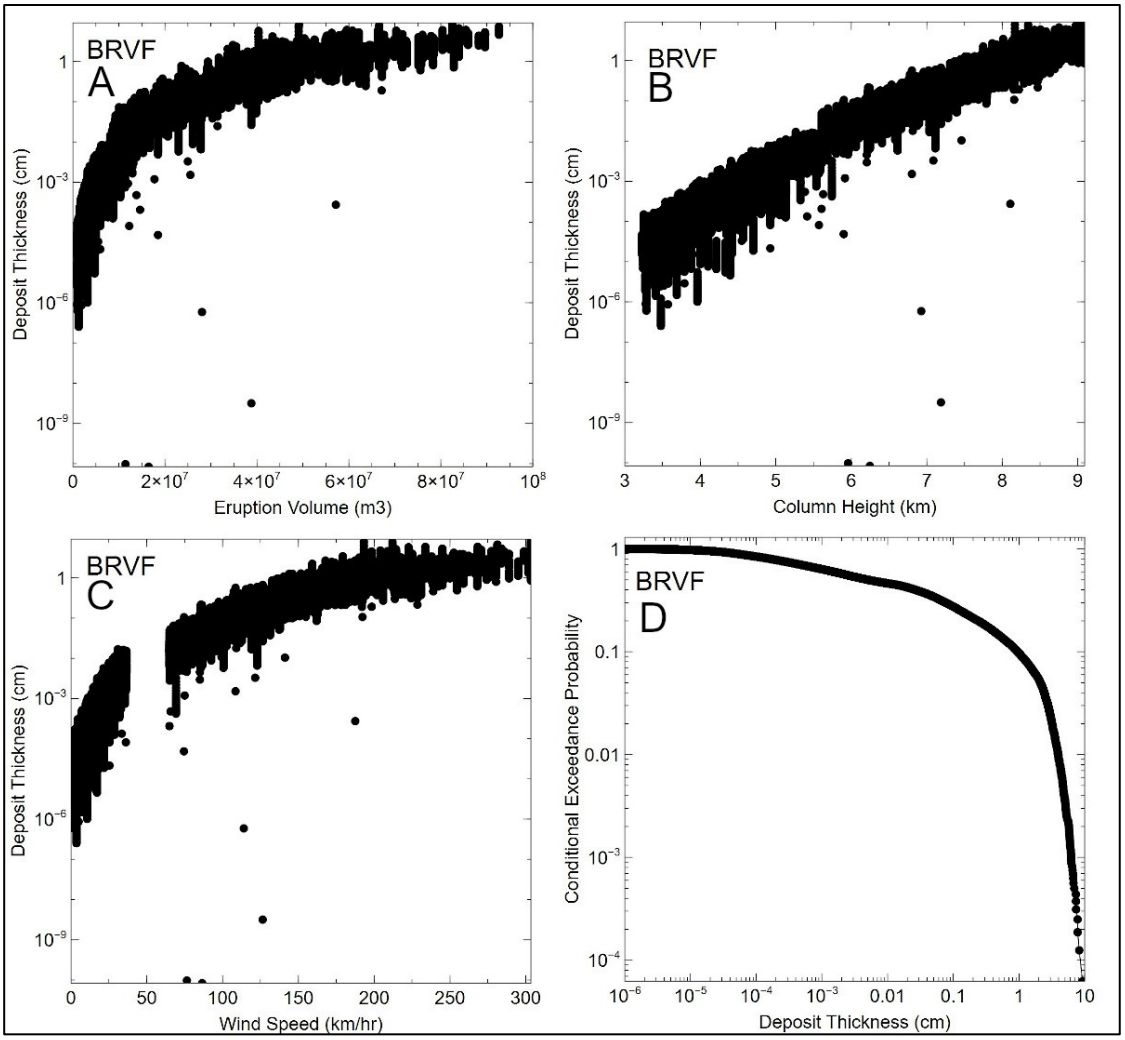

Figure 33. Results of silicic tephra-fall hazard calculations for BRVF eruption sources.

To calculate a fully probabilistic tephra-fall hazard curve for potential BRVF silicic eruption sources, the following three probabilities must be determined:

1) *Probability of a future silicic eruption in the BRVF:*

There have been 7 silicic eruptive events in the BRVF since 1.6 Ma, with each vent representing a single eruptive event (Section 7.1.1.2), which represents a recurrence rate of 4.4×10^{-6}/yr. Using a 4.4×10^{-6}/yr recurrence rate in Equation 4 results in an annual probability of 4.4×10^{-6}/yr for a future silicic eruption in the BRVF. As an additional perspective on reasonableness of this probability value, there is a >99% likelihood that no events would have occurred in the BRVF since the last activity at 57 ka (i.e., age of youngest rhyolite dome), if these eruptions were randomly distributed in time with a 4.4×10^{-6}/yr recurrence rate (i.e., Equation 4).

2) Probability the BRVF silicic eruption will be VEI2–3

The silicic tephra-fall hazard analyses for the BRVF assume conservatively that all future silicic eruptions (100%) will have VEI2–3 eruption explosivity and produce tephra falls.

3) Probability that winds will be directed from BRVF to proposed site

The calculated column heights for the 11,000 realizations were binned into the corresponding altitude ranges used in the ASHPLUME2 model, and used to calculate a weighted value for each altitude range (Table 41). This weight is applied to the percentage of time the winds in each altitude range are directed towards the site (i.e., from the corresponding sector in Table 38**)**, and used to calculate a weighted percentage for the amount of time the wind in each altitude range is directed toward the site. The sum of the weighted percents shows that for the 11,000 BRVF realizations, 7.4% of the eruptions would have had winds directed towards the proposed site.

Table 41. Probability that winds from BRVF silicic eruptions are directed towards the proposed site.

Bin (km)	*Frequency*	Weight	Sector %	Weight Percent
1.5	0	0%	4.7%	0.00%
5.6	0	0%	6.5%	0.00%
10.4	10986	100%	7.4%	7.40%
15.8	0	0%	2.0%	0.00%
			Winds to Site 7.4%	

Thus, the probability of a tephra-fall eruption from a future eruption from the BRVF volcanic field is

$$4.4\text{x}10^{-6}\text{/yr x 1 x 0.074} = 3.3\text{x}10^{-7}\text{/yr,}$$

which is then multiplied by the conditional probability of exceedance for tephra-deposit thickness, to generate the exceedance probabilities for mafic tephra-falls from the BRVF (Figure 34). There is $1.6\text{x}10^{-8}$/yr probability of exceeding the 95th percentile thickness of 0.94 cm, and a $1.7\text{x}10^{-7}$/yr probability of exceeding the average thickness of 0.034 cm. No tephra-fall hazard occurs at an exceedance probability of $5\text{x}10^{-7}$/yr, which represents the smallest likelihood for a potential initiating event associated with beyond-design-basis event sequences (Nuclear Energy Institute, 2019).

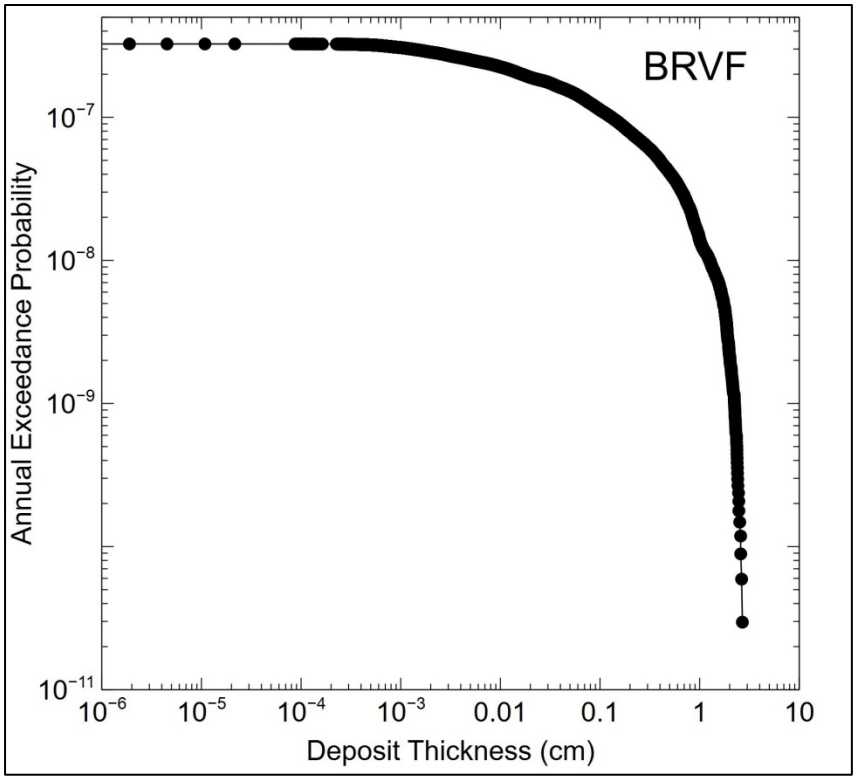

Figure 34. Annual exceedance probabilities for silicic tephra-fall hazards from the BRVF.

7.6.2 Silicic Tephra-fall Hazards for the Curlew Valley Volcanic Field

Silicic vents for the CVVF are located 200–210 km from the proposed Natrium™ site, in the area of Wildcat Hills. To account for spatial variability in potential vent locations, 1,000 ASHPLUME realizations were conducted every 1 km along a 10-km-long axis, for a total of ≈11,000 realizations.

Results of the ASHPLUME hazard calculations are presented in Table 42 and Figure 35. The calculated range of deposit volumes ($8.6x10^6$–$1.3x10^8$ m^3) corresponds reasonably to the interpreted range of deposit volumes for the CVVF (Table 34; $3x10^7$–$1.5x10^8$ m^3), and the calculated range of eruption column heights (7.3–9.7 km) compares reasonably with the interpreted range of column heights for VEI2–3 eruptions (Table 35; 10.9–13.0 km). The calculated tephra-fall deposit thicknesses form a log-normal distribution, which is reflected in the summary statistics (Table 42).

Table 42. Summary of ASHPLUME2 calculations for CVVF silicic tephra hazards.

	Power (W)	*Duration (s)*	*Deposit Volume (m^3)*	*Col H (km)*	*Wind (km/hr)*	*Deposit Thick (cm)*
Avg	1.2E+12	2.5E+04	3.9E+07	8.5	83	0.019
Min	6.3E+11	1.0E+04	8.6E+06	7.3	0.10	1.25E-10
Max	2.0E+12	5.0E+04	1.3E+08	9.7	290	2.38
95^{th} percentile thickness: 0.59 cm						

As would be expected, the thickest calculated deposits at the proposed site result from the largest eruption volumes (Figure 35A), the highest eruption columns (Figure 35B), and the fastest wind speeds (Figure 35C). The conditional tephra-fall hazard curve is shown in Figure 35D, which yields a 95th percentile deposit thickness of 0.59 cm. Note that this amount of tephra-fall assumes that i) a silicic eruption occurs in the CVVF volcanic field, ii) the eruption produces a buoyant tephra plume, and iii) the prevailing wind is directed from the CVVF vent towards the proposed Natrium™ site.

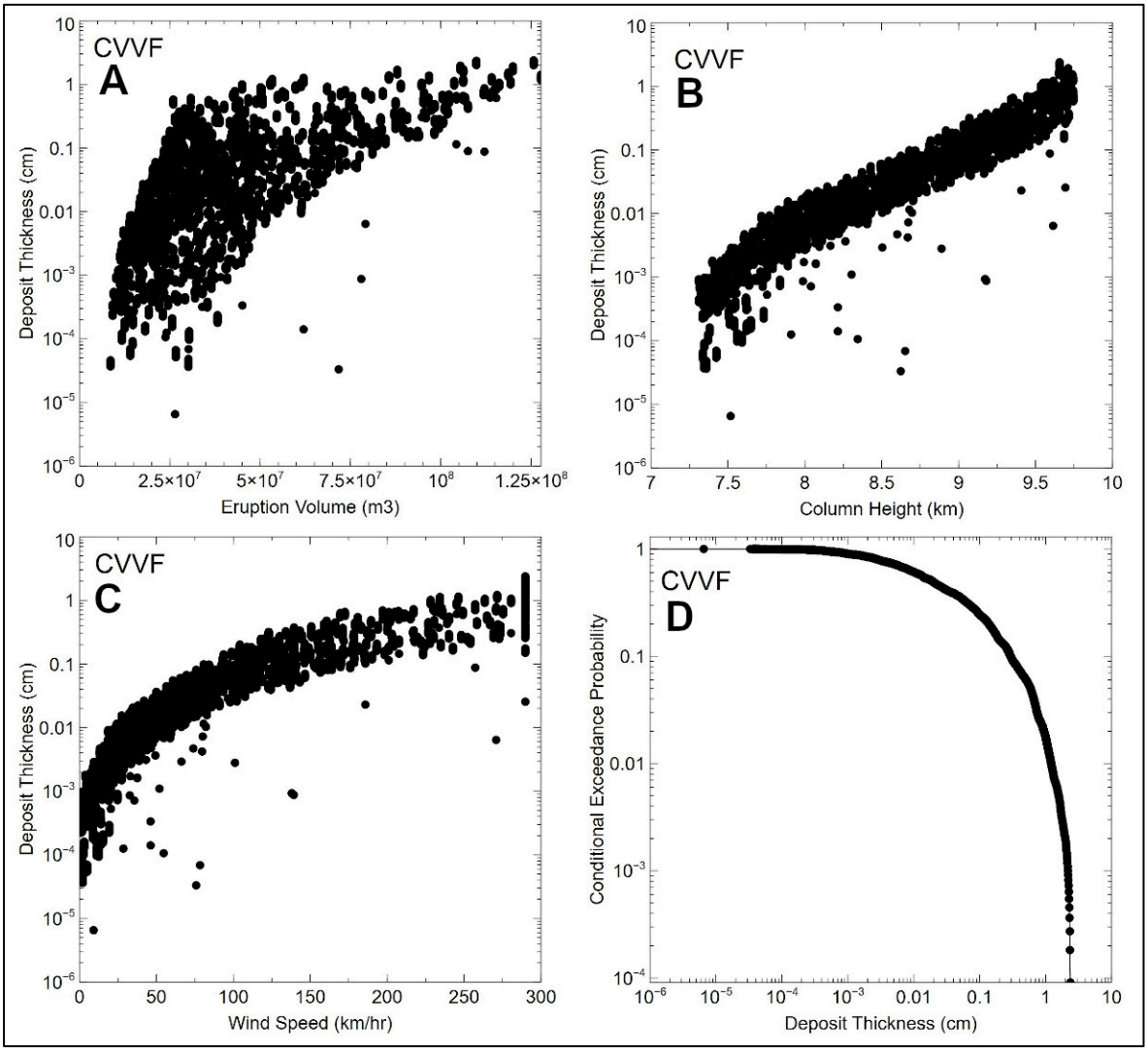

Figure 35. Results of silicic tephra-fall hazard calculations for CVVF eruption sources.

To calculate a fully probabilistic tephra-fall hazard curve for potential CVVF silicic eruption sources, the following three probabilities must be determined:

1) *Probability of a future silicic eruption in the CVVF:*

There have been 4 silicic eruptive events in the CVVF since 4.9 Ma, (Section 7.1.1.3), which represents a recurrence rate of 8.2x10^{-7}/yr. Using a 8.2x10^{-7}/yr recurrence rate in Equation 4 results in an annual probability of 8.2x10^{-7}/yr for a future silicic eruption in the

CVVF. As an additional perspective on reasonableness of this probability value, there is an 18% likelihood that no events would have occurred in the CVVF since the last activity at 2.1 Ma (i.e., age of youngest rhyolite), if these eruptions were randomly distributed in time with an 8.2×10^{-7}/yr recurrence rate (i.e., Equation 4).

2) Probability the CVVF silicic eruption will be VEI2–3

The silicic tephra-fall hazard analyses for the CVVF assume conservatively that all future silicic eruptions (100%) will have VEI2–3 eruption explosivity and produce tephra falls.

3) Probability that winds will be directed from CVVF to proposed site

The calculated column heights for the 11,000 realizations were binned into the corresponding altitude ranges used in the ASHPLUME2 model, and used to calculate a weighted value for each altitude range (Table 43). This weight is applied to the percentage of time the winds in each altitude range are directed towards the site (i.e., from the corresponding sector in Table 38**)**, and used to calculate a weighted percentage for the amount of time the wind in each altitude range is directed toward the site. The sum of the weighted percents shows that for the 11,000 ASHPLUME2 realizations, 37.1% of the eruptions would have had winds directed towards the proposed site.

Table 43. Probability that winds from CVVF silicic eruptions are directed towards the proposed site.

Bin (km)	*Frequency*	Weight	Sector %	Weight Percent
1.5	0	0%	29.4%	0.00%
5.6	0	0%	38.1%	0.00%
10.4	10971	100%	37.1%	37.10%
15.8	0	0%	51.7%	0.00%
			Winds to Site 37.1%	

Thus, the probability of a tephra-fall eruption from a future eruption from the CVVF volcanic field is

$$8.2 \times 10^{-7}\text{/yr} \times 1 \times 0.371 = 3.0 \times 10^{-7}\text{/yr},$$

which is then multiplied by the conditional probability of exceedance for tephra-deposit thickness, to generate the exceedance probabilities for silicic tephra-fall hazards from the CVVF (Figure 36).

There is 1.5×10^{-8}/yr probability of exceeding the 95th percentile thickness of 0.59 cm, and a 1.5×10^{-7}/yr probability of exceeding the average thickness of 0.019 cm. No tephra-fall hazard occurs at an exceedance probability of 5×10^{-7}/yr, which represents the smallest likelihood for a potential initiating event associated with beyond-design-basis event sequences (Nuclear Energy Institute, 2019).

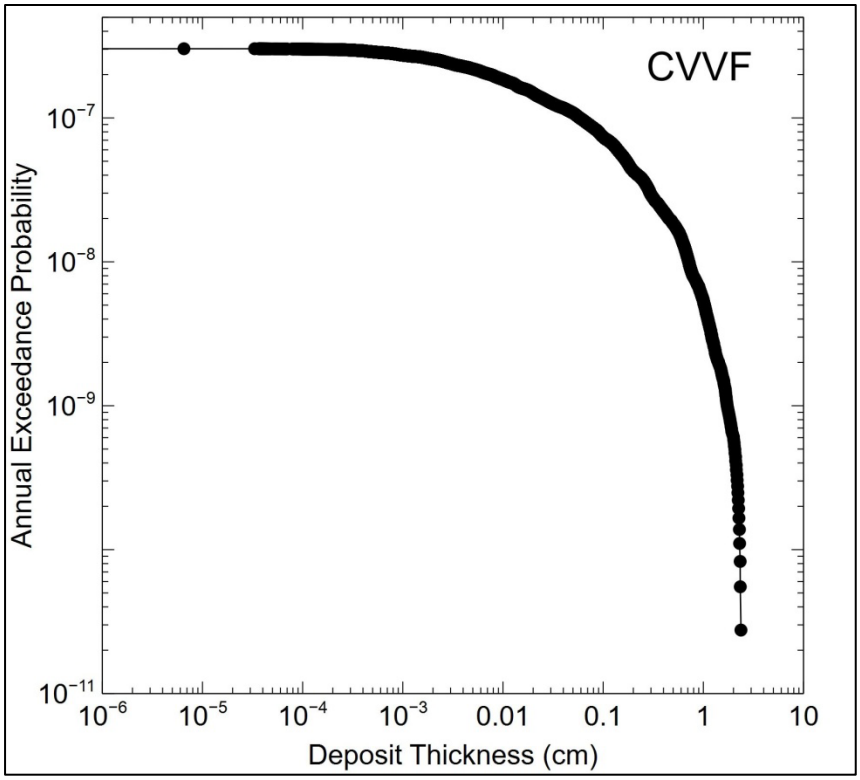

Figure 36. Tephra-fall hazard curve for CVVF volcanic field silicic eruptions.

7.6.3 Silicic Tephra-fall Hazards for the Eastern Snake River Plain Volcanic Field

Silicic vents for the ESRP are located 260–280 km from the proposed Natrium™ site, in the area of the Axial Volcanic Zone (e.g., Figure 12). To account for spatial variability in potential vent locations, 1,000 ASHPLUME realizations were conducted every 2 km along a 20-km-long axis, for a total of ≈11,000 realizations.

Results of the ASHPLUME hazard calculations are presented in Table 44 and Figure 37. The calculated range of deposit volumes ($8.7x10^6$–$1.3x10^8$ m^3) corresponds reasonably to the interpreted range of deposit volumes for the ESRP (Table 34; $1.5x10^7$–$1.5x10^8$ m^3). Note that the estimated tephra volumes for Big Southern Butte in Table 34 were interpreted as unrealistic, and are not used in these analyses. The calculated range of eruption column heights (7.3–9.7 km) compares reasonably with the interpreted range of column heights for VEI2–3 eruptions (Table 35; 10.9–13.0 km). The calculated tephra-fall deposit thicknesses form a log-normal distribution, which is reflected in the summary statistics (Table 44).

Table 44. Summary of ASHPLUME2 calculations for ESRP silicic tephra hazards.

	Power (W)	*Duration (s)*	*Deposit Volume (m^3)*	*Col H (km)*	*Wind (km/hr)*	*Deposit Thick (cm)*
Avg	1.2E+12	2.4E+04	3.8E+07	8.5	84	0.008
Min	6.3E+11	1.0E+04	8.7E+06	7.3	0.1	1.25E-10
Max	2.0E+12	5.0E+04	1.3E+08	9.7	286	1.07
95^{th} percentile thickness: 0.21 cm						

As would be expected, the thickest calculated deposits at the proposed site result from the largest eruption volumes (Figure 37A), the highest eruption columns (Figure 37B), and the fastest wind speeds (Figure 37C). The conditional tephra-fall hazard curve is shown Figure 37D, which yields a 95th percentile deposit thickness of 0.21 cm. Note that this amount of tephra-fall assumes that i) a silicic eruption occurs in the ESRP volcanic field, ii) the eruption produces a buoyant tephra plume, and iii) the prevailing wind is directed from the ESRP vent towards the proposed Natrium™ site.

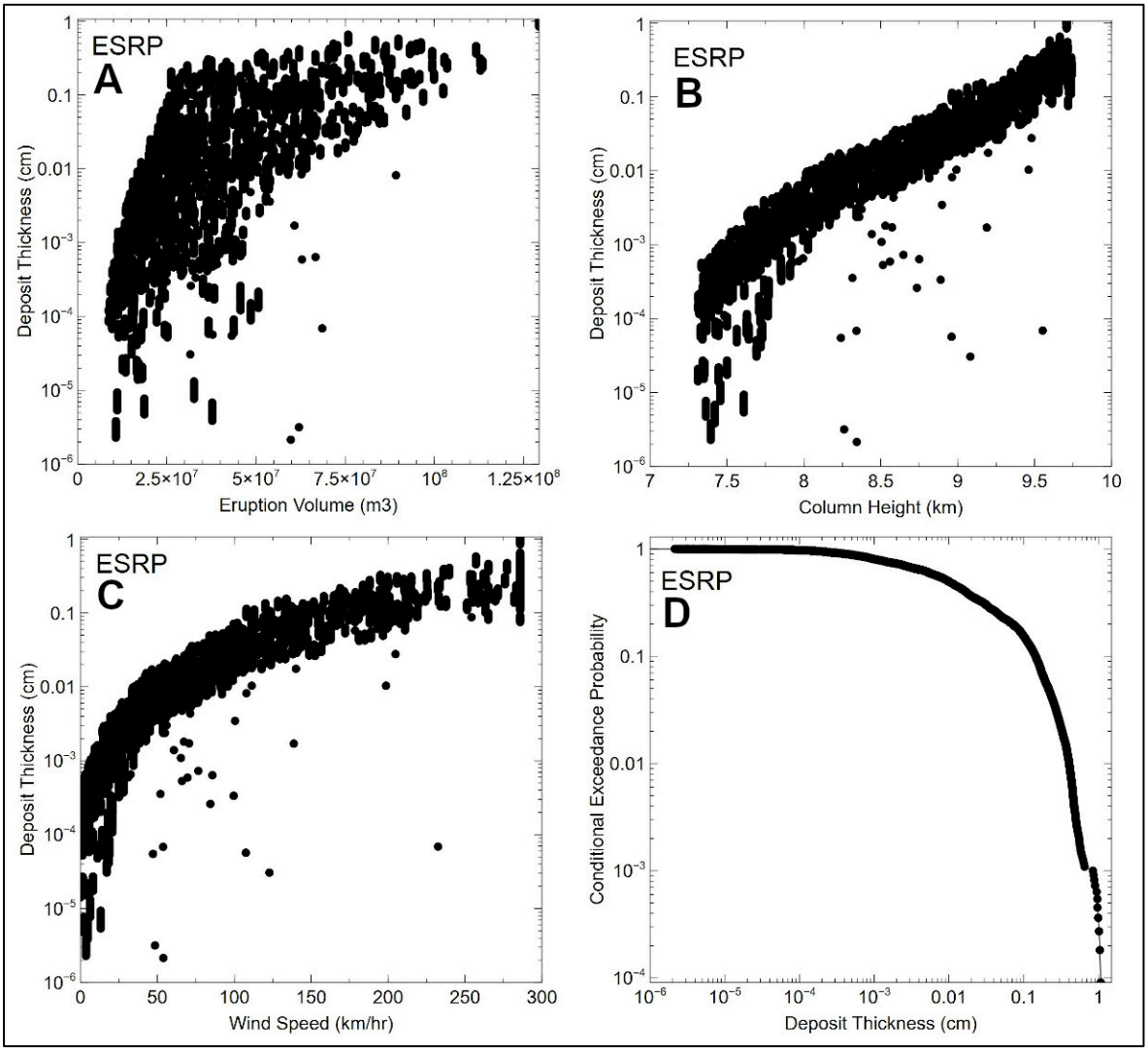

Figure 37. Results of silicic tephra-fall hazard calculations for ESRP eruption sources.

To calculate a fully probabilistic tephra-fall hazard curve for potential ESRP silicic eruption sources, the following three probabilities must be determined:

1) *Probability of a future silicic eruption in the ESRP:*

There have been 4 silicic eruptive events in the ESRP since 1.42 Ma, (Section 7.1.1.4), which represents a recurrence rate of 2.8x10^{-6}/yr. Using a 2.8x10^{-6}/yr recurrence rate in Equation 4 results in an annual probability of 2.8x10^{-6}/yr for a future silicic eruption in the

ESRP. As an additional perspective on reasonableness of this probability value, there is a 40% likelihood that no events would have occurred in the ESRP since the last activity at 0.304 Ma (i.e., age of youngest rhyolite), if these eruptions were randomly distributed in time with a 2.8×10^{-6}/yr recurrence rate (i.e., Equation 4).

2) Probability the ESRP silicic eruption will be VEI2–3

The silicic tephra-fall hazard analyses for the ESRP assume conservatively that all future silicic eruptions (100%) will have VEI2–3 eruption explosivity and produce tephra falls.

3) Probability that winds will be directed from the ESRP to the proposed site

The calculated column heights for the 11,000 realizations were binned into the corresponding altitude ranges used in the ASHPLUME2 model, and used to calculate a weighted value for each altitude range (Table 45). This weight is applied to the percentage of time the winds in each altitude range are directed towards the site (i.e., from the corresponding sector in Table 38**)**, and used to calculate a weighted percentage for the amount of time the wind in each altitude range is directed toward the site. The sum of the weighted percents shows that for the 11,000 ASHPLUME2 realizations, 22.7% of the eruptions would have had winds directed towards the proposed site.

Table 45. Probability that winds from ESRP silicic eruptions are directed towards the proposed site.

Bin (km)	*Frequency*	Weight	Sector %	Weight Percent
1.5	0	0%	12.9%	0.00%
5.6	0	0%	23.9%	0.00%
10.4	10990	100%	22.7%	22.70%
15.8	0	0%	20.5%	0.00%
			Winds to Site 22.7%	

Thus, the probability of a tephra-fall eruption from a future eruption from the ESRP volcanic field is

$$2.8 \times 10^{-6}\text{/yr} \times 1 \times 0.227 = 6.4 \times 10^{-7}\text{/yr},$$

which is then multiplied by the conditional probability of exceedance for tephra-deposit thickness, to generate the exceedance probabilities for silicic tephra-fall hazards from the ESRP (Figure 38).

There is 3.2×10^{-8}/yr probability of exceeding the 95th percentile thickness of 0.24 cm, and a 3.4×10^{-7}/yr probability of exceeding the average thickness of 0.008 cm. A 0.001 cm tephra-fall hazard occurs at an exceedance probability of 5×10^{-7}/yr, which represents the smallest likelihood for a potential initiating event associated with beyond-design-basis event sequences (Nuclear Energy Institute, 2019).

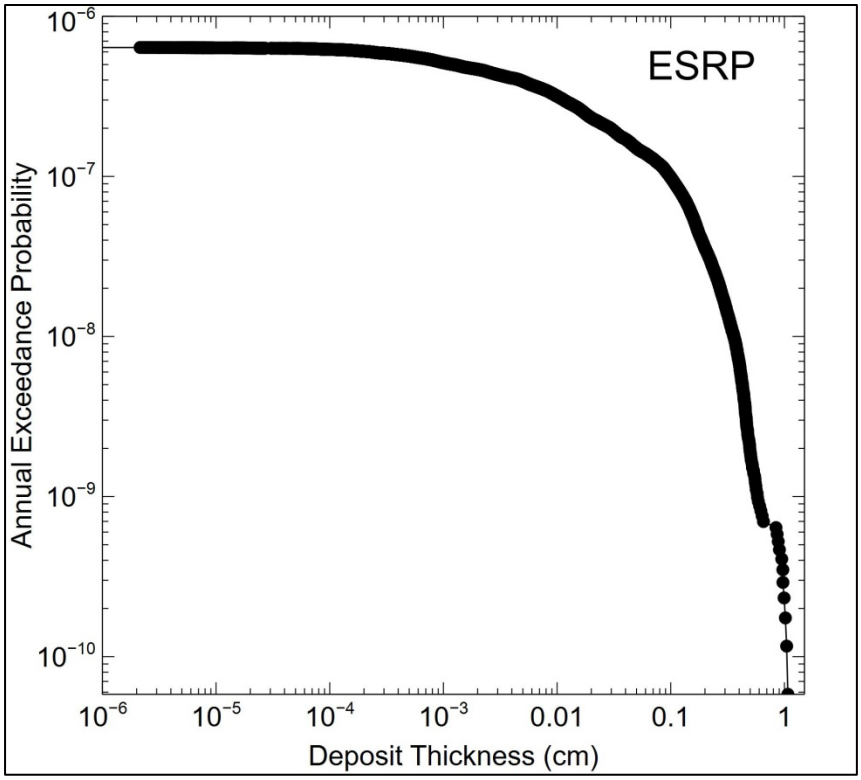

Figure 38. Annual exceedance probabilities for silicic tephra-fall hazards from the ESRP volcanic field.

7.6.4 Silicic Tephra-fall Hazards for Yellowstone Volcanic Field VEI3–4 Eruptions

Silicic vents in the YVF are located 280–320 km from the proposed Natrium™ site, in the intra-caldera area encompassing the Central Plateau Rhyolite (e.g., Figure 4). To account for spatial variability in potential vent locations, 1,000 ASHPLUME realizations were conducted every 4 km along a 40-km-long axis, for a total of ≈11,000 realizations.

Results of the ASHPLUME hazard calculations are presented in Table 46 and Figure 39. The calculated range of deposit volumes ($1.4x10^8$–$2.5x10^9$ m^3) corresponds reasonably to the interpreted range of deposit volumes for the YVF VEI3–4 eruptions (Table 34; $1x10^8$–$3x10^9$ m^3), and the calculated range of eruption column heights (9.8–17.3 km) compares reasonably with the interpreted range of column heights for YVF VEI3–4 eruptions (Table 35; 13.0–19.8 km). The calculated tephra-fall deposit thicknesses form a log-normal distribution, which is reflected in the summary statistics (Table 46).

Table 46. Summary of ASHPLUME2 calculations for YVF VEI3–4 silicic tephra hazards.

	Power (W)	*Duration (s)*	*Deposit Volume (m^3)*	*Col H (km)*	*Wind (km/hr)*	*Deposit Thick (cm)*
Avg	7.8E+12	7.3E+04	7.5E+08	13.2	21.8	0.005
Min	2.0E+12	5.0E+04	1.4E+08	9.8	0.2	1.3E-10
Max	2.0E+13	1.0E+05	2.5E+09	17.3	116.3	1.6
95^{th} percentile thickness: 0.26 cm						

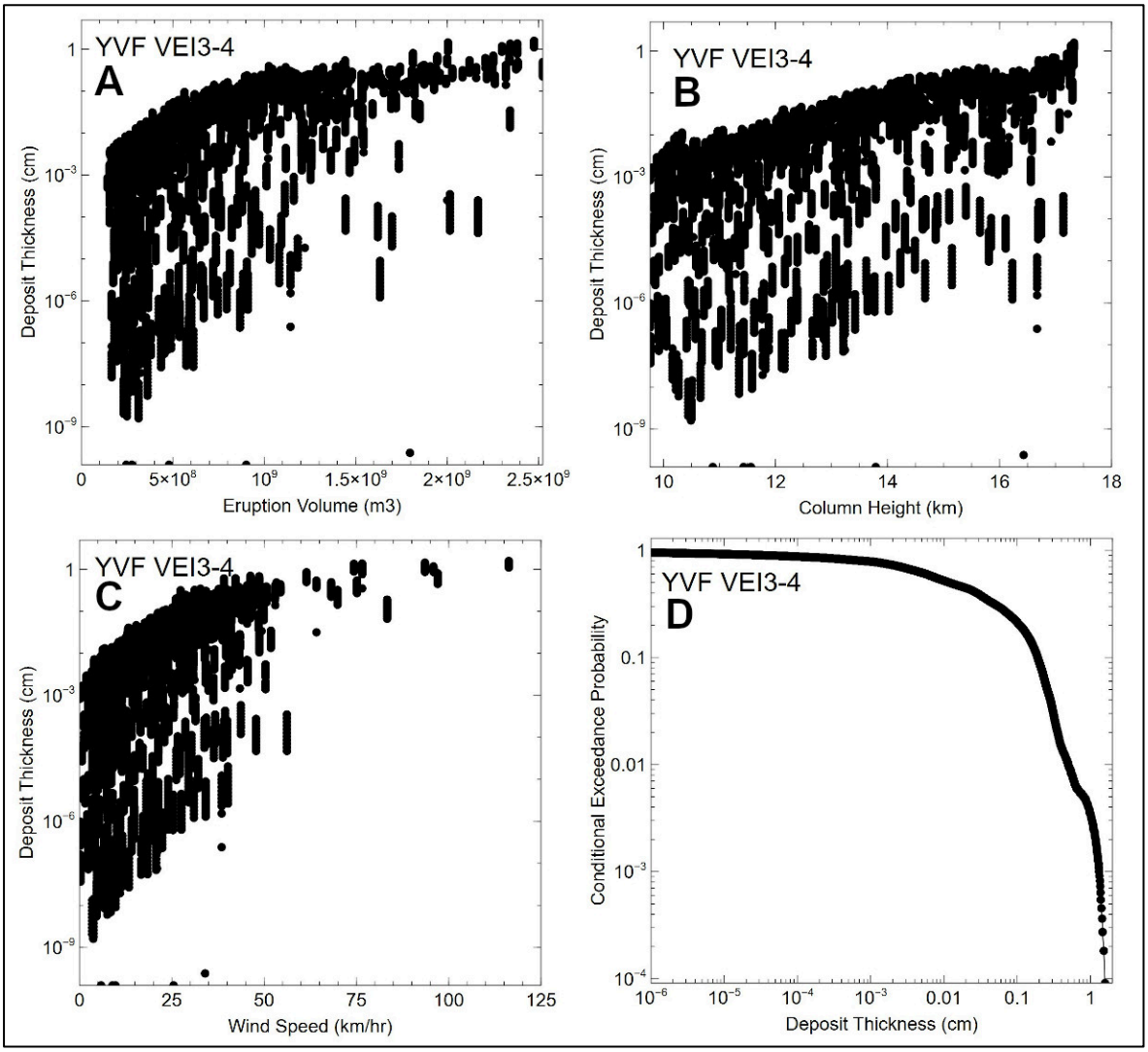

Figure 39. Results of silicic tephra-fall hazard calculations for YVF VEI3–4 eruption sources.

As would be expected, the thickest calculated deposits at the proposed site result from the largest eruption volumes (Figure 39A), the highest eruption columns (Figure 39B), and the fastest wind speeds (Figure 39C). The conditional tephra-fall hazard curve is shown in Figure 39D, which yields a 95th percentile deposit thickness of 0.26 cm. Note that this amount of tephra-fall assumes that i) a silicic eruption occurs in the YVF volcanic field, ii) the eruption produces a buoyant tephra plume, and iii) the prevailing wind is directed from the YVF vent towards the proposed Natrium™ site.

To calculate a fully probabilistic tephra-fall hazard curve for potential YVF VEI3–4 silicic eruption sources, the following three probabilities must be determined:

1) *Probability of a future VEI3–4 silicic eruption in the YVF:*

There have been 26 silicic eruptions in the CPR since 170 ka, (Section 7.1.1.1). Christiansen et al. (2007) analyzed the patterns of past rhyolite lava eruptions, and developed a mixed-exponential probability model that accounts for the clustered recurrence

of YVF-CPR eruptions. Their model calculates a $5x10^{-5}$/yr probability for a future rhyolite lava eruption, with volume estimates ranging from a mean of 10 km^3 and a 95th percentile of ~80 km^3. This model accounts for observed time-volume relationships, and appears more realistic than a simple homogeneous Poisson recurrence model (i.e., Equation 4).

2) Probability the YVF silicic eruption will be VEI3–4

The silicic tephra-fall hazard analyses for the YVF assume conservatively that all future silicic eruptions (100%) will have VEI3–4 eruption explosivity and produce tephra falls.

3) Probability that winds will be directed from the YVF to the proposed site

The calculated column heights for the 11,000 realizations were binned into the corresponding altitude ranges used in the ASHPLUME2 model, and used to calculate a weighted value for each altitude range (Table 47). This weight is applied to the percentage of time the winds in each altitude range are directed towards the site (i.e., from the corresponding sector in Table 38**)**, and used to calculate a weighted percentage for the amount of time the wind in each altitude range is directed toward the site. The sum of the weighted percents shows that for the 11,000 YVF realizations, 3.6% of the eruptions would have had winds directed towards the proposed site.

Table 47. Probability that winds from YVF VEI3–4 silicic eruptions are directed towards the proposed site.

Bin (km)	*Frequency*	Weight	Sector %	Weight Percent
1.5	0	0%	4.7%	0.00%
5.6	0	0%	6.5%	0.00%
10.4	1089	10%	7.4%	0.73%
15.8	8218	75%	2.0%	1.50%
19.3	1672	15%	8.7%	1.32%
25.9	0	0%	8.7%	0.00%
				Winds to Site 3.6%

Thus, the probability of a tephra-fall eruption from a future VEI3–4 eruption from the YVF-CPR volcanic field is

$$5x10^{-5}/yr \times 1 \times 0.036 = 1.8x10^{-6}/yr,$$

which is then multiplied by the conditional probability of exceedance for tephra-deposit thickness, to generate the exceedance probabilities for silicic tephra-fall hazards from YVF VEI3–4 eruptions (Figure 40).

There is $8.9x10^{-8}$/yr probability of exceeding the 95th percentile thickness of 0.26 cm, and a $1.1x10^{-6}$/yr probability of exceeding the average thickness of 0.005 cm. A 0.06 cm tephra-fall hazard occurs at an exceedance probability of $5x10^{-7}$/yr, which represents the smallest likelihood for a potential initiating event associated with beyond-design-basis event sequences (Nuclear Energy Institute, 2019).

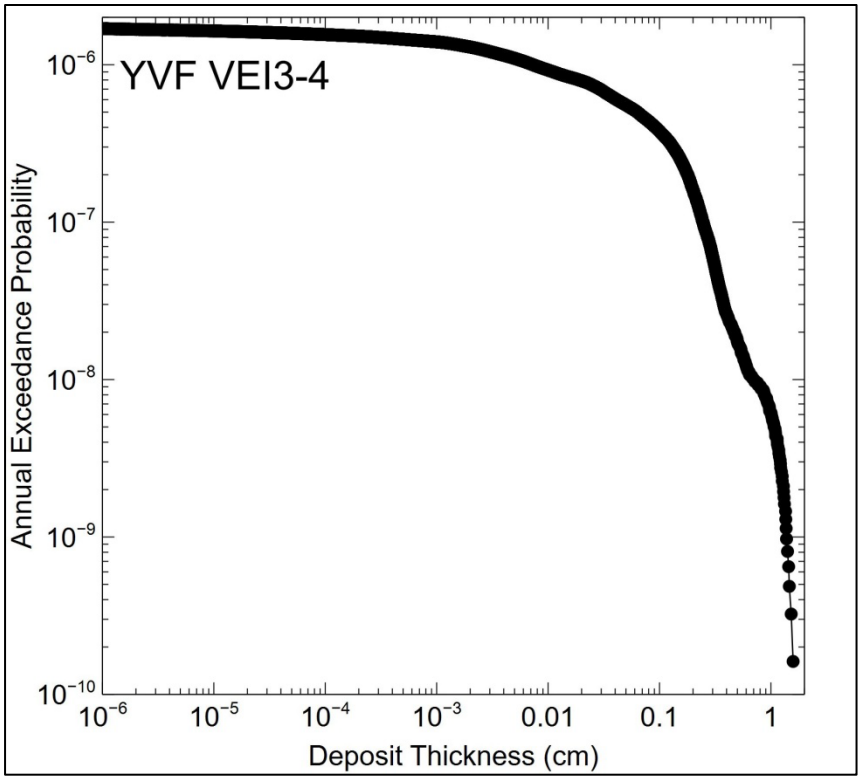

Figure 40. Annual exceedance probabilities for silicic tephra-fall hazards from YVF VEI3–4 eruptions.

7.6.5 Silicic Tephra-fall Hazards for Yellowstone Volcanic Field VEI4–5 Eruptions

Since 170 ka, two of the 26 eruptions from the YVF-CPR produced significant pyroclastic flows and tephra falls. Although the total erupted volume of these deposits was small (3–15 km^3 DRE) relative to the largest CPR eruptions (15–70 km^3 DRE), the total volumes of tephra from these two eruptions was likely larger than for the more effusive CPR eruptions (Section 7.1.1.1). The vent locations for these two pyroclastic eruptions are not well resolved, but they are thought to originate from within the CPR (Christiansen et al., 2007). The vent location for potential future eruptions is therefore assumed to occur within the CPR, 280–320 km from the proposed Natrium™ (e.g., Figure 4). To account for spatial variability in potential vent locations, 1,000 ASHPLUME realizations were conducted every 4 km along a 40-km-long axis, for a total of ≈11,000 realizations.

Results of the ASHPLUME hazard calculations are presented in Table 48 and Figure 41. The calculated range of deposit volumes (2.2×10^9–1.6×10^{10} m^3) corresponds reasonably to the interpreted range of deposit volumes for the YVF VEI4–5 pyroclastic eruptions (Table 34; 2×10^9–1×10^{10} m^3), and the calculated range of eruption column heights (19.5–27.5 km) compares reasonably with the interpreted range of column heights for YVF VEI4–5 eruptions (Table 35; 23.7–35.9 km). The calculated tephra-fall deposit thicknesses form a log-normal distribution, which is reflected in the summary statistics (Table 48).

Table 48. Summary of ASHPLUME2 calculations for YVF VEI4–5 silicic tephra hazards.

	Power (W)	*Duration (s)*	*Deposit Volume (m^3)*	*Col H (km)*	*Wind (km/hr)*	*Deposit Thick (cm)*
Avg	6.8E+13	7.3E+04	6.6E+09	23.2	42.6	0.02
Min	3.2E+13	5.0E+04	2.2E+09	19.5	0.01	1.3E-10
Max	1.3E+14	1.0E+05	1.6E+10	27.5	288	85
95^{th} percentile thickness: 11.9 cm						

As would be expected, the thickest calculated deposits at the proposed site result from the largest eruption volumes (Figure 41A), the highest eruption columns (Figure 41B), and the fastest wind speeds (Figure 41C). The conditional tephra-fall hazard curve is shown in Figure 41D, which yields a 95^{th} percentile deposit thickness of 11.9 cm. Note that this amount of tephra-fall assumes that i) a VEI4–5 silicic eruption occurs in the YVF volcanic field, ii) the eruption produces a buoyant tephra plume, and iii) the prevailing wind is directed from the YVF vent towards the proposed Natrium™ site.

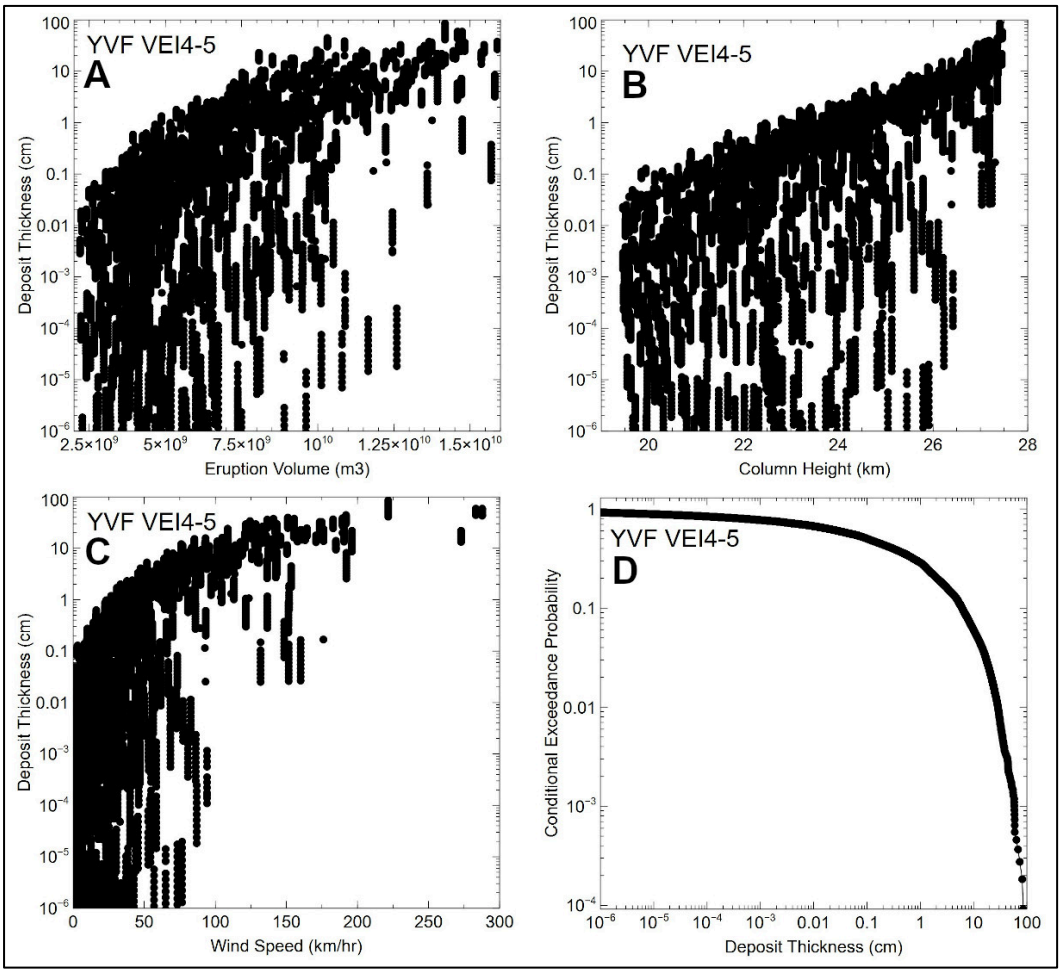

Figure 41. Results of silicic tephra-fall hazard calculations for YVF VEI4–5 silicic pyroclastic eruptions.

To calculate a fully probabilistic tephra-fall hazard curve for potential YVF VEI4–5 silicic pyroclastic eruptions, the following three probabilities must be determined:

1) *Probability of a future VEI4–5 silicic eruption in the YVF:*

The $5x10^{-5}$/yr probability for future silicic eruptions in the CPR that was used for the VEI3–4 analysis applies to the VEI4–5 analysis.

2) Probability the YVF silicic eruption will be VEI4–5 pyroclastic eruption

The VEI4–5 pyroclastic eruptions represent 2/26 = 7.7% of the <170 ka events in the CPR.

3) Probability that winds will be directed from the YVF to the proposed site

The calculated column heights for the 11,000 realizations were binned into the corresponding altitude ranges used in the ASHPLUME2 model, and used to calculate a weighted value for each altitude range (Table 49). This weight is applied to the percentage of time the winds in each altitude range are directed towards the site (i.e., from the corresponding sector in Table 38**)**, and used to calculate a weighted percentage for the amount of time the wind in each altitude range is directed toward the site. The sum of the weighted percents shows that for the 11,000 ASHPLUME2 realizations, 8.7% of the eruptions would have had winds directed towards the proposed site.

Table 49. Probability that winds for YVF VEI4–5 silicic pyroclastic eruptions are directed towards the proposed site.

Bin (km)	*Frequency*	Weight	Sector %	Weight Percent
1.5	0	0%	4.7%	0.00%
5.6	0	0%	6.5%	0.00%
10.4	0	0%	7.4%	0.00%
15.8	0	0%	2.0%	0.00%
19.3	0	0%	8.7%	0.00%
25.9	9160	84%	8.7%	7.31%
35.0	1749	16%	8.7%	1.39%
			Winds to Site 8.7%	

Thus, the probability of a tephra-fall eruption from a future VEI4–5 pyroclastic eruption from the YVF volcanic field is

$$5x10^{-5}/yr \times 0.077 \times 0.087 = 3.3x10^{-7}/yr,$$

which is then multiplied by the conditional probability of exceedance for tephra-deposit thickness, to generate the exceedance probabilities for silicic tephra-fall hazards from YVF VEI4–5 pyroclastic eruptions (Figure 42).

There is $1.7x10^{-8}$/yr probability of exceeding the 95th percentile thickness of 11.9 cm, and a $2.1x10^{-7}$/yr probability of exceeding the average thickness of 0.02 cm. No tephra-fall hazard occurs at an exceedance probability of $5x10^{-7}$/yr, which represents the smallest likelihood for a potential initiating event associated with beyond-design-basis event sequences (Nuclear Energy Institute, 2019).

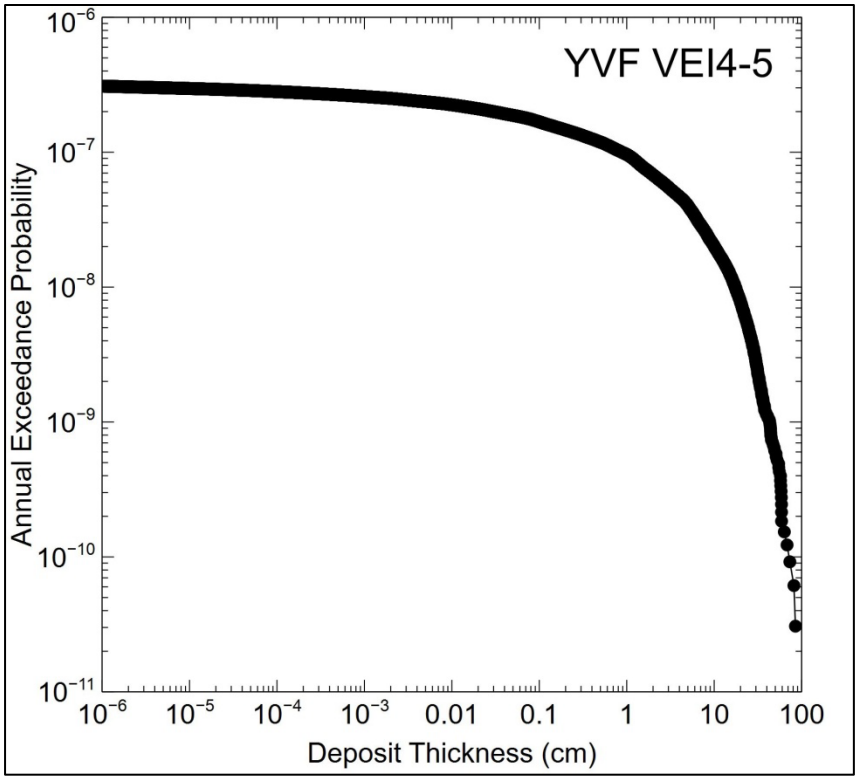

Figure 42. Annual exceedance probabilities for silicic tephra-fall hazards from YVF VEI4–5 pyroclastic eruptions.

7.6.6 Silicic Tephra-fall Hazards for Yellowstone Caldera (VEI8+) Eruptions

The Yellowstone caldera produced three large-volume pyroclastic eruptions (i.e., “supervolcano eruptions,” Miller and Wark, 2008) in the Quaternary Period, which distributed tephra falls throughout much of the western United States (Section 2.1). Such large-magnitude (i.e., VEI7–8) eruptions have not been observed, and the dynamics of these eruptions have been inferred through many detailed scientific investigations (e.g., Branney and Acocella, 2015). Not all caldera-forming eruptions produce Plinian eruption columns and associated tephra-fall deposits, which essentially represent a sustained eruption column that controls the vertical ascent of tephra to altitudes where neutral buoyancy and lateral spreading of the plume occurs.

In contrast, some caldera-forming eruptions produce continuous ejections of tephra along extensive rift or fissure networks, which form large-volume pyroclastic flows. As these pyroclastic flows travel away from the caldera, turbulent entrainment of air elutriates large amounts of ash from the flows, which rises buoyantly and is dispersed by wind (Sparks and Walker, 1977). The formation and dispersal of co-ignimbrite ash deposits is not reasonably represented by the types of advection-diffusion-sedimentation relationships used in ASHPLUME2 and related models (e.g., Costa et al., 2018).

For caldera-forming eruptions that might have formed Plinian-type eruption columns, the ASHPLUME2 code is not suitable for evaluating the distribution of tephra-fall deposits for several significant reasons. Most importantly, ASHPLUME2 does not capture the dynamics of large umbrella clouds, which can form rapidly and diffuse upwind radially for hundreds of kilometers above the vent. In addition, eruption column heights can reach 30–50 km, or potentially higher, altitudes. Tephra particles that fall from the plume will have a complex

interaction between winds at different atmospheric levels, which is not well represented by the ASHPLUME2 single-speed, single-direction approach to calculating particle fall times and directions. Consequently, modeling these types of caldera-forming Plinian eruptions requires an advanced modeling approach, which captures the dynamics of large umbrella clouds and the complex pathways that tephra particles travel during transport and deposition through the atmosphere.

The Ash3d model was used by Mastin et al. (2014) to evaluate tephra dispersion from a potential 330 km^3 (DRE) Plinian eruption from Yellowstone caldera. Ash3d is Eulerian transport model that divides the atmosphere into 3D cells, and tracks the dispersal and sedimentation of tephra through the grid cells. Mastin et al. (2014) also implemented a model in Ash3d to represent the formation of umbrella clouds by lateral spreading as a density current at the atmospheric level of neutral buoyancy in the plume. They demonstrated that this approach reasonably represented umbrella-cloud formation for the 1981 Mt. Pinatubo eruption. The Ash3d model, however, is computationally intensive because of the complexities in representing the 3D atmospheric model and the advection, diffusion, and sedimentation of tephra particles through the model domains.

Mastin et al. (2014) note that only a fraction of the total volume of a supervolcano eruption would form tephra falls, with most of the eruption forming pyroclastic flows or intracaldera deposits. They determined that the 330 km^3 (DRE) tephra volume used in their analyses is one- to two-thirds of the total volume of a potential 500–1,000 km^3 eruption, which reasonably represented a potential supervolcano eruption (Mastin et al., 2014). Although the total volume of Yellowstone caldera-forming eruptions is 280–2,450 km^3 DRE, the volume of tephra-fall deposits from these eruptions has not been constrained (Christiansen, 2001). Nevertheless, the 330 km^3 (DRE) tephra volume used by Mastin et al. (2014) appears reasonable to represent a future Yellowstone supervolcano eruption, given the uncertainties associated with tephra-fall volumes for past Yellowstone caldera eruptions.

Mastin et al. (2014) provide summary statistics in their Table 3 for both Billings, MT (227 km from Yellowstone) and Missoula, MT (375 km from Yellowstone). They note that proximal (i.e., <1,000 km) isopachs are essentially circular in distribution around the vent area. The average distance between Billings and Missoula is 301 km, which also reasonably represents the distance between the proposed site and the Yellowstone vent area (e.g., Figure 2). Consequently, averaging the Mastin et al. (2014) deposit thicknesses between Billings and Missoula gives a minimum thickness of 54 cm, an average of 84 cm, and a maximum of 113 cm for the proposed site.

These deposit statistics are derived from 15 realizations of the Ash3d code (i.e., Figure 10, Mastin et al., 2014). Assuming a Gaussian distribution to the realization data and constraining the probability of a future Yellowstone caldera-forming eruption to $<1x10^{-6}$/yr (i.e., Christiansen et al., 2007), the average thickness of 84 cm likely represents an approximately $<5x10^{-7}$/yr probability of exceedance, and the maximum thickness of 113 cm represents an approximately (1/15 x $<10^{-6}$/yr) $<7x10^{-8}$/yr probability of exceedance.

7.6.7 Summary of Silicic Tephra-fall Hazards at the Proposed Natrium™ Site

In summary, tephra-fall hazards for VEI2–5 silicic eruptions from the BRVF, CVVF, ESRP, and YVF have been analyzed using the ASHPLUME2 code. These analyses evaluated a range of potential conditions that appear representative of the types of VEI2–5 eruptions that can be interpreted from preserved characteristics of volcano and tephra-fall deposits in these fields.

Potential sources of future tephra falls are located 150–320 km from the proposed site, and regional winds can be directed from these sources to the site approximately 2–38% of the year. The conditional silicic tephra-fall hazards and associated eruption characteristics for these volcanic fields are summarized in Table 50.

Table 50. Summary of conditional tephra-fall hazards at the proposed site, from silicic volcanoes in the site region. YVF* = VEI8 eruption data from Mastin et al. (2014).

Volcanic Field	VEI	Average Deposit (cm)	95th% deposit (cm)	Column Heights (km)	Max. Wind Speed (km/hr)	Wind to site (%yr)	Distance from site (km)
BRVF	2–3	0.034	0.94	7.3–9.7	303	7.4	150–170
CVVF	2–3	0.019	0.59	7.3–9.7	290	37.1	200–210
ESRP	2–3	0.001	0.21	7.3–9.7	286	22.7	260–280
YVF	3–4	0.005	0.26	9.8–17.3	116	3.6	280–320
YVF	4–5	0.02	11.9	19.5–27.5	288	8.7	280–320
YVF*	8	84	113	15–35	252	8.7	280–320

Table 51. Summary of exceedance probabilities for silicic tephra-fall hazards at the proposed site, from potential silicic eruptions in the site region. Statistical metrics for YVF VEI8 eruption interpreted from Mastin et al. (2014).

Volcanic Field	Avg Deposit (cm)	Avg Prob (/yr)	95% deposit (cm)	95% Prob (/yr)	5E-7/yr deposit (cm)
BRVF	0.034	1.7E-07	0.94	1.6E-08	0.0
CVVF	0.019	1.5E-07	0.59	1.5E-08	0.0
ESRP	0.001	3.4E-07	0.21	3.2E-08	0.001
YVF VEI3–4	0.005	1.1E-06	0.26	8.9E-08	0.06
YVF VEI4–5	0.02	2.1E-07	11.9	1.7E-08	0.0
YVF VEI8	84	<5.0E-07	113	<7.0E-08	84
Total	**84.1**	**<2.5E-06**	**127**	**<2.4E-07**	**84.1**

Silicic tephra-fall eruptions represent independent events in the site region, as the likelihood of an eruption in one volcanic field does not affect the likelihood of an eruption in a separate volcanic field. Consequently, the probability of exceeding specific thicknesses of a tephra-fall deposit can be represented by the sum of the probabilities for that thickness (i.e., eruptions represent mutually exclusive, independent events). Considering the six silicic eruption types in the site region, this approach shows that an average silicic tephra-fall deposit of 84.1 cm has a $<2.5 \times 10^{-6}$/yr probability of exceedance (Table 51). The 95th percentile tephra-fall hazard is 127 cm with a $<2.4 \times 10^{-7}$/yr probability of exceedance. As discussed in Section 1.1, average and 95th percentile deposit thicknesses are calculated for use in the evaluation of potential event sequences (e.g., Nuclear Regulatory Commission, 2020).

Not unexpectedly, most of the hazard (≈99%) is contributed from potential VEI8 supervolcano eruptions of the YVF. VEI2–3 silicic eruptions from the BRVF, CVVF, and ESRP represent potential hazards of <1 cm tephra-fall deposits with 95th percentile confidence.

The analysis of Yellowstone caldera VEI8 eruptions by Mastin et al (2014) did not develop sufficient information to produce a distribution of annual exceedance probabilities. Consequently, a cumulative hazard curve for silicic tephra falls can only be developed for VEI2–5 eruptions. The combined annual probabilities of exceedance for specific deposit thicknesses for each VEI2–5 silicic volcanic field and eruption intensity are shown in Figure 43. The cumulative distribution shows that the probability of exceeding 0.1 cm of silicic tephra at the proposed site is approximately 8.3×10^{-7}/yr. The probability of exceeding 1 cm is approximately 1.2×10^{-7}/yr, which decreases to 2.0×10^{-8}/yr for exceeding 10 cm.

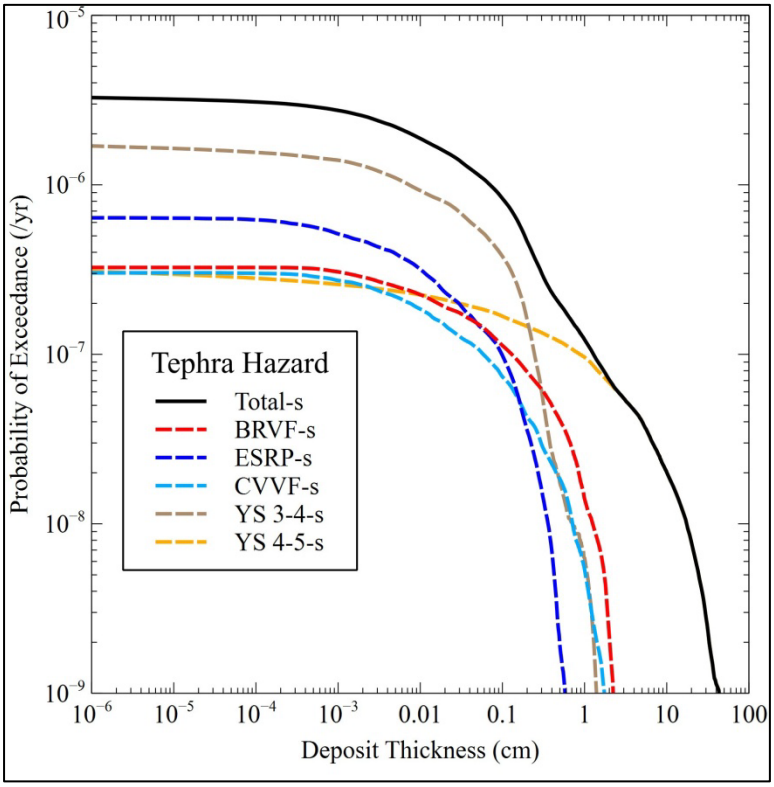

Figure 43. Compilation of annual exceedance probabilities for silicic tephra-fall hazards from potential VEI2–5 silicic eruptions in the site region. Note that potential VEI8 supervolcano eruptions from the Yellowstone caldera system are not included in this compilation.

The VEI8 analyses in Mastin et al. (2014) using the ash3D model provide additional confidence that the deposit thicknesses for VEI4–5 and VEI3–4 eruptions are calculated reasonably by the ASHPLUME2 model. Using 95th percentile deposit thicknesses, Mastin et al. (2014) calculated that a 330 km^3 eruption would deposit 130 cm of tephra at the proposed site. In comparison, ASHPLUME2 calculates that an approximately order-of-magnitude decrease in volume for VEI4–5 eruptions (i.e., 2–16 km^3) results in an approximately order-of-magnitude decrease in deposit thickness (i.e., 11.5 cm). ASHPLUME2 also calculates that an additional order-of-magnitude decrease in volume for VEI3–4 eruptions (i.e., 0.1–3 km^3) results in an approximately order-of-magnitude decrease in deposit thickness (i.e., 0.3 cm). These straightforward comparisons provide additional confidence that the deposit thicknesses calculated with ASHPLUME2 are reasonable, and do not underestimate hazard at the proposed site (cf. Section 6.2).

7.7 Potential for Debris-flow Hazards from Silicic Tephra-fall Deposits

The methodology developed in Section 6.4.6 for the analysis of debris-flow potential from remobilized mafic tephra-fall deposits can be used to assess this potential for silicic tephra-fall deposits in the NFLMC basin. The equivalent scour depths for fine-grained suspended load sediments ranges from 2.9–5.3 cm for low recurrence floods (i.e., 2 yr), which roughly doubles for 10-yr recurrence floods, and ranges from 8–25 cm for 100-yr floods (Table 29). Silicic tephra-fall deposits also are assumed to have all particle sizes <0.25 mm diameter (i.e., suspendable particulates) which are instantaneously available for fluvial transport. Ambient floods are assumed to have a maximum of 10% suspended particles, which are all derived from the channel scour zone (i.e., Section 6.4.6).

For VEI2–4 silicic eruptions, the thickest tephra deposits at the proposed site originate from the BRVF, which has a 95th percentile thickness of 0.94 cm and a 1.6x10^{-8}/yr probability of exceedance (Table 51). Using a minimum equivalent scour depth of 2.9 cm, the addition of an additional 0.94 cm of tephra fall would likely increase the amount of suspended sediment load from ≤10% to ≤13%. This increase in the amount of suspended load sediments is significantly less than the 60% load needed to transition the flood to debris-flow conditions (i.e., Section 6.4.6).

VEI4–5 silicic pyroclastic eruptions from the YVF have a 95th percentile thickness of 11.9 cm with a 1.7x10^{-8}/yr probability of exceedance (Table 51). Recognizing that ambient floods contain a maximum of 10% suspended particles, a 6x increase in the amount of suspended particles is needed to transition from flood-flow to debris-flow conditions. The equivalent thickness of additional particles is calculated in Table 52 by multiplying the scour depths from Table 29 by 6x and subtracting the ambient sediment depth.

Table 52. Thickness of additional tephra-fall deposits that would be required to transition from flood flow (10% suspended particles) to flood flow (60% suspended particles) conditions.

Channel Width (m)	*2yr (cm)*	*5yr (cm)*	*10yr (cm)*	*25yr (cm)*	*50yr (cm)*	*100yr (cm)*
1	26	52	70	79	115	123
5	19	32	42	45	65	68
10	17	26	33	35	51	52
15	15	23	29	30	44	45
20	14	21	27	28	40	40

The 11.9 cm tephra-fall deposit from a YVF VEI4–5 pyroclastic eruption does not appear to have the potential for creating debris-flow conditions for potential flood and channel conditions in the NFLMC basin. Nevertheless, this thickness is close to the 14 cm limit for the widest channels experiencing a 2-yr recurrence flood. Although these debris flows might fill the 15–20 m active channels, these channels are incised 2–5 m into broader, less active channels that are 300–400-m-wide (Figure 44). Any debris flow that overtopped the active channel would be contained within the broader, inactive channels. In addition, the likelihood for such a potential debris flow is 8.5x10^{-9}/yr (i.e., 1.7x10^{-8}/yr x 0.5/yr flood).

A VEI8 supervolcano eruption from Yellowstone caldera could potentially deposit 54–113 cm of tephra (i.e., Mastin et al., 2014) in the 67 km^3 NFLMC basin. These thicknesses of tephra fall appear sufficient to initiate debris-flow conditions within most of the active stream channels near the proposed site, using the simplified scour-depth methodology (cf. Table 52). For a tephra-fall deposit of this thickness, the potential for debris-flow conditions also could persist for years following the eruption, if large amounts of tephra are washed into channels from surrounding hill slopes during extreme rainfall events (e.g., Thouret et al., 2020).

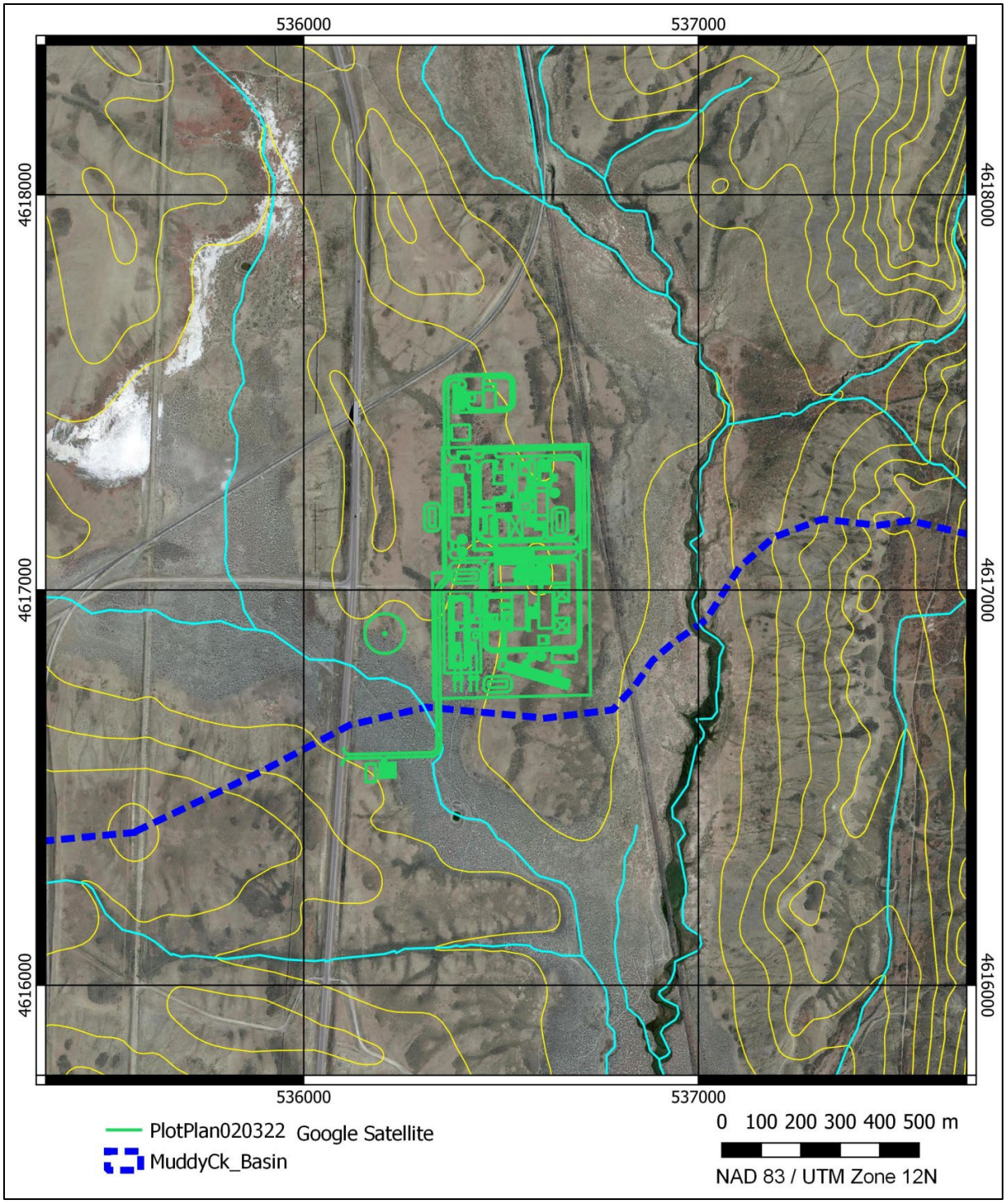

Figure 44. Site location map showing nearby stream channels (aqua lines). Proposed plot plan in green lines, 20 foot contours (yellow lines), and southern margin of the NFLMC drainage basin (dashed blue line), superimposed on satellite imagery from Google (2022). Note that active stream channels are incised in broader, inactive channels.

The active channels in the NFLMC basin are 5–20-m-wide, and are incised 2–5 m into broader, less active channels that are 300–400-m-wide (Figure 44). The proposed site is located on a

topographic high that rises approximately 6–8 m above these broader, less active channels (Figure 44). Potential debris-flow hazards might occur at the proposed site if the flow has sufficient volume to overtop both the main stream channel, and the broader inactive channel, at the elevation of the site.

The addition of the remobilized tephra-fall deposit will increase the bulk volume of the flow by some factor, which is referred to as the bulking factor (Scott, 1988; Doyle et al., 2011). The bulking factor typically is used to evaluate the additional amount of material incorporated into an already established debris flow, which has been generated by essentially instantaneous release of material upstream and rapid generation of peak-flow conditions (Scott et al., 1995; Pierson and Major, 2014). Nevertheless, bulking factor can be used in this analysis to calculate the increase in flow volume that would occur with the instantaneous addition of potential tephra-fall deposits.

The bulking factor and associated flow volumes for potential debris flows in the NFLMC basin can be estimated from a simple volumetric relationship. Normal flood flows contain <10 volume percent suspended particulates (i.e., 9 parts water and 1 part particulates). Increasing the suspended particulates to 60 volume percent thus would result in a bulking factor of 1.5 (i.e., 9 parts water and 6 parts particulates).

Peak discharge rates calculated for NFLMC stream channels during flood conditions (i.e., Table 27) consist of ≤10 volume percent particles ≤0.25 mm. The scour-depth calculations in Table 52 show that most of the active channels would support debris-flow conditions with 60 volume percent suspended particles, following deposition of 54–113 cm of Yellowstone tephra. Using a bulking factor of 1.5 and a less-active channel width of 300 m (i.e., minimum inactive channel widths near proposed site, Figure 44), the channel depths needed to contain the debris flow are calculated in Table 53 by multiplying the peak-discharge rates from Table 27 by the 1.5 bulking factor, and dividing by a 300 m less-active channel width. This approach incorporates all of the potential tephra-fall in the less active channels into the debris flow.

Table 53. Calculated depths needed for a 300-m-wide channel to contain potential debris flows in the NFLMC basin following deposition of a Yellowstone VEI8 tephra fall.

Channel Width (m)	*2yr (m)*	*5yr (m)*	*10yr (m)*	*25yr (m)*	*50yr (m)*	*100yr (m)*
1	0.01	0.02	0.03	0.04	0.1	0.1
5	0.1	0.2	0.3	0.4	0.8	0.8
10	0.2	0.5	0.7	0.8	1.7	1.8
15	0.3	0.8	1.3	1.4	2.9	3.0
20	0.5	1.2	1.8	2.0	4.2	4.2

This simplified approach indicates that a potential debris flow would not overtop the 6–8-m-deep inactive channels during flooding events, following deposition of 54–113 cm of tephra from a Yellowstone caldera eruption. The analysis assumes that debris flows incorporate all of the tephra fall in the channel instantaneously, and that peak flow occurs instantaneously in the channel. These are conservative assumptions, because studies of debris-flow evolution show that there is considerable lag between peak flow times and peak bulking of the flow (e.g., Thouret et al., 2020). In addition, erosion of tephra-fall deposits is a gradual process, and that more frequent and less severe flooding events will scour the tephra deposit without reaching debris-flow conditions (e.g., Pierson and Major, 2014).

8 TEPHRA-FALL HAZARDS AT THE PROPOSED NATRIUM™ SITE

Excluding potential supervolcano eruptions from the Yellowstone caldera system, the VEI1–5 tephra-fall hazard at the proposed Natrium™ site from both mafic and silicic eruptions is calculated at an average deposit thickness of 0.12 cm, which has a 5.6×10^{-6}/yr probability of exceedance (i.e., Table 54). The 95th percentile deposit thickness from VEI1–5 eruptions is 16.6 cm, which has a 5×10^{-7}/yr probability of exceedance. As discussed in Section 1.1, average and 95th percentile deposit thicknesses are calculated for use in the evaluation of potential event sequences (e.g., Nuclear Regulatory Commission, 2020).

The most significant contributors to these values are from potential VEI4–5 pyroclastic eruptions from the CPR in the YVF, and potential mafic and silicic eruptions from the BRVF (Table 54). Mobilization of these tephra-fall deposits by extreme rainfall events in the small drainage basin encompassing the proposed site is not expected to produce debris-flow hazards, because the active channel drainages have sufficient capacity to contain potential debris flows within their banks.

Table 54. Combined mafic (Table 26) and silicic (Table 51) tephra-fall hazards from all potential volcanic sources in the proposed site region.

VolcanicField	Avg. Deposit (cm)	Avg. Prob. (/yr)	95%ile deposit (cm)	95%ile Prob. (/yr)	5×10^{-7}/yr deposit (cm)
LHVF - mafic	0.001	8.3E-09	0.063	9.10E-10	0.0
UWRB - mafic	0.010	9.0E-07	0.172	7.90E-08	0.038
BRVF - mafic	0.006	5.9E-07	2.106	6.00E-08	0.022
ESRP - mafic	0.019	2.1E-06	0.324	1.90E-07	0.210
BRVF - silicic	0.034	1.7E-07	0.94	1.6E-08	0.0
CVVF - silicic	0.019	1.5E-07	0.59	1.5E-08	0.0
ESRP - silicic	0.001	3.4E-07	0.21	3.2E-08	0.001
YVF VEI3-4 - silicic	0.005	1.1E-06	0.26	8.9E-08	0.06
YVF VEI4-5 - silicic	0.02	2.1E-07	11.9	1.7E-08	0.0
YVF VEI8 - silicic	84	<5.0E-07	113	<7.0E-08	84
Total	**84.12**	**<6.1E-06**	**129.6**	**<5.7E-07**	**84.3**

Interpreting the results from Mastin et al. (2014) in a statistical context, a potential supervolcano eruption from the Yellowstone caldera system increases the average and 95th percentile VEI1–5 tephra-fall hazards by approximately an order of magnitude. Nevertheless, only a small increase in the annual probabilities of exceedance occurs by including these VEI8 hazards, because of the estimated low likelihood of such an eruption occurring (Table 54).

The tephra-fall deposit from a potential Yellowstone super-eruption could be mobilized from hill slopes and stream channels during heavy rainfall events. Based on conservative, first-order stream flow and bulking relationships, the resulting debris flows might overtop some active channels in the NFLMC basin. However, those debris flows would then flow in the wider, less active channels that contain the incised active channels. The less active channels have sufficient depth to accommodate the increased volumes of potential debris flows, and these flows would not create flooding conditions at the proposed site.

Although a total tephra-fall hazard curve can be calculated for VEI1–5 eruptions, VEI8 eruptions cannot be included in this calculation because the limited number of analyses (i.e., 15) in Mastin et al. (2014) are insufficient to represent a statistically significant distribution. For the VEI1–5 eruptions (Figure 45), there is a 5.6×10^{-6}/yr probability of exceeding 0.1 cm of tephra fall at the proposed site, which decreases to 2.4×10^{-7}/yr probability of exceeding 1 cm of tephra fall.

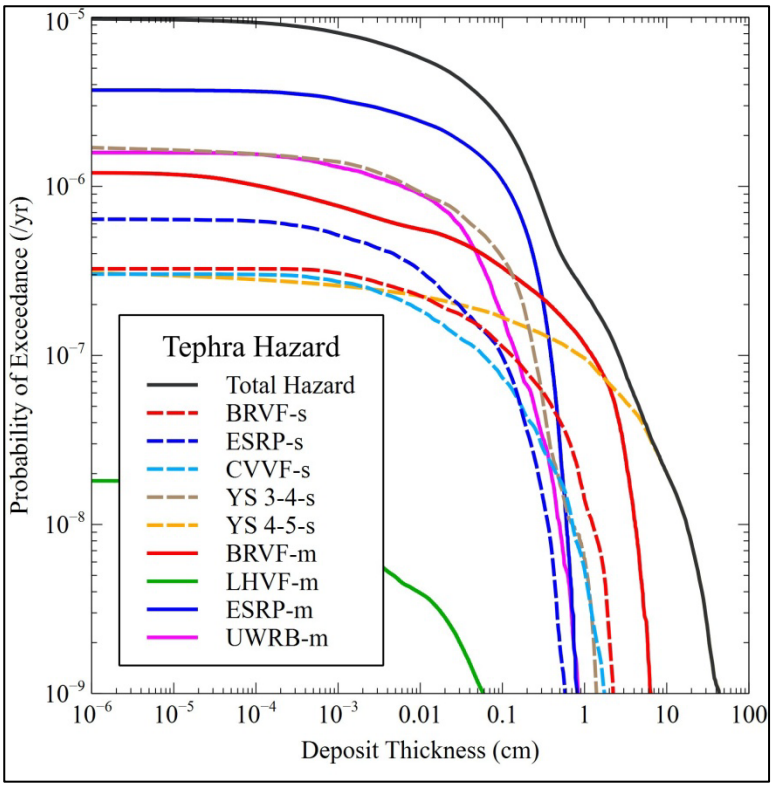

Figure 45. Summary of annual exceedance probabilities for tephra-fall hazards from potential VEI1–5 eruptions in the site region.

Volcanic tephra-falls at the proposed site represent a potential beyond-design-basis event, in that the likelihood of any tephra fall occurring at the site is $<1 \times 10^{-5}$/yr (Figure 45). In the context of guidance in Nuclear Regulatory Commission (2020) and Nuclear Energy Institute (2019), potential beyond-design-basis event sequences might need to consider initiation from tephra-fall deposits with an average thickness of 84 cm and a probability of exceedance of $<6.1 \times 10^{-6}$/yr (Table 54). This hazard can be bounded by a 95th percentile thickness of 130 cm, which has a probability of exceedance of $<5.7 \times 10^{-7}$/yr (Table 54). These hazards include consideration of a potential VEI8 supervolcano eruption from the Yellowstone caldera system.

9 CHARACTERISTICS OF TEPHRA FALLS

The purpose of Section 9 is to provide a description of the physical characteristic of tephra-fall deposits, which can be used to evaluate the potential significance of these deposits on the performance of structures, systems, and components (SSCs) for the proposed Natrium™ facility. In addition, these characteristics can be used to guide the development of operational procedures to mitigate the potential effects of tephra-fall events at the site, if such procedures are warranted.

9.1 Composition

Tephra is a generic term used to describe particles of volcanic rock that typically range in size from approximately 1 μm to 6 cm diameter. The particles can consist of:

- Fragments of solidified magma (i.e., pyroclasts), which contain 10–90 volume percent void space (i.e., vesicles) created by the expansion of magmatic gas during the eruption. The smallest fragments (i.e., less than approximately 30 μm) represent individual pieces of fragmented magma that typically lack vesicles.

- Fragments of crystals that formed in the magma prior to eruption. Although entire crystals can occur in larger pyroclasts, most of the free crystals in tephra are fragmented during the eruption process.

- Fragments of older rock that were detached and entrained during the eruption of magma. These fragments are not vesiculated and have high densities relative to pyroclasts. Consequently, these rock fragments settle from the eruption closer to the volcano than similarly sized pyroclasts.

Magmas in the site region have compositional ranges that can be generalized as either mafic (i.e., 46–58 wt% silica) or silicic (i.e., 59–76 wt% silica). These compositional ranges affect the viscosity and density of the erupting magma, and occur with variations in other elements that control the volatile content of the magma and formation of crystal phases. As a result, the viscosities of erupting magma can range from 10–20 Pa s for mafic magmas, to 10^5–10^6 Pa s for the most silicic magmas (i.e., McBirney and Murase, 1984). Magma densities can range from 2.6–2.7 g/cm^3 for mafic magmas, to 2.2–2.3 g/cm^3 for silicic magmas (i.e., McBirney and Murase, 1984). In contrast, typical crystals in these magmas have densities of approximately 2.6–4.0 g/cm^3.

Volcanic ash (i.e., tephra <2 mm diameter) typically has a hardness of ≈5 on the Mohs scale (i.e, equivalent to Rockwell C = 51.4, Vickers = 535 kgf/mm^2), although higher silicic ash shards (<0.1 mm) can have hardness approaching 6 on the Mohs scale (i.e., Rockwell C = 64.6, Vickers = 817 kgf/mm^2) (U.S. Geological Survey, 2022d). Some of the crystals in volcanic ash have similar hardness, but the minerals olivine and quartz can have hardness up to 7 on the Mohs scale (i.e., Rockwell C = 71, Vickers = 1160 kgf/mm^2) (U.S. Geological Survey, 2022d). Consequently, volcanic ash can be moderately to highly abrasive and adversely affect the performance of mechanical systems (e.g., Wilson et al., 2014).

During transport in the eruption plume, volcanic gasses deposit cations and anions on the surfaces of tephra particles, primarily Na^+, K^+, Ca^{2+}, Mg^{2+}, Cl^-, F^- and SO_4^{2-} (e.g., Jones and Gislason, 2008). These ions can deliquesce readily under high humidity conditions, which increases the conductivity of the tephra and affects the flow of electrical current (e.g., Wardman

et al., 2012). In addition, these ions are readily soluble and can form corrosive fluids as leachates (e.g., Jones and Gislason, 2008).

9.2 Particle Sizes

Tephra potentially deposited at the proposed Natrium™ site will have undergone 100–320 km of transport from the eruption source. Most of the tephra >2 mm in diameter will have settled from the eruption plume within approximately 50 km of the vent (Cashman and Rust, 2016). One limitation of advection-diffusion-sedimentation models such as ASHPLUME2 is the assumption that particles settle gravitationally from the plume, which does not fully capture the complex settling dynamics of very fine grained (i.e., <30 μm) ash particles (i.e., Alfano et al., 2011). In addition, these very fine grained ash particles can aggregate to larger diameters in eruption plumes, which leads to enhanced sedimentation (e.g., Carey and Sigurdsson, 1982). Consequently, deposits from analogous eruptions provide more accurate estimates than models on the grain-size characteristics of potential tephra-fall deposits at the proposed site.

Few basaltic eruptions that are reasonably analogous to the mafic eruptions in the site region (i.e., VEI2–3) have tephra-fall deposits that have been investigated >100 km from the vent. These deposits suggest that at 100 km from the vent, median diameters are <0.1 mm. In addition, ash <0.063 mm diameter represents 35–45% of the deposit, with the remainder in the 0.063–1 mm size range (Rose et al., 2008; Gudnason et al., 2017).

The 1980 eruption of Mount St. Helens, WA, represents one of the best-studied tephra-fall deposits. This VEI4 eruption is not directly analogous to eruptions in the site region, but the general eruption characteristics are representative of potential VEI4–5 eruptions in the site region. At 106 km from the vent, the 1980 tephra-fall deposits have median diameters of 0.1 mm, which decreases to 0.03 mm at 216 km and 0.02 mm at 300 km (Sarna-Wojcicki et al., 1981; Carey and Sigurdsson, 1982).

General relationships for VEI4–6 eruptions also show that by 100 km from the vent, tephra median diameters are 0.3–0.8 mm, which decrease to ≈0.5 mm by 150 km distance. In addition, by 100 km ash <0.063 mm in diameter accounts for 10–60% of the deposit, which increases to 60–80% by 300 km distances (Cashman and Rust, 2016). Detailed studies for VEI3–4 silicic eruptions show that median diameters can be 0.02–0.4 mm by 100 km from the vent, and decrease to 0.02–0.03 mm by 300 km (Sparks et al., 1981; Alfano et al., 2016)

Most deposits from VEI8 supervolcano eruptions are sparsely preserved and grain-size distributions have not been investigated at distal locations. The Rangitawa tephra from a VEI8 eruption in the Taupo volcanic zone, New Zealand, has median diameters of 0.1–0.35 mm at 200 km, with 15–75% of the deposit <0.063 mm and 4–17% <0.01 mm (Matthews et al., 2012).

In summary, potential mafic tephra fall deposits at the proposed site would likely have median particle diameters <0.1 mm, with about 50% in the 0.1–0.063 mm size fraction and the remainder <0.063 mm. Silicic tephra-fall deposits from VEI2–5 eruptions would likely have median diameters of 0.02–0.4 mm, with 60–80% of the deposit <0.063 mm. The tephra-fall deposits from a potential VEI8 Yellowstone eruption would likely have median diameters of 0.1–0.35 mm, with 15–75% of the deposit <0.063 mm.

9.3 Thermal Conductivity

Thermal conductivity in tephra is strongly controlled by the degree of vesicularity in the particles, because of the void spaces created by vesicles. As tephra particles are broken apart by energetic eruption processes, these particles fracture along vesicle walls. As a result, the vesicularity of the tephra particle will decrease with decreasing particle size. Ultimately, very fine ash particles represent small pieces of vesicle walls, which lack internal vesicles. These densities are needed to estimate the thermal conductivity of characteristic tephra in the site region from data at analogous deposits,

From general relationships in Cashman and Rust (2016), mafic ash with diameters >1 mm has densities of ≈1 g/cm^3. As diameters decrease to 0.1 mm, particle densities increase to ≈2 g/cm^3. When the ash has a diameter of 0.01 mm, particle densities are approximately equal to magmatic densities of ≈2.6 g/cm^3.

For silicic tephra, ash with diameters >1 mm has densities of ≈0.6 g/cm^3. As diameters decrease to 0.1 mm, particle densities increase to ≈1.2 g/cm^3. When the ash has a diameter of 0.01 mm, particle densities are approximately equal to magmatic densities of ≈2.3 g/cm^3 (Cashman and Rust, 2016).

Thermal conductivity in volcanic tephra can range from ~0.1 to ~2 W m^{-1} K^{-1}, depending on tephra composition and degree of vesicularity (i.e., density) (e.g., Fountain and West, 1970). For mafic and silicic compositions representative of tephra in the site region, thermal conductivity is ≈10% high for silicic compositions relative to mafic compositions (Lesher and Spera, 2015).

Using measured conductivities in Kuznetzova (2017) and Horai (1991), dry tephra particles with densities of ≈0.6–1 g/cm^3 have thermal conductivities of 0.2–0.4 W m^{-1} K^{-1}. For densities of ≈1–2 g/cm^3, thermal conductivities are 0.4–0.9 W m^{-1} K^{-1}. As density increases to ≈2–2.6 g/cm^3, thermal conductivities are 0.9–1.4 W m^{-1} K^{-1}. Nonvesiculated particles (i.e., vesicle walls) have conductivities equivalent to magmatic conductivities, which are 1.15 W m^{-1} K^{-1} for mafic compositions and 1.34 W m^{-1} K^{-1} for silicic compositions (Lesher and Spera, 2015).

9.4 Thermal Emissivity

Thermal emissivity data for volcanic ash have been determined to assist in the interpretation of eruption plumes in satellite imagery, and the remote sensing of mineral phases on terrestrial and extraterrestrial rocks (Christensen et al., 2000). These data focus on infrared radiation with 4–30 μm wavelengths, which is used by several remote sensing platforms. In general, thermal emissivities for mafic and silicic ash show a gradual increase from ≈0.95–0.97 between 4–8 μm, to local maxima at approximately 8 μm that range from ≈0.97–0.99 (Figure 46) (Carter et al., 2009; Williams and Ramsey, 2019). Average emissivity in the 6–12 μm wavelengths decreases to as much as ≈0.75 for silicic tephra, but remains relatively high (≈0.9) for mafic tephra at these wavelengths (Logan et al., 1973).

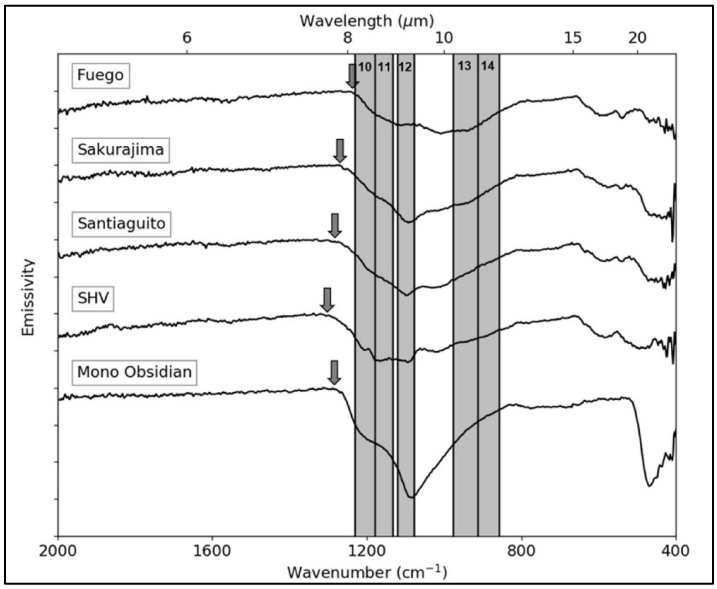

Figure 46. Representative thermal emissivities of volcanic tephra, from figure 2 in Williams and Ramsey (2019). Tephra compositions are mafic (Fuego, Sakurajima), intermediate (Santiaguito, Soufriere Hills Volcano), and silicic (Mono Craters).

The size of ash particles has a potentially significant effect on thermal emissivity, with finer particle sizes having relatively higher emissivities than coarser particle sizes. This sensitivity for particle size is shown in Figure 47, and is most significant for more silicic compositions. Note that the spectra in Figure 47 are enlargements of the 8–12 μm wavelength data in Figure 46 for >150 μm particle sizes.

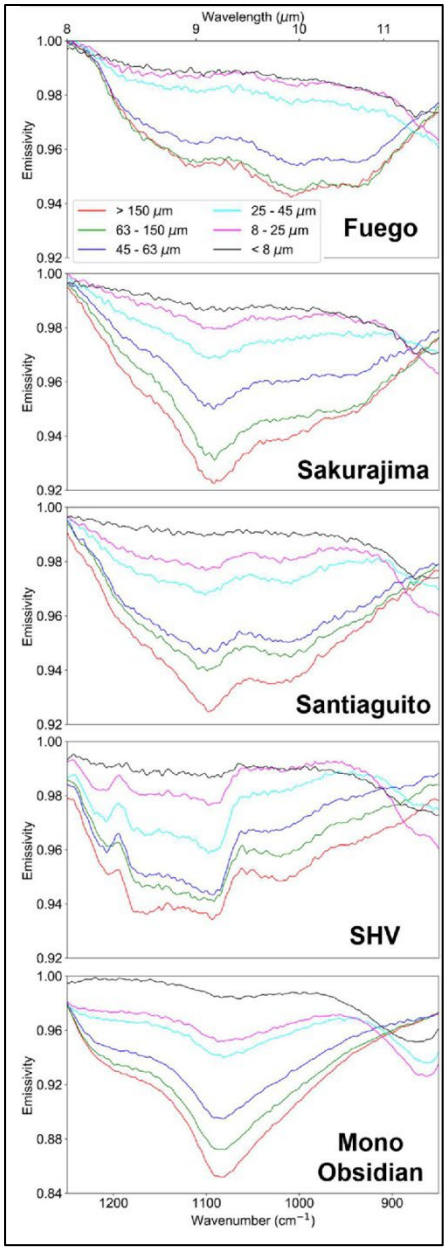

Figure 47. Detailed thermal emissivities of volcanic tephra, showing sensitivity to particle size. From figure 3 in Williams and Ramsey (2019). Tephra compositions are the same as in Figure 46, colored lines show different particle diameters (legend shown for Fuego).

9.5 Deposit Densities

Tephra-fall deposit densities typically are measured within 50–100 km of a volcano, where deposits are relatively thick and well preserved. These deposits contain abundant large (i.e., >2 mm) particles, which generally increases the deposit density at proximal locations. Consequently, deposit densities <100 km from a volcano might not accurately represent densities 100–300 km from a volcano, which are the distances between the proposed site and potential eruption sources in the site region.

Historical volcanic eruptions show large variations in deposit densities, which do not correlate with either magma composition or eruption VEI (Osman et al., 2022). Some of these variations are caused by comparisons between fresh, noncompacted deposits and older deposits that have been compacted by rainfall and infiltration. Deposits from single eruptions can increase in density from ≈25% to >100% with distances of tens-to-hundreds of kilometers from the volcano (Osman et al., 2022). There also is a general trend of decreasing deposit density with increasing silica content (i.e., lowering density) of the magma. Based on an analysis of eruption deposits and experiments with synthetic deposits, Osman et al. (2022) developed representative tephra-fall deposit densities of ≈600 kg/m^3 for fine-grained silicic tephra, and ≈1,500 kg/m^3 for fine-grained basaltic scoria. In comparison, deposit densities from the 1980 eruption of Mount St. Helens ranged from 800 kg/m^3 at 100 km from the vent, to 500 kg/m^3 300 km from the vent (Sarna-Wojcicki et al., 1981).

Deposit densities will increase when wetted by rainfall, because water fills open voids between the tephra particles. Measured deposit densities typically show a 50–100% increase in density when water saturated (e.g., Blong, 1981; Sarna-Wojcicki et al., 1981). Assuming water has a density of 1,000 kg/m^3, a silicic tephra-fall deposit with a dry density of 600 kg/m^3 and a porosity of 68% (i.e., Macedonio and Costa, 2012) would have a water-saturated density of 1,280 kg/m^3 (i.e., 113% increase). In contrast, a mafic tephra-fall deposit with a dry density of 1,500 kg/m^3 and a porosity of 68% would have a water-saturated density of 2,180 kg/m^3 (i.e., 45% increase).

9.6 Tephra Eruption Characteristics

Most volcanic eruptions are preceded by periods of unrest at the volcano or volcanic field, which is often represented by increases in the frequency of earthquakes as magma ascends through the crust. Other signs of a potential eruption include small changes in rates or patterns of ground deformation, or changes in water composition at nearby springs (e.g., Pallister and McNutt, 2015). In the United States, the U.S. Geological Survey (USGS) has statutory authority to monitor all potentially active volcanoes in the United States. The USGS Yellowstone Volcano Observatory (https://www.usgs.gov/observatories/yvo) is responsible for monitoring potentially active volcanoes in the site region. Current monitoring efforts in the site region are focused on volcanic fields that have erupted since ≈10 ka (ESRP and BRVF), and the YVF. Seismic monitoring is conducted in partnership with the University of Utah, which operates an extensive network of seismographs in the site region (https://quake.utah.edu/). In the unlikely event that volcanic unrest occurs at the volcanic fields in the site region, there is reasonable confidence that the seismic signals of this potential unrest would be detected and analyzed by Yellowstone Volcano Observatory staff. If sufficient data indicated the potential for a volcanic eruption, the USGS staff would issue public alerts to describe the nature of unrest, and the potential for a volcanic eruption.

If an eruption did occur in the site region, the arrival time for tephra falls at the site would be dependent on the height of the eruption column, and the speed and direction of prevailing winds. For VEI1–3 eruptions, column heights would be less than approximately 10 km and large umbrella clouds would not be expected to form. If winds were directed towards the site, tephra fall from these eruptions could reach the proposed site in approximately 1.5 hr (BVF eruptions, average wind speed 75 km/hr) to 2.5 hr (CVVF silicic eruption, average wind speed 83 km/hr). Larger VEI3–4 eruptions from the YVF would likely produce umbrella clouds at 10–20 km altitudes, which could spread to tens of kilometers in diameter in <1 hr (e.g., Sarna-Wojcicki et al., 1981). With winds at these altitudes averaging 22 km/hr, tephra from these eruptions could reach the site in approximately 10 hr. The potentially large VEI4–5 pyroclastic eruptions from

Yellowstone would likely form extensive umbrella clouds at 20–30 km altitudes, which could spread to above the proposed site in approximately 1 hr (i.e., Constantinescu et al., 2021).

The duration of a potential eruption event depends on whether the eruption is represented by a single continuous episode, or multiple episodes that occur hours, days, or potentially months apart. The modeled tephra-fall hazards for the proposed site assume the eruption occurs as a single continuous episode, with durations of approximately 14–28 hr. This range of actual eruption durations appears reasonable for the types of VEI1–5 eruptions that characterize the site region (e.g., Siebert et al., 2011). A VEI8 supervolcano eruption from the Yellowstone caldera, however, might continue for days to months (Mastin et al., 2014). Nevertheless, an "eruption" might consist of multiple episodes of intermittent activity that can persist for several years, and sometimes for decades, following the initial activity. The duration of these episodes cannot be forecast, and vary widely amongst different types of volcanoes in different tectonic settings (e.g., Siebert et al., 2011). In addition, there are no reliable criteria to determine when an eruption has ceased, to the point where additional episodes of activity will not occur within a relatively short period of time (i.e., months to years).

The concentration of airborne tephra particles during an eruption can be calculated using deposit concentrations (g/cm^2), thicknesses (cm) and eruption durations (sec) from the ASHPLUME2 models. The VEI2–3 BRVF eruptions represent the thickest mafic tephra-fall deposits at the proposed site (Section 6.4.5), which indicate that total airborne particle concentrations of 12–24 g/m^3 likely persist for the duration of these eruptions. VEI3–4 and VEI4–5 silicic YVF eruptions would have 8–16 g/m^3 total airborne particle concentrations. In comparison, total suspended particulate (i.e., ≤0.1 mm) concentrations of 33.4 g/m^3 were measured in Yakima, WA (135 km from the volcano) during the 1980 Mount St. Helens eruption (Bernstein et al., 1986). Note that the calculated airborne particle concentrations include all grain sizes in the tephra fall. In contrast, most other measurements of airborne particle concentrations during eruptions only include particles <0.01 mm (e.g., Mastin et al., 2020).

Using the calculated deposit thicknesses and eruption durations, tephra-fall accumulation rates at the proposed site are bounded by <5 mm/hr for potential mafic VEI2–3 eruptions from the BRVF, and <1 mm/hr for VEI3–4 to <4 mm/hr for VEI4–5 potential eruptions from the YVF. The potential VEI8 eruptions modeled by Mastin et al. (2014) used eruption durations of 3 days to 1 month, suggesting the 54–113 cm tephra deposit at the proposed site might accumulate at rates of 1–2 mm/hr to 1–2 cm/hr.

Tephra-fall deposits will mantle topographic features with low slope angles, but will be unstable at higher slope angles. Shear-box tests by Osman et al. (2022) show that fresh tephra-fall deposits have internal friction angles of 36–37º, for both mafic and silicic compositions.

9.7 Post-Eruption Characteristics

After the tephra-fall eruption has ended, the deposit will begin to erode and stabilize in response to rainfall and chemical reactions. Erosion rates on newly formed tephra-fall deposits can be several orders-of-magnitude higher that pre-eruption rates, in the first year after the eruption (e.g., Collins and Dunne, 1986; Pierson and Major, 2014). These high erosion rates decrease exponentially in subsequent years, and often return to ambient levels within a decade (Major et al., 2000). Thin tephra-fall deposits (i.e., <10 cm) might erode or stabilize on the order of a year, depending on local rain fall rates, topographic slope, and vegetation recovery (Collins and Dunne, 1986).

Chemical and mechanical processes can form mineralogical “crusts” on the surface layer of some tephra-fall deposits (e.g., Segerstrom et al., 1956; Smith and Swanson, 1987). In addition to significantly reducing infiltration rates (Leavesley et al., 1989), crust formation can reduce the airborne entrainment potential for fine-grained particles. The timing for crust formation depends on the composition and grain size of the deposit, and local environmental variables. Finer-grained deposits that appear analogous to potential deposits at the proposed site might form crusts after several rainfall events, over periods of tens of days (i.e., Sehmel, 1982).

Resuspension of fine (<0.1 mm) tephra particles occurs when the wind velocity over a static or disturbed tephra deposit exceeds the threshold velocity for particle saltation and airborne entrainment (Alfaro et al., 1998; Del Bello et al., 2021). Field and laboratory measurements show that particle saltation and subsequent resuspension can occur with wind speeds <0.5 m/s (Alfaro et al., 1998; Etyemezian et al., 2019; Del Bello et al., 2021). As discussed in Del Bello et al. (2021), the roughness of the tephra deposit, deposit moisture, and local vegetation can strongly affect the potential for particle entrainment. The sparse vegetation and semi-arid conditions at the proposed site would enhance the ability for entrainment and resuspension of <0.1 mm tephra particles.

Measurements of post-eruption airborne particle concentrations on undisturbed deposits show large variations that reflect distances to the volcano, particle grain sizes, and local environmental conditions. Most of these measurements, however, focus on deposits <100 km from the volcano, and on the <0.01 mm particles that can potentially affect human health. Several studies have examined deposits >100 km from the source volcano, which also appear reasonably analogous to potential conditions at the proposed site:

- For 2 months after the 2010 andesitic eruption of Eyjafjallajökull volcano, Iceland, airborne particle concentrations (<0.01 mm diameter) were as high as 2 mg/m^3 at a location 130 km from the volcano (Thorsteinsson et al., 2012).

- In the first month after the dacitic 1980 eruption of Mount St. Helens, WA, air monitoring stations at locations with tephra-fall deposits 100–500 km from the volcano recorded airborne concentrations of <0.1 mm particles that reached daily maximums of 0.2–3.5 mg/m^3 (Olsen and Fruchter, 1986).

- Three years of monitoring for the 1995 dacitic eruption of Montserrat volcano, West Indies measured annual average concentrations of <0.01 mm tephra particles on the order of 0.03–0.15 mg/m^3, with daily measurements ranging from <5–900 mg/m^3 (Searl, 2002). Based on measured grain-size characteristics in the tephra-fall deposits, the airborne concentrations of all <0.1 mm particles are likely 4x these values.

- In the first four months after the 2011 rhyolitic eruption of Cordón Calle volcano, Chile, airborne particle (<0.01 mm) concentrations measured 240 km from the vent ranged from <0.1 mg/m^3 to 1.5 mg/m^3 in areas that had 5-cm-thick tephra-fall deposits (Elissondo et al., 2016). These concentrations decreased to <0.1 mg/m^3 in the subsequent 6 months.

These examples indicate that the airborne concentrations of tephra particles <0.1 mm diameter might be as high as 1–4 mg/m^3 in the first month or several months immediately after the eruption, and decrease by an order of magnitude in subsequent months.

Surface-disturbing activities can significantly increase airborne particle concentrations for short periods of time. Activities with light disturbances (e.g., walking) result in small (<2x) increases in airborne particle concentrations. In contrast, heavy surface-disturbing activities (e.g., driving, sweeping, shoveling) can result in an order-of-magnitude increase in airborne particle concentrations while the activities are ongoing (e.g., Buist et al., 1986; Searl, 2002; Martin et al., 2009).

A detailed study by Sehmel (1982) measured the airborne concentrations of tephra particles in the five months following the May 1980 eruption of Mount St. Helens, WA. Although this study mostly evaluated particles <0.06 mm in diameter, the observed variations in airborne particle concentrations appear to correlate with the limited number of measurements of <0.1 mm concentrations. All measurements were conducted at two sites approximately 200 km east of the volcano, which received 1–4 mm of ash from the May 18, 1980 eruption (Sehmel, 1982).

Sehmel (1982) observed that decreases in airborne particle concentrations correlated with two rainfall events in May and June 1980, which led to the formation of a thin crust on the tephra deposit. Subsequent rainfall events in June, however, did not affect airborne particle concentrations, which remained relatively constant for the crusted deposit. Higher airborne particle concentrations correlated with higher daily wind speeds, which averaged approximately 3.6 m/s (Sehmel, 1982). From May 19 through June, airborne particle concentrations decreased by an order of magnitude, then decreased very gradually from July through September 1980. Sehmel (1982) concluded that the half-life for decay of the airborne particle concentrations was greater than 4 months, and that the effective weathering rate of the deposit had a half-life on the order of 50 days.

10 CONSIDERATIONS FOR POTENTIAL TEPHRA-FALL EVENTS AT THE PROPOSED FACILITY

Potential tephra falls represent unanticipated events, which have annual likelihoods $<10^{-6}$ but the potential to form deposits at the proposed site from <1 mm to approximately 1 m thick in episodes of tens to possibly hundreds of hours duration. The possible effects of tephra falls on nuclear installations are only broadly constrained, but appear to have the potential to affect human health, performance of SSCs, and operations of nuclear power plants and other nuclear installations (e.g., International Atomic Energy Agency, 2016). This section provides considerations for evaluating the potential effects of tephra-fall events at the proposed Natrium™ facility, using general information on human health, SSC characteristics, and operational activities. This information can be used to guide more focused evaluations of these topics using plant-specific information, as warranted.

10.1 Human Health and Safety

Volcanic ash has the potential to present both acute and chronic health effects in humans. Most of these effects result from inhalation of fine-grained (i.e., <10 μm) ash, but airborne ash can also cause trauma to eyes, and inhalable particles (i.e., <100 μm) can affect the upper respiratory system (Horwell and Baxter, 2006). Consequently, personnel involved in outdoor activities should be equipped with appropriate respiration protection, such as a fitted N95 or higher mask, and closed goggles that lack side vents. Although light wetting of tephra deposits can reduce airborne particle concentrations during removal activities, too much wetting can result in the deposit becoming cohesive and difficult to remove (e.g., https://www.ivhhn.org/).

Thin (0.1–5 mm) tephra deposits on roads and walkways can create a small reduction in skid resistance, which can be accommodated by lowering vehicle speeds and enhanced caution on walkways (Blake et al., 2017b). In addition, visibility will be reduced on roads with even thin (i.e., 1 mm) deposits, due to mechanical disturbance from vehicles (Blake et al., 2017a). Airborne ash can enter most openings in vehicles and abrade moving parts (e.g., brake assemblies), due to the relatively high hardness of tephra particles (Section 9.1). Ash will etch glass and significantly reduce visibility, if trapped by moving components such as windshield wipers or window scrapers. Most importantly, ash will rapidly clog air filters, requiring increased maintenance cycles for air and oil filtration systems to avoid significant wear to internal components (Wilson et al., 2012). All of these factors could lead to the inability of personnel to travel to the proposed facility for scheduled operations.

A volcanic tephra-fall event would affect a wide area outside of the proposed site, and would likely cause disruption of electrical supplies and potentially contaminate surface or municipal water systems (Wilson et al., 2014). These factors might affect the ability of personnel to perform required functions, if they are occupied with mitigating the effects of the tephra-fall event at their homes or community.

10.2 SSC Performance

The effects of volcanic tephra on nuclear SSCs is generally constrained by information from analogous industrial systems, most of which is based on empirical observations rather than rigorous testing (International Atomic Energy Agency, 2016). The generalized information from International Atomic Energy Agency (2016) and elsewhere is discussed in context of the specific hazards at the proposed site.

10.2.1 Air Handling Systems

Airborne tephra (<2 mm diameter) can reach concentrations of 10–30 g/m^3 during the eruption, with concentrations of 1–10 mg/m^3 for resuspended <0.1 mm particles in the days immediately after the eruption (Sections 9.6–9.7). The concentrations of resuspended airborne particles <0.1 mm diameter might be as high as 1–4 mg/m^3 in the first month or months immediately after the eruption, and decrease by an order of magnitude in subsequent months. Surface disturbing activities also can result in transient concentrations of 1–10 mg/m^3. Consequently, heating, ventilation, and air conditioning (HVAC) systems, in addition to other air handling systems, could be disrupted by ingress of airborne tephra.

The site-specific tephra-fall hazard has a 95th percentile deposit thickness of 11.9 cm for a VEI4–5 eruption from the Yellowstone volcanic field (1.7x10^{-8}/yr probability of exceedance), and a 95th percentile deposit thickness of 113 cm for a VEI8 supervolcano eruption from Yellowstone caldera (7x10^{-8}/yr probability of exceedance) (Table 51). Consequently, air intakes located <113 cm above ground or roof level have the potential to be physically blocked by a non-mitigated tephra-fall deposit.

The relatively high concentrations of airborne tephra particles 1–100 µm in diameter have the potential to degrade the performance of air filtration systems, which could reduce overall system performance and the function of dependent systems. HVAC systems also are vulnerable to abrasion and corrosion from volcanic ash, and have the potential to inject ash into building interiors if not properly filtered and maintained (Wilson et al., 2012).

10.2.2 Electrical Systems

Electrical generation and transmission facilities are susceptible to insulator flashover from tephra-fall deposits, which can disrupt the power supply to the proposed facility. The flashover susceptibility is enhanced if the ash is lightly wetted (e.g., light rainfall or high humidity), which enhances the solubility of leachable salts on the particle surfaces (Wardman et al., 2012).

Gravel substrate in electrical substations and switch yards has a known resistivity to provide protection from electrical hazards. Moistened tephra-fall deposits could reduce the resistivity of these substrates, and potentially increase the likelihood of electrocution hazard (Wardman et al., 2012).

Electrical switches that have mechanical components (e.g., self-cleaning contacts) can experience abrasion, clogging, and potentially corrosion if exposed to volcanic ash (Wilson et al., 2012). Modern computer components and electronics, however, do not appear to be vulnerable to exposures of dry volcanic ash, and minor ash accumulations on keyboards and internal components can be safely removed with compressed air (Gordon et al., 2005).

10.2.3 Mechanical Systems

The hardness of volcanic tephra is typically 5–6 on the Moh's scale (i.e., Rockwell C 51.4–64.6, Vickers 535–817 kgf/mm^2), but some mineral components can have hardness of 7 on the Moh's scale (Rockwell C = 71, Vickers = 1160 kgf/mm^2). Consequently, volcanic ash can be abrasive and adversely affect the performance of mechanical systems (e.g., Wilson et al., 2014).

Electrical motors and fans are particularly susceptible to abrasion effects, as electrostatically charged ash particles favor deposition on weak electrical fields (i.e., Wardman et al., 2012). Enhanced abrasion also can occur on drive belt assemblies exposed to volcanic ash. The

impacts of volcanic ash on mechanical systems, however, can be largely mitigated by preventing ash ingress into controlled areas, and enhancing maintenance to remove ash accumulations on mechanical equipment (Wilson et al., 2012).

10.2.4 Structural Loads

Tephra deposits will accumulate on surfaces with <36–37º slopes (Osman et al., 2022). Potential tephra-deposit densities at the proposed site can range from 600–1,500 kg/m^3 when dry, to 1,280–2,180 kg/m^3 when wet (Section 9.5). Mafic tephra deposits have a 95th percentile thickness of 2.7 cm (Table 26), which could give loads of 40.5 kg/m^2 (8.3 lbs/ft^2) when dry to 58.9 kg/m^2 (12.2 lbs/ft^2) when wet.

Excluding deposits from VEI8 Yellowstone supervolcano eruption, silicic tephra deposits have a 95th percentile thickness of 14 cm (Table 51), which could give loads of 84 kg/m^2 (17.2 lbs/ft^2) when dry to 179 kg/m^2 (36.7 lbs/ft^2) when wet.

If a VEI8 Yellowstone eruption occurs, 113 cm of tephra deposit could accumulate at the site (Table 51), which could give loads of 678 kg/m^2 (139 lbs/ft^2) when dry to 1,450 kg/m^2 (296 lbs/ft^2) when wet.

10.3 Operational Activities

Tephra-fall events should be preceded by at least 1 hr of warning between the onset of an eruption and arrival of tephra falls at the proposed site, based on the time it takes for large eruption plumes to spread and for tephra to fall to the ground from high altitudes. In addition, episodes of volcanic unrest are expected to occur in the days to potentially weeks preceding an eruption. Consequently, mitigation actions appear practicable to assure the continued safe operation, or controlled shutdown, of the proposed facility in the event of a tephra-fall hazard at the site.

Many of the potentially adverse effects from tephra-fall hazards can be mitigated by operational actions:

- Dry tephra deposits can be removed from building roofs by shoveling or sweeping. If practicable, these deposits should be removed before rainfall increases the deposit weight and increases cohesivity. Removal from paved surfaces also is advisable, to reduce hazards from loss of traction due to tephra deposits.

- Dry tephra deposits can be removed from electrical insulators and mechanical equipment using compressed air. If practicable, these deposits should be removed before high humidity or light rainfall increases the conductivity of the deposit.

- Air filtration systems will likely require enhanced monitoring and maintenance due to elevated concentrations of airborne particles that might persist for weeks to months after an eruption.

- Internal combustion engines will likely require enhanced maintenance cycles for air and oil filtration systems. Addition inspections should also be conducted for degradation of mechanical systems from the abrasive effects of ash.

- Reduced visibility during vehicle operations can be mitigated by lowering speeds and increasing following distances between vehicles.

- Personnel involved in mitigation activities will need to be equipped with fitted respirators (i.e., N95 or greater) and closed-sided goggles, in addition to other routine personal protective equipment. In particular, respirator filters will need to be changed frequently due to the high airborne particle concentrations associated with surface-disturbing activities.

If a volcano in the site region shows indications of unrest (i.e., above-background activity in one or several processes associated with potential eruptions), staff at the USGS Yellowstone Volcano Observatory will have primary responsibility to evaluate those indications and issue potential alert notices. Alert notices are distributed through a Web service subscription at https://www.usgs.gov/programs/VHP/volcano-updates. These notices indicate:

- Normal = Volcano is in typical background, non-eruptive state, or has returned to that state following an increase in alert level.

- Advisory = Volcano is exhibiting signs of elevated unrest above known background level.

- Watch = Volcano is exhibiting heightened or escalating unrest with increased potential of eruption, but the timeframe for the eruption is uncertain.

- Warning = Hazardous eruption is imminent, underway, or suspected.

The hazards assessments in this report were conducted within a probabilistic framework that evaluates a broad range of potential conditions or scenarios. In the event of an actual volcanic eruption, these hazard estimates can be refined with more advanced models such as the USGS Ash3d code, using parameters that evaluate real-time conditions for the forecast eruption and atmosphere. Even though a volcano might potentially erupt in the site region, the characteristics of the eruption and the actual atmospheric conditions at the time of the eruption could preclude deposition of tephra at the proposed site.

11 REFERENCES

Alfano, F., Bonadonna, C., Delmelle, P., and Costantini, L., 2011, Insights on tephra settling velocity from morphological observations: Journal of Volcanology and Geothermal Research, v. 208, p. 86–98, doi:10.1016/j.jvolgeores.2011.09.013.

Alfano, F., Bonadonna, C., Watt, S., Connor, C., Volentik, A., and Pyle, D.M., 2016, Reconstruction of total grain size distribution of the climactic phase of a long-lasting eruption: the example of the 2008–2013 Chaitén eruption: Bulletin of Volcanology, v. 78, p. 46, doi:10.1007/s00445-016-1040-5.

Alfano, F., Ort, M.H., Pioli, L., Self, S., Hanson, S.L., Roggensack, K., Allison, C.M., Amos, R., and Clarke, A.B., 2019, Subplinian monogenetic basaltic eruption of Sunset Crater, Arizona, USA: Geological Society of America Bulletin, v. 131, p. 14.

Alfaro, S.C., Gaudichet, A., Gomes, L., and Maillé, M., 1998, Mineral aerosol production by wind erosion: Aerosol particle sizes and binding energies: Geophysical Research Letters, v. 25, p. 991–994, doi:10.1029/98GL00502.

Anders, M.H., Geissman, J.W., Piety, L.A., and Sullivan, J.T., 1989, Parabolic distribution of circumeastern Snake River Plain seismicity and latest Quaternary faulting: Migratory pattern and association with the Yellowstone hotspot: Journal of Geophysical Research, v. 94, p. 1589, doi:10.1029/JB094iB02p01589.

Anderson, S.R., Liszewski, M.J., and Cecil, L.D., 1997, Geologic Ages and Accumulation Rates of Basalt-Flow Groups and Sedimentary Interbeds in Selected Wells at the Idaho National Engineering Laboratory, Idaho: U.S. Geological Survey Water-Resources Investigations Report 97–4010, 43 p.

Armstrong, R.L., Leeman, W.P., and Malde, H.E., 1975, K-Ar dating, Quaternary and Neogene volcanic rocks of the Snake River Plain, Idaho: American Journal of Science, v. 275, p. 225–251, doi:10.2475/ajs.275.3.225.

Autenrieth, K., McCurry, M., Welhan, J., and Poulon, S., 2011, Conceptual Subsurface Model of the Blackfoot Volcanic Field, Southeast Idaho: A Potential Hidden Geothermal Resource: Geothermal Resources Council Transactions, v. 35, p. 695–697.

Bebbington, M., 2013, Models for Temporal Volcanic Hazard: Statistics in Volcanology, v. 1, doi:http://dx.doi.org/10.5038/2163-338X.1.1.

Befus, K., and Gardner, J., 2016, Magma storage and evolution of the most recent effusive and explosive eruptions from Yellowstone Caldera: Contributions to Mineralogy and Petrology, v. 171, doi:10.1007/s00410-016-1244-x.

Benson, L.V., Lund, S.P., Smoot, J.P., Rhode, D.E., Spencer, R.J., Verosub, K.L., Louderback, L.A., Johnson, C.A., Rye, R.O., and Negrini, R.M., 2011, The rise and fall of Lake Bonneville between 45 and 10.5 ka: Quaternary International, v. 235, p. 57–69, doi:10.1016/j.quaint.2010.12.014.

Bernstein, R.S., Baxter, P.J., Falk, H., Ing, R., Foster, L., and Frost, F., 1986, Immediate public health concerns and actions in volcanic eruptions: lessons from the Mount St. Helens

eruptions, May 18-October 18, 1980: American journal of public health, v. 76 3 Suppl, p. 25–37.

Blackstone, D.L., 1966, Pliocene vulcanism, southern Absaroka Mountains, Wyoming: Rocky Mountain Geology, v. 5, p. 21–30.

Blake, D.M., Deligne, N.I., Wilson, T.M., and Wilson, G., 2017a, Improving volcanic ash fragility functions through laboratory studies: example of surface transportation networks: Journal of Applied Volcanology, v. 6, p. 16, doi:10.1186/s13617-017-0066-5.

Blake, D., Wilson, T., Cole, J., Deligne, N., and Lindsay, J., 2017b, Impact of Volcanic Ash on Road and Airfield Surface Skid Resistance: Sustainability, v. 9, p. 1389, doi:10.3390/su9081389.

Blong, R.J., 1981, Some Effects of Tephra Falls on Buildings, *in* Self, S. and Sparks, R.S.J. eds., Tephra Studies, Dordrecht, Springer Netherlands, NATO Advanced Study Institutes Series, p. 405–420, doi:10.1007/978-94-009-8537-7_27.

Bonadonna, C., Connor, C.B., Houghton, B.F., Connor, L., Byrne, M., Laing, A., and Hincks, T.K., 2005, Probabilistic modeling of tephra dispersal: Hazard assessment of a multiphase rhyolitic eruption at Tarawera, New Zealand: Journal of Geophysical Research, v. 112, p. B03203, doi:doi:10.1029/2003JB002896.

Bonadonna, C., and Phillips, J.C., 2003, Sedimentation from strong volcanic plumes: Journal of Geophysical Research: Solid Earth, v. 108, doi:10.1029/2002JB002034.

Bonasia, R., and Scaini, C., 2015, A Review of Tephra Transport and Dispersal Modeling Strategies and Applications to Far-Range Hazard Assessment at Some of the Most Active Volcanoes in the World, *in* Danielle Graver, ed., Volcanic Ash, Nova Science Publishers, Inc., p. 41–68.

Branney, M., and Acocella, V., 2015, Chapter 16 - Calderas, *in* Sigurdsson, H. ed., The Encyclopedia of Volcanoes (Second Edition), Amsterdam, Academic Press, p. 299–315, doi:10.1016/B978-0-12-385938-9.00016-X.

Brown, R.J., and Andrews, D.M., 2015, Chapter 36 - Deposits of Pyroclastic Density Currents, *in* Sigurdsson, H. ed., The Encyclopedia of Volcanoes (Second Edition), Amsterdam, Academic Press, p. 631–648, doi:10.1016/B978-0-12-385938-9.00036-5.

Brueseke, M.E., Downey, A.C., Dodd, Z.C., Hart, W.K., Adams, D.C., and Benowitz, J.A., 2018, The leading wisps of Yellowstone: Post–ca. 5 Ma extension-related magmatism in the upper Wind River Basin, Wyoming (USA), associated with the Yellowstone hotspot tectonic parabola: Geosphere, v. 14, p. 74–94, doi:10.1130/GES01553.1.

Buckland, H.M., Cashman, K.V., Engwell, S.L., and Rust, A.C., 2020, Sources of uncertainty in the Mazama isopachs and the implications for interpreting distal tephra deposits from large magnitude eruptions: Bulletin of Volcanology, v. 82, p. 23, doi:10.1007/s00445-020-1362-1.

Buist, A.S., Martin, T.R., Shore, J.H., Butler, J., and Lybarger, J.A., 1986, The development of a multidisciplinary plan for evaluation of the long-term health effects of the Mount St.

Helens eruptions: American Journal of Public Health, v. 76, p. 39–44, doi:10.2105/AJPH.76.Suppl.39.

Calder, E.S., Lavallée, Y., Kendrick, J.E., and Bernstein, M., 2015, Chapter 18 - Lava Dome Eruptions, *in* Sigurdsson, H. ed., The Encyclopedia of Volcanoes (Second Edition), Amsterdam, Academic Press, p. 343–362, doi:10.1016/B978-0-12-385938-9.00018-3.

Camp, V.E., Pierce, K.L., and Morgan, L.A., 2015, Yellowstone plume trigger for Basin and Range extension, and coeval emplacement of the Nevada–Columbia Basin magmatic belt: Geosphere, v. 11, p. 203–225, doi:10.1130/GES01051.1.

Camp, V., and Wells, R., 2021, The Case for a Long-Lived and Robust Yellowstone Hotspot: GSA Today, v. 31, p. 4–10, doi:10.1130/GSATG477A.1.

Carey, S.N., and Sigurdsson, H., 1982, Influence of particle aggregation on deposition of distal tephra from the MAy 18, 1980, eruption of Mount St. Helens volcano: Journal of Geophysical Research: Solid Earth, v. 87, p. 7061–7072, doi:10.1029/JB087iB08p07061.

Carter, J.R., and Green, A.R., 1963, Floods in Wyoming, magnitude and frequency: U.S. Geological Survey Circular 478, doi:10.3133/cir478.

Carter, A.J., Ramsey, M.S., Durant, A.J., Skilling, I.P., and Wolfe, A., 2009, Micron-scale roughness of volcanic surfaces from thermal infrared spectroscopy and scanning electron microscopy: Journal of Geophysical Research: Solid Earth, v. 114, doi:10.1029/2008JB005632.

Cas, R.A.F., and Wright, J.V., 1987, Volcanic Successions Modern and Ancient: Dordrecht, Springer Netherlands, doi:10.1007/978-94-009-3167-1.

Cashman, K., and Rust, A., 2016, Volcanic Ash: Generation and Spatial Variations, *in* Mackie, S., Cashman, K., Ricketts, H., Rust, A., and Watson, M. eds., Volcanic Ash, Elsevier, p. 5–24, doi:10.1016/B978-0-08-100405-0.00002-1.

Christensen, P.R., Bandfield, J.L., Hamilton, V.E., Howard, D.A., Lane, M.D., Piatek, J.L., Ruff, S.W., and Stefanov, W.L., 2000, A thermal emission spectral library of rock-forming minerals: Journal of Geophysical Research: Planets, v. 105, p. 9735–9739, doi:10.1029/1998JE000624.

Christiansen, R.L., 2001, The Quaternary and Pliocene Yellowstone Plateau Volcanic Field of Wyoming, Idaho, and Montana: U.S. Geological Survey Professional Paper 729-G.

Christiansen, R.L., and Blank Jr., H.R., 1972, Volcanic Stratigraphy of the Quaternary Rhyolite Plateau in Yellowstone National Park: U.S. Geological Survey Professional Paper 729-B, doi:10.3133/pp729B.

Christiansen, R.L., Lowenstern, J.B., Smith, R.B., Heasler, H., Morgan, L.A., Nathenson, M., Mastin, L.G., Muffler, L.J.P., and Robinson, J.E., 2007, Preliminary Assessment of Volcanic and Hydrothermal Hazards in Yellowstone National Park and Vicinity: U.S. Geological Survey Open-File Report Report 2007–1071, doi:10.3133/ofr20071071.

Collini, E., Osores, M.S., Folch, A., Viramonte, J.G., Villarosa, G., and Salmuni, G., 2013, Volcanic ash forecast during the June 2011 Cordón Caulle eruption: Natural Hazards, v. 66, p. 389–412, doi:10.1007/s11069-012-0492-y.

Collins, B.D., and Dunne, T., 1986, Erosion of tephra from the 1980 eruption of Mount St. Helens: Geological Society of America Bulletin, v. 97, p. 896, doi:10.1130/0016-7606(1986)97<896:EOTFTE>2.0.CO;2.

Commission for Environmental Cooperation, 2022a, North America Rivers and Lakes - ScienceBase-Catalog: North America Rivers and Lakes, https://www.sciencebase.gov/catalog/item/4fb55df0e4b04cb937751e02.

Commission for Environmental Cooperation, 2022b, North America Watersheds - ScienceBase-Catalog: North America Watersheds, https://www.sciencebase.gov/catalog/item/4fb697b2e4b03ad19d64b47f.

Connor, C., Bebbington, M., and Marzocchi, W., 2015, Chapter 51 - Probabilistic Volcanic Hazard Assessment, *in* Sigurdsson, H. ed., The Encyclopedia of Volcanoes (Second Edition), Amsterdam, Academic Press, p. 897–910, doi:10.1016/B978-0-12-385938-9.00051-1.

Connor, L.J., and Connor, C.B., 2006, Inversion is the key to dispersion: understanding eruption dynamics by inverting tephra fallout, *in* Mader, H.M., Coles, S.G., Connor, C.B., and Connor, L.J. eds., Statistics in Volcanology, The Geological Society of London on behalf of The International Association of Volcanology and Chemistry of the Earth's Interior, p. 231–242, doi:10.1144/IAVCEI001.18.

Connor, C., Connor, L., Germa, A., Richardson, J., Bebbington, M., Gallant, E., and Saballos, A., 2019, How to use kernel density estimation as a diagnostic and forecasting tool for distributed volcanic vents: Statistics in Volcanology, v. 4, doi:10.5038/2163-338X.4.3.

Connor, L., Connor, C.B., and Hill, B.E., 2002, PVHA_YM Version 2.0 - Probabilistic Volcanic Hazards Assessment Methods for a Proposed High-Level Radioactive Waste Repository at Yucca Mountain, Nevada: U.S. Nuclear Regulatory Commission ADAMS ML033640083, 22 p.

Connor, L.J., Connor, C.B., Meliksetian, K., and Savov, I., 2012, Probabilistic approach to modeling lava flow inundation: a lava flow hazard assessment for a nuclear facility in Armenia: Journal of Applied Volcanology, v. 1, p. 3, doi:10.1186/2191-5040-1-3.

Connor, C.B., and Hill, B.E., 1995, Three nonhomogeneous Poisson models for the probability of basaltic volcanism: Application to the Yucca Mountain region, Nevada: Journal of Geophysical Research: Solid Earth, v. 100, p. 10107–10125, doi:10.1029/95JB01055.

Constantinescu, R., Hopulele-Gligor, A., Connor, C.B., Bonadonna, C., Connor, L.J., Lindsay, J.M., Charbonnier, S., and Volentik, A.C.M., 2021, The radius of the umbrella cloud helps characterize large explosive volcanic eruptions: Communications Earth & Environment, v. 2, p. 3, doi:10.1038/s43247-020-00078-3.

Costa, A., J. Suzuki, Y., and Koyaguchi, T., 2018, Understanding the plume dynamics of explosive super-eruptions: Nature Communications, v. 9, p. 654, doi:10.1038/s41467-018-02901-0.

Costa, A., Macedonio, G., and Folch, A., 2006, A three-dimensional Eulerian model for transport and deposition of volcanic ashes: Earth and Planetary Science Letters, p. 14.

Costa, A., Pioli, L., and Bonadonna, C., 2016, Assessing tephra total grain-size distribution: Insights from field data analysis: Earth and Planetary Science Letters, v. 443, p. 90–107, doi:10.1016/j.epsl.2016.02.040.

Del Bello, E., Taddeucci, J., Merrison, J.P., Rasmussen, K.R., Andronico, D., Ricci, T., Scarlato, P., and Iversen, J.J., 2021, Field-based measurements of volcanic ash resuspension by wind: Earth and Planetary Science Letters, v. 554, p. 116684, doi:10.1016/j.epsl.2020.116684.

Dickinson, W.R., Klute, M.A., Hayes, M.J., Janecke, S.U., Lundin, E.R., McKittrick, M.A., and Olivares, M.D., 1988, Paleogeographic and paleotectonic setting of Laramide sedimentary basins in the central Rocky Mountain region: Geological Society of America Bulletin, v. 100, p. 1023–1039, doi:10.1130/0016-7606(1988)100<1023:PAPSOL>2.3.CO;2.

Dixon, J.S., 1982, Regional Structural Synthesis, Wyoming Salient of Western Overthrust Belt: AAPG Bulletin, v. 66, doi:10.1306/03B5A98A-16D1-11D7-8645000102C1865D.

Doe, B.R., Leeman, W.P., Christiansen, R.L., and Hedge, C.E., 1982, Lead and strontium isotopes and related trace elements as genetic tracers in the Upper Cenozoic rhyolite-basalt association of the Yellowstone Plateau Volcanic Field: Journal of Geophysical Research: Solid Earth, v. 87, p. 4785–4806, doi:10.1029/JB087iB06p04785.

Donnelly-Nolan, J.M., Champion, D.E., and Grove, T.L., 2016, Late Holocene volcanism at Medicine Lake Volcano, northern California Cascades: U.S. Geological Survey Professional Paper 1822, doi:10.3133/pp1822.

Dover, J.H., 1995, Geologic map of the Logan 30’ x 60’ Quadrangle, Cache and Rich counties, Utah, and Lincoln and Uinta counties, Wyoming: U.S. Geological Survey Miscellaneous Investigations Map I-2210.

Dover, J.H., and McGonigle, J.W., 1993, Geologic map of the Evanston 30’ x 60’ Quadrangle, Uinta and Sweetwater counties, Wyoming: U.S. Geological Survey Miscellaneous Investigations Map I-2168.

Downey, A.C., 2015, Cenozoic Mafic to Intermediate Volcanism at Lava Mountain and Spring Mountain, Upper Wind River Basin, Wyoming [Thesis]: SUNY Oneanta, 109 p.

Doyle, E.E., Cronin, S.J., and Thouret, J.-C., 2011, Defining conditions for bulking and debulking in lahars: Geological Society of America Bulletin, v. 123, p. 1234–1246, doi:10.1130/B30227.1.

Dufek, J., Esposti Ongaro, T., and Roche, O., 2015, Chapter 35 - Pyroclastic Density Currents: Processes and Models, *in* Sigurdsson, H. ed., The Encyclopedia of Volcanoes (Second

Edition), Amsterdam, Academic Press, p. 617–629, doi:10.1016/B978-0-12-385938-9.00035-3.

Elissondo, M., Baumann, V., Bonadonna, C., Pistolesi, M., Cioni, R., Bertagnini, A., Biass, S., Herrero, J.-C., and Gonzalez, R., 2016, Chronology and impact of the 2011 Cordón Caulle eruption, Chile: Natural Hazards and Earth System Sciences, v. 16, p. 675–704, doi:10.5194/nhess-16-675-2016.

Etyemezian, V., Gillies, J.A., Mastin, L.G., Crawford, A., Hasson, R., Van Eaton, A.R., and Nikolich, G., 2019, Laboratory Experiments of Volcanic Ash Resuspension by Wind: Journal of Geophysical Research: Atmospheres, v. 124, p. 9534–9560, doi:10.1029/2018JD030076.

Farquharson, J.I., James, M.R., and Tuffen, H., 2015, Examining rhyolite lava flow dynamics through photo-based 3D reconstructions of the 2011–2012 lava flowfield at Cordón-Caulle, Chile: Journal of Volcanology and Geothermal Research, v. 304, p. 336–348, doi:10.1016/j.jvolgeores.2015.09.004.

Felger, T.J., Miller, D.M., Langenheim, V.E., and Fleck, R.J., 2016, Geologic and geophysical maps and volcanic history of the Kelton Pass SE and Monument Peak SW quadrangles, Box Elder County, Utah: Salt Lake City, Utah, Utah Geological Survey, Miscellaneous Publication 16–1DM.

Fenneman, N., and Johnson, D., 1946, Physical Divisions of the USA: U.S. Geological Survey.

Fink, J.H. (Ed.), 1990, Lava Flows and Domes: Berlin, Heidelberg, Springer Berlin Heidelberg, IAVCEI Proceedings in Volcanology, v. 2, doi:10.1007/978-3-642-74379-5.

Folch, A., 2012, A review of tephra transport and dispersal models: Evolution, current status, and future perspectives: Journal of Volcanology and Geothermal Research, v. 235–236, p. 96–115, doi:10.1016/j.jvolgeores.2012.05.020.

Ford, M.T., 2005, The Petrogenesis of Quaternary Rhyolite Domes in the Bimodal Blackfoot Volcanic Field, Southeastern Idaho [Thesis]: Idaho State University, 145 p.

Fountain, J.A., and West, E.A., 1970, Thermal conductivity of particulate basalt as a function of density in simulated lunar and Martian environments: Journal of Geophysical Research, v. 75, p. 4063–4069, doi:10.1029/JB075i020p04063.

Gallant, E., Richardson, J., Connor, C., Wetmore, P., and Connor, L., 2018, A new approach to probabilistic lava flow hazard assessments, applied to the Idaho National Laboratory, eastern Snake River Plain, Idaho, USA: Geology, v. 46, p. 895–898, doi:10.1130/G45123.1.

Galyardt, G.L., and Rush, F.E., 1981, Geologic map of the Crater Springs Known Geothermal Resources Area and vicinity, Juab and Millard counties, Utah: U.S. Geological Survey Miscellaneous Investigation Series Map I–1297, doi:10.3133/i1297.

Ganseke, R.R., 2006, The Geology and Petrology of the East Butte Area, Bingham County, Idaho [Thesis]: Idaho State University, 163 p.

Gardner, J.E., Carey, S., and Sigurdsson, H., 1998, Plinian eruptions at Glacier Peak and Newberry volcanoes, United States: Implications for volcanic hazards in the Cascade Range: GSA Bulletin, v. 110, p. 173–187, doi:10.1130/0016-7606(1998)110<0173:PEAGPA>2.3.CO;2.

Goff, F., 2010, The Valles Caldera: New Mexico's Supervolcano: New Mexico Bureau Geology & Mineral Resources New Mexico Earth Matters Volume 10.

Gordon, K.D., Cole, J.W., Rosenberg, M.D., and Johnston, D.M., 2005, Effects of Volcanic Ash on Computers and Electronic Equipment: Natural Hazards, v. 34, p. 231–262, doi:10.1007/s11069-004-1514-1.

Grove, T.L., and Donnelly-Nolan, J.M., 1986, The evolution of young silicic lavas at Medicine Lake Volcano, California: Implications for the origin of compositional gaps in calc-alkaline series lavas: Contributions to Mineralogy and Petrology, v. 92, p. 281–302, doi:10.1007/BF00572157.

Gudmundsson, M.T., 2015, Chapter 56 - Hazards from Lahars and Jökulhlaups, *in* Sigurdsson, H. ed., The Encyclopedia of Volcanoes (Second Edition), Amsterdam, Academic Press, p. 971–984, doi:10.1016/B978-0-12-385938-9.00056-0.

Gudnason, J., Thordarson, T., Houghton, B.F., and Larsen, G., 2017, The opening subplinian phase of the Hekla 1991 eruption: properties of the tephra fall deposit: Bulletin of Volcanology, v. 79, p. 34, doi:10.1007/s00445-017-1118-8.

Gunter, W.D., Hoinkes, G., Ogden, P., and Pajari, G.E., 1990, Origin of leucite-rich and sanidine-rich flow layers in the Leucite Hills Volcanic Field, Wyoming: Journal of Geophysical Research, v. 95, p. 15911, doi:10.1029/JB095iB10p15911.

Hackett, W.R., Smith, R.P., and Khericha, S., 2002, Volcanic Hazards of the Idaho National Engineering and Environmental Laboratory, Southeast Idaho, *in* Bill Bonnichsen, C.M. White, and Michael McCurry, eds., Tectonic and Magmatic Evolution of the Snake River Plain Volcanic Province, Idaho Geological Survey, Bulletin 30, p. 461–482.

Harry, D.L., and Leeman, W.P., 1995, Partial melting of melt metasomatized subcontinental mantle and the magma source potential of the lower lithosphere: Journal of Geophysical Research: Solid Earth, v. 100, p. 10255–10269, doi:10.1029/94JB03065.

Hastings, M.S., Connor, C.B., Wetmore, P., Malservisi, R., Connor, L.J., Rodgers, M., and La Femina, P.C., 2021, Large-Volume and Shallow Magma Intrusions in the Blackfoot Reservoir Volcanic Field (Idaho, USA): Journal of Geophysical Research: Solid Earth, v. 126, doi:10.1029/2021JB022507.

Hayden, K., 1992, The Geology and Petrology of Cedar Butte, Bingham County, Idaho [Thesis]: Idaho State University, 119 p.

Hedman, E.R., and Osterkamp, W.R., 1982, Streamflow characteristics related to channel geometry of streams in western United States: U.S. Geological Survey Water Supply Paper 2193, doi:10.3133/wsp2193.

Heiken, G., 1978, Plinian-type eruptions in the Medicine Lake Highland, California, and the nature of the underlying magma: Journal of Volcanology and Geothermal Research, v. 4, p. 375–402, doi:10.1016/0377-0273(78)90023-9.

Heumann, A., 2004, Timescales of evolved magma generation at Blackfoot Lava Field, SE Idaho , USA:, *in* IAVCEI 2004 General Assembly: Proceedings with Abstracts, Pucon, Chile, IAVCEI, doi:10.13140/RG.2.2.21107.27682.

Hildreth, W., Halliday, A.N., and Christiansen, R.L., 1991, Isotopic and Chemical Evidence Concerning the Genesis and Contamination of Basaltic and Rhyolitic Magma Beneath the Yellowstone Plateau Volcanic Field: Journal of Petrology, v. 32, p. 63–138, doi:10.1093/petrology/32.1.63.

Hildreth, W., and Wilson, C.J.N., 2007, Compositional Zoning of the Bishop Tuff: Journal of Petrology, v. 48, p. 951–999, doi:10.1093/petrology/egm007.

Hill, B.E., Connor, C.B., Jarzemba, M.S., La Femina, P.C., Navarro, M., and Strauch, W., 1998, 1995 eruptions of Cerro Negro volcano, Nicaragua, and risk assessment for future eruptions: Geological Society of America Bulletin, v. 110, p. 1231–1241, doi:10.1130/0016-7606(1998)110<1231:EOCNVN>2.3.CO;2.

Horai, K., 1991, Thermal conductivity of Hawaiian basalt: A new interpretation of Robertson and Peck's data: Journal of Geophysical Research: Solid Earth, v. 96, p. 4125–4132, doi:10.1029/90JB02452.

Horton, J.D., 2017, The State Geologic Map Compilation (SGMC) Geodatabase of the Conterminous United States:, doi:10.5066/F7WH2N65.

Horwell, C.J., and Baxter, P.J., 2006, The respiratory health hazards of volcanic ash: a review for volcanic risk mitigation: Bulletin of Volcanology, v. 69, p. 1–24, doi:10.1007/s00445-006-0052-y.

Hughes, S.S., Wetmore, P.H., and Casper, J.L., 2002, Evolution of Quaternary Tholeiitic Basalt Eruptive Centers on the Eastern Snake River Plain, Idaho, *in* Bill Bonnichsen, C.M. White, and Michael McCurry, eds., Tectonic and Magmatic Evolution of the Snake River Plain Volcanic Province, Idaho Geological Survey, Bulletin 30, p. 363–385.

International Atomic Energy Agency, 2016, Volcanic Hazard Assessments for Nuclear Installations: Methods and Examples in Site Evaluation: International Atomic Energy Agency IAEA-TECDOC 1795, https://www.iaea.org/publications/11063/volcanic-hazard-assessments-for-nuclear-installations-methods-and-examples-in-site-evaluation.

Iwahashi, G.S., 2010, Physical and compositional implications for the evolution of Spencer-High Point Volcanic Field, Idaho [Thesis]: Idaho State University, 179 p.

Izett, G.A., 1981, Volcanic ash beds: Recorders of Upper Cenozoic silicic pyroclastic volcanism in the western United States: Journal of Geophysical Research: Solid Earth, v. 86, p. 10200–10222, doi:10.1029/JB086iB11p10200.

Izett, G.A., Obradovich, J.D., and Mehnert, 1988, The Bishop ash bed (middle Pleistocene) and some older (Pliocene and Pleistocene) chemically and mineralogically similar ash beds

in California, Nevada, and Utah: U.S. Geological Survey Bulletin 1675, doi:10.3133/b1675.

Izett, G., and Wilcox, R., 1982, Map showing localities and inferred distributions of the Huckleberry Ridge, Mesa Falls, and Lava Creek ash beds (Pearlette family ash beds) of Pliocene and Pleistocene age in the western United States and southern Canada: U.S. Geological Survey Miscellaneous Investigations Map I-1325, doi:10.3133/i1325.

Janecke, S.U., 2007, Cenozoic extensional processes and tectonics in the northern Rocky Mountains: southwest Montana and eastern Idaho: Northwest Geology, v. 36, p. 111–132.

Jarzemba, M., LaPlante, P., and Poor, K., 1997, ASHPLUME Version 1.0 - A Code for Contaminated Ash Dispersal and Deposition - Technical Description and User's Guide: U.S. Nuclear Regulatory Commission ADAMS ML040200038.

Johnsen, R.L., Smith, E.I., and Biek, R.F., 2010, Subalkaline Volcanism in the Black Rock Desert and Markagunt Plateau Volcanic Fields of South-Central Utah, *in* S.M Carney, D.E. Tabet, and C.L. Johnson, eds., Geology of South-Central Utah, Utah Geological Association, Publication 39, p. 42.

Jones, M., and Gislason, S., 2008, Rapid releases of metal salt and nutrient following the deposition of volcanic ash into aqueous environments: Geochimica et Cosmochimica Acta, v. 72, p. 3661–3680, doi:10.1016/j.gca.2008.05.030.

Jones, R., Thomas, R.E., Peakall, J., and Manville, V., 2017, Rainfall-runoff properties of tephra: Simulated effects of grain-size and antecedent rainfall: Geomorphology, v. 282, p. 39–51, doi:10.1016/j.geomorph.2016.12.023.

Kappel, B., Muhlestein, G., Hultstrand, D., McGlone, D., Steinhilber, K., Lawrence, B., Rodel, J., Parzybok, T., and Tomlinson, E., 2014, Probable Maximum Precipitation Study for Wyoming: Wyoming Water Development Office, 154 p., https://wwdc.state.wy.us/PMP/final-report.pdf.

Keefer, W.R., 1957, Geology of the Du Noir Area, Fremont County, Wyoming: U.S. Geological Survey Professional Paper Professional Paper 294-E.

Kellogg, K.S., and Marvin, R.F., 1988, New potassium-argon ages, geochemistry, and tectonic setting of upper Cenozoic volcanic rocks near Blackfoot, Idaho: U.S. Geological Survey Bulletin 1806, doi:10.3133/b1806.

Kerr, S.B., 1987, Petrology of Pliocene (?) Basalts of Curlew Valley (Box Elder Co.), Utah [Thesis]: Utah State University, 95 p.

Kienle, J., Kyle, P.R., Self, S., Motyka, R.J., and Lorenz, V., 1980, Ukinrek Maars, Alaska, I. April 1977 eruption sequence, petrology and tectonic setting: Journal of Volcanology and Geothermal Research, v. 7, p. 11–37, doi:10.1016/0377-0273(80)90018-9.

Kilburn, C.R.J., 1996, Patterns and Predictability in the Emplacement of Subaerial Lava Flows and Flow Fields, *in* Scarpa, R. and Tilling, R.I. eds., Monitoring and Mitigation of Volcano Hazards, Berlin, Heidelberg, Springer, p. 491–537, doi:10.1007/978-3-642-80087-0_15.

Klawonn, M., Houghton, B.F., Swanson, D.A., Fagents, S.A., Wessel, P., and Wolfe, C.J., 2014, Constraining explosive volcanism: subjective choices during estimates of eruption magnitude: Bulletin of Volcanology, v. 76, p. 793, doi:10.1007/s00445-013-0793-3.

Kuntz, M.A., Champion, D.E., Lefebvre, R.H., and Covington, H.R., 1988, Geologic map of the Craters of the Moon, Kings Bowl, and Wapi Lava Fields, and the Great Rift Volcanic Rift Zone, south-central Idaho: U.S. Geological Survey Miscellaneous Investigations MAP-1632.

Kuntz, M.A., Champion, D.E., Spiker, E.C., and Lefebvre, R.H., 1986, Contrasting magma types and steady-state, volume-predictable, basaltic volcanism along the Great Rift, Idaho: Geological Society of America Bulletin, v. 97, p. 579, doi:10.1130/0016-7606(1986)97<579:CMTASV>2.0.CO;2.

Kuntz, M.A., Covington, H.R., and Schorr, L.J., 1992, Chapter 12: An overview of basaltic volcanism of the eastern Snake River Plain, Idaho, *in* Link, P.K., Kuntz, M.A., and Piatt, L.B. eds., Regional Geology of Eastern Idaho and Western Wyoming, Geological Society of America, Memoir 179, p. 0, doi:10.1130/MEM179-p227.

Kuntz, M.A., and Dalrymple, B., 1979, Geology, geochronology, and potential volcanic hazards in the Lava Ridge-Hells Half Acre area, eastern Snake River Plain, Idaho: U.S. Geological Survey Open-File Report Open-File Report 79–1657.

Kuntz, M.A., Elsheimer, H.N., Espos, L.F., and Klock, P.R., 1985, Major-element analyses of latest Pleistocene-Holocene lava fields of the Snake River Plain, Idaho: U.S. Geological Survey, Open-File Report 85–593, doi:10.3133/ofr85593.

Kuntz, M.A., and Kork, J.O., 1978, Geology of the Arco-Big Southern Butte area, eastern Snake River Plain, and potential volcanic hazards to the radioactive waste management complex, and other waste storage and reactor facilities at the Idaho National Engineering Laboratory, Idaho: U.S. Geological Survey Open-File Report 78–691, doi:10.3133/ofr78691.

Kuznetsova, E., 2017, Thermal conductivity and the unfrozen water contents of volcanic ash deposits in cold climate conditions: A review: Clays and Clay Minerals, v. 65, p. 168–183, doi:10.1346/CCMN.2017.064057.

Lange, R.A., Carmichael, I.S.E., and Hall, C.M., 2000, 40Ar/39Ar chronology of the Leucite Hills, Wyoming: eruption rates, erosion rates, and an evolving temperature structure of the underlying mantle: Earth and Planetary Science Letters, v. 174, p. 329–340, doi:10.1016/S0012-821X(99)00267-8.

Leavesley, G.H., Lusby, G.C., and Lichty, R.W., 1989, Infiltration and erosion characteristics of selected tephra deposits from the 1980 eruption of Mount St. Helens, Washington, USA: Hydrological Sciences Journal, v. 34, p. 339–353, doi:10.1080/02626668909491338.

Leeman, W., 1982, Olivine tholeiitic basalts of the Snake River Plain, Idaho, *in* B. Bonnichsen, R.M. Breckenridge, Cenozoic Geology of Idaho, Idaho Bureau of Mines and Geology, Bulletin 26, p. 181–191.

Leeman, W.P., and Harry, D.L., 1993, A Binary Source Model for Extension-Related Magmatism in the Great Basin, Western North America: Science, v. 262, p. 1550–1554, doi:10.1126/science.262.5139.1550.

Legros, F., and Kelfoun, K., 2000, On the ability of pyroclastic flows to scale topographic obstacles: Journal of Volcanology and Geothermal Research, v. 98, p. 235–241, doi:10.1016/S0377-0273(99)00184-5.

Leopold, L.B., Emmett, W.W., and Myrick, R.M., 1966, Channel and hillslope processes in a semiarid area, New Mexico: U.S. Geological Survey Professional Paper 352-G, 193–249 p., doi:10.3133/pp352G.

Lesher, C.E., and Spera, F.J., 2015, Chapter 5 - Thermodynamic and Transport Properties of Silicate Melts and Magma, *in* Sigurdsson, H. ed., The Encyclopedia of Volcanoes (Second Edition), Amsterdam, Academic Press, p. 113–141, doi:10.1016/B978-0-12-385938-9.00005-5.

Lochridge, W.K., 2016, Constraining the Petrogenesis of the Quaternary Topaz Rhyolite Lava Domes in the Bimodal Blackfoot Volcanic Field, Southeastern Idaho [Thesis]: Idaho State University, 113 p.

Logan, L.M., Hunt, G.R., Salisbury, J.W., and Balsamo, S.R., 1973, Compositional implications of Christiansen frequency maximums for infrared remote sensing applications: Journal of Geophysical Research (1896-1977), v. 78, p. 4983–5003, doi:10.1029/JB078i023p04983.

Long, X., Ballmer, M.D., Córdoba, A.M. -C., and Li, C., 2019, Mantle Melting and Intraplate Volcanism Due to Self-Buoyant Hydrous Upwellings From the Stagnant Slab That Are Conveyed by Small-Scale Convection: Geochemistry, Geophysics, Geosystems, v. 20, p. 4972–4997, doi:10.1029/2019GC008591.

Luedke, R.G., and Smith, R.L., 1983, Map showing distribution, composition, and age of Late Cenozoic volcanic centers in Idaho, western Montana, west-central South Dakota, and northwestern Wyoming: U.S. Geological Survey Miscellaneous Investigations Map I-1091-E, 2 p.

Mabey, D.R., and Oriel, S.S., 1970, Gravity and magnetic anomalies in the Soda Springs region, southeastern Idaho: U.S. Geological Survey Professional Paper 646-E, doi:10.3133/pp646E.

Macedonio, G., and Costa, A., 2012, Brief Communication “Rain effect on the load of tephra deposits”: Natural Hazards and Earth System Sciences, v. 12, p. 1229–1233, doi:10.5194/nhess-12-1229-2012.

Major, J.J., Pierson, T.C., Dinehart, R.L., and Costa, J.E., 2000, Sediment yield following severe volcanic disturbance— A two-decade perspective from Mount St. Helens: Geology, v. 28, p. 819–822.

Malone, D.H., Craddock, J.P., and Konstantinou, A., 2022, Timing and structural evolution of the Sevier thrust belt, western Wyoming, *in* Craddock, J.P., Malone, D.H., Foreman, B.Z., and Konstantinou, A. eds., Tectonic Evolution of the Sevier-Laramide Hinterland, Thrust

Belt, and Foreland, and Postorogenic Slab Rollback (180–20 Ma), Geological Society of America, v. 555, p. 0, doi:10.1130/2022.2555(04).

Martin, R.S., Watt, S.F.L., Pyle, D.M., Mather, T.A., Matthews, N.E., Georg, R.B., Day, J.A., Fairhead, T., Witt, M.L.I., and Quayle, B.M., 2009, Environmental effects of ashfall in Argentina from the 2008 Chaitén volcanic eruption: Journal of Volcanology and Geothermal Research, v. 184, p. 462–472, doi:10.1016/j.jvolgeores.2009.04.010.

Mastin, L.G., Eaton, A.R.V., and Schwaiger, H.F., 2020, A probabilistic assessment of tephra-fall hazards at Hanford, Washington, from a future eruption of Mount St. Helens: U.S. Geological Survey Open-File Report 2020–1133, doi:10.3133/ofr20201133.

Mastin, L.G., Van Eaton, A.R., and Lowenstern, J.B., 2014, Modeling ash fall distribution from a Yellowstone supereruption: Geochemistry, Geophysics, Geosystems, v. 15, p. 3459–3475, doi:10.1002/2014GC005469.

Matthews, N.E., Smith, V.C., Costa, A., Durant, A.J., Pyle, D.M., and Pearce, N.J.G., 2012, Ultra-distal tephra deposits from super-eruptions: Examples from Toba, Indonesia and Taupo Volcanic Zone, New Zealand: Quaternary International, v. 258, p. 54–79, doi:10.1016/j.quaint.2011.07.010.

McBirney, A.R., and Murase, T., 1984, Rheological Properties of Magmas: Annual Review of Earth and Planetary Sciences, v. 12, p. 337–357.

McClurg, L., 1970, Source Rocks and Sediments in Drainage Area of North Eden Creek, Bear Lake Plateu, Utah-Idaho [Thesis]: Utah State University, 94 p.

McCurry, M., Hackett, W.R., and Hayden, K., 1999, Cedar Butte and Cogenetic Quaternary Rhyolite Domes of the Eastern Snake River Plain, *in* Hughes, S.S., and Thackray, G.D., eds., Guidebook to the Geology of Eastern Idaho, Idaho Museum of Natural History, p. 169–179.

McCurry, M., Hayden, K.P., Morse, L.H., and Mertzman, S., 2008, Genesis of post-hotspot, A-type rhyolite of the Eastern Snake River Plain volcanic field by extreme fractional crystallization of olivine tholeiite: Bulletin of Volcanology, v. 70, p. 361–383, doi:10.1007/s00445-007-0143-4.

McCurry, M., Pearson, D.M., Welhan, J., Natwotniak, S.K., and Fisher, M., 2015, Origin and Potential Geothermal Significance of China Hat and Other Late Pleistocene Topaz Rhyolite Lava Domes of the Blackfoot Volcanic Field, SE Idaho: Geothermal Resources Council Transactions, v. 39, p. 35–48.

McCurry, M., and Welhan, J., 2012, Do Magmatic-Related Geothermal Energy Resources Exist in Southeast Idaho? Geothermal Resources Council Transactions, v. 36, p. 699–707.

McCurry, M., Welhan, J., Poulon, S., Autenrieth, K., and Rodgers, David W., 2011, Geothermal Potential of the Blackfoot Reservoir-Soda Springs Volcanic Field: A Hidden Geothermal Resource and Natural Laboratory in SE Idaho: Geothermal Resources Council Transactions, v. 35, p. 917–924.

McGetchin, T.R., Settle, M., and Chouet, B.A., 1974, Cinder cone growth modeled after Northeast Crater, Mount Etna, Sicily: Journal of Geophysical Research, v. 79, p. 3257–3272, doi:10.1029/JB079i023p03257.

M'Gonigle, J.W., 1992, Geologic map of the Elkol quadrangle, southwestern Wyoming: U.S. Geological Survey Coal Investigations Map C–141, doi:10.3133/coal141.

M'Gonigle, J.W., 1979, Preliminary geologic map of the Warfield Creek Quadrangle, Lincoln County, southwestern Wyoming: U.S. Geological Survey Open-File Report Open-File Report 79–1176.

M'Gonigle, J.W., and Dover, J.H., 2004, Geologic map of the Kemmerer 30' x 60' quadrangle, Lincoln, Uinta, and Sweetwater counties, Wyoming: Wyoming State Geological Survey Open-File Report 04–7.

Miller, C.D., 1985, Holocene eruptions at the Inyo volcanic chain, California: Implications for possible eruptions in Long Valley caldera: Geology, v. 13, p. 14–17, doi:10.1130/0091-7613(1985)13<14:HEATIV>2.0.CO;2.

Miller, D., Nakata, J., Oviatt, C., Nash, B., and Fiesinger, D., 1995, Pliocene and Quaternary Volcanism in the Northern Great Salt Lake Area and Inferred Volcanic Hazards, *in* Environmental and Engineering Geology of the Wasatch Front Region, Utah Geol. Association, Publ. 24, v. 24, p. 469–482.

Miller, C.F., and Wark, D.A., 2008, Supervolcanoes and their Explosive Supereruptions: Elements, v. 4, p. 11–15, doi:10.2113/GSELEMENTS.4.1.11.

Mirnejad, H., and Bell, K., 2006, Origin and Source Evolution of the Leucite Hills Lamproites: Evidence from Sr-Nd-Pb-O Isotopic Compositions: Journal of Petrology, v. 47, p. 2463–2489, doi:10.1093/petrology/egl051.

Mitchell, V.E., and Bennet, E.H., 1979, Geologic Map of the Driggs Quadrangle, Idaho: Idaho Bureau of Mines & Geology Geologic Map GM-06.

Mitchell, R.H., and Bergman, S.C., 1991, Petrology of Lamproites: Boston, MA, Springer US, doi:10.1007/978-1-4615-3788-5.

Morgan, W.J., 1972, Deep Mantle Convection Plumes and Plate Motions: AAPG Bulletin, v. 56, p. 203–213, doi:10.1306/819A3E50-16C5-11D7-8645000102C1865D.

Mueller, S.B., Houghton, B.F., Swanson, D.A., Fagents, S.A., and Klawonn, M., 2018, Intricate episodic growth of a Hawaiian tephra deposit: case study of the 1959 Kīlauea Iki eruption: Bulletin of Volcanology, v. 80, p. 73, doi:10.1007/s00445-018-1249-6.

Mullineaux, D., 1974, Pumice and other pyroclastic deposits in Mount Rainier National Park, Washington: U.S. Geological Survey Bulletin 1326, doi:10.3133/b1326.

National Park Service DataStore - Geospatial Dataset - (Code: 1044842):, https://irma.nps.gov/DataStore/Reference/Profile/1044842 (accessed August 2022).

Nawotniak, S.E.K., and Bursik, M., 2010, Subplinian fall deposits of Inyo Craters, CA: Journal of Volcanology and Geothermal Research, v. 198, p. 433–446, doi:10.1016/j.jvolgeores.2010.10.005.

Newhall, C.G., and Self, S., 1982, The volcanic explosivity index (VEI) an estimate of explosive magnitude for historical volcanism: Journal of Geophysical Research: Oceans, v. 87, p. 1231–1238, doi:10.1029/JC087iC02p01231.

NOAA, 2022, NCEP/DOE Reanalysis II: NOAA Physical Sciences Laboratory NCEP/DOE Reanalysis II:, https://psl.noaa.gov/data/gridded/data.ncep.reanalysis2.html.

Nuclear Energy Institute, 2019, Risk-Informed Performance-Based Technology Guidance for Non-Light Water Reactors: Nuclear Energy Institute Technical Report 18–04, 95 p., https://www.nrc.gov/docs/ML1924/ML19241A472.pdf.

Nuclear Regulatory Commission, 1997, ASHPLUME Version 1.0: U.S. Nuclear Regulatory Commission, CNWRA Software Control Documentation, 61 p., ADAMS ML040020193.

Nuclear Regulatory Commission, 2020, Guidance for a Technology-Inclusive, Risk-Informed, and Performance-Based Methodology to Inform the Licensing Basis and Content of Applications for Licenses, Certifications, and Approvals for Non-Light Water Reactors: Regulatory Guide 1.233, Rev 0.

Nuclear Regulatory Commission, 2002, PVHA_YM Version 2.0: U.S. Nuclear Regulatory Commission, Software Release Notice, 32 p., ADAMS ML040780533.

Nuclear Regulatory Commission, 2021, Volcanic Hazards Assessment for Proposed Nuclear Power Reactor Sites: U.S. Nuclear Regulatory Commission, Regulatory Guide 4.26, Rev. 0, 28 p., ADAMS ML040780533.

Ogden, P., 1979, The geology, major element geochemistry, and petrogenesis of the Leucite Hills volcanic rocks, Wyoming [Thesis]: University of Wyoming, 166 p.

Olsen, K.B., and Fruchter, J.S., 1986, Chapter 5: Identification of the Physical and Chemical Characteristics of Volcanic Hazards: American Journal of Public Health, v. 76, p. 45–52, doi:10.2105/AJPH.76.Suppl.45.

OpenTopography, 2013, Shuttle Radar Topography Mission (SRTM) Global:, doi:10.5069/G9445JDF.

Oriel, S.S., and Platt, L.B., 1980, Geologic map of the Preston 1 degree by 2 degrees Quadrangle, southeastern Idaho and western Wyoming: U.S. Geological Survey Miscellaneous Investigation Series Map I–1127, doi:10.3133/i1127.

Osman, S., Thomas, M., Crummy, J., and Carver, S., 2022, Investigation of geomechanical properties of tephra relevant to roof loading for application in vulnerability analyses: Journal of Applied Volcanology, v. 11, p. 9, doi:10.1186/s13617-022-00121-2.

Oviatt, C.G., 1989, Quaternary Geology of Part of the Sevier Desert, Millard County, Utah: Utah Geological and Mineral Survey Special Series 70, 48 p.

Oviatt, C.G., Currey, D.R., and Sack, D., 1992, Radiocarbon chronology of Lake Bonneville, Eastern Great Basin, USA: Palaeogeography, Palaeoclimatology, Palaeoecology, v. 99, p. 225–241, doi:10.1016/0031-0182(92)90017-Y.

Pallister, J., and McNutt, S.R., 2015, Chapter 66 - Synthesis of Volcano Monitoring, *in* Sigurdsson, H. ed., The Encyclopedia of Volcanoes (Second Edition), Amsterdam, Academic Press, p. 1151–1171, doi:10.1016/B978-0-12-385938-9.00066-3.

Parfitt, E.A., and Wilson, L., 1995, Explosive volcanic eruptions—IX. The transition between Hawaiian-style lava fountaining and Strombolian explosive activity: Geophysical Journal International, v. 121, p. 226–232, doi:10.1111/j.1365-246X.1995.tb03523.x.

Parsons, T., and Thompson, G.A., 1991, The Role of Magma Overpressure in Suppressing Earthquakes and Topography: Worldwide Examples: Science, v. 253, p. 1399–1402, doi:10.1126/science.253.5026.1399.

Payne, S.J., McCaffrey, R., King, R.W., and Kattenhorn, S.A., 2012, A new interpretation of deformation rates in the Snake River Plain and adjacent basin and range regions based on GPS measurements: Deformation rates in the Snake River Plain: Geophysical Journal International, v. 189, p. 101–122, doi:10.1111/j.1365-246X.2012.05370.x.

Pelletier, J.D., DeLong, S.B., Cline, M.L., Harrington, C.D., and Keating, G.N., 2008, Dispersion of channel-sediment contaminants in distributary fluvial systems: Application to fluvial tephra and radionuclide redistribution following a potential volcanic eruption at Yucca Mountain: Geomorphology, v. 94, p. 226–246, doi:10.1016/j.geomorph.2007.05.014.

Peterson, J.B., and Nash, W.P., 1980, II. Geology and Petrology of the Fumarole Butte Volcanic Complex, Utah, *in* Studies in Late Cenozoic Volcanism in Utah, Utah Geological and Mineral Survey, Special Paper 52, p. 35–53.

Pickett, K.E., 2004, Physical Volcanology, Petrography, and Geochemistry of Basalts in the Bimodal Blackfoot Volcanic Field, Southeastern Idaho [Thesis]: Idaho State University, 100 p.

Pierce, K.L., and Morgan, L.A., 1992, Chapter 1: The track of the Yellowstone hot spot: Volcanism, faulting, and uplift, *in* Link, P.K., Kuntz, M.A., and Platt, L.B. eds., Regional Geology of Eatern Idaho and Western Wyoming, Geological Society of America, Geological Society of America Memoir, v. 179, p. 1–54, doi:10.1130/MEM179-p1.

Pierson, T.C., 2005, Hyperconcentrated flow — transitional process between water flow and debris flow, *in* Jakob, M. and Hungr, O. eds., Debris-flow Hazards and Related Phenomena, Berlin, Heidelberg, Springer, Springer Praxis Books, p. 159–202, doi:10.1007/3-540-27129-5_8.

Pierson, T.C., and Major, J.J., 2014, Hydrogeomorphic Effects of Explosive Volcanic Eruptions on Drainage Basins: Annual Review of Earth and Planetary Sciences, v. 42, p. 469–507, doi:10.1146/annurev-earth-060313-054913.

Pioli, L., Erlund, E., Johnson, E., Cashman, K., Wallace, P., Rosi, M., and Delgado Granados, H., 2008, Explosive dynamics of violent Strombolian eruptions: The eruption of Parícutin

Volcano 1943–1952 (Mexico): Earth and Planetary Science Letters, v. 271, p. 359–368, doi:10.1016/j.epsl.2008.04.026.

Polun, S.G., 2011, Kinematic Analysis of Late Pleistocene Faulting in the Blackfoot Lava Field, Caribou County, Idaho [Thsiss]: Idaho State University, 96 p.

Puchy, B., 1981, Mineralogy and Petrology of Lava Flows (Tertiary-Quaternary) In Southeastern Idaho and at Black Mountain, Rich County, Utah [Thesis]: Utah State University, 82 p.

Putirka, K., and Platt, B., 2012, Basin and Range volcanism as a passive response to extensional tectonics: Geosphere, v. 8, p. 1274–1285, doi:10.1130/GES00803.1.

Richardson, G.B., 1941, Geology and mineral resources of the Randolph quadrangle, Utah-Wyoming: U.S. Geological Survey Bulletin 923, doi:10.3133/b923.

Robinson, S., Taylor, C., and Moore, D., 2016, Volumes of Recently-Erupted Rhyolite Lava Flows in the Yellowstone Plateau Volcanic Field, doi:10.1130/abs/2016AM-284059.

Rodgers, D.W., Long, S.P., McQuarrie, N., Burgel, W.D., and Hersley, 2006, Geologic Map of the Inkom Quadrangle, Bannock County, Idaho: Idaho Geologic Survey Technical Report 06-2.

Root, F.K., 1972, Pumice and Scoria Prospects in the Leucite Hills, Sections 4, 10, 12, 14, and 24, T. 21 N., R. 102 W., Sweetwater County, Wyoming: Geological Survey of Wyoming Mineral Report 72–1, 5 p.

Rose, W.I., Self, S., Murrow, P.J., Bonadonna, C., Durant, A.J., and Ernst, G., 2008, Nature and significance of small volume fall deposits at composite volcanoes: Insights from the October 14, 1974 Fuego eruption, Guatemala: Bulletin of Volcanology, v. 70, p. 1043–1067, doi:10.1007/s00445-007-0187-5.

Rubin, M., and Alexander, C., 1960, U. S. Geological Survey Radiocarbon Dates V: American Journal of Science. Radiocarbon Supplement, v. 2, p. 129–185, doi:10.1017/S1061592X00020652.

Sarna-Wojcicki, A.M., Lajoie, K.R., Meyer, C.E., Adam, D.P., and Rieck, H.J., 1991, Tephrochronologic correlation of upper Neogene sediments along the Pacific margin, conterminous United States, *in* Morrison, R.B. ed., Quaternary Nonglacial Geology, Boulder, Colorado, Geological Society of America, The Geology of North America, v. K-2, p. 117–140, doi:10.1130/DNAG-GNA-K2.117.

Sarna-Wojcicki, A.M., Shipley, S., Waitt, R.B., Dzurisin, D., and Wood, S.H., 1981, Areal Distribution, Thickness, Mass, Volume, and Grain Size of Air-Fall Ash from the Six Major Eruptions of 1980, *in* The 1980 Eruptions of Mount St. Helens, Washington, U.S. Geological Survey, Professional Paper 1250, p. 577–600.

Schmandt, B., Lin, F., and Karlstrom, K.E., 2015, Distinct crustal isostasy trends east and west of the Rocky Mountain Front: Geophysical Research Letters, v. 42, doi:10.1002/2015GL066593.

Schmitt, R.G., 2017, Quaternary Faults Web Application:, doi:10.5066/F7S75FJM.

Schroeder, M.L., 1981, Geologic map and coal sections of the Elkol SW Quadrangle, Lincoln and Uinta counties, Wyoming: U.S. Geological Survey Open-File Report 81–716.

Schroeder, M.L., 1982, Geologic map and coal sections of the Meadow Draw Quadrangle, Uinta County, Wyoming: U.S. Geological Survey Open-File Report 82–533.

Schroeder, M.L., and Lunceford, R.A., 1979a, Preliminary geologic map and coal sections of the Cumberland Gap Quadrangle, Lincoln and Uinta counties, Wyoming: U.S. Geological Survey Open-File Report 79–1633.

Schroeder, M.L., and Lunceford, R.A., 1979b, Preliminary geologic map and coal sections of the west half of the Bridger Quadrangle, Uinta County, Wyoming: U.S. Geological Survey Open-File Report 79–1632.

Scollo, S., Folch, A., and Costa, A., 2008a, A parametric and comparative study of different tephra fallout models: Journal of Volcanology and Geothermal Research, v. 176, p. 199–211, doi:10.1016/j.jvolgeores.2008.04.002.

Scollo, S., Tarantola, S., Bonadonna, C., Coltelli, M., and Saltelli, A., 2008b, Sensitivity analysis and uncertainty estimation for tephra dispersal models: Journal of Geophysical Research, v. 113, p. B06202.

Scott, W.E., 1987, Holocene rhyodacite eruptions on the flanks of South Sister volcano, Oregon, *in* Fink, J.H. ed., The Emplacement of Silicic Domes and Lava Flows, Geological Society of America, Special Paper, v. 212, p. 0, doi:10.1130/SPE212-p35.

Scott, K.M., 1988, Origins, Behavior, and Sedimentology of Lahars and Lahar-Runout Flows in the Toutle-Cowlitz River System: U.S. Geological Survey Professional Paper 1447-A, 83 p.

Scott, K.M., Vallance, J.W., and Pringle, P.T., 1995, Sedimentology, Behavior, and Hazards of Debris Flows at Mount Rainier, Washington: U.S. Geological Survey Professional Paper 1547, doi:10.3133/pp1547.

Searl, A., 2002, Assessment of the exposure of islanders to ash from the Soufriere Hills volcano, Montserrat, British West Indies: Occupational and Environmental Medicine, v. 59, p. 523–531, doi:10.1136/oem.59.8.523.

Segerstrom, K.K., Williams, H., Wilcox, R.E., Foshag, W.P., and Gonzales, J.R., 1956, Geologic investigations in the Parícutin area, Mexico: U.S. Geological Survey Bulletin 965, doi:10.3133/b965.

Sehmel, G.A., 1982, Ambient airborne solids concentrations including volcanic ash at Hanford, Washington sampling sites subsequent to the Mount St. Helens eruption: Journal of Geophysical Research, v. 87, p. 11087, doi:10.1029/JC087iC13p11087.

Self, S., Goff, F., Gardner, J.N., Wright, J.V., and Kite, W.M., 1986, Explosive rhyolitic volcanism in the Jemez Mountains: Vent locations, caldera development and relation to regional structure: Journal of Geophysical Research: Solid Earth, v. 91, p. 1779–1798, doi:10.1029/JB091iB02p01779.

Self, S., Heiken, G., Sykes, M.L., Wohletz, K., Fisher, R.V., and Dethier, D.P., 1996, Field excursions to the Jemez Mountains, New Mexico: New Mexico Bureau of Geology & Mineral Resources, Bulletin 134, 73 p.

Self, S., Kienle, J., and Huot, J.-P., 1980, Ukinrek Maars, Alaska, II. Deposits and formation of the 1977 craters: Journal of Volcanology and Geothermal Research, v. 7, p. 39–65, doi:10.1016/0377-0273(80)90019-0.

Shen, W., and Ritzwoller, M.H., 2016, Crustal and uppermost mantle structure beneath the United States: Journal of Geophysical Research: Solid Earth, v. 121, p. 4306–4342, doi:10.1002/2016JB012887.

Shervais, J., 2015, Snake River Plain Geothermal Play Fairway Analysis - Volcanic Vents, Lacustrine Sediments, and post-Miocene Faults KMZ files:, doi:10.15121/1254475.

Shervais, J.W., Vetter, S.K., and Hanan, B.B., 2006, Layered mafic sill complex beneath the eastern Snake River Plain: Evidence from cyclic geochemical variations in basalt: Geology, v. 34, p. 365, doi:10.1130/G22226.1.

Siebert, L., Simkin, T., and Kimberly, P., 2011, Volcanoes of the World: University of California Press, 568 p.

Smith, R.D., and Swanson, F.J., 1987, Sediment routing in a small drainage basin in the blast zone at Mount St. Helens, Washington, U.S.A.: Geomorphology, v. 1, p. 1–13, doi:10.1016/0169-555X(87)90003-1.

Sparks, R.S.J., and Walker, G.P.L., 1977, The significance of vitric-enriched air-fall ashes associated with crystal-enriched ignimbrites: Journal of Volcanology and Geothermal Research, v. 2, p. 329–341, doi:10.1016/0377-0273(77)90019-1.

Sparks, R.S.J., Wilson, L., Sigurdsson, H., and Walker, G.P.L., 1981, The pyroclastic deposits of the 1875 eruption of Askja, Iceland: Philosophical Transactions of the Royal Society of London. Series A, Mathematical and Physical Sciences, v. 299, p. 241–273, doi:10.1098/rsta.1981.0023.

Spear, D.B., 1979, The Geology and Volcanic History of the Big Southern Butte - East Butte Area, Eastern Snake River Plain, Idaho [Thesis]: SUNY Buffalo, 148 p.

Spear, D., and King, J.S., 1982, The Geology of Big Southern Butte, Idaho, *in* B. Bonnichsen, R.M. Breckenridge, Cenozoic Geology of Idaho, Idaho Bureau of Mines and Geology, Bulletin 26, p. 395–403.

Spell, T.L., and McDougall, I., 1992, Revisions to the age of the Brunhes - Matuyama Boundary and the Pleistocene geomagnetic polarity timescale: Geophysical Research Letters, v. 19, p. 1181–1184, doi:10.1029/92GL01125.

Sulpizio, R., Dellino, P., Doronzo, P.M., and Sarocchi, D., 2014, Pyroclastic density currents: state of the art and perspectives: Journal of Volcanology and Geothermal Research, v. 283, p. 36–65, doi:10.1016/j.jvolgeores.2014.06.014.

Suzuki, T., 1983, A theoretical model for dispersion of tephra., *in* Yokoyama, I. and International Association of Volcanology and Chemistry of the Earth's Interior eds., Arc volcanism: Physics and Tectonics, Springer Dordrecht, Advances in earth and planetary sciences, p. 95–113.

Takei, Y., 2017, Effects of Partial Melting on Seismic Velocity and Attenuation: A New Insight from Experiments: Annual Review of Earth and Planetary Sciences, v. 45, p. 447–470, doi:10.1146/annurev-earth-063016-015820.

Thorsteinsson, T., Jóhannsson, T., Stohl, A., and Kristiansen, N.I., 2012, High levels of particulate matter in Iceland due to direct ash emissions by the Eyjafjallajökull eruption and resuspension of deposited ash.: Journal of Geophysical Research: Solid Earth, v. 117, doi:10.1029/2011JB008756.

Thouret, J.-C., Antoine, S., Magill, C., and Ollier, C., 2020, Lahars and debris flows: Characteristics and impacts: Earth-Science Reviews, v. 201, p. 103003, doi:10.1016/j.earscirev.2019.103003.

Tuffen, H., James, M.R., Castro, J.M., and Schipper, C.I., 2013, Exceptional mobility of an advancing rhyolitic obsidian flow at Cordón Caulle volcano in Chile: Nature Communications, v. 4, p. 2709, doi:10.1038/ncomms3709.

Turley, C.H., and Nash, W.P., 1980, I. Petrology of Late Tertiary and Quaternary Volcanism in Western Juab and Millard Counties, Utah, *in* Studies in Late Cenozoic Volcanism in Utah, Utah Geological and Mineral Survey, Special Paper 52, p. 1–34.

US Department of Commerce, 2022, NWS JetStream - The Jet Stream:, https://www.weather.gov/jetstream/jet (accessed September 2022).

U.S. Geological Survey, 2022a, Earthquake Catalog:, https://earthquake.usgs.gov/earthquakes/search/ (accessed August 2022).

U.S. Geological Survey, 1978, Geological Survey research 1978: U.S. Geological Survey Professional Paper 1100, 194 p., doi:10.3133/pp1100.

U.S. Geological Survey, 2022b, North America Rivers and Lakes - ScienceBase-Catalog:, https://www.sciencebase.gov/catalog/item/4fb55df0e4b04cb937751e02 (accessed August 2022).

U.S. Geological Survey, 2022c, The National Map Downloader v2: The National Map Downloader, https://apps.nationalmap.gov/downloader/ (accessed September 2022).

U.S. Geological Survey, 2022d, Volcanic Ash Impacts & Mitigation - Density & Hardness:, https://volcanoes.usgs.gov/volcanic_ash/density_hardness.html.

Valentine, G.A., and Connor, C.B., 2015, Chapter 23 - Basaltic Volcanic Fields, *in* Sigurdsson, H. ed., The Encyclopedia of Volcanoes (Second Edition), Amsterdam, Academic Press, p. 423–439, doi:10.1016/B978-0-12-385938-9.00023-7.

Vergniolle, S., and Jaupart, C., 1986, Separated two-phase flow and basaltic eruptions: Journal of Geophysical Research: Solid Earth, v. 91, p. 12842–12860, doi:10.1029/JB091iB12p12842.

Walker, G.P.L., 1973, Explosive volcanic eruptions — a new classification scheme: Geologische Rundschau, v. 62, p. 431–446, doi:10.1007/BF01840108.

Walker, G.P.L., Huntingdon, A.T., Sanders, A.T., and Dinsdale, J.L., 1973, Lengths of Lava Flows [and Discussion]: Philosophical Transactions of the Royal Society of London. Series A, Mathematical and Physical Sciences, v. 274, p. 107–118.

Walker, G.P.L., Self, S., and Wilson, L., 1984, Tarawera 1886, New Zealand — A basaltic plinian fissure eruption: Journal of Volcanology and Geothermal Research, v. 21, p. 61–78, doi:10.1016/0377-0273(84)90016-7.

Wardman, J.B., Wilson, T.M., Bodger, P.S., Cole, J.W., and Johnston, D.M., 2012, Investigating the electrical conductivity of volcanic ash and its effect on HV power systems: Physics and Chemistry of the Earth, Parts A/B/C, v. 45–46, p. 128–145, doi:10.1016/j.pce.2011.09.003.

Welhan, J., 2016, Gigawatt-Scale Power Potential of a Magma-Supported Geothermal System in the Fold and Thrust Belt of Southeast Idaho, *in* Proceedings, Fourty first Workshop on Geothermal Reservoir Engineering, Stanford University, Stanford California, p. 1–16.

Welhan, J., Gwynn, M., Payne, S., McCurry, M., Plummer, M., and Wood, T., 2014, The Blackfoot Volcanic Field, Southeast Idaho: A Hidden High-Temperature Geothermal Resource in the Idaho Thrust Belt., *in* Proceedings, Thirty-Ninth Workshop on Geothermal Reservoir Engineering, Stanford University, Stanford California, p. 1–13.

Westgate, J.A., WoldeGabriel, G., Halls, H.C., Bray, C.J., Barendregt, R.W., Pearce, N.J.G., Sarna-Wojcicki, A.M., Gorton, M.P., Kelley, R.E., and Schultz-Fellenz, E., 2018, Quaternary tephra from the Valles caldera in the volcanic field of the Jemez Mountains of New Mexico identified in western Canada: Quaternary Research, v. 91, p. 813–828, doi:10.1017/qua.2018.139.

Whitney, M., 2015, Evaluation of Alternatives to Address Volcanic Natural Phenomena Hazards at the Waste Treatment and Immobilization Plant: U.S. Department of Energy Attachment to Letter 14-NSD-0048, 217 p.

Williams, H., 1942, The Geology of Crater Lake National Park, Oregon: Carnegie Institution of Washington Publication 540.

Williams, D.B., and Ramsey, M.S., 2019, On the Applicability of Laboratory Thermal Infrared Emissivity Spectra for Deconvolving Satellite Data of Opaque Volcanic Ash Plumes: Remote Sensing, v. 11, p. 2318, doi:10.3390/rs11192318.

Wilson, L., 1976, Explosive Volcanic Eruptions—III. Plinian Eruption Columns: Geophysical Journal of the Royal Astronomical Society, v. 45, p. 543–556, doi:10.1111/j.1365-246X.1976.tb06909.x.

Wilson, C.J.N., 2008, Supereruptions and Supervolcanoes: Processes and Products: Elements, v. 4, p. 29–34, doi:10.2113/GSELEMENTS.4.1.29.

Wilson, L., and Huang, T.C., 1979, The influence of shape on the atmospheric settling velocity of volcanic ash particles: Earth and Planetary Science Letters, v. 44, p. 311–324, doi:10.1016/0012-821X(79)90179-1.

Wilson, L., Sparks, R.S.J., Huang, T.C., and Watkins, N.D., 1978, The control of volcanic column heights by eruption energetics and dynamics: Journal of Geophysical Research: Solid Earth, v. 83, p. 1829–1836, doi:10.1029/JB083iB04p01829.

Wilson, T.M., Stewart, C., Sword-Daniels, V., Leonard, G.S., Johnston, D.M., Cole, J.W., Wardman, J., Wilson, G., and Barnard, S.T., 2012, Volcanic ash impacts on critical infrastructure: Physics and Chemistry of the Earth, Parts A/B/C, v. 45–46, p. 5–23, doi:10.1016/j.pce.2011.06.006.

Wilson, G., Wilson, T.M., Deligne, N.I., and Cole, J.W., 2014, Volcanic hazard impacts to critical infrastructure: A review: Journal of Volcanology and Geothermal Research, v. 286, p. 148–182, doi:10.1016/j.jvolgeores.2014.08.030.

Wittke, S.J., and Heffern, E.L. Surficial Geologic Map of the Fontenelle Reservoir 30’ x 60’ Quadrangle, Lincoln, Sublette, and Sweetwater Counties, Wyoming (2013): Wyoming State Geological Survey Open-File Report 13–04.

Wood, C.A., 1980, Morphometric evolution of cinder cones: Journal of Volcanology and Geothermal Research, v. 7, p. 387–413, doi:10.1016/0377-0273(80)90040-2.

Woods, A.W., 1988, The fluid dynamics and thermodynamics of eruption columns: Bulletin of Volcanology, v. 50, p. 169–193, doi:10.1007/BF01079681.

Woods, A.W., and Wohletz, K., 1991, Dimensions and dynamics of co-ignimbrite eruption columns: Nature, v. 350, p. 225–227, doi:10.1038/350225a0.

Wyoming State Climate Office, 2022, Wyoming Climate Atlas: Precipitation - Wyoming State Climate Office and Water Resources Data System:, http://www.wrds.uwyo.edu/sco/climateatlas/precipitation.html.

Wyoming State Geological Survey, 2022, GIS Maps:, https://www.wsgs.wyo.gov/pubs-maps/gis (accessed August 2022).

Young, S.R., 1990, Physical volcanology of holocene airfall deposits from Mt Mazama, Crater Lake, Oregon. [Thesis]: University of Lancaster.

Yuill, B.T., and Nichols, M.H., 2011, Patterns of grain-size dependent sediment transport in low-ordered, ephemeral channels: Earth Surface Processes and Landforms, v. 36, p. 334–346, doi:10.1002/esp.2041.